

Long-term Variations in HF radar Backscatter



UNIVERSITY OF
LEICESTER

Hammed Adeniyi Lawal

Radio and Space Plasma Physics Group
Department of Physics & Astronomy
University of Leicester

A thesis submitted to the University of Leicester
for the degree of *Doctor of Philosophy*

June 2017

Abstract

Hammed Adeniyi LAWAL

Long-term variations in Ionospheric Morphology and activity observed with HF Radars

This thesis studies the long term variation of the high latitude ionosphere and its activity. A statistical analysis of backscatter data spanning 20 years from 1996 to 2015 in the total field of view of the two HF radars was carried out in order to determine the solar cycle, the annual and the diurnal variations of backscatter (ionospheric scatter and ground scatter) in both Super Dual Auroral Radar Network (SuperDARN) radars over a longer time period. Increase in ionospheric scatter during solar maximum previously anticipated by Milan et al., (1997b) and higher occurrence of ground scatter than ionospheric scatter were observed in the analysis.

The study in this thesis also includes investigation on the propagation mode responsible for the occurrence of ionospheric and ground backscatter. Similar to the data used in the first analysis, 20 years of data from three selected beams were employed. In this study, it was found that occurrence of ionospheric backscatter is prominent at far ranges at local day during solar cycle 23 than solar cycle 24. The analysis shows that occurrence of ionospheric scatter is seen at mid-range gates during summer in contrast to similar study carried out by Milan et al.(1997b) which identifies near range gates ionospheric scatter during similar period.

In addition, a study to identify the parameter or parameters that can be used for adequate prediction and forecast of occurrence of ionospheric backscatter for both short and long term durations was carried out. The percentage occurrence of ionospheric scatter as a function of the selected parameters in spring, summer, autumn and winter from January 1996 to January 2016 in the four magnetic local times were analysed. The study increases our understanding on the global factors responsible for the occurrence of ionospheric scatter and the local time variation on the occurrence rate. It also raises some interesting questions.

Declaration

I, Hammed Adeniyi Lawal, confirm that the research presented in this thesis is my own. Information which has been taken from external sources has been appropriately referenced.

Dedication

To my CREATOR

&

To those who live to put smile
on other peoples' face

Acknowledgements

First and foremost, all praises and adoration go to Almighty ALLAH for HIS mercy and blessings on me. In HIM I put my trust.

My deepest gratitude goes to my wife and my kids for their perseverance, endurance and going through the pain brought to us during the PhD journey. I would like to specifically thank my supervisor, Prof Mark Lester for his guidance, exceptional support, encouragement and patience starting from my first day at the University of Leicester, thank you Mark. Also, my appreciation goes to my second supervisor, Professor Tim Yeoman for his guidance, support and encouragement throughout the journey. Dr. Suzie Imber's immense contribution during this study is appreciated. Also, I do appreciate the willingness and ever-ready approach of Prof Steve Milan even at the shortest notice, thanks Steve. Dr Gabby's regular check on the welfare of my family and me is well appreciated. Prof. Stanley Cowley's encouragement throughout is appreciated. The support of Timothy David is well appreciated.

I am also grateful to all members of the Radio and Space Plasma Physics Group for their support. Nigel, your memory lives on!

Also, many thanks go to the Federal Government of Nigeria (TETFUND) for providing financial support to undertake this Ph.D programme. I am also indebted to the management of Olabisi Onabanjo University for providing the platform for me to access the funds, even though I had to struggle to complete the programme due to financial constraints as a result of their nonchalant attitude towards my welfare and my plight even at a time when I was suspended due to non-payment of balance of my tuition fees.

Finally, I will like to express my sincere appreciation to all my family and friends for the support given to me in the course of this Ph.D programme.

Table of contents

Abstract	ii
Declaration	iii
Acknowledgements	v
Table of contents	vi
List of Figures	xi
List of Tables	xv
1 Solar-Terrestrial interactions	1
1.1 Introduction	1
1.2 Plasma Physics	1
1.2.1 Particle motion	2
1.2.2 The Lorentz forces	2
1.2.3 Particle motion in a parallel magnetic field (gyromotion)	3
1.2.4 Particle motion in a convergent magnetic field (magnetic mirroring)	4
1.2.5 Particle motion with a parallel electric field	5
1.2.6 Particle motion with a perpendicular electric field (particle drift)	6
1.2.7 Particle gradients and curvature drifts	7
1.3 The Solar Wind-Magnetosphere Interactions	9
1.3.1 The Solar Wind	9
1.3.2 Solar Wind Parameters near the Earth	12
1.3.3 CME's and Fast Streams	15
1.3.4 Magnetosphere	16
1.3.5 Solar Wind-Magnetosphere Coupling	18
1.4 The Ionosphere	22

Contents

1.5	Magnetosphere-Ionosphere Coupling	23
1.5.1	Magnetosphere-Ionosphere Current system	25
1.6	Summary of the thesis	27
2	Literature review	28
2.1	Introduction	28
2.2	The Earth's Ionosphere	28
2.2	Ionospheric Structure	28
2.3	Ionospheric processes	29
2.4	D, E and F regions of the ionosphere	37
2.5	Ionospheric Variations	38
2.4.1	Diurnal Variations	39
2.4.2	Seasonal Variations	39
2.4.3	Solar cycle Variations	40
2.6	Ionospheric irregularities	40
2.7	Remote Sensing of The Ionosphere with Radio propagation ...	43
2.7.1	Radio propagation	43
2.7.2	HF propagation	46
2.8	Previous studies on ionospheric backscatter	48
2.8	Summary	57
3	Instrumentation & Data sources	58
3.0	Instrumentation	58

Contents

3.1	Introduction	58
3.2	SuperDARN	59
3.3	Pulse sequence	64
3.4	Data from Spacecraft Instruments	66
3.5	Magnetic Indices	67
3.6	Coordinates Systems	69
3.6.1	Geocentric Solar Ecliptic Coordinates (GSE)	69
3.6.2	Geocentric Solar Magnetic Coordinates (GSM)	69
3.6.3	Magnetic Local Time (MLT)	70
4	Backscatter occurrence over the life time of SuperDARN	72
4.1	Introduction	72
4.2	Instrumentation	72
4.3	Data	72
4.3	Monthly mean statistics of backscatter.....	74
4.4.1	Ionospheric backscatter	74
4.4.2	Ground backscatter	76
4.4.3	Solar cycle variation summary	77
4.5	Hourly-mean percentage occurrence statistics	78
4.5.1	Diurnal variation of ionospheric scatter	79
4.5.2	Ground backscatter hourly-mean statistics	80
4.6	Diurnal and seasonal variations	81

Contents

4.7	Discussion	86
4.7.1	Solar cycle dependence of backscatter	87
4.7.2	Annual dependences of backscatter	89
4.7.3	Diurnal variations of backscatter	90
4.8	Summary	91
5	Long term spatial variation of the Ionosphere with SuperDarn radar data	93
5.1	Introduction	93
5.2	Instrument and Data selection	93
5.3	Ground backscatter point occupancy statistics... ..	95
5.4	Ionospheric backscatter point occupancy statistics	102
5.5	Summary	109
5.6	Point occupancy as a function of radar azimuth.....	110
5.6.1	Hankasalmi ground backscatter	111
5.6.2	Hankasalmi ionospheric backscatter.....	112
5.6.3	Pykkvibaer ground backscatter	113
5.6.4	Pykkvibaer ionospheric backscatter	114
5.7	Summary	115
5.8	Discussion	116
5.8.1	Solar cycle dependences of backscatter	119
5.8.2	Seasonal dependences of backscatter	121
5.9	Conclusion	123

6	Effects of energy drivers on occurrence of backscatter	124
6.1	Introduction	124
6.2	Data	124
6.3	Occurrence of Ionospheric backscatter as a function of upstream solar wind drivers	128
6.4	Summary	140
6.5	Occurrence of Ionospheric backscatter as a function of magnetic indices	140
6.6	Summary	147
6.7	Discussion	147
6.8	Conclusions	150
7	Conclusion and Future work	196
7.1	Conclusion	152
7.2	Future work	154
	Appendices	156
	References	198

List of Figures

1.1	Schematic illustration of magnetic mirroring.	5
1.2	Schematic diagram of particle motion in a magnetic field	8
1.3	Illustration of the direction of energetic charged particles drift	9
1.4	The Interplanetary magnetic field (IMF) in the solar wind.	11
1.5	The ballerina model of current sheet in the solar wind.	13
1.6	The spiral interplanetary magnetic field in the ecliptic plane.	14
1.7	Schematic illustration of CIR structure in solar equatorial plane.	16
1.8	Illustration of regions of the Earth's Magnetosphere.	18
1.9	Magnetic reconnection of the interplanetary and terrestrial magnetic fields. . . .	20
1.10a	Dungey diagram illustrating reconnection.	21
1.10b	Dungey diagram illustrating northward and southward reconnection.	21
1.11	Schematic illustration of the two-cell convection pattern.	22
1.12	Illustration of the plasma flow regimes in the Earth's Ionosphere.	23
1.13	Illustration of the physics of magnetosphere-ionosphere coupling	24
1.14	Schematic illustrations of magnetosphere-ionosphere current systems. . . .	25
1.15	Illustration of ionospheric convection with Dungey cycle.	26
2.1	Typical daytime electron concentration (blue curve) profile.	30
2.2	Schematic representation of photo-ionization	33
2.3	Atmospheric wind system in the northern hemisphere	35
2.4	Illustration of electromagnetic drift caused by west-to-east electric	36
2.5	Schematic diagram showing the basic mechanics of $\mathbf{E} \wedge \mathbf{B}$ instability	42
2.6	A schematic diagram of some of the possible propagation modes	47
2.7	Scattering occurrence for different years, from Ruohoniemi	49
2.8	Ionospheric and ground backscatter occurrence	51
2.9	Quiet-time echo statistics with each column of panels represents one year	53
2.10	Plots of raw occurrence versus magnetic local time (MLT)	54
2.11	Echo occurrence rates for periods of minimum.	56
2.12	Monthly average plots of ionospheric backscatter occurrence.	57
3.1	Fields-of-view of SuperDARN Radars	63

3.2	Range time intensity plot	
3.3	Schematic representation of SuperDARN radar seven-pulse sequence	66
3.4	AU index and AL index.....	68
3.5	Orthographic plot illustrating the GSM coordinate systems.....	70
4.1	Radar field of view of Hankasalmi and Pykkvibaer	73
4.2	Monthly mean percentage occurrence of backscatter.....	75
4.3	Hourly percentage occurrence of ionospheric backscatter as a function of UT	79
4.4	Hourly percentage occurrence of ground backscatter as a function of UT	81
4.5	Seasonal variation of percentage occurrence of ionospheric backscatter as a function of UT for Hankasalmi radar.....	82
4.6	Seasonal variation of percentage occurrence of ionospheric backscatter as a function of UT for Pykkvibaer radar	83
4.7	Seasonal variation of percentage occurrence of ground backscatter as a function of UT for Hankasalmi radar.....	84
4.8	Seasonal variation of percentage occurrence of ground backscatter as a function of UT for Pykkvibaer radar	86
5.1	Illustration of the selected beams within the field of view of Hankasalmi and Pykkvibaer	94
5.2	Point occupancy statistics of ground backscatter of Hankasalmi and Pykkvibaer for the month of March	96
5.3	Point occupancy statistics of ground backscatter of Hankasalmi and Pykkvibaer for the month of June	97
5.4	Point occupancy statistics of ground backscatter of Hankasalmi and Pykkvibaer for the month of September	99
5.5	Point occupancy statistics of ground backscatter of Hankasalmi and Pykkvibaer for the month of December	101
5.6	Point occupancy statistics of ionospheric backscatter of Hankasalmi and Pykkvibaer for the month of March	103
5.7	Point occupancy statistics of ionospheric backscatter of Hankasalmi and Pykkvibaer for the month of June	105
5.8	Point occupancy statistics of ionospheric backscatter of Hankasalmi and Pykkvibaer for the month of September	107
5.9	Point occupancy statistics of ionospheric backscatter of Hankasalmi and Pykkvibaer for the month of March	108

5.10	Point occupancy statistics of ground backscatter of Hankasalmi beam 1 And beam 14 for the month of March.....	111
5.11	Point occupancy statistics of ionospheric backscatter of Hankasalmi beam 1 for the month of March.....	113
5.12	Point occupancy statistics of ground backscatter of Pykkvibaer beam 1 for the month of March.....	114
5.13	Point occupancy statistics of ionospheric backscatter of Pykkvibaer beam 1 for the month of March	115
6.1a	Hankasalmi Not-normalised percentage occurrence of ionospheric scatter as a function of Bz (winter seasons)	126
6.1b	Hankasalmi Not-normalised percentage occurrence of ionospheric scatter as a function of Bz (summer season).....	127
6.2a	Hankasalmi Normalised percentage occurrence of ionospheric scatter as a function of Bz (winter seasons).....	129
6.2b	Hankasalmi Normalised percentage occurrence of ionospheric scatter as a function of Bz (summer seasons).....	130
6.3	Hankasalmi Normalised percentage occurrence of ionospheric scatter as a function of Pressure (spring seasons)	132
6.4	Hankasalmi Normalised percentage occurrence of ionospheric scatter as a function of Bz (spring seasons)	133
6.5	Hankasalmi Normalised percentage occurrence of ionospheric scatter as a function of By (spring seasons)	135
6.6	Pykkvibaer Normalised percentage occurrence of ionospheric scatter as a function of Pressure (spring seasons)	137
6.7	Pykkvibaer Normalised percentage occurrence of ionospheric scatter as a function of Bz (spring seasons)	138
6.8	Pykkvibaer Normalised percentage occurrence of ionospheric scatter as a function of By (spring seasons)	139
6.9	Hankasalmi Normalised percentage occurrence of ionospheric scatter as a function of AU (spring seasons)	141
6.10	Hankasalmi Normalised percentage occurrence of ionospheric scatter as a function of AE (spring seasons)	143

6.11	Pykkvibaer Normalised percentage occurrence of ionospheric scatter as a function of AU (spring seasons)	144
6.12	Pykkvibaer Normalised percentage occurrence of ionospheric scatter as a function of AE (spring seasons)	146

List of Tables

1.1	Typical Solar Wind Parameters at 1 AU	14
3.1	SuperDARN radars in the northern hemisphere	61
3.2	SuperDARN radars in the southern hemisphere	62
5.1	Frequency of operation of Hankasalmi radar	120
5.2	Frequency of operation of Pykkvibaer radar	120

Chapter 1.

Solar-Terrestrial Interactions

1.1 Introduction

The Earth is surrounded by a highly dynamic, coupled system of plasmas and magnetic fields, whose complex interplay constitutes the subject of solar terrestrial physics. Extreme events in the solar terrestrial system are often referred to as space weather which requires an understanding of the origins and manifestations of solar activity and the propagation of solar originated effects through the heliosphere to locations where human activities take place (Hapgood, 2002). These effects include biological effects, technical or engineering effects at the surface e.g electric power brownouts and blackouts due to damaging currents induced in electric power grids, damage to satellites caused by high energy particles, loss of HF communications, changes in atmospheric drag on satellites, disruption of UHF satellite links and errors in Global Positioning Systems (GPS). Space weather dynamics and the coupled system of plasmas can only be understood with adequate knowledge of the Earth's ionosphere and magnetosphere (magnetosphere-ionosphere coupling). This chapter gives a brief overview of the solar terrestrial interaction starting with a discussion of the basic plasma physics underpinning the work which is followed by general descriptions of the solar wind, magnetosphere, solar wind magnetosphere interactions, the Earth's ionosphere and finally ionosphere-magnetosphere coupling.

1.2 Plasma Physics

A plasma is a gas which comprises of electrically charged particles, which is considered to possess the property of quasi-neutrality property, i.e. it is electrically neutral, when considered as a whole. Plasmas in solar terrestrial environments are referred to as space plasma. Plasma consists of an almost equal number of charged particles, ions (positive) and electrons (negative). Different types of forces including electric, magnetic, gravitational and other forces affect space plasmas. The dominant force in the interactions of ions and electrons with electric and magnetic fields, or plasma dynamics, is the electromagnetic force. Grant and Phillips (1990) note that four equations, known as Maxwell's equation are very important when considering electromagnetism. The equations are also used to describe a magnetised

fluid. The equations are, Gauss' law (given in equation 1.1) which states that there is a relationship between any divergence in an electric field and some finite charge density. The second law is the law of no magnetic monopoles (given in equation 1.2) which states that a magnetic field has no overall divergence. The third equation is Faraday's law (given in equation 1.3) which illustrates the electric field induced in the presence of a magnetic field which varies with time. Finally, the fourth is known as Ampere-Maxwell's law (given in equation 1.4) which implies that a current sheet (e.g., magnetospheric currents discussed in section 1.1) always separates two different magnetic fields which are next to each other.

$$(a) \quad \nabla \cdot \mathbf{E} = \frac{\rho_q}{\epsilon_0} \quad (b) \quad \int E \cdot dS = \frac{Q}{\epsilon_0} \quad (1.1)$$

$$(a) \quad \nabla \cdot \mathbf{B} = 0 \quad (b) \quad \int B \cdot dS = 0 \quad (1.2)$$

$$(a) \quad \nabla \times \mathbf{E} = -\frac{\partial \mathbf{B}}{\partial t} \quad (b) \quad \int E \cdot dI = -\int \frac{\partial \mathbf{B}}{\partial t} \cdot d\mathbf{S} \quad (1.3)$$

$$(a) \quad \nabla \times \mathbf{B} = \mu_0 \mathbf{j} + \mu_0 \epsilon_0 \frac{\partial \mathbf{E}}{\partial t} \quad (b) \quad \int B \cdot dI = \mu_0 I + \mu_0 \epsilon_0 \int \frac{\partial \mathbf{E}}{\partial t} \cdot d\mathbf{S} \quad (1.4)$$

where E is the electric field in volts, ρ_q is the charge density in Coulombs per cubic metre, $\epsilon_0 = 8.854 \times 10^{-12}$ farads per metre is the permittivity of free space, B in Teslas (T) is the magnetic field, j is the current density in Amperes per square metre, and $\mu_0 = 4\pi \times 10^{-7}$ Henry's per metre. The next section discusses the approach in solving those equations in the use of plasma.

1.2.1 Particle motion

The motion of a particle in an electromagnetic medium can be describe by understanding how particle behaves under different forces acting on it.

1.2.2 The Lorentz forces

Charged particles in an electromagnetic environment (background electric and magnetic fields) will be accelerated by a force known as Lorentz force (Grant and Phillips, 1990), \mathbf{F}_L , which is represented in equation 1.5.

$$\mathbf{F}_L = q(\mathbf{E} + \mathbf{v} \times \mathbf{B}) \quad (1.5)$$

where the charge on the particle q is in Coulombs, with mass m and the velocity of the particle \mathbf{v} in metres per second.

Adding a non-electromagnetic force term acting \mathbf{F}_g , to equation 1.5 gives the total force \mathbf{F}_T acting on the charged particle. Hence, we obtain equation 1.6;

$$\mathbf{F}_T = \mathbf{F}_L + \mathbf{F}_g = q(\mathbf{E} + \mathbf{v} \times \mathbf{B}) + \mathbf{F}_g \quad (1.6)$$

We can derive the rate of change of momentum from equation 1.6 as follows;

$$\mathbf{F}_T = m \frac{d\mathbf{v}}{dt} = q(\mathbf{E} + \mathbf{v} \times \mathbf{B}) + \mathbf{F}_g \quad (1.7)$$

This total force can then be used to calculate the rate of change of momentum, $m\mathbf{v}$, on a particle.

1.2.3 Particle motion in a parallel magnetic field (gyromotion)

If we consider a charged particle moving in a region that consists of a uniform magnetic field \mathbf{B} and no electric field, the particle experiences a Lorentz force (given in equation 1.8). If the force acting on such particle is perpendicular to the magnetic field \mathbf{B} , the force does no work on the particle. If the velocity \mathbf{v} of the charge particle is perpendicular to the magnetic field lines, the particle moves in a circular motion. The circular motion is called gyromotion. The radius, r , of the circle known as the gyroradius can be obtained by equating the Lorentz force with the centripetal force.

$$\mathbf{F}_L = q(\mathbf{v} \times \mathbf{B}) \quad (1.8)$$

$$m \frac{v^2}{r} = q(\mathbf{v} \times \mathbf{B}) \Rightarrow r_g = \frac{mv_{\perp}}{qB} \quad (1.9)$$

The gyroperiod of the particle is obtained by dividing the distance travelled by the particle (the circumference) by its velocity;

$$\tau_g = \frac{2\pi m}{qB} \quad (1.10)$$

The frequency at which the particle gyrates, the gyrofrequency, can be obtained from equation 1.10.

$$\Omega_g = \frac{qB}{m} \quad (1.11)$$

1.2.4 Particle motion in a convergent magnetic field (magnetic mirroring)

Imagine a charged particle that travels in a converging magnetic field, with the direction of travel of the particle is in the direction of increasing field strength the Lorentz force derived in equation 1.5, will have a component pointing away from the direction of travel if the force acts perpendicular to the magnetic field, \mathbf{B} . Hence, the particle will accelerate in the opposite direction to its initial velocity and is reflected from the ambient magnetic field. The reflection process of the particle is known as magnetic mirroring and is illustrated in Figure 1.1. We can deduce the point at which such a particle mirrors at $t = 0$ through the first adiabatic invariants which change very slowly and are associated with each type of motion the particle can perform (Baumjohann and Treumann, 1997) as follows:

$$\frac{v_{\perp}^2}{B} = \text{constant} = \frac{v_{\perp 0}^2}{B_0} \quad (1.12)$$

where v_{\perp} is the component of the particles velocity perpendicular to B , the constant is known as the first adiabatic invariant, $v_{\perp 0}$ is the component of the particles velocity perpendicular to B at $t = 0$ and B_0 is the magnetic field at $t=0$.

The point at which the particle mirror along the field lines given in equation 1.13 can be determined by conserving the first adiabatic invariant during the motion of the particle,

$$B_m = B_0 \left(\frac{v}{v_{\perp 0}} \right)^2 \quad (1.13)$$

The motion of the particle can be quantified using the pitch angle which is the angle between the vector of the particle's velocity and the direction of the magnetic field, given by equation 1.14

$$\tan \alpha = \frac{v \sin \alpha}{v \cos \alpha} = \frac{v_{\perp}}{v_{\parallel}} \quad (1.14)$$

If we substitute $v \sin \alpha$ into the left hand side of equation 1.12, the first adiabatic invariant becomes

$$\frac{v^2 \sin^2 \alpha}{B} = \text{constant} \quad (1.15)$$

If $\alpha \rightarrow \pi/2$, $B \rightarrow B_m$, and v is constant, we can re-write equation 1.14 as follows;

$$\frac{v^2 \sin^2 \alpha}{B} = \frac{v^2}{B_m} \quad (1.15)$$

The magnetic mirror point, B_m can be calculated from equation 1.15 if v is constant and α is measured at some field strength B .

$$B_m = \frac{B}{\sin^2 \alpha} \quad (1.16)$$

where $\alpha = 90^\circ$. Equation 1.16 shows that a particle mirror point depends only on the particles pitch angle.

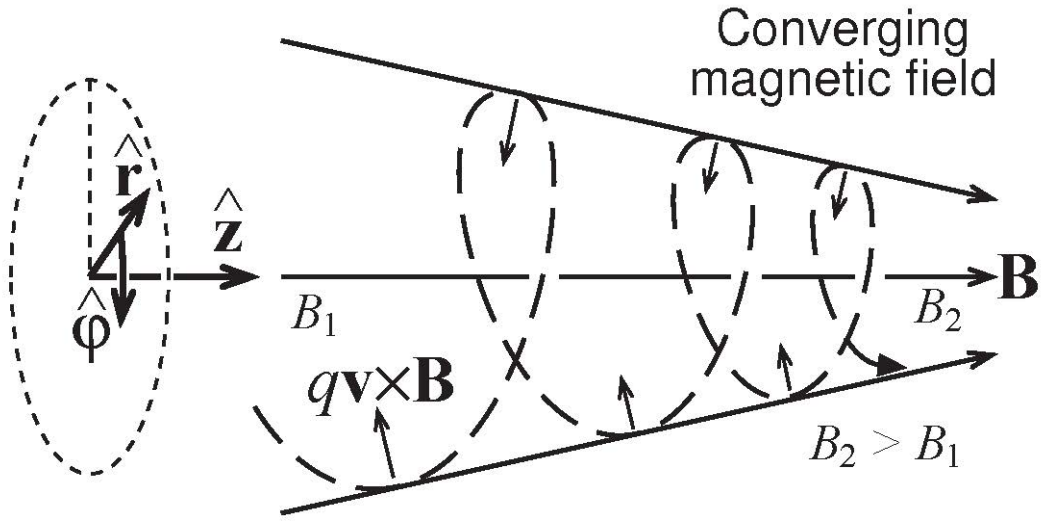


Figure 1.1 Schematic illustration of magnetic mirroring, the \hat{z} direction shows the direction of the converging magnetic field lines, the dashed line represents the path of a gyrating particle around z-axis with a component of its velocity in the \hat{z} direction and the small arrows indicate the Lorentz force on the particle. (Courtesy S.E. Milan).

1.2.5 Particle motion with a parallel electric field

The velocity of a particle along a magnetic field will be constant if the particle travels in an environment where the electric field is zero, that is, in the absence of an electric field. The velocity will no longer be constant if an electric field \mathbf{E} is introduced. Let us consider a case where the electric field introduced has some component \mathbf{E}_{\parallel} parallel to the magnetic field \mathbf{B} in the z direction. We can derive the time derivative of the particle velocity in the z direction as;

$$\frac{dv_z}{dt} = \frac{qE_{\parallel}}{m} \quad (1.17)$$

Equation 1.17 can be integrated with respect to t to obtain the velocity of the particle in the z direction as a function of the applied parallel electric field E_{\parallel} . The implication of the dependence of the velocity along the z direction, v_z , on q is that positively charged particles will move in the direction of the parallel electric field and the negatively charged particles will move in the opposite direction to the direction of the parallel electric field creating an electric field which is exactly opposite to E_{\parallel} due to the separation of charge. A state of equilibrium between the two fields will be reached due to the first field causing the movement of particles and the second field becoming larger which result in the net electric field parallel to B to become zero, i.e.

$$E_{\parallel} = 0 \quad (1.18)$$

1.2.6 Particle motion with a perpendicular electric field (particle drift)

If we consider a case where the electric field is perpendicular to the magnetic field, the presence of perpendicular electric field gives an additional velocity independent of charge and mass known as the drift velocity of the particle (Baumjohann and Treumann, 1997) given by equation 1.19

$$\mathbf{v}_d = \frac{\mathbf{E} \times \mathbf{B}}{B^2} \quad (1.19)$$

Due to the non-dependence of drift velocity on charge and mass, particles having different charge and mass will move at the same velocity.

Consider the motion of a particle with a perpendicular electric field where $\mathbf{B} = B\hat{\mathbf{z}}$, and the $\mathbf{E} = E_{\perp}$. Due to the presence of the electric field, the particle at rest will be accelerated and gains velocity. The particle will gyrate due to the Lorentz force, $q\mathbf{v} \times \mathbf{B}$ term. Increase in the Lorentz force on the particles leads to the particle moving in the opposite direction due to the acceleration provided by the electric field. The particle motion along the y direction will slow down, ultimately reverse and then the particle will move in the direction of the acceleration due to electric field, \mathbf{E} . The effect of the motion results in the particle exhibiting hopping motion with a resultant flow of particles in the direction of $\mathbf{E} \times \mathbf{B}$.

The total velocity of the particle given by equation 1.20 will include the drift velocity and any other velocity along the magnetic field.

$$\mathbf{v} = \frac{\mathbf{E} \times \mathbf{B}}{B^2} + v_z \hat{\mathbf{B}} \quad (1.20)$$

Particles moving in a bulk plasma motion frame will gyrate in circles due to the magnetic field with no effect from the electric field and no drift in such frame. Hence, if there is plasma drift, V , there is a corresponding perpendicular electric field given by equation 1.21

$$\mathbf{E} = -\mathbf{V} \times \mathbf{B} \quad (1.21)$$

Equation 1.21 and 1.20 can be shown to be equivalent to each other by crossing equation 1.21 with \mathbf{B} . The magnetic field and the direction of the motion of plasmas within the magnetosphere of planets are not constant. There exist gradients in the magnetic field \mathbf{B} and curvature of \mathbf{B} experienced by such plasmas. Hence, the effect of gradients is discussed in section 1.1.6.

1.2.7 Plasma gradients and curvature drifts

It was discussed in section 1.1 that a particle in a uniform magnetic field will gyrate around its guiding centre with a radius r_g given in equation 1.22 with no electric field.

$$r_g = \frac{v_{\perp}}{\Omega} = \frac{mv_{\perp}}{qB} \quad (1.22)$$

The instantaneous gyroradius of a particle that gyrates in a magnetic field with a gradient perpendicular to \mathbf{B} will change with time due to the fact that the gyroradius depends on the strength of the magnetic field. The radius of the particle will alternate with a drift velocity given by

$$\mathbf{v}_g = \frac{1}{2} m v_{\perp}^2 \frac{\mathbf{B} \times \nabla B}{qB^3} \quad (1.23)$$

From equation 1.23, the direction of the drift velocity is perpendicular to both the gradient in the magnetic field, ∇B , and the magnetic field, \mathbf{B} and depends on the charge of the plasma particles which implies that the gradient drift of the plasma induced a current.

If we consider a dipolar magnetic field, particles gyrating about the curved field lines will experience a centrifugal acceleration. Bittencourt (2013), noted that the particles gyroradius will increase away from the field curvature hence, the direction the particles will drift will be perpendicular to the magnetic field and the radius of curvature with a velocity \mathbf{v}_c given by

$$\mathbf{v}_c = -\frac{mv_{\parallel}^2}{R_c q B^2} \mathbf{B} \times \hat{\mathbf{n}} \quad (1.24)$$

where \hat{n} is the unit vector normal to the field curvature and R_c is the radius of the field curvature. Equation 1.24 shows that the curvature drift depends on charge which also implies that a plasma drifting in a curved magnetic field will produce a current.

Particles in a dipolar or near dipolar magnetic field are subjected to both gradient and curvature drifts with the occurrence of both drifts in same direction. Hence, gradient and curvature drifts of particles in planetary magnetosphere such as Earth's magnetosphere can be considered together as one drift, gradient-curvature drift (shown in figure 1.2). A schematic illustration of the particle motion in a magnetic field is shown in figure 1.2. The drift motion of the particle due to the gradient and curvature of a dipolar magnetic field is shown on the right, the diagram in the middle shows the bounce motion of a particle trapped between two areas of increasing magnetic field strength and the diagram on the left illustrate a particle frozen –into the magnetic field gyrating along field line.

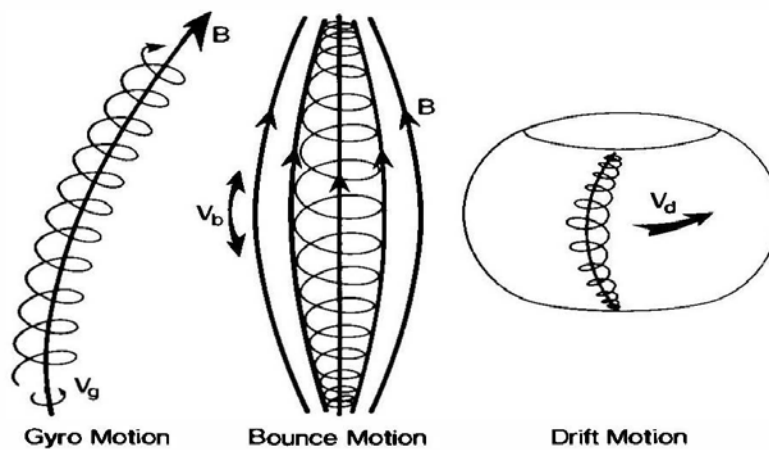


Figure 1.2 Schematic diagram of particle motion in a magnetic field, the diagram on the right shows the drift motion of particle due to the gradient and curvature of a dipolar field, the diagram in the middle shows the bounce motion of a particle trapped between two areas of increasing magnetic field strength and the diagram on the left illustrate a particle frozen –into the magnetic field gyrating along field line. Adapted from Kivelson and Russell (1995).

The direction of the gradient-curvature drift in the earth's magnetosphere is such that positively charged particles (ions) drift around the earth in the westward direction and electrons drift in the eastward direction shown in Figure 1.3. The positive ions drift forms the westward flowing current known as the ring current which reduces the strength of the magnetic field in low latitude.



Figure 1.3 Illustration of the direction of energetic charged particles drift in the earth's dipolar magnetic field; electrons drift eastward in the direction of the earth's rotation, and protons drift westward. Taken from Kivelson and Russell (1995).

1.3 The Solar Wind -Magnetosphere Interactions

1.3.1 The Solar Wind

The existence of the solar wind was theoretically modelled by Eugene N. Parker in 1958 and experimentally verified in 1962 (Schwenn, 2001). The solar wind is a stream of energized, charged particles, primarily electrons and protons, which flow outward from the sun, through the solar system. At 1 AU the solar wind speed is typically 400 km s^{-1} and can increase to values in excess of 900 km s^{-1} while the temperature is $100,000 \text{ K}$. The solar wind is a streaming dynamic flux of particles generated from the sun's corona due to changes in the pressure of the sun's atmosphere (gas) between the hot, dense gas in the solar atmosphere and the cold, tenuous gas in the background interstellar medium (Dryer, 1987). Dryer (1987) noted that the pressure difference easily overcomes the sun's gravitational pull on the plasma. The solar wind can be classified into two categories. The first category is the slow streaming charged particles originating above and near the sun's closed magnetic field loops and from the corona which reach the typical values of 400 km s^{-1} . The second category is the fast streaming plasma which originates in the cooler, less dense regions associated with coronal holes (Dryer, 1987). The magnetic field lines are said to be open in this region and the fast solar wind can reach speeds above 700 km s^{-1} .

The solar wind flows into interplanetary space and interacts with the Earth's magnetic field, ionosphere and the atmosphere. Due to its conducting (electrical conductivity) nature, the solar wind carries along with it the sun's magnetic field, also known as the Interplanetary Magnetic Field (IMF), from its origin into outer space in a spiral pattern with a radial trajectory illustrated in Figure 1.4 This is known as frozen-in flow and the spiral pattern of the IMF, is due to the solar rotation added to the radial trajectory of the solar wind flow. The radial motion of the solar wind is the reason why the interplanetary magnetic field lines become stretched (Wilcox, 1968). This phenomenon can also be explained in terms of the kinetic energy of the two components, the solar wind and the interplanetary magnetic field. The kinetic energy of the solar wind particles is higher than the energy density of the magnetic field by a factor of about eight, which has been identified as the reason why the motion of the IMF-plasma (IMF embedded in the solar wind) is governed by the motion of the particles rather than by the solar magnetic field (Hunsucker, 2002). Solar wind parameters at 1 AU are discussed at section 1.2.2.

One of the properties of magnetic field lines is their ability to act like perfect conductors transmitting perpendicular electric fields and voltages across vast distances with no change in the potential in the direction parallel to **B** (Kelley 1989a). Such a property of the magnetic field makes the IMF-plasma or similarly magnetised plasma act as a voltage source if there is a component of **V**, the flow velocity, perpendicular to **B**. The relationship between the electric field, **E** and the velocity of such magnetised plasma has been expressed mathematically by equations 1.21 and 1.25

$$\mathbf{V}_{\perp} = \mathbf{E} \wedge \mathbf{B}/B^2 \quad (1.25)$$

A very important early finding of solar-terrestrial interactions is the fact that the embedded IMF within the solar wind has different magnetic sectors (Figure 1.4) as it expands into space giving the interplanetary magnetic field lines an alternating inward and outward sectors (Hunsucker, 2002; Kelley, 1989). The pattern of the interplanetary magnetic field in the solar wind and the interplanetary magnetic field sectors structure showing inward (negative) and outward (positive) polarity as observed from the Earth is illustrated in Figure 1.4.

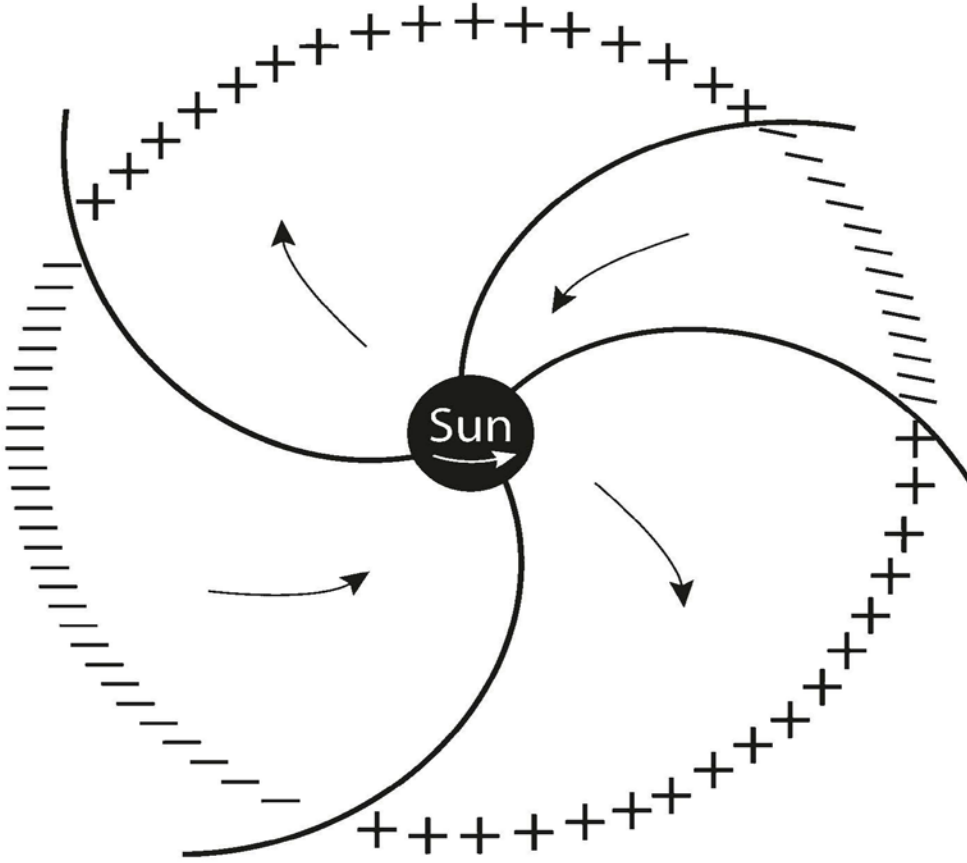


Figure 1.4 The Interplanetary magnetic field (IMF) in the solar wind showing the IMF sectors structure with inward (negative) and outward (positive) polarity as observed from the Earth taken from Zolesi (2013).

In the solar wind model, Ampere-Maxwell's equation (given in equation 1.4) shows the presence of a current sheet separating the sectors of the stretched magnetic field lines if the adjacent magnetic fields geometries are antiparallel (Kelley 1989). Equation 1.4 can be written as equation 1.26.

$$\nabla \wedge \mathbf{B} = \mu_o \mathbf{J} \quad (1.26)$$

The magnetic field line spirals into a disc like geometry that has flutes similar to a ballerina skirt with the outward-pointing field lines lying above the current sheet which lies near the sun's equator and the inward-pointing field lines is shown lying below the current sheet (Schunk & Nagy, 2009). The rotation of the sun will make an observer near the ecliptic reference frame, e.g. near Earth, appear alternately above and below the current sheet and also see the changing sector pattern of the interplanetary magnetic field. This implies that the spiralled interplanetary magnetic

field will be directed toward or away from the sun. The sun's rotation rate is 27 days per cycle. The observed IMF at Earth tends to make an angle of $\sim 45^\circ$ or $\sim 225^\circ$ with the Sun-Earth direction whether it is directed away or towards the earth (Schrijver & Siscoe, 2009).

The position of the current sheet determines the direction of the interplanetary magnetic field lines at least in the Geocentric Solar Ecliptic (GSE) Y-X plane, where X points towards the Sun, Z is perpendicular to the ecliptic plane and Y completes the Cartesian system. The implication of the changing sector of the spiralled interplanetary magnetic field lines and the position of the current sheet is that the Earth system will be affected when the direction of the IMF is toward or away from the sun. The axis of rotation of the sun discussed above is illustrated in Figure 1.5 represented by Ω and the axis of the current sheet represented by M. Also, the inclination of the current sheet with respect to the ecliptic plane has been identified to produce a northward or southward component of the interplanetary magnetic field relative to an axis normal to the plane (Kelley, 1989). Solar wind parameters including the embedded IMF are often specified in three mutually perpendicular components with respect to the fixed axes in the GSE system described above (Kelley, 1989). Figure 1.6 is adapted from (Kelley, 1989) and illustrates the magnetic field in the GSE system. The orientation of the interplanetary magnetic field in the z axis of GSE system, B_z could either be positive or negative, i.e. northward or southward respectively.

1.3.2 Solar Wind Parameters near the Earth

The Sun's streaming plasma is highly structured and varies over many different temporal and spatial scales in the solar system due to small scale time variations, waves, coronal mass ejections, shocks and flares (Schwenn, 2001; Schunk & Nagy, 2009). Typical average solar wind parameters for both slow streams and fast streams at 1 AU are given in Table 1.1.

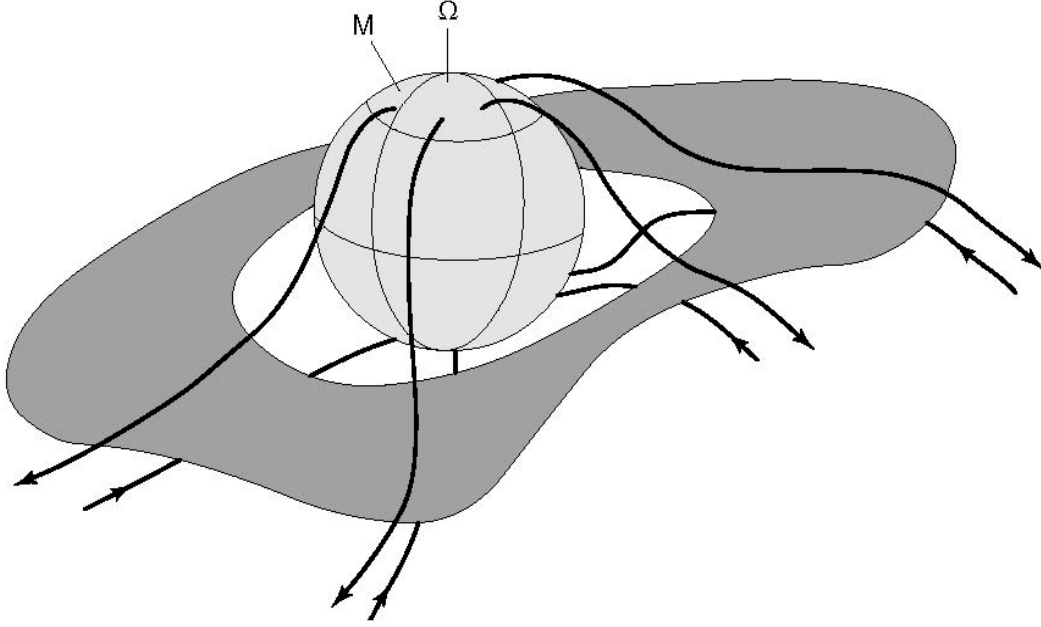


Figure 1.5. The ballerina model of current sheet in the solar wind, illustrating the axis of rotation of the sun and the current sheet axis, taken from Hunsucker (2002).

The solar wind dynamic pressure, P_G , and the solar wind magnetic pressure, P_B , are given by equation 1.27 and 1.28 respectively.

$$P_G = q = \rho u^2 / 2 \quad (1.27)$$

$$P_B = B^2 / (8\pi) \quad (1.28)$$

where ρ the mass density, u the flow velocity and B is the magnetic field.

The time taken for a packet of the solar wind leaving the Sun to reach the Earth is typically 2 to 3 days with its speed ranging from 200 to 900 km s⁻¹ and the density ranging from 1 to 80 cm⁻³ (Schunk & Nagy, 2009). As the solar wind moves away from the Sun, it expands and cools with a decrease in the electron temperature from a temperature of one million kelvin in the corona to 100,000K near the Earth environment, while the interplanetary magnetic field strength decreases with distance from the Sun from 100,000 nT at the solar surface to about 5 nT near the Earth environment (Schunk & Nagy, 2009).

The parameters given in Table 1.1 include solar wind flow speed, solar wind dynamic pressure and the composition of the streaming plasma. The solar wind flow speed is usually much higher than the local sound and Alfvén speeds which is the speed at which hydromagnetic waves (Alfvén waves) can be propagated in magnetically dominated plasma.

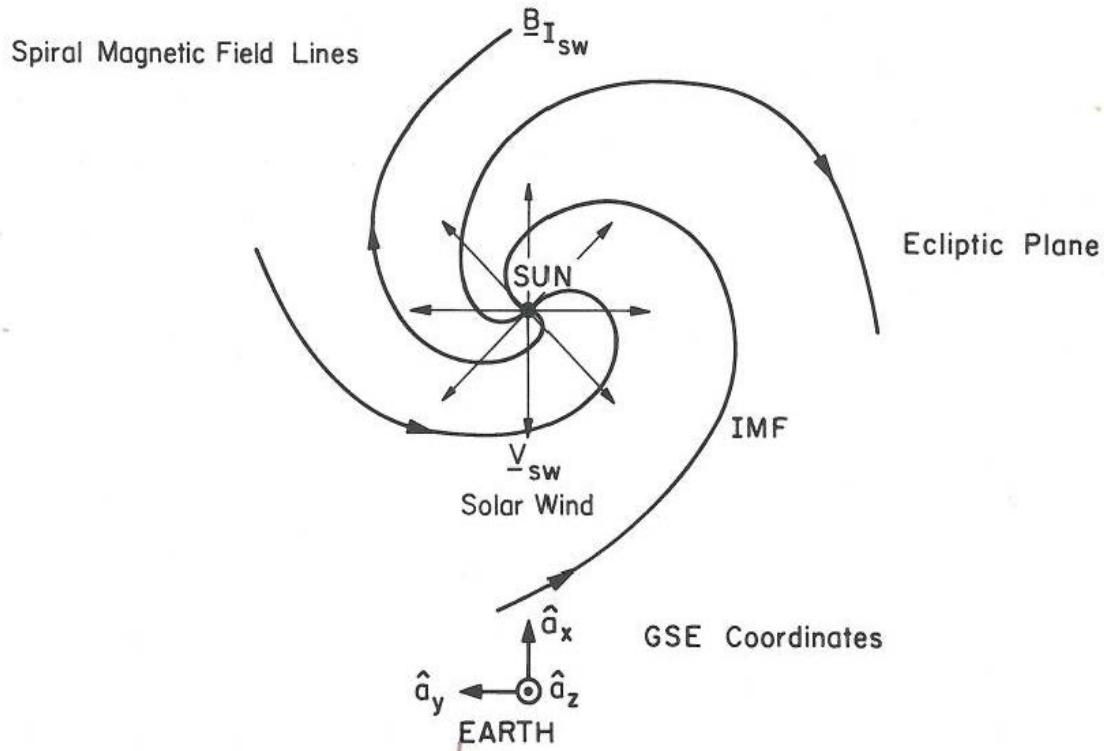


Figure 1.6. The spiral interplanetary magnetic field in the ecliptic plane in the solar wind stretching out from the surface of the sun in GSE coordinate system showing one away and one inward sector as it sweeps by the terrestrial planet, the earth adapted from Kelley (1989a).

Table 1.1: Typical Solar Wind Parameters at 1 AU.

Properties	Slow Wind	Fast Wind
Flow speed (u_p)	250 – 350 kms ⁻¹	400 – 800 kms ⁻¹
Magnetic field (B)	4 nT	5 nT
Proton density (n_p)	10.7 cm ⁻³	3.0 cm ⁻³
Proton flux density ($n_p v_p$)	3.7 x 10 ⁸ cm ⁻² s ⁻¹	2.0 x 10 ⁸ cm ⁻² s ⁻¹
Proton Temperature (T_p)	3.4 x 10 ⁴ K	2.3 x 10 ⁵ K
Electron Temperature (T_e)	1.3 x 10 ⁵ K	1 x 10 ⁵ K
Momentum flux density	2.12 x 10 ⁸ dyn cm ⁻²	2.26 x 10 ⁸ dyn cm ⁻²
Total energy flux density	1.55 erg cm ⁻² s ⁻¹	1.43 erg cm ⁻² s ⁻¹
Protons (H ⁺) content	93-95 %	96 %
α -particle (He ⁺⁺) content	4-5 %	4 %
Solar wind dynamic pressure (P_G)	0.87	1
Solar wind magnetic pressure (P_B)	0.636	0.994

A typical Mach number for the solar wind at the Earth is around 10 meaning that the solar wind dynamic pressure which is a function of the speed of the solar wind and the density is much higher than both the magnetic pressure and the thermal pressure and thus the plasma is supersonic. Furthermore, the magnetic field is frozen-in to the streaming flow

(Schwenn, 2001). In the solar system, the dynamic pressure of the solar wind expressed in equation 1.27 dominates the solar wind magnetic pressure expressed in equation 1.28. The dominance of the dynamic pressure over the magnetic pressure is of great importance in the geo-effectiveness of the solar wind. The rotation of the Sun and changes in solar activity subject the solar wind to change.

The interaction of the solar wind with the Earth's magnetic field creates a magnetic cavity called the Earth's Magnetosphere, which is discussed in section 1.3.6. Before that, however, the way in which extremely high values in the solar wind parameters are caused is discussed.

1.3.3 CME's and Fast Streams

Coronal Mass Ejections are impulsive solar/coronal ejecta which consist of large eruptions or structures of plasma and magnetic field from the sun expelled into the heliosphere (Kamide et al., 1998b; Howard, 2011). These large eruptions or structures of plasma become entrained on an expanding magnetic field, in the form of helical field lines often referred to as a flux rope (Webb and Howard, 2012). CME's can contain a mass larger than 10^{13} kg and may achieve a speed of several thousand kilometres per second, although a typical CME has a mass of around $10^{11} - 10^{12}$ kg and has a speed between 400 and 1,000 km/s and spans several tens of degrees of heliographic latitude and longitude. They may erupt from any region of the corona but are more often associated with lower latitude regions, particularly at or close to solar minimum, and associated with the heliospheric current sheet (the region where the Sun's magnetic field polarity changes) (Howard, 2011; Webb and Howard, 2012). The occurrence rate of CME's is around four or five per day during solar cycle maxima and about once per day during solar minima.

Coronal mass ejections transition to what are known as interplanetary coronal mass ejections (ICME) in the interplanetary medium and these are regarded as the heliospheric counterpart of CME's at much larger distances from the Sun (> 50 Solar radius) (Howard, 2011). Although, an ICME often appears to be slower than the original CME, their speed is faster than the speed of sound in the solar wind and hence they are supersonic which means they often cause shocks in the interplanetary medium. Extreme Space Weather effects at Earth have been associated with the occurrence of ICME's as a result of its impact and related shock (Baker et al., 2008; Howard, 2011).

An important component of ICME is the highly structured magnetic field which is not only variable but also typically higher in value than the surrounding interplanetary magnetic field. This structured helical or spiral magnetic field are called magnetic clouds and are regarded as a continuation of the magnetic field of CME's (Howard, 2011; Gurman, 1999).

Fast solar wind streams are another extreme regime of the solar wind which is cooler and less dense than slow streaming solar wind (Dryer, 1987). The solar wind regimes including both the fast streams and slow solar wind streamers are illustrated by Figure 1.7. Fast streaming solar wind is less tightly wound in the Parker spiral compared to slower ones, and at various distances the faster solar wind “overtakes” the slower streaming solar wind. The interactions of different solar wind streams of different speeds, the fast streams which at low latitudes rotates with the Sun and the surrounding slow streams give rise to corotating interaction regions which develop into interplanetary shocks, i.e. forward and reverse shock waves’ at large distances from the Sun due to their high pressure (Howard, 2011).

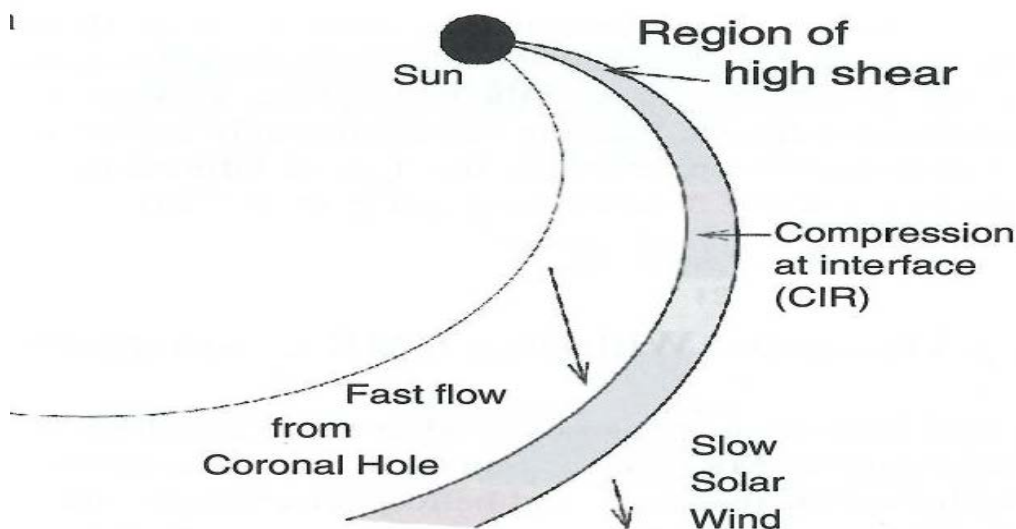


Figure 1.7. Schematic illustration of CIR structure in solar equatorial plane adapted from Howard, 2011.

1.3.4 Magnetosphere

The magnetosphere is the volume of space around an astronomical object that is controlled by that object's magnetic field. The Earth has a dipole magnetic field which reaches at least 57,937 km into space and its interaction with the solar wind creates and controls the magnetosphere as illustrated in Figure 1.8 (Schunk & Naggy, 2009). This interaction deforms the earth's dipolar magnetic field compressing the geomagnetic field lines on the dayside, the

Earth's sunward side, and stretching the field line out to form a comet-like tail (the magnetotail) on the night side. Thermal plasma and energetic particles from the solar wind and the earth populate the magnetosphere, which contains various large-scale regions with different plasma composition, energies and densities. The sources of the plasmas that populate these regions are the solar wind and the Earth's ionosphere whose contributions to magnetospheric plasma vary according to the level of magnetic activity. In this section, some of the regions of the magnetosphere will be discussed.

The interaction of the supersonic plasma with the earth's magnetic field, particle collisions with oscillating electric fields (non inter particle collision) creates a collisionless shock wave called the **bow shock** (Figure 1.8) whose shape and orientation varies with the direction of the interplanetary magnetic field and the speed of the solar wind. Its location or distance from Earth is determined by the pressure balance between the solar wind dynamic pressure and the compressed earth's magnetic field pressure (Russell, 1987; Schunk & Nagy, 2009). At the bow shock, the supersonic plasma decelerates to subsonic flow and as a result is heated and deflected around the Earth in the **magnetosheath**, whose thickness is about $3R_E$, where R_E is the earth radii. There is a boundary layer known as the **magnetopause**, a current sheet, which separates the deflected solar wind plasma in the magnetosheath from the terrestrial magnetic field. There is a current that flows along the magnetopause layer which is part of the current systems in the magnetosphere discussed in section 1.3.5. A certain fraction of the solar wind enters the earth's magnetosphere and deposits energy into the upper atmosphere through the regions known as the **polar cusp**. The **magnetotail** is the region of the magnetosphere that extends in the anti-solar direction from the Earth. The magnetotail includes the northern and southern **tail lobes** where the geomagnetic field is directly connected to the IMF.

The **plasma sheet** is the region of the magnetosphere that serves as a reservoir of hot plasma for the magnetosphere. It is populated by solar wind particles and thermal plasma that escapes from the Earth's upper atmosphere, the ionosphere, along magnetic lines of force (Burch, 1987; Schunk & Nagy, 2009). The plasma sheet particles drift towards the Earth along the magnetic field lines. In addition to these are also large-scale current systems within the magnetotail such as the **current sheet** where the current flows from dawn to dusk (Burch, 1987; Schunk & Nagy 2009).

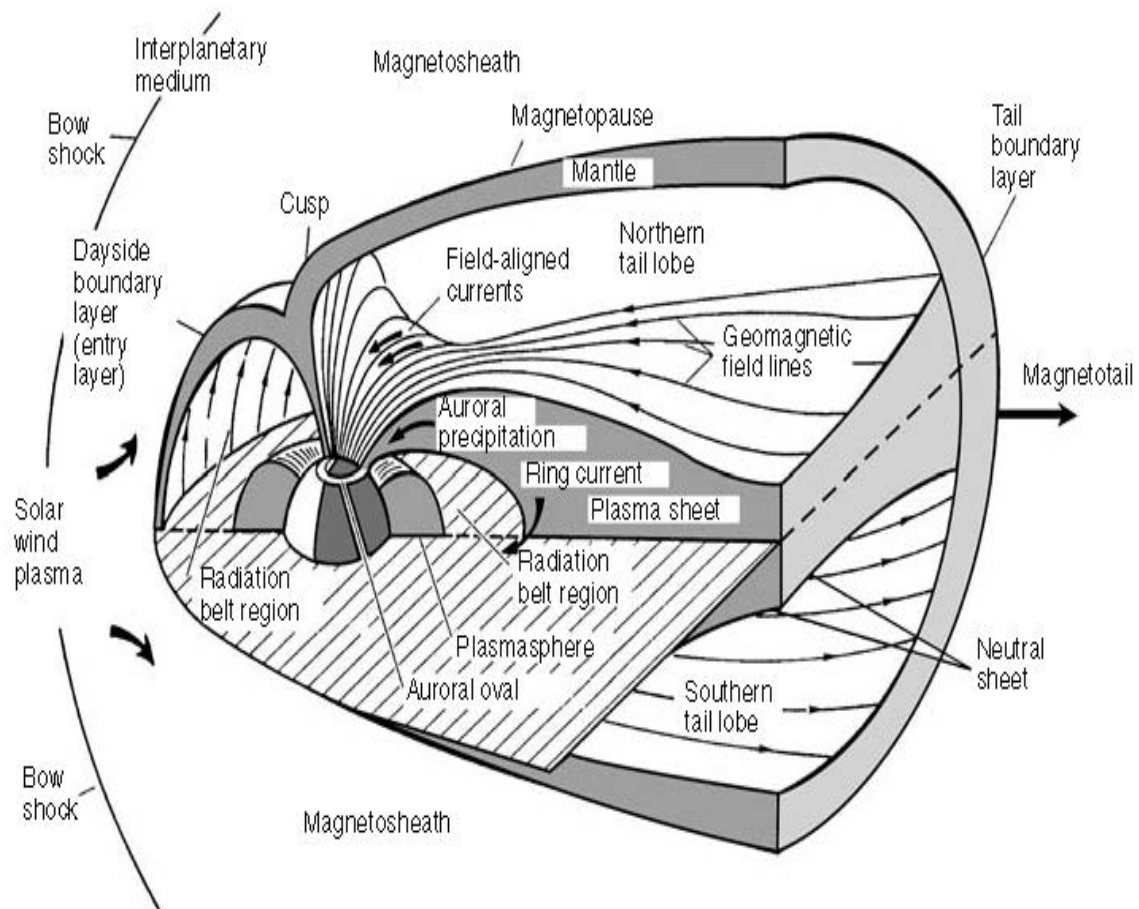


Figure 1.8 Illustration of regions of the Earth's Magnetosphere culled from Schunk & Nagy, (2009)

1.3.5 Solar Wind-Magnetosphere Coupling

The source of energy for the magnetosphere is its interaction with the solar wind. Kelley (1989a) noted that the most effective mode of energy transport between the solar wind and the magnetosphere occurs when the IMF is oriented anti-parallel to the orientation of the Earth's magnetic field (Figure 1.9). This configuration is particularly efficient for the process known as ***"magnetic reconnection"*** which allows interplanetary and geomagnetic field lines to merge at the dayside boundary of the magnetosphere (Figure 1.9 step 1). Reconnection involves the breaking of both the IMF and geomagnetic field lines and subsequent reconnection of IMF field lines with geomagnetic field lines. The effect of the magnetic reconnection results in the opening of the magnetosphere to the solar wind, thereby allowing plasma to have access into the magnetosphere's cusp region and the inner magnetosphere (as shown in Figure 1.9 step 2).

The interconnected interplanetary field lines are carried past the Earth by the motion of the solar wind (as shown in Figure 1.9 step 3), while being anchored to the Earth. Magnetic flux builds up in the magnetotail resulting in a stretched tail configuration (as shown in Figure 1.9 step 4). This magnetic flux build-up results in further reconnection, but this time in the magnetotail. This reconnection event sends the tailward stretched magnetic field back towards the Earth (as shown in Figure 1.9 step 5) as well as returning magnetic flux to the solar wind tail-ward or downstream.

Plasma energy which is converted from the stored magnetic energy travels along magnetic field lines and down to the ionosphere as field-aligned currents which transmit stress between the magnetosheath-magnetosphere and ionosphere-thermosphere (Cowley, 2000) and precipitating particles (as shown in Figure 1.9 step 6). Dungey (1961), proposed that reconnection at the magnetopause and in the magnetotail causes convection of magnetospheric plasma. Fig. 1.10, taken from Dungey (1961), shows that at the sunward direction (left in Figure 1.10a) the solar wind interplanetary and terrestrial magnetic field lines reconnect resulting in flows along the magnetopause. When the interplanetary magnetic field lines are anti-parallel to the geomagnetic field, the transfer of solar energy across the magnetopause is very high, while in the magnetotail region (right in Figure 1.10a), the build-up of magnetic flux and strong plasma flows cause magnetic reconnection which returns magnetic energy back towards the earth. The process of flux opening at the dayside of the magnetosphere and closing at the night-side of the magnetosphere is known as Dungey cycle. Howard (2011), noted that magnetic reconnection does not occur only when the interplanetary field is southward, it also occurs when it is northward. Figure 1.10b illustrates reconnection processes when the interplanetary field is in the southward and northward directions. The interactions of the solar-wind with the magnetosphere impose constrain on the magnetospheric plasma which result in a two-cell convection motion illustrated in Figure 1.11.

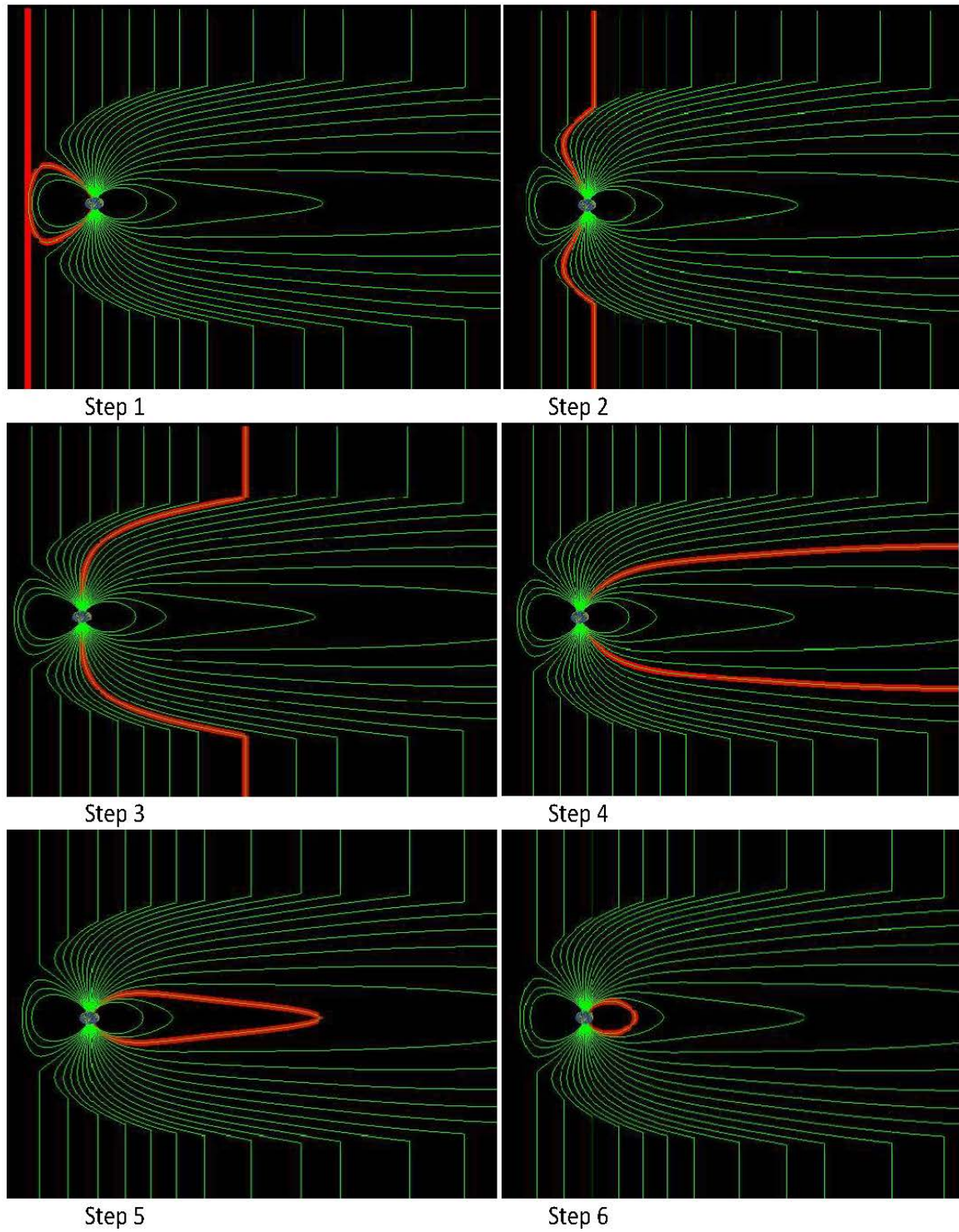


Figure 1.9 Magnetic reconnection of the interplanetary and terrestrial magnetic fields resulting in magnetospheric plasma transport (culled from CISM Summer School material, 2005).

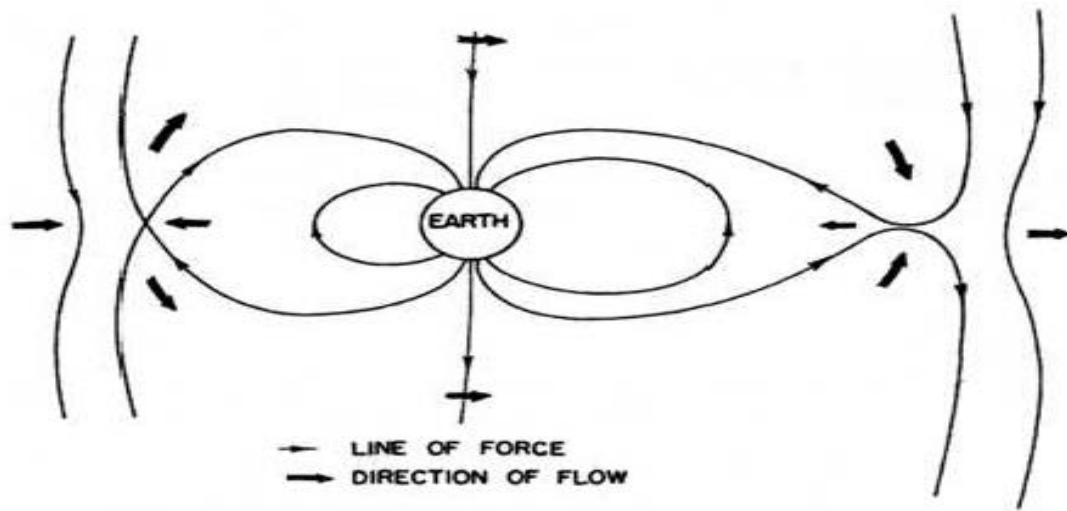


Figure 1.10a. Dungey diagram illustrating reconnection (Dungey, 1961).

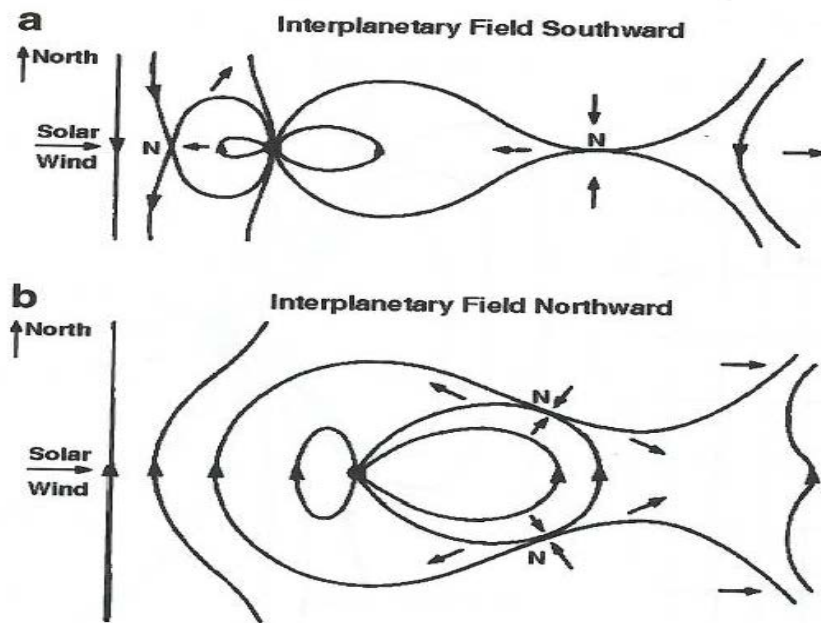


Figure 1.10b. Dungey diagram illustrating northward and southward reconnection (Dungey, 1961).

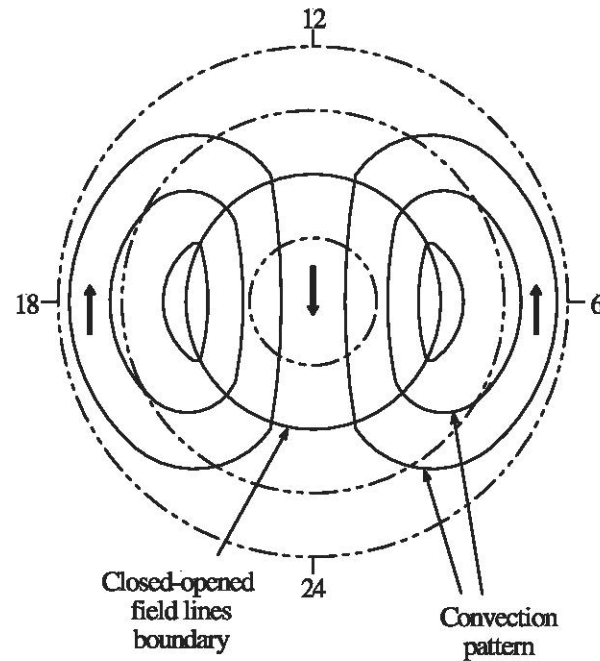


Figure 1.11 Schematic illustration of the two-cell convection pattern showing plasma moving across magnetic field line the convection electric field equipotential, the antisunward convection in the polar cap as a result of the motion indicated by the arrows from the noon sector towards the midnight sector and a return flow in the auroral regions in the dawn and dusk sectors. The closed-opened field line boundary approximately corresponds to the region where the motion changes from antisunward to sunward. Adapted from Kamide & Chian, 2007.

1.4 The Ionosphere

Rishbeth (1989) defined the ionosphere as that part of the upper atmosphere where free electrons are sufficiently numerous to influence the propagation of radio waves i.e the ionosphere makes long distance radio communication possible by reflecting the radio waves back to Earth. The Earth's ionosphere is the uppermost part of the terrestrial atmosphere where charged particles with a typical energy lower than 1 eV are created (Kamide & Chian, 2007) acting as an electrical conductor with the capability to reflect, refract and diffract radio waves. This region of the earth's atmosphere extends from 50km from the Earth's ground surface to about 1000km (including the topside ionosphere) and completely encircles the Earth (Schunk & Nagy, 2009). The free electrons and ions populating the ionosphere, or ionospheric plasma, are mainly produced through photoionization of the atmospheric gases (the neutral particles) in the neutral atmosphere by solar extreme ultraviolet radiation together with ionization by energetic particle precipitation also known as impact ionization or collisions with energetic particles penetrating the earth's atmosphere. Other sources of

plasma include galactic cosmic rays. The ionization products from the above processes can combine chemically with neutral particles, recombine with electrons, they can also undergo diffusion from one altitude to the other and can also be transported horizontally (Kamide & Chian 2007; Schunk & Nagy, 2009; Hunsucker, 2002). The terrestrial magnetic field which is dipolar at all altitudes of the ionosphere controls the impact of the diffusion and transportation mechanisms in the ionosphere. Figure 1.12 illustrates the plasma flow in the plasma flow regimes in the Earth's ionosphere.

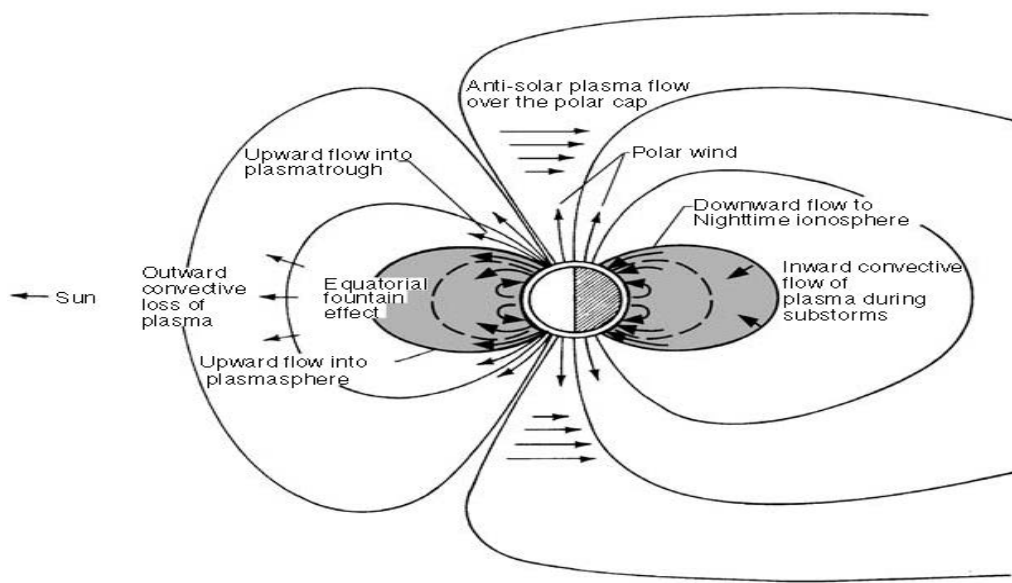


Figure 1.12. Illustration of the plasma flow regimes in the Earth's Ionosphere culled from (Schunk & Nagy, 2009)

1.5 Magnetosphere-Ionosphere Coupling

Magnetosphere-ionosphere coupling refers to processes which interconnect the lower-altitude, solar-produced, ionospheric plasma with the energized plasmas and processes of the high-altitude magnetosphere (Mitchell, 2007). The coupling operation may be considered as similar to a circuit operation where one part provides the energy and the other part works as a resistance. The magnetosphere and ionosphere are coupled via field-aligned currents (FACs) (Russell, 2000). These currents transmit stress between the magnetosheath-magnetosphere and ionosphere-thermosphere (Cowley, 2000). The illustration of the physics of magnetosphere-ionosphere coupling is shown in Figure 1.13.

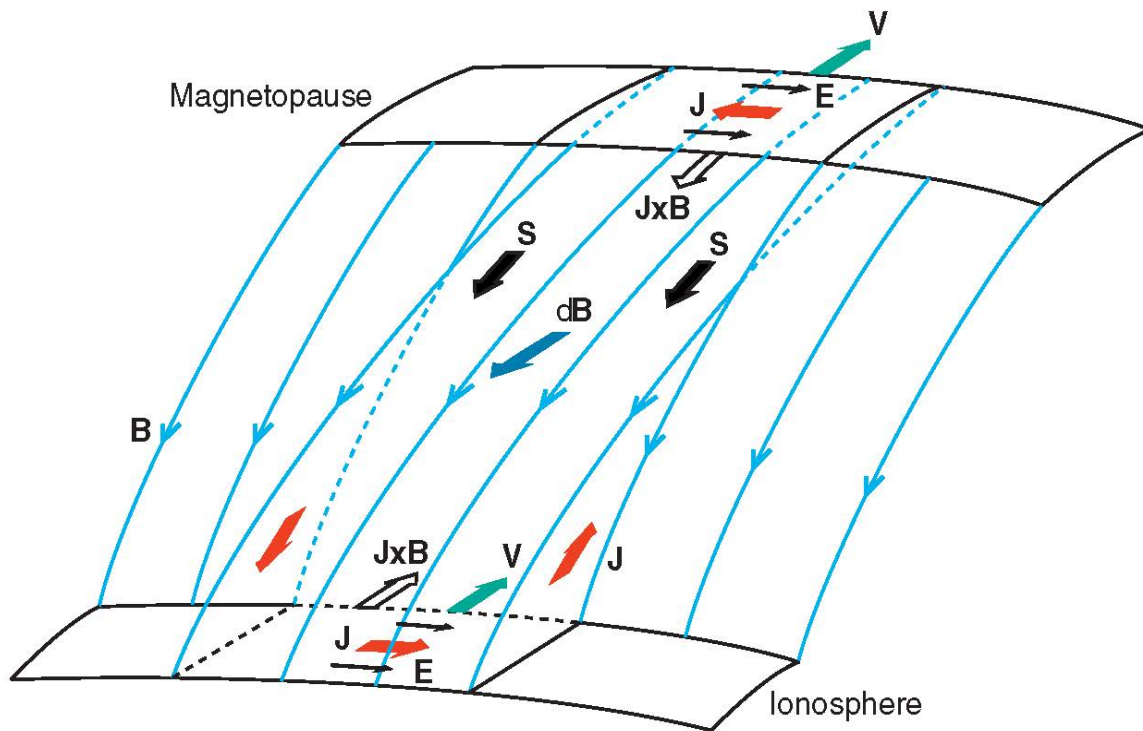


Figure 1.13; Illustration of the physics of magnetosphere-ionosphere coupling (Russell, 2000)

The top of the figure shows the magnetopause where the stress transmitted by FACs is applied to the magnetosphere which pulls bundles of magnetic field lines. The resultant shear in the magnetic field is similar to a parallel current which began in the “generator” region of the magnetosphere, closing across field lines in a pressure gradient and acting in the direction to slow the solar wind. There is now a “load” in the ionosphere where it applies a stress to the ionospheric plasma in the same direction as the stress in the magnetosphere so that the ionosphere begins to flow in the same direction as the solar wind. If the plasma flows in response to this stress, then the product of the magnetic field distortion, dB , and the electric field, $\mathbf{V} \wedge \mathbf{B}$, is a Poynting flux, \mathbf{S} , into the ionosphere. It is this energy that is dissipated in the ionosphere as Joule dissipation (Russell, 2000).

The next section will briefly discuss the magnetosphere-ionosphere current systems.

1.5.1 Magnetosphere-Ionosphere current system

The terrestrial magnetosphere and ionosphere consists of various current systems that determine the magnetic field and connect different regions. The current systems are the magnetospheric currents, i.e., the day-side magnetopause and the night-side magnetopause (magnetotail) currents, the ring current, and the ionospheric currents (Hall and Pedersen currents). Currents in the magnetosphere are connected to currents in the ionosphere by FAC. The magnetosphere-ionosphere current systems are illustrated in Figure 1.25.

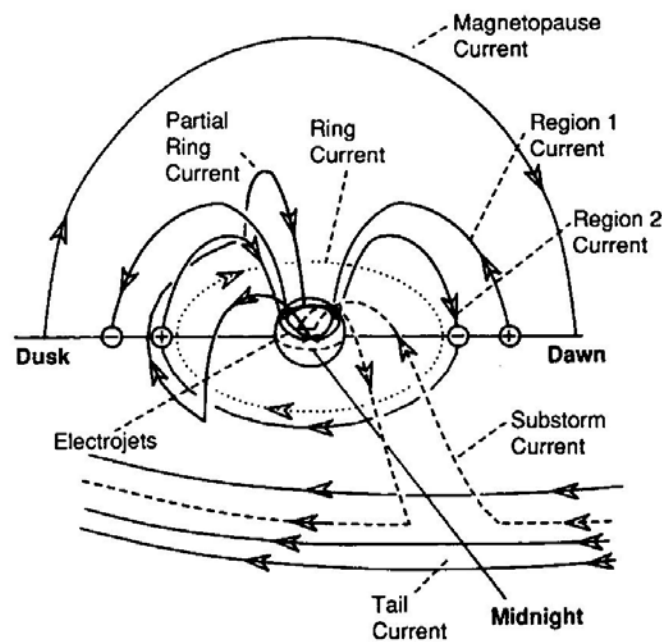


Figure 1.14 Schematic illustrations of magnetosphere-ionosphere current systems. Taken from Kivelson and Russell (1995).

The magnetopause current (Chapman-Ferraro current) is the current that flows at the magnetopause layer. A current flows from dawn to dusk on the dayside at the region of the magnetopause which is adjacent to the closed magnetic field lines while a current flows from dusk to dawn at the magnetopause region adjacent to the open field lines. Part of the day-side magnetopause current closes on the magnetopause and part of it closes via region 1 (shown in Figure 1.26) FAC in the ionosphere.

The terrestrial ring current is an electric current flowing toroidally around the Earth, centered at the equatorial plane with the stronger ring current flowing on the night side of the earth. The ring current is formed by the injection of ions originating in the solar wind and the terrestrial ionosphere. The injection process involves electric fields, associated with enhanced

magnetospheric convection and/or magnetospheric substorms. The Terrestrial ring current closes partially within the magnetosphere and partially through ionospheric currents through the region 2 FAC.

Hall and Pedersen currents are currents generated by the $\mathbf{E} \times \mathbf{B}$ drift. Their presence in the Earth's ionosphere is due to collisions with neutral particles. The Hall current is the ionospheric current which occurs in the perpendicular direction of both the electric field \mathbf{E} and the magnetic field \mathbf{B} in the terrestrial ionosphere and is strongest near 100 km altitude. The Pedersen current is the net current which occurs in the direction of the electric field when the Lorentz force accelerates plasma particles resulting in positive particles to move in one direction and negative particles to move in the opposite direction and is strongest near 125 km altitude. Hall and Pedersen currents are connected to the magnetospheric currents through FAC. The illustration of ionospheric convection driven by Dungey cycle flow with the current systems is shown in figure 1.26.

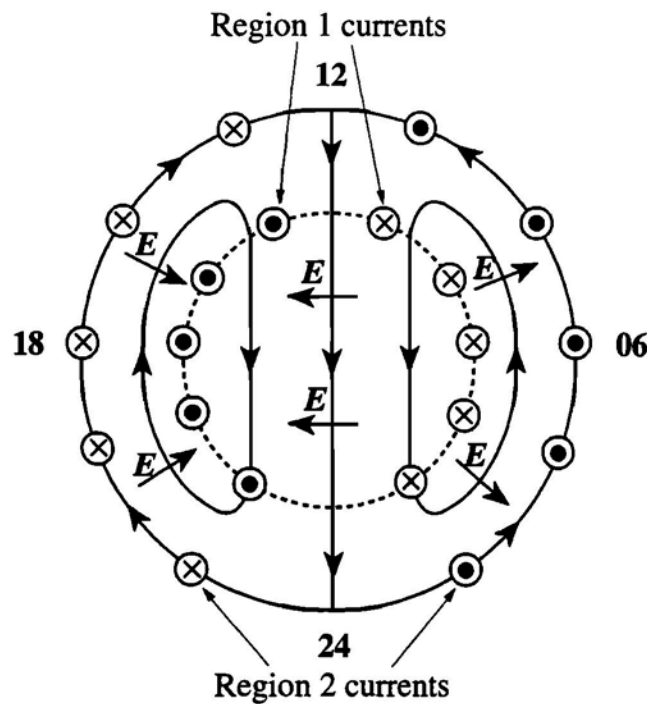


Figure 1.15 Illustration of ionospheric convection with Dungey cycle flow mapped into the ionosphere where the solid arrows are plasma streamlines, the dashed line is the open-close boundary (OCB) and the short arrows is the direction of the electric field \mathbf{E} with the convection coming out of the board. The Pedersen current flows in the direction of the \mathbf{E} and the Hall current flows in the opposite direction to the particle motion. Taken from Cowley (2000).

1.6 Summary of the thesis

Long term variations of the Earth's ionosphere which arise as a result of the interactions between the Earth's ionosphere, the magnetosphere, the interplanetary field and the solar wind are investigated in this thesis. Two different types of data spanning 20 years have been used for the analysis, data from ground-based and space-based instruments. The main data source is the two SuperDARN radars at Hankasalmi in Finland and Pykkvibaer in Iceland. Supplementary data are from the solar wind data measured by a variety of spacecraft and magnetic indices which have been derived from ground based magnetometers. The thesis consists of 7 chapters.

Chapter 2 presents more detail discussion on the ionosphere, discuss radio propagation and literature review of previous studies carried out on backscatter with SuperDARN data. Detailed information of the instrumentation used is presented in Chapter 3. Chapter 4 presents Solar cycle dependence, seasonal effects and the diurnal variations of ionospheric and ground backscatter observed in the two SuperDARN radars, while Chapter 5 illustrates the spatial (range gates) distribution of ionospheric and ground backscatter in the radars. Chapter 6 presents a statistical study of the effects of both external and internal drivers on the occurrence of ionospheric scatter and ground scatter from 1996-2015. Chapter 7 is the conclusion and recommendations for further work.

Chapter 2

2.1 Introduction

This chapter presents a more detailed discussion on the ionosphere, radio propagation and a review of previous studies on the use of HF backscatter to study variations in the Earth's ionosphere with special reference to the use of data from SuperDARN radars. The nature and operation of the SuperDARN radars are discussed in chapter 3. An important motivation for long term studies of ionospheric variations is to further analyse and understand the role of external drivers in ionospheric variability and to possibly predict their influence on the occurrence of backscatter. This chapter also presents a review of previous studies that have investigated the role of solar wind parameters and magnetic activity on the occurrence of HF backscatter.

2.2 The Earth's Ionosphere

The Earth's ionosphere has been discussed briefly in chapter 1, section 1.4. The next section presents detail discussion on the ionosphere.

2.2 Ionospheric Structure

The classification of the Earth's ionosphere into regions is based on the peak density of the ionosphere at an altitude, decrease in density with altitude, plasma sources of the ionosphere (photoionization of the atmospheric gases in a neutral atmosphere by solar extreme ultraviolet radiation and ionization by energetic-particle precipitation, impact ionization) and dynamic processes in the ionosphere (Kivelson & Russell, 1995; Schunk, 2009). These plasma sources, magnetospheric electric fields and particle precipitation have a significant effect on the formation of the structure of the ionosphere (Schunk, 2009) which can be due to the variation in the strength and form of the magnetospheric processes primarily determined by variation in the orientation of the interplanetary magnetic field (IMF) as well as the solar wind dynamic pressure, and variation in the tides and gravity waves that propagate up from the mesosphere (Rishbeth & Garriott, 1969; Schunk, 2009). Ionospheric particles are governed by three basic equations which are the equations governing any kind of particles (Rishbeth 1988). These equations are the continuity

equation (conservation of mass), force equation (conservation of momentum) and the heat equation (conservation of energy) and are represented by equation 2.1, 2.2 and 2.3, respectively.

$$\partial N / \partial t = \{Production\} - \{Loss\} - \{Transport\} \quad (2.1)$$

$$\partial V / \partial t = \{Driving\ Force\} - \{Drag\} - \{Advection\} \quad (2.2)$$

$$\partial T / \partial t = \{Heating\} - \{Cooling\} - \{Conduction\} \quad (2.3)$$

Based on the plasma sources, magnetospheric electric fields and particle precipitation, the ionosphere can be split into three regions, the D region, E region and the F region which in turn, can be split into two separate regions, the F1 and F2 regions. The research reported in this thesis focuses on the E region and the F region. Figure 2.1 illustrates the ionospheric layers (blue curve) discussed in this thesis showing the electron density versus height profile. During the day and at sunspot maximum, the layers have higher densities in the normal ionosphere. The figure also shows the atmospheric temperature profile with altitude (red curve), with the increasing scale towards the left. This illustrates that the ionospheric regions occur in the warmest part of the atmosphere known as the thermosphere.

The next section discusses the production of ions and electrons in the ionosphere, the loss of ions, energetic particle precipitation and the transport mechanism of ionospheric particles to enable us to understand the ionospheric processes leading to the formation of the ionospheric regions, after which each of the three regions of the ionospheric layers will be discussed.

2.3 Ionospheric processes

Ionization by photons of solar extreme ultra violet radiation and ionization by energetic particle impact on the neutral particles are the two sources of ion and electron production in the ionosphere (Kelley, 1989a) with each of the processes creating an ion-electron pair and also absorbing some amount of energy (Kamide & Chian, 2007). Photoionization of atmospheric gases such as O, O₂ and N₂ by solar radiation with wavelengths not more than 1026Å together with X-rays are responsible for most of the ionization in the lower and middle latitudes of the ionosphere resulting in ion–electron production and heating (Hunsucker and Hargreaves, 2002). To understand the process of photoionization in the upper atmosphere, I start the discussion with the simple structure predicted by Sydney Chapman, referred to as Chapman theory, which forms the basis of our understanding of

the ionospheric layers. The theory is used to describe the rate of production of ions or ionization (q) in the upper atmosphere as a function of height using a radiation absorption cross section σ and assuming that ion production depends on the amount of absorbed radiative energy (Kivelson & Russell, 1995).

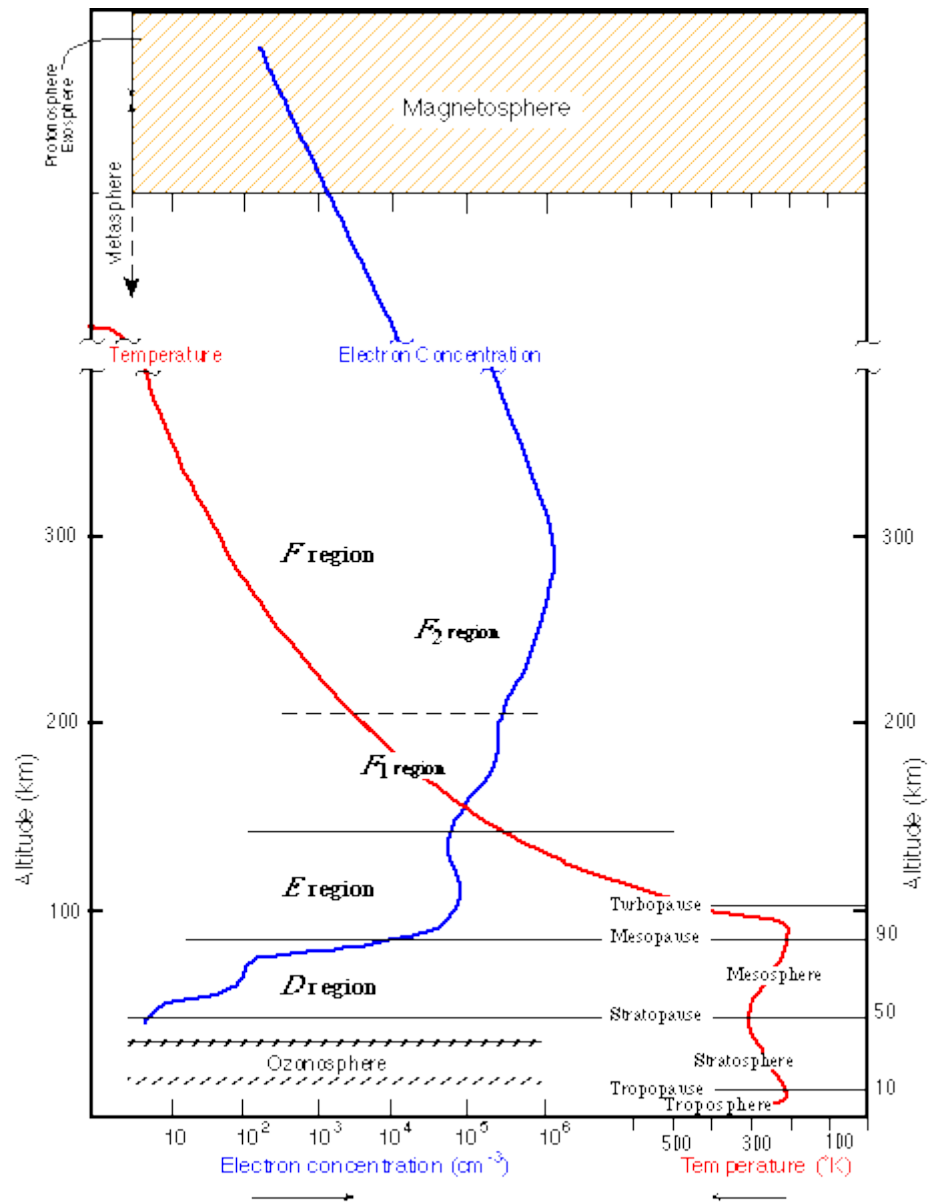


Figure 2.1. Typical daytime electron concentration (blue curve) profile with height with different ionospheric layers and temperature profile with altitude (red curve) with increasing scale towards the left (adapted from <http://www.ion.le.ac.uk/ionosphere/profile.html>).

In the original theory, details of the absorption of photons were not included in the radiation absorption cross section due to its complexity (Kivelson & Russell 1995).

Rishbeth and Garriott (1969) summarise the four simplifying assumptions in Chapman theory as follows:

- I. The radiation from the sun is monochromatic with photon flux $I(h)$
- II. The Earth's atmosphere consists of a single absorbing or ionisable gas with concentration of $n(h)$, where n is the density and h is the height.
- III. The terrestrial atmosphere is flat (plane) and horizontally stratified with a fixed solar zenith angle χ .
- IV. The scale height H is independent or varies linearly with height. It represents the height at which the pressure and density of a gas will decrease by a factor of $1/e$. It is represented in equation 2.4 where k is the Boltzmann's constant, T is the temperature, m is the mass of atmospheric particles, and g is the planet's (earth) gravitational acceleration. Its dependence on the particle mass implies that the lightest molecules and atoms have the largest scale heights (Kivelson & Russell)

$$H = \frac{kT}{mg} \quad (2.4)$$

The rate of production of ions in Chapman theory is represented by equation 2.5 where I is the intensity of radiation, n is the density of the particles, σ is the absorption cross section and η is the ionizing efficiency or heating efficiency.

$$Q = I\eta\sigma n \quad (2.5)$$

The radiation attenuation, the fractional loss of radiation during ionization depends on the path length of the radiation and the absorption coefficient, $n\sigma$ with the radiation path given by equation 2.6 where dh is an altitude variable.

$$\text{Radiation path} = dh \sec\chi \quad (2.6)$$

Equation 2.7 shows the decrease in the intensity of radiation as it is absorbed downwards.

$$(dI/I) = -\sigma n dh \sec\chi \quad (2.7)$$

If we integrate equation 2.7 along the radiation path from the uppermost level down, we obtain equation 2.8 where I_o is the initial intensity which strikes the upper atmosphere at the zenith angle χ .

$$I(h) = I_o \exp(-n\sigma \sec\chi) = I_o e^{-\tau(h)} \quad (2.8)$$

By substituting equation 2.8 for the radiation intensity in equation 2.7 above, we express the production rate of ions as in equation (2.9)

$$Q(h) = I(h) \eta \sigma n(h) = I_o \eta \sigma n(h) e^{-\tau(h)} \quad (2.9)$$

Differentiating equation (2.9) shows that the peak value of the production rate of ionization occurs at a height where the optical depth (τ) equals unity (1), and gives equation (2.10)

$$Q = (\eta I_0 / eH) \cos \chi \quad (2.10)$$

The Chapman production rate in terms of the reduced height z is given in equation 2.11.

$$Q(z, \chi) = Q_0 \exp(1 - z - e^{-z} \sec \chi); \text{ when } z = \frac{h-h_0}{H} \quad (2.11)$$

The extension of the Chapman production rate to the production maximum Q_{m0} at subsolar point will give equation 2.12.

$$Q = Q_{m0} \exp(1 - z - e^{-z} \sec \chi) \quad (2.12)$$

$$h_m = h_{m0} + \ln(\sec \chi)$$

$$Q_m = Q_{m0} \cos \chi$$

where $z = (h - h_{m0})/H$.

Equation 2.12 implies that in an isothermal atmosphere the altitude of the peak production increases with solar zenith angle and the rate of ionization decreases with solar zenith angle (Kivelson & Russell, 1995). In the derivation of the Chapman ionization production rate, Sydney Chapman assumed that the terrestrial planet is flat with the consequence that the value of the solar zenith angle does not change with respect to position at the surface. The assumption of a plane stratified atmosphere, where the $\sec \chi \, dz$ approximation for ds/λ , non-varying solar zenith angle used by Chapman is good when the value of χ is less than about 75° . The theory cannot, however be used to explain the complete behaviour of the terrestrial ionosphere due to the fact that at larger zenith angles the curvature of the planetary surface and changing densities with solar zenith angle makes the atmospheric column content a much more complicated function of χ . Hence, the major peak in the terrestrial ionosphere cannot be described by simple Chapman-layer theory alone (Davies, 1990; Kivelson & Russell, 1995; Hunsucker and Hargreaves, 2002; Kamide & Chian, 2007; Schunk, 2009).

Figure 2.2 is a simple schematic representation of a photoionization process where EUV radiation detaches an electron from an atmospheric neutral atom which absorbs the photon energy hc/λ , where h is the Plank's constant (6.62×10^{-34} Js), c is the speed of light and λ is the wavelength of the incident electromagnetic waves. The equation describing the process can be given by equation 2.13, where a is used to represent a generic neutral atom, a^+ represents an ion and e^- represents a free electron (Zolesi and Cander, 2014).

$$a + \frac{hc}{\lambda} \rightarrow a^+ + e^- \quad (2.13)$$

In addition to photoionization by solar EUV radiation, energetic precipitating charged particles which occur at high magnetic latitudes can also produce ions in the upper atmosphere but with a different ion production altitude profile from that of the ion production altitude profiles of photoionization derived above (Kivelson & Russell, 1995) due to the absence of Beer–Lambert law in photoionization which shows that the intensity of radiation decrease is proportional to the number of absorbing molecular along the optical path.

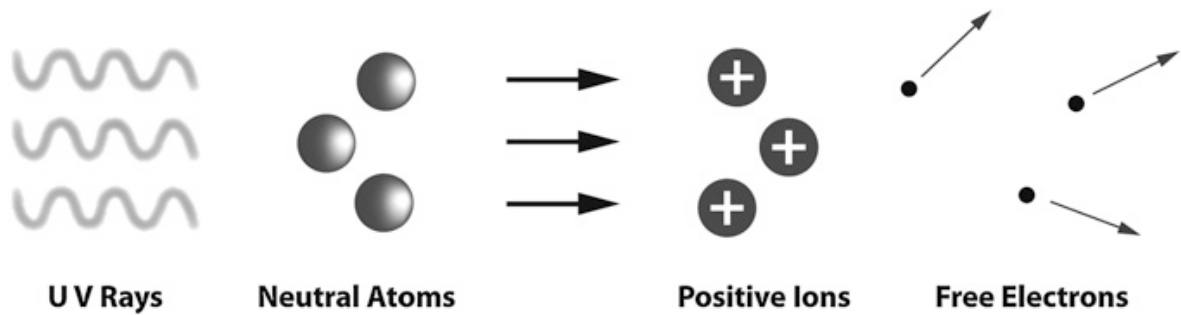


Figure 2.2 Schematic representation of photo-ionization: detachment of electrons from the neutral atoms by the solar UV rays energy, producing ions and free electrons. (Culled from Ionospheric prediction and forecasting, Zolesi B. and Cander, L.R., 2014)

In the case of energetic particle precipitation, the attenuation of particle energy flux with decreasing altitude as the density of the atmosphere increases is the major factor for ion production by energetic particle precipitation (Kivelson & Russell, 1995). The mechanism for the movement of the charged particles and the loss of energy to the atmosphere also differs from the production and loss processes in photoionization. Energetic particles lose energy in a gradual process during excitation and they also remove bounded electrons as they travel through the atmosphere via Coulomb collisions.

Kamide & Chian, (2007) noted that the ionization process associated with energetic particle precipitation is also related to the transport of energetic particles in the atmosphere. Transport of plasma can be through diffusion, neutral wind flow and vertical electromagnetic drift (Davies, 1990). The movement of plasma can also occur in the horizontal and the vertical planes of the atmosphere. I now briefly discuss the three transport mechanisms mentioned above in the vertical planes due to their importance in the formation of F region of the ionosphere.

Ions and electrons in the Earth's upper atmosphere diffuse together in a process known as ambipolar diffusion. Ambipolar diffusion can be expressed mathematically if we re-write the equation of continuity in terms of Q (production rate), L (loss rate) and express the transport term in the equation in relation to the mean velocity of the particles \mathbf{v} .

$$\frac{\partial N}{\partial t} = Q - L - \text{div}(N\mathbf{v}) \quad (2.14)$$

Neglecting the effects of production and loss due to photoionization, we can express equation 2.15 in terms of the vertical diffusion speed w , and hence, equation (2.14) becomes;

$$\frac{\partial N}{\partial t} = - \frac{\partial(wN)}{\partial h} \quad (2.15)$$

where $w = -D(h) \sin^2 I \left(\frac{1}{N_e} \frac{dN_e}{dh} + \frac{Mg}{2KT} \right)$

where M is the ion mass, I is the magnetic dip, and $D(h)$ is the ambipolar diffusion coefficient which is inversely proportional to the neutral density (Davies, 1990).

The variation in the temperature of the upper atmosphere at the sub-solar point and at the nightside creates a pressure difference which drives horizontal neutral winds from the dayside of the terrestrial atmosphere to the night side as illustrated in Figure 2.3 (Davies, 1990). The motion of the wind is transferred to the ions by neutral-ion collisions or Coulomb attraction to electrons. At certain regions of the ionosphere, the collision frequency of ions and electrons is very low such that transport of ions across the magnetic field is not possible. If we consider the vertical component of the plasma motion which tends to move in the same direction as the component of the neutral wind along the magnetic field, the vertical component of the plasma velocity can be represented by equation 2.16

$$w = V \sin I \cos I = \frac{1}{2} V \sin(2I) \quad (2.16)$$

where V is the neutral wind speed in the magnetic meridian and I is the magnetic dip angle. Similar to plasma diffusion, equation 2.16 implies that there will be no vertical motion at the equator where the magnetic dip angle I tends to 0° but in contrast to diffusion being a maximum at the poles, there will not be vertical motion of the neutral wind at the poles. The vertical component of the wind maximizes where the magnetic dip angle is 45° (Davies, 1990; Hunsucker and Hargreaves, 2002).

The transport of plasma across the magnetic field lines is attributable to electromagnetic drift, the so-called $\mathbf{E} \wedge \mathbf{B}$ drift. A west-to-east electric field in the northern hemisphere will produce a vertical drift in the magnetic meridian illustrated by Figure 2.4 (Davies, 1990). For a given electric field strength, the magnitude of w expressed in equation 2.17 is zero at the poles and E/B_0 at the dip equator.

$$w = \frac{E}{B_0} \cos I \quad (2.17)$$

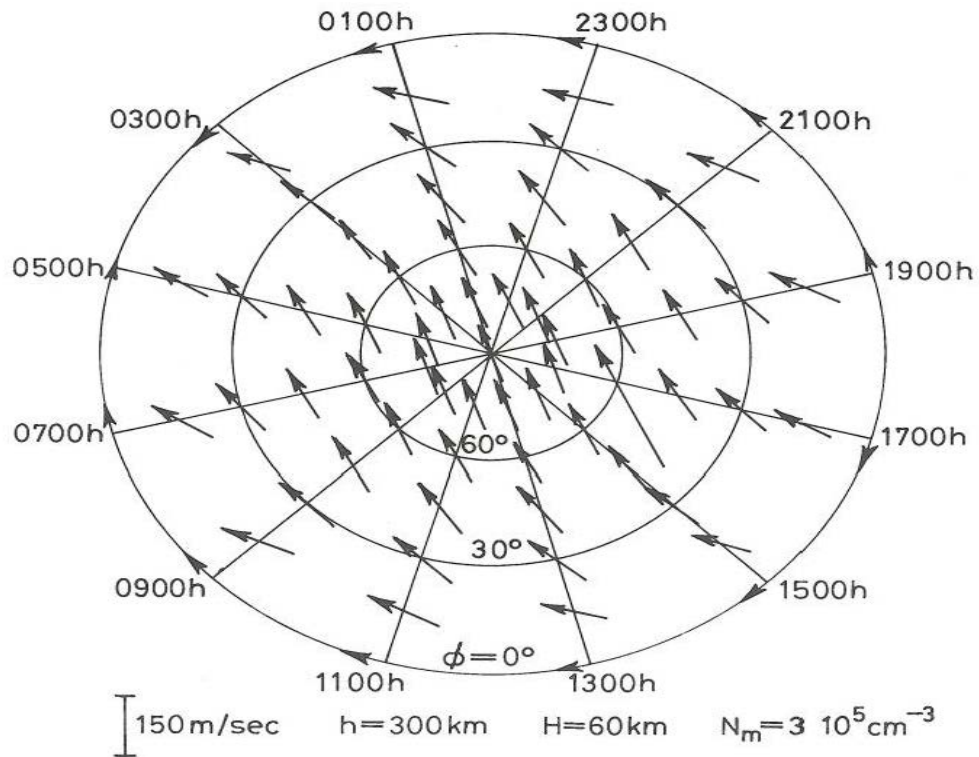


Figure 2.3 Atmospheric wind system in the northern hemisphere (adapted from Davies, 1990)

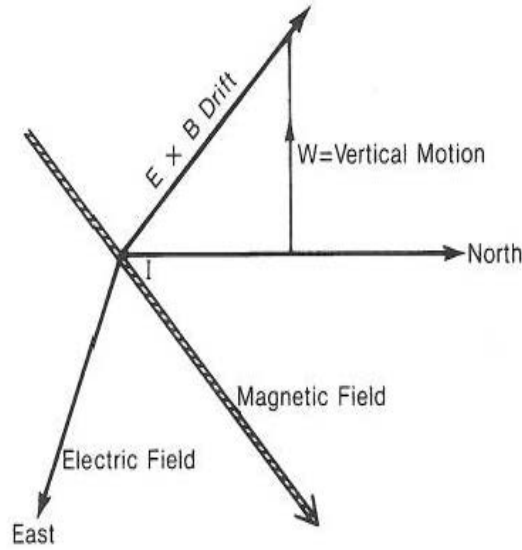


Figure 2.4 Illustration of electromagnetic drift caused by west-to-east electric field culled from (Davies, 1990).

The net concentration of free electrons in the upper atmosphere, the electron density, depends on the production rate and loss rate of ions and electrons for a dynamic equilibrium thus making the loss process of ions or electrons through recombination an important process in the formation and structure of the ionosphere. Recombination as a loss process is the reverse of photo-ionization; in this case positive ions recombine with free electrons resulting in the production of neutral atoms or they interact with other gaseous elements to produce ions. There are three ways in which recombination processes can take place. The first is a radiative recombination which involves the direct interaction between electrons with positive ions to produce a neutral atom or a molecule together with excess energy. The second is dissociative recombination which requires the interaction of an existing bi-atomic neutral molecule with a positive ion a^+ which originates from the photoionization reaction and the combination of the positive molecules with electrons. The third way is known as attachment (Kivelson & Russell, 1995; Zolesi & Cander, 2014). The three methods are represented by equations (2.18), (2.19) and (2.20), respectively.



2.4 D, E and F regions of the ionosphere

Of the ionospheric layers, the D region occurs at the lowest altitudes typically between 70km to 90km altitudes. The absorption of HF radio waves mainly takes place in this region where major sources of ionization are Lyman α (121.6nm), galactic cosmic rays and X-rays. The D region is present during the day but virtually disappears at night unless there is significant energetic particle precipitation. The weak ionization in the D region is particularly responsible for the absorption of HF radio signals at these altitudes, which is directly relevant for SuperDARN.

The E region lies above the D region and normally extends between 90km and 160km above the surface of the earth. Different ionizing sources such as X-rays (1-17nm) and ultraviolet radiation are responsible for the production of this region. The E region has the ability to reflect HF radio waves and also has the capability of absorption of certain frequencies of HF radio signals. It has been shown that the E region of the ionosphere occurs mainly during the day time with its development immediately after sunrise and the disappearance some hours after sunset. The E region is highly variable in space and time with a remarkable anomaly referred to as sporadic-E seen in E region. The anomaly has little direct relationship with solar ionizing radiation. Occurrence of sporadic-E at high latitudes has been identified to be a night time phenomenon and it's attributed to ionization by energetic particles in the energy range of 1 – 10 keV sometimes known as auroral electrojet. The scale size of irregularities within a Sporadic-E layer determines the impact of sporadic E on radio propagation. If the dimension of a sporadic E is comparable to one half of the wavelength of the incident radio signal, the irregularities can scatter radio waves. A sporadic-E layer can also reflect radio signals that would otherwise penetrate to the F region and it may cause scintillation of trans-ionospheric signals (Hunsucker and Hargreaves, 2002).

Above the E region is the F region which extends from 150km to 1000km and stretches to the exosphere. Two layers called F1 layer and F2 layer respectively can exist in the F region of the Earth's ionosphere. The F1 layer is less dense than the F2 layer and it is present or noticed during the day time. Molecular ions such as NO^+ and O_2^+ are present in the F1 layer while predominantly O^+ ions are present in the F2 layer which can persist during night time. The presence of the F2 layer during night time makes the ionosphere important for HF propagation (Nisbet, 1971; Bent et al., 1978; Rush et al., 1983, 1984)

due to the region's ability to allow the possible longest propagation paths and the ability to refract frequencies in the HF signals range.

2.5 Ionospheric Variations

Ionospheric plasma varies with universal time, altitude, latitude, longitude, solar activity (solar cycle) and magnetic activity as a result of the coupling, time delays, and feedback mechanisms operating in the ionosphere-thermosphere system and the coupling of the ionosphere to other regions of the solar-terrestrial system, i.e. the Sun, interplanetary magnetic field, the magnetosphere (the energetic particles from the magnetosphere), the mesosphere, as well as propagation of tides and gravity waves (Schunk, 2009), the Earth's orientation, its tilt and movement around the sun and the sun's orientation. Hence the Earth's ionosphere is not always in equilibrium or steady state, and variability in the ionization density of the earth's ionosphere in turn affects the characteristics of HF propagation e.g. the signal intensity, Doppler shift of the signal and the polarization of the radio wave.

Ionospheric variations can be classified into two major categories, (i) regular variations and (ii) non-regular variations. Regular ionospheric variations are repeatable or cyclic in nature and can be predicted to some degree of correctness using the magnitude of the ionization in the ionosphere as an index. Such regular ionospheric variations can be classified into five main categories which are: (i) diurnal variations (semi-diurnal and diurnal variations') (Forbes et al., 2000; Rishbeth and Mendillo, 2001) (ii) seasonal variations, such as the semi-annual and annual variations (Millward et al., 1996; Rishbeth and Garriot, 1969), (iii) the 27-day variation which is the variation as a result of the sun's rotation (Ma, 2015); (iv) geographical variation which is a result primarily of the changing EUV (Schunk and Sagay, 2009) and (v) solar cycle variations which is the variation of the ionosphere in relation to solar activity, often represented by sunspot number, and which is an approximately eleven-year cycle (Rishbeth and Garriot, 1969; Tor and Torr, 1973; Bilitza et al., 1979; Hargreaves, 1979).

Non-regular ionospheric variations are these which are not repeatable or are non-cyclic in nature and, therefore, cannot easily be predicted. These variations are due to unpredictable activity in the sun which can negatively affect HF propagation (see section 2.6.2) without warning such as CME's. The irregular ionospheric variations can be classified into three

main categories which are; (i) sporadic E; (ii) sudden ionospheric disturbances; (iii) ionospheric storms.

It is important to note that ionospheric variability does not allow the use of the same value of frequency or singular frequency for radio waves propagation (see section 2.6.1) throughout the day, season, and latitudes and throughout the year. This research has focused on three of these variations and these are discussed below.

2.5.1 Diurnal Variations

The rotation of the earth about the sun has a strong effect on the region which overlaps the uppermost part of the neutral atmosphere, the ionosphere. This rotation around the sun causes sunrise and sunset every day which can be described by the solar zenith angle. As discussed in the previous section, the formation of the earth's ionosphere is directly related to incident solar radiation and the electron density of the ionosphere, therefore, varies with the time of the day and with respect to the solar zenith angle for any geographical location (McNamara, 1994). The gravitational and thermal effects of the sun on the earth make the earth's atmosphere including the ionosphere undergo a regular variation of 24 solar-hours (solar day). Also, there is an additional daily variation known as the lunar day variation (24.83 lunar hours) which is the effect of the gravitational attraction between the Earth and the moon due to the revolving moon around the earth. All three layers of the ionosphere experience diurnal variations of the ionosphere, although the F region is less controlled by solar zenith angle due to transport processes.

2.5.2 Seasonal Variations

The tilt and rotation of the Earth on its own axis has a very strong effect on the ionosphere. The Earth revolves around the sun in a way that the relative position of the sun changes from one hemisphere to the other hemisphere resulting in changes with seasons. Similarly, all the regions of the ionosphere exhibit seasonal variations which correspond to the greatest angle of the sun. Rishbeth and Setty (1961) noted that ionization is greater at noon during winter than in summer which is the inverse of what is expected and referred to as the winter anomaly. Due to the winter anomaly, the values of the frequency for propagation of HF signals during winter are much higher than during summer.

2.5.3 Solar-cycle Variations

The periodic rise and fall in solar activity, which describes the solar cycle, occurs over a period of approximately 11 years. The variation in solar activity affects radio wave propagation in the ionosphere. The peak electron density of the F layer (F2 region) depends not directly on sunspot number. It depends on the ionizing radiation emission (EUV) from the sun. The solar cycle can be categorised into two major classifications namely the solar minimum and the solar maximum. During solar minimum, the production rate of electrons in the ionosphere is lower in comparison to the solar maximum. The ionizing radiation emission (EUV) from the sun peaks during solar maxima.

2.6 Ionospheric irregularities

The normal ionosphere departs from an equilibrium state due to large scale disturbances which affect the ionosphere leading to irregularities or anomalies in the ionospheric layers. HF radio wave propagation in the ionosphere is influenced by such ionospheric irregularities.

Ionospheric irregularities in the high latitude are associated with solar/magnetosphere/ionosphere disturbances. Three mechanisms have been identified which produce ionospheric irregularities in the high latitude ionosphere. These processes are (i) plasma instabilities, (ii) particle precipitation and (iii) electrostatic turbulence. It has been shown that most ionospheric electron density structure is produced by plasma instability processes present in the E and F regions of the Earth's ionosphere (Fejer and Kelly, 1980). The sizes of the structures of ionospheric irregularities have been used to classify them into three groups namely; (i) small scale (< 100 m), (ii) intermediate scale (0.1-10 km) and (iii) large-scale (> 10 km) (Vickrey and Kelley, 1983).

The ionospheric irregularities that results from the plasma instability processes in the E region are categorised into two classifications based on the plasma instability mechanism which creates the irregularities from which the radar signals are backscattered (Fejer and Kelley, 1980; Fejer and Providakes, 1987). The first category of plasma instability processes which produce ionospheric irregularities generated in the E region is due to ion collisions with neutrals which constrain the ion population to the neutral flow speed in the E region and allows electrons to convect under the influence of the electric field with the $\mathbf{E} \wedge \mathbf{B}$ drift leading to a difference in the velocities of electrons and ions. The differential velocity of the ions and electrons due to the collisions generated results in the Farley-

Buneman (also known as two-stream) instability (Farley, 1963; Buneman, 1963). The Farley-Buneman instability is typically identified in radar backscatter (see section 2.7.2) with low spectral width and the measured velocity is restricted very close to the local ion acoustic speed, C_s with a typical value of $350 \pm 40 \text{ ms}^{-1}$ at about 110 km. This is the velocity threshold that is required for the plasma instability processes to generate the Farley-Buneman instability (Sudan, 1983; Nielsen and Schlegel, 1983). Irregularities with such spectral characteristics are referred to as Type I.

The second category of plasma instability processes in the E region is due to gradients in the electron density and is referred to as the gradient-drift ($\mathbf{E} \wedge \mathbf{B}$) instability (Ossakow and Chaturvedi, 1979). The gradient-drift instability produces a second type of spectra in radar backscatter, referred to as Type II Doppler spectra. Unlike the Farley-Buneman instability which produces the type I Doppler spectra due to higher value in the differential velocity of electrons and ions than the ion-acoustic speed, the gradient-drift instability does not have an upper or lower velocity threshold for it to be generated, and it is assumed the instabilities drift at the $\mathbf{E} \wedge \mathbf{B}$ velocity. A schematic illustration of the gradient-drift instability mechanism is shown in Figure 2.5.

It is important to note that the ion-neutral collision frequency is very low in the F region altitudes such that the generation of the two-stream instability is inhibited. The dominant plasma instability process that generates ionospheric irregularities in the F region is therefore the gradient drift instability (Simon, 1963; Hoh, 1963) which involves the interchange of two elements. Other sources of ionospheric irregularities in the high latitude F region are structured particle precipitation, Rayleigh-Taylor, Kelvin-Helmholtz and current convective instabilities (Ossakow and Chaturvedi, 1979; Keskinen et al., 1988). The gradient drift mechanism in the F region is somewhat different from the mechanism in the E region. The mechanism for the gradient drift instabilities in the F region is due to the fact that the electric field must be perpendicular to the plasma density gradient while in the E region it must be parallel to the plasma gradient drift. The presence of an external force which acts on a constant volume of plasma will enhance the plasma and produce a slight distortion leading to charge separation which produces a small polarization electric field which due to the presence of a magnetic field will increase the disturbance, that is, the instability. This instability is a common mechanism by which irregular structures in the F-region break down into smaller ones. Tsunoda, (1988) pointed out that magnetic-flux tube interchange (MFTI) processes appear to play a major role in irregularity production in the

high-latitude F region where different drivers act at different irregularities' scale sizes. Tsunoda, (1988) noted that at scales greater than 10 km, the MFTI process seems to be produced by irregular electric fields mapped to the F layer from other regions while at the largest scales, patches are reconfigured into boundary and sub auroral blobs by the magnetospheric convection pattern with the boundary (and sub auroral) blobs also subject to structuring by the MFTI process produce by smaller-scale, irregular electric fields whose sources include magnetospheric turbulence and E region polarization and dynamo effects. In addition, the characteristics of small scale size irregularities are identified to be controlled by the $\mathbf{E} \wedge \mathbf{B}$ instability (Tsunoda, 1988).

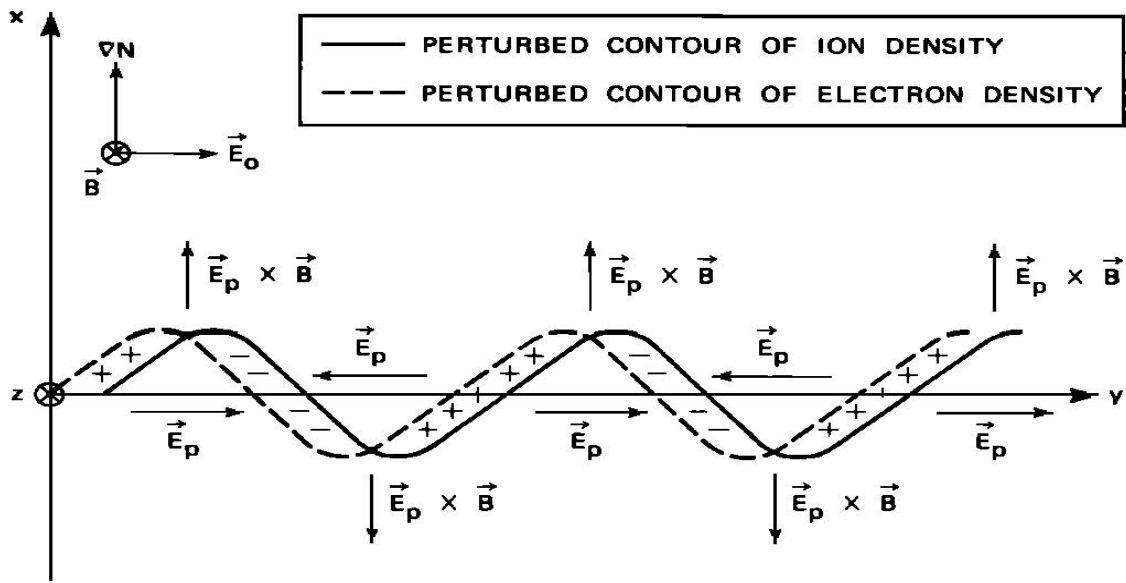


Figure 2.5 Schematic diagram showing the basic mechanics of $\mathbf{E} \wedge \mathbf{B}$ instability A Pedersen ion drift (to the right) leads to charge separation and the development of polarization electric fields (adapted from Tsunoda, 1988).

Coherent HF scatter radars receive ionospheric scatter from plasma irregularities which are field-aligned in the ionosphere through a process which is similar to Bragg scatter. The scale length of the ionospheric medium which produces the backscatter (ionospheric irregularities) ranges from a few meters to several kilometres across the magnetic field and irregularities occur in the auroral and polar cap ionosphere almost all the time (Perkins 1975). The wavelength of the radar signal, λ_R is related to the wavelength of the plasma irregularities λ_{pi} as follows,

$$\lambda_R = 2\lambda_{pi} \sin (\theta/2) \quad (2.21)$$

which can be written as equation 2.35 for direct backscatter where $\theta = 180^\circ$.

$$\lambda_R = 2\lambda_{pi} \quad (2.22)$$

The backscatter of the radar signal \mathbf{k}_r occurring from the plasma irregularities satisfies the Bragg condition $\mathbf{k} = 2\mathbf{k}_r$ where \mathbf{k} is the irregularities' wave vectors. In addition, at operational frequencies in the HF band, radars will also receive scatter from the surface of the planet, whether it is ground or sea, or occasionally ice. Currently the most used coherent scatter radars are those from the Super Dual Auroral Radar Network (SuperDARN) (Greenwald et al., 1995, Chisham et al., 2007, Lester, 2013).

2.7 Remote Sensing of The Ionosphere with Radio propagation

The remaining part of this chapter will focus on remote sensing of the ionosphere with radio propagation. The ionosphere is a good conductor which can reflect, refract and diffract electromagnetic (radio) waves in a pattern similar to that for heat and light spectra. Our current understanding of the terrestrial ionosphere comes from the remote sensing of the ionosphere with the use of ground based frequency techniques of radio signals to measure time of flight, the amplitude, the phase, polarization and the angles of arrival of reflection by refractive bending by coherent or incoherent scatter (Davies, 1989). Transmitters and /or receivers on satellites have also been used to investigate the horizontal structure of the ionosphere. Sweep-frequency techniques from both ground and space are used to probe the vertical structure of the ionosphere.

2.7.1 Radio propagation

The transmission of electromagnetic waves from one point on the Earth to a targeted point or to various parts of the targeted medium, which by simplification is governed by the distance and the frequency of transmission, is known as radio propagation. Modes of propagation of electromagnetic waves or electromagnetic radiation can be line of sight propagation (LOS) i.e., earth to satellites or vice versa, ground propagation, and sky wave propagation. The dispersion relation of electromagnetic waves in a hot and isotropic magnetised plasma is determined by the refractive index of radio waves propagating through the plasma and is governed by a relationship known as the Appleton-Hartree equation (Hargreaves, 1979), which is given below. Several phenomena affect propagation

of electromagnetic waves, such as, reflection, refraction, dispersion, diffraction, polarization, absorption, scattering and attenuation (Hunsucker and Hargreaves, 2002).

The Appleton-Hartree formula is given in equation 2.23. If we consider an electromagnetic wave travelling through an isotropic ionized medium in the presence of magnetic field, such a wave will have a complex refractive index n :

$$n^2 = (\mu + i\chi)^2 = 1 - \frac{X}{1 - iZ - \frac{Y_T^2}{2(1 - X - iZ)} \pm \left[\frac{Y_T^2}{4(1 - X - iZ)^2} + Y_L^2 \right]^{1/2}} \quad (2.23)$$

To identify the components of the waves in relation to the phase propagation direction, L and T is used to denote longitudinal and transverse components to the magnetic field, respectively, in equation 2.23. The magnetic field of the Earth splits the incidence wave into ordinary waves and extraordinary waves which is accounted for by the \pm sign in the equation. X, Y and Z in equation 2.23 are given as follows;

$$X = \frac{\omega_p^2}{\omega^2} = \frac{N_e e^2}{\epsilon_0 m_e \omega^2} \quad (2.24)$$

$$Y = \frac{\omega_H}{\omega} = \frac{eB}{m_e \omega} \quad (2.25)$$

$$Z = \frac{\nu}{\omega} \quad (2.26)$$

where ω is the angular frequency, ω_p is the angular plasma frequency, ω_H is the angular electron gyro frequency, N_e is the electron density which is related to the plasma frequency by equation 2.27, e is the electronic charge, m_e is the electron mass, B is the magnetic field, ϵ_0 is the permittivity of free space and ν is the collision frequency that exist between the neutrals and the electrons. The radio wave frequency is related to the angular frequency, ω , by the equation 2.28 and the natural frequency of oscillation of electrons in the ionosphere, the plasma frequency, is related to the angular plasma frequency (ω_p) by equation 2.29.

$$N_e = \frac{\epsilon_0 m_e}{e^2} \omega_p^2 = 0.0124 f_p^2 \quad (2.27)$$

$$\omega = 2\pi f \quad (2.28)$$

$$\omega_p = 2\pi f_p \quad (2.29)$$

The principles of ionospheric propagation can be simplified by two basic assumptions. The first assumption is to assume that the collision frequency is negligible and the second assumption is that the magnetic field is negligible. The collision frequency during propagation of high-frequency signals through the ionosphere is always very small, i.e., Z tends to zero, and therefore this term can be neglected. In addition, if the magnetic field is negligible i.e., $Y \ll 1$, equation 2.20 reduces to equation 2.30

$$\mu = 1 - X = 1 - \frac{f_p^2}{f^2} \quad (2.30)$$

The implication of equation 2.30 is that μ must lie between 0 and 1, i.e., μ must be real and that for a particular frequency, an increase in the density of electrons will result in a decrease in the refractive index and for a given electron density, the refractive index will decrease as the frequency decreases. If we consider a plane refracting layer, the electron density increases as the wave incident at an angle \emptyset_0 penetrates into the layer and the direction of the vector \mathbf{k} changes according to equation 2.31

$$\mu \sin \emptyset = \mu_0 \sin \emptyset_0 \quad (2.31)$$

where \emptyset is the angle between direction of the vector \mathbf{k} and the perpendicular to the surfaces when the refractive index μ is constant. Equation 2.31 becomes 2.32 when the wave is reflected where $\emptyset = 90^\circ$ and μ is 1.

$$\mu_r = \sin \emptyset_0 \quad (2.32)$$

If the HF wave propagates vertically, \emptyset_0 equals zero, the refractive index at reflection equals zero which implies that reflection will occur vertically when the plasma frequency (f_p) equals the frequency of the wave (f). Hence, a wave propagated vertically will penetrate the layer when the wave frequency is higher than the maximum plasma frequency of the refracting layer. Reflection occurs for oblique propagation when the refractive index is expressed as in equation 2.33.

$$\mu = \sin \emptyset \quad 2.33$$

If we consider a flat or curved earth approximation, the refractive index can be expressed as follows;

$$n = \mu \left(\frac{R_e}{h_r + R_e} \right) \sin \emptyset \quad 2.34$$

where incident angle of the wave on the terrestrial ionosphere is \emptyset , the radius of the earth is given by R_e and the height of reflection of the incident wave is h_r .

If a wave propagates vertically at a frequency f_v and another wave propagates obliquely at f_o with both waves reflected at the same plasma frequency, there is a relationship between their frequencies which is expressed in equation 2.35.

$$f_o = f_v \sec \emptyset_0 \quad 2.35$$

Equation 2.33 is called the secant law and it shows that for oblique propagation the ionosphere can reflect much higher frequencies than with vertical propagation. Hence, oblique propagation is the propagation mode used by SuperDARN radars.

2.7.2 HF Propagation

The propagation of radio waves in the HF frequency band (3-30 MHz) is classified often as skywave propagation or point-to-point propagation. Transmission of HF radio waves for communication or ionospheric probing requires the frequency of the waves to be transmitted at frequencies close to the local ionospheric plasma frequency. The transmission of HF signals at such frequencies will result in the waves being continually refracted as they move through the ionosphere. The ability of HF signals to be continually refracted in the ionosphere makes them capable of achieving orthogonality with the magnetic field in both the E and the F region. The ability of HF coherent scatter radars to achieve the orthogonality condition with the magnetic field in F region gives them preference over VHF radars (Milan et al., 1997). The low cost of the terminal equipment, low power requirements, adequate signal strength budget and adequate transmission bandwidths are some of the advantages of HF propagation.

HF propagation nomenclature was originally developed for point to point communications between ground stations and hence whole hops (i.e. propagation from ground to ionospheric reflection point back to the ground) are labelled with integer numbers and a letter denoting the reflecting layer or layers, e.g. 1F for 1 hop propagation via the F-region. A comprehensive nomenclature was introduced to describe regions of ionospheric backscatter, e.g. the $1 \frac{1}{2}F$ mode which is also termed the F-F/ mode. The possible propagation modes by which backscatter information can be returned to HF radars are

presented schematically in Figure 2.7 (from Milan et al., 1997). In the diagram, three rays, A, B and C are illustrated. The diagram shows Ray A having a low elevation angle such that backscatter and reflection occur in the E region. Multiple hops are possible in this mode. Ray B has a higher elevation angle and reflects in the F region, producing backscatter in both the E and F regions while Ray C has the highest elevation angle and ionospheric refraction is insufficient to produce reflection, so the ray penetrates the ionosphere. In this case, though ionospheric backscatter can be observed in the E and F regions ($\frac{1}{2}E$ and $\frac{1}{2}F$ modes) no ground scatter or far range ionospheric scatter ($1\frac{1}{2}F$) is produced. In this way HF radars can receive scatter from both the ionosphere and the ground.

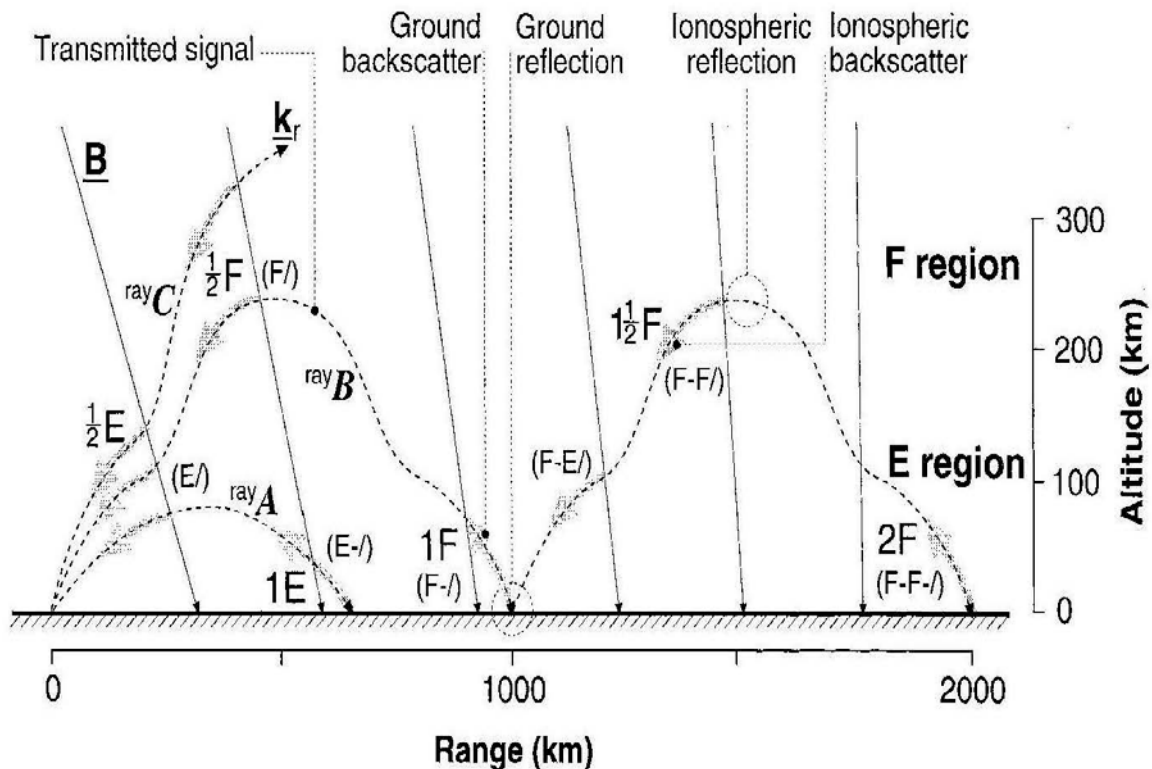


Figure 2.6. A schematic diagram of some of the possible propagation modes and regions from which backscatter can occur. *Milan et al (1997)*

2.8 Previous studies on HF backscatter

The ionospheric irregularities discussed in section 2.5 are responsible for the ionospheric backscatter which is received by the SuperDARN radars. Here we discuss previous statistical studies of ionospheric scatter.

Ruohoniemi and Greenwald (1997) carried out a 6-year study on scatter occurrence statistics of the Goose Bay SuperDARN radar. The study focused primarily on F region scatter using a subset of the Goose Bay radar data archive for the 6-year period from 1988 to 1993 which corresponds to the solar cycle maximum of solar cycle 22. The results of this study are summarised in Figure 2.8. Ruohoniemi and Greenwald found that HF backscatter is not confined to distinct latitudes either in the aggregate statistics or in individual events.

They observed that the backscatter occurrence level was low in summer in both the noon and afternoon sectors, while the occurrence rate during winter shows a high level in both noon and afternoon sectors. They identified a seasonal effect in the occurrence rate of backscatter with higher contrast in the occurrence rate in the noon and afternoon sectors, where the occurrence rates are much lower in summer than in winter. They attributed this observation to density gradients being suppressed by the intense photoionization during the summer, while in the winter structuring of the F region density was more likely to occur.

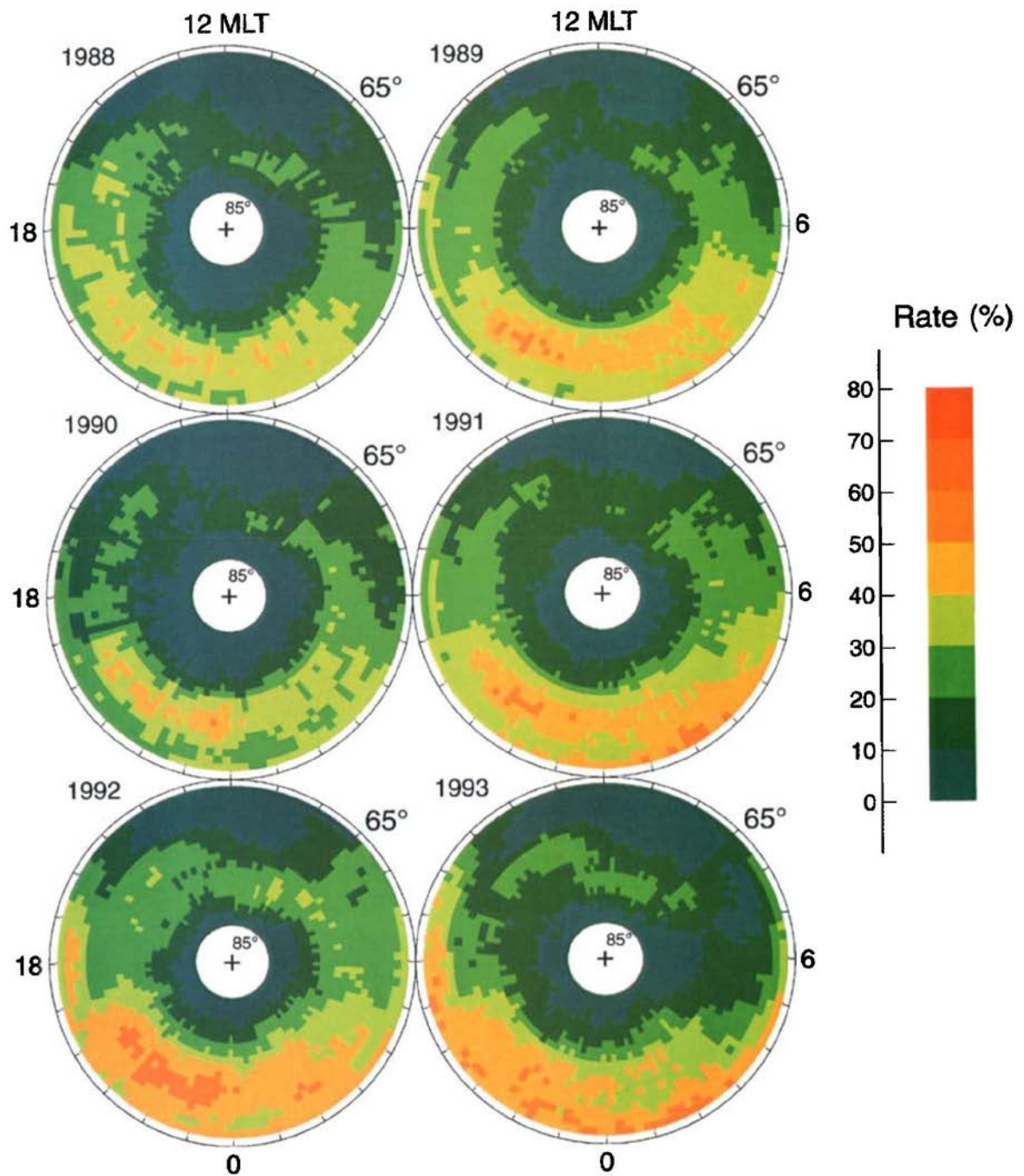


Figure 2.7. Scattering occurrence for different years, from Ruohoniemi et al. (1997)

Milan et al. (1997b) carried out a statistical analysis of the occurrence of ionospheric and ground scatter for the first twenty months of the operation of the two SuperDARN radars located at Hankasalmi and Pykkvibaer (Figure 2.9). This study was based on a subset of the total data set by using so-called 16 summary points aligned approximately along a magnetic meridian within each radar field of view. Findings from the work of Milan et al.

(1997b) include the observation that the location and occurrence of ionospheric backscatter varies dramatically between the seasons.

For example, ionospheric backscatter was observed to be present at near ranges in the midnight local time sector during the summer months while being observed to occur most frequently at far ranges during winter and equinoctial months.

In the work of Ballatore et al. (2000) on the influence of the interplanetary medium on SuperDARN ionospheric scatter occurrence, a two-year data set from 1997 to 1998 from the six northern hemisphere radars operating at the time of their study was used. These radars included Hankasalmi, Pykkviaber, Stokkseyri, Goose Bay, Kapuskasin and Saskatoon. Ballatore et al. (2000) demonstrated the dependence of HF scatter occurrence on the Magnetic Local Time (MLT), the magnetic latitude and the local season. In addition, they also found that the interplanetary parameter which influences the daily modulation of ionospheric scatter occurrence is the interplanetary electric field. The observations in the work were taken during the minimum between solar cycles 22 and 23.

A study of the seasonal variation of midnight F region echoe, or backscatter, occurrence was carried out by Koustov et al. (2004) using a data set of a half-solar cycle duration (1996 - 2001) with data from the meridional beams only of the Hankasalmi, Pykkvibaer, Saskatoon, Kodiak, Halley and Syowa East radars selected. Koustov et al. (2004) observed enhancements of backcatter occurrence during the summer in Hankasalmi for the years near the solar cycle minimum. They noted the presence of a seasonal variation in the occurrence of backscatter at midnight for most of the radars investigated with the variability in occurrence depending on the radar's location. Also, they concluded that there is an increase in the midnight ionospheric backscatter occurrence as the solar cycle approaches its maximum with no significant increase in noon sector observations, while there was also a dependence of seasonal variations of ionospheric backscatter occurrence on the geographic location of the radar.

A statistical study of the diurnal variations of the E-region ionospheric backscatter occurrence was carried out by Carter and Makarevich (2009). This study focussed on scatter only from near range gates ($r \leq 765$ km) of the field of view of the two TIGER radars which are located on Bruny Island, Tasmania, Australia and on the South Island of New Zealand and referred to as the Bruny Island and Unwin radars, respectively for a 2-year (2004-2006) period dataset and ground scatter data were excluded.

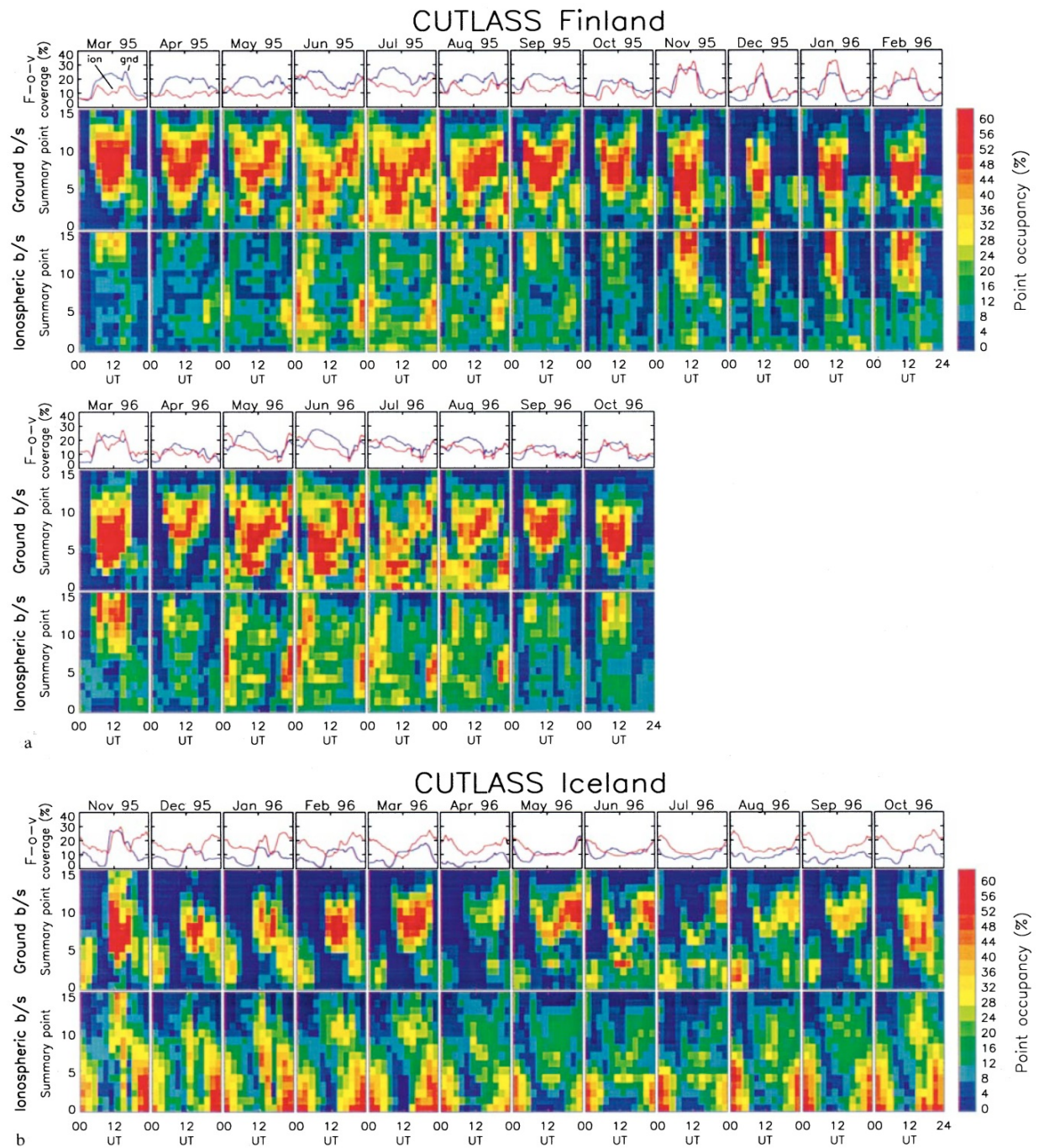


Figure 2.8. Ionospheric and ground backscatter occurrence in Finland (figure a) and Iceland (figure b) radars, the top panels in figure a and b is the diurnal variation in the field of view for the months of March 1995 to June 1996 for Finland radar and for the months of November 1995 to June 1996 for Iceland radar, the middle and bottom panels is the point occupancy as a function of range (summary points) in a & b culled from Milan et al. (1997b).

Carter and Makarevich (2009) observed a similarity in the pattern of the daily occurrence of E-region scatter for most of the radars investigated during low geomagnetic activity. In addition, they noted that the structures of most of the E-region backscatter were diffuse echoes and demonstrated the existence of the relationship between ion precipitation and E-region backscatter.

Kane et al. (2012) analysed the quiet time coherent backscatter in the F region of the ionosphere observed by the Tasman International Geospace Environment Radar (TIGER) to determine the trends and the controlling factors in the occurrence of ionospheric echoes. Kane et al. (2012) observed that the solar cycle effects in the daytime occurrence are much weaker as compared to those during the night. Also, they reported the control of the occurrence of backscatter in the F region by the electrical conductance of the ionosphere and the electron density of the F region.

Makarevich et al. (2012) carried out an investigation of the IMF control and magnetic conjugacy of the E region backscatter with data from a conjugate pair of radars, Pykkvibaer in Iceland and Syowa East in Antarctica in the SuperDARN array in conjunction with the ACE IMF measurements. In the study, a data set spanning 1 year period from January–December 2000 near the peak of the solar cycle 23 from Pykkvibaer in Iceland and Syowa East in Antarctica within the E region FOV of each of the radars were used. Figure 2.10 show the plots of raw occurrence versus magnetic local time (MLT). Panel a and c in Figure 2.11 show the occurrence for Syowa East and panel b and d for Pykkvibaer radars respectively. The results from the study demonstrates the daily variations of ionospheric backscatter occurrence are dominated by the diurnal cycle with the IMF dependence which is most prominent when ionospheric backscatter occurrence rates are adjusted using quiet time daily trends. In addition, the study shows that IMF Bz effects dominate and the occurrence increases strongly when Bz becomes more negative while any By effects are a factor of 2 weaker and manifest differently for negative and positive Bz.

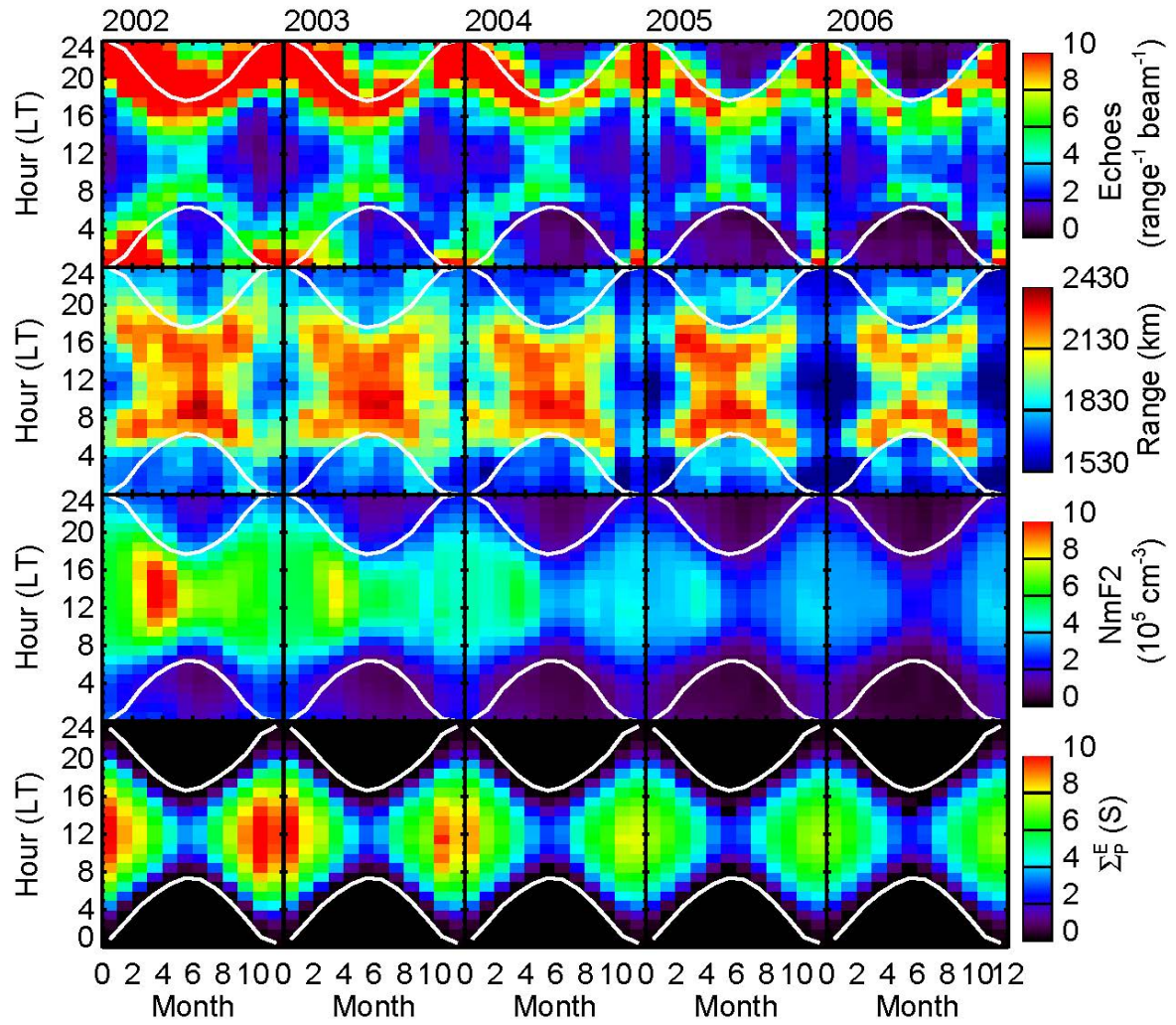


Figure 2.9 Quiet-time echo statistics with each column of panels represents one year of data, and each row of panels represents one of the parameters with the parameters from top to bottom: the radar echo occurrence, average slant range of the ionospheric echoes, model $NmF2$ and model conductance culled from Kane et al (2012).

The By effect was related to the increase in electric field merging and the relative orientation of the radar with respect to the average plasma flow direction (Makarevich et al. 2012).

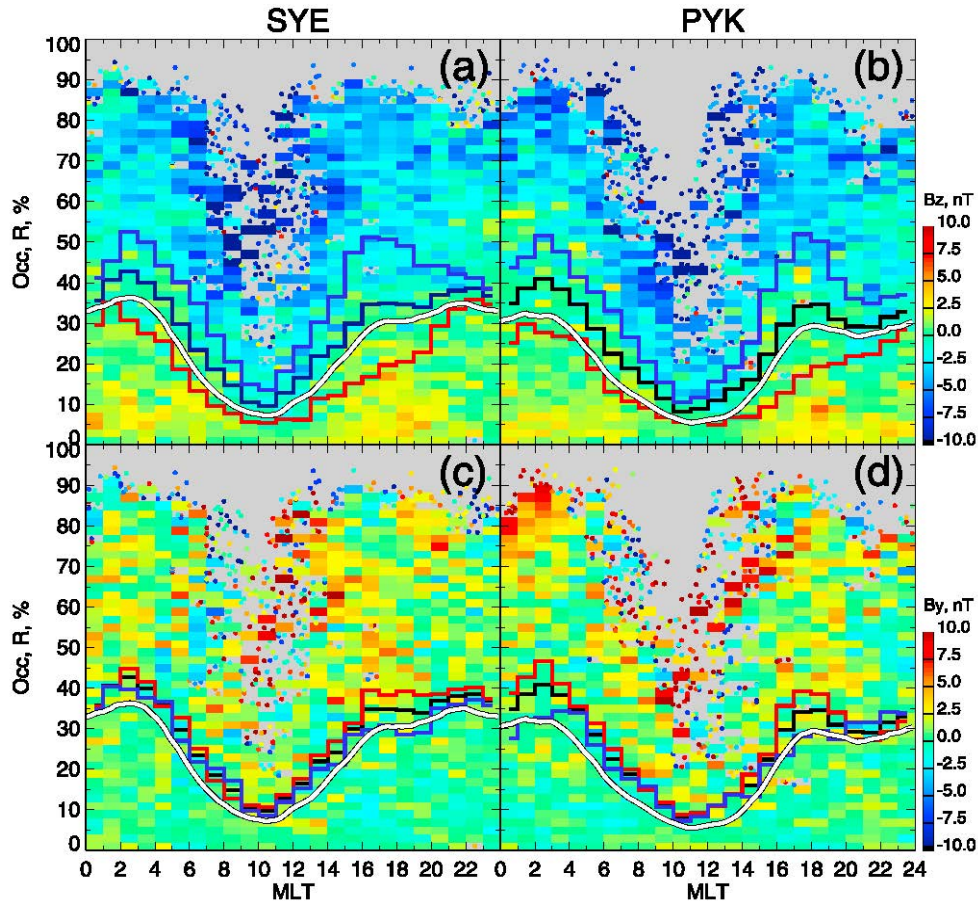


Figure 2.10. Plots of raw occurrence versus magnetic local time (MLT) for (a and c) Syowa East and (b and d) Pykkvibaer. The parameter used for color-coding each plot cell is the average IMF Bz (Figures 2.10a and 2.10b) and IMF By (Figures 2.10c and 2.10d) from Makarevich et al. (2012).

In a separate study, Ghezelbash et al. (2014) studied the variations in the occurrence rates of F region echoes with special focus on the Saskatoon SuperDARN radar data for 1994 – 2012. The radar backscatter occurrence for periods of maximum solar activity (2000–2002) and minimum solar activity (2008–2010) as a function of Magnetic Local Time (MLT) is illustrated in Figure 2.12. The findings from their study include repetitive patterns of ionospheric backscatter occurrence in both months and MLT. They observed changes in the pattern of occurrence of ionospheric backscatter during solar cycle maximum in comparison with the pattern during solar cycle minimum conditions. Also, the conclusion from their study indicates that a maximum occurrence of echoes during winter noon hours at solar cycle minimum, maximum echo occurrence in equinoctial dusk/dawn hours and summer mid- night hours during solar cycle minimum and observation of echoes during nighttime for all seasons during solar cycle maximum conditions, the latter having more

extended periods of time during the winter than summer. In addition they noticed that the occurrence of ionospheric backscatter during nighttime increases by a factor of 3 towards the solar cycle maximum while there was no significant change in the nearnoon backscatter occurrence for summer and fall equinox.

In another study, Lamarche et al. (2015) carried out a statistical analysis of ionospheric backscatter observed by the SuperDARN McMurdo Antarctica (MCM) station radar of the polar F region using a 4 year data set to investigate the role of solar wind and illumination in production of small-scale F region plasma irregularities. In the analysis, four months were chosen as representatives of different seasons. The result of the investigation indicates that the occurrence of ionospheric backscatter detected by MCM shows that it is seen in wide and persistent bands in range which displays systematic changes with local time, season, and solar cycle. In addition, their observations indicate that solar illumination control of irregularity production is strong and not restricted to the nightside and that indirect solar wind control is also exerted by the IMF-dependent convection pattern, since the gradient-drift instability favours certain orientations between the plasma density gradients and the convection velocity. Their analysis shows an enhancement in the occurrence of ionospheric backscatter for negative IMF B_y and B_z with higher occurrence for more negative IMF B_z (Lamarche et al., 2015).

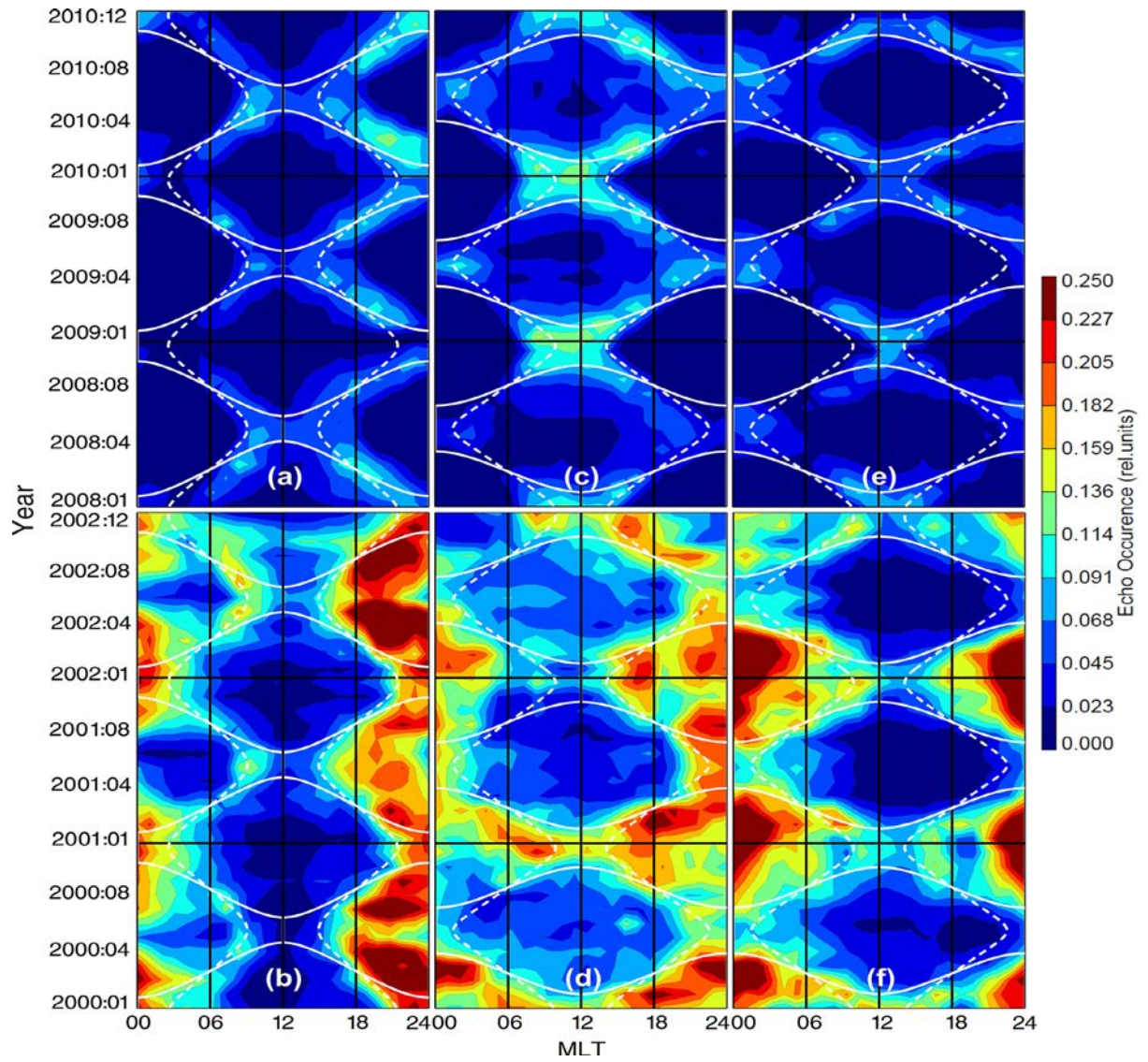


Figure 2.11 Echo occurrence rates for periods of minimum (2008–2010, top row) and maximum solar activity (2000–2002, bottom row) as a function of MLT time for the meridional beams for each of Bruny Island (TIG, a and b), Prince George (PGR, c and d) and Hankasalmi (HAN, e and f) SuperDARN radars (Ghezelbash et al, 2014).

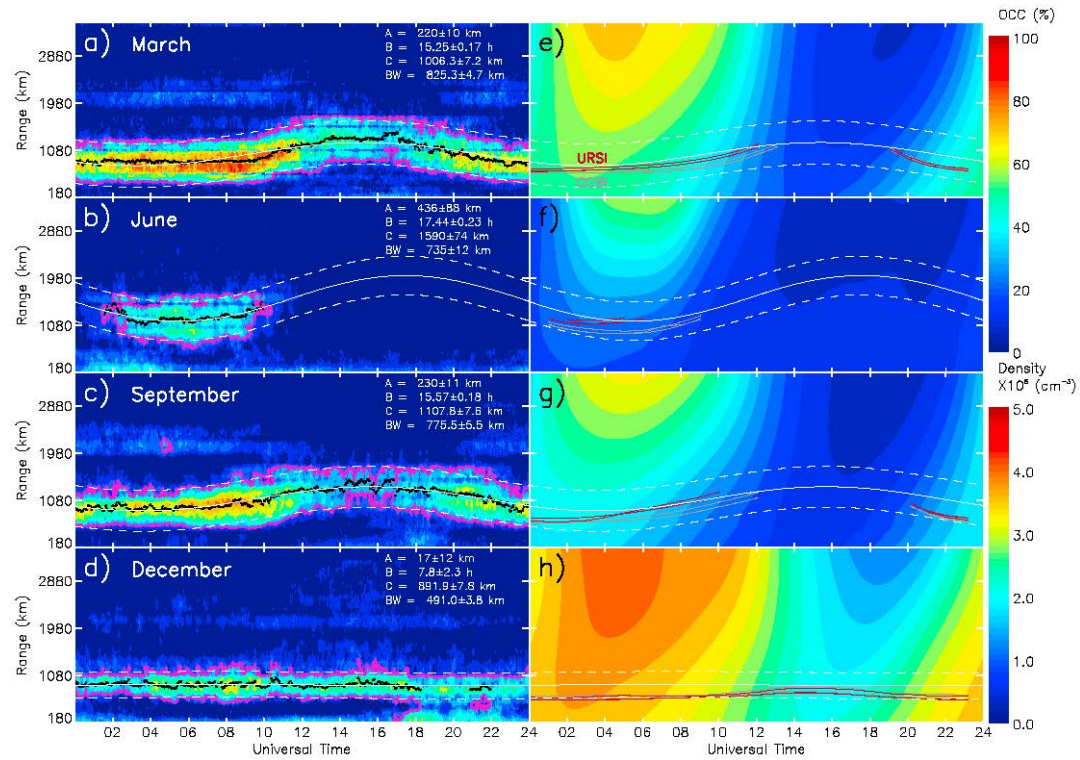


Figure 2.12 Monthly average plots of ionospheric backscatter occurrence (a–d) and (e–h) peak electron density for 2010 showing seasonal variations. Four months are selected (one for each season) to show seasonal variations (Lamarche et al, 2015).

2.8 Summary

This chapter has reviewed the ionosphere in detail and has discussed some of the previous studies on the use of HF backscatter to study variations in the Earth's ionosphere and previous studies that have investigated the role of solar wind parameters and magnetic indices on HF backscatter with special reference to the use of data from SuperDARN radars. The aim of this thesis is to carry out longer term studies of ionospheric variations to further analyse and understand the role of external drivers in ionospheric variability and to possibly predict their relationship on the occurrence of backscatter. Chapter 4 begins with the temporal study of the ionospheric scatter and ground scatter variation over twenty years, which includes a solar cycle variation, seasonal variation and diurnal variation, by investigating the suggestions and assumptions made by Milan et al. (1997b). The study is then extended in Chapter 5 which focuses on the spatial study of backscatter by investigating the distribution of backscatter in selected beams and distribution with range. The investigation of the role of external drivers in ionospheric variability their relationship on the occurrence of backscatter is carried out in Chapter 6.

Chapter 3

Instrumentation & Data Sources

3.0 Instrumentation

The main data sources are the two Super Dual Auroral Radar Network (SuperDARN) radars at Hankasalmi in Finland and Pykkvibaer in Iceland. Supplementary data include solar wind data and magnetic indices, the latter having been derived from ground based magnetometers. This chapter discusses the basic features and the modes of operation of the radars used in this thesis.

3.1 Introduction

Radio waves undergo total or partial reflection in the ionospheric plasma when their frequency is equal to the critical or plasma frequency, f_N . The wave can exhibit coherent scatter depending on a number of factors which include the wave frequency or plasma turbulence (direct perturbation of the ionization structure) generated by instabilities in the ionosphere. Knowledge of the ionosphere and its interactions with the sun has been greatly enhanced by the application of radar techniques to atmospheric and ionospheric science.

Radar methods and techniques have been and continue to be used for scientific studies and have provided major contributions to our knowledge of the Earth's ionosphere, Earth's magnetosphere and solar-terrestrial interactions (Rottger, 2004). Radar methods involve transmitting a radio pulse or pulse code, which is scattered by, or reflected from, irregularities in the refractive index. The nature of the returned signals received as the returned "echo", which have been reflected or scattered back from the targets to the receiver at a time after transmission, provides detailed knowledge of the medium and the nature of the scatter. The radio signal is reflected in the ionosphere when its frequency f is equal to the local plasma frequency f_{pe} ,

$$f_{pe} = \sqrt{(n_e \cdot e^2 / 2\pi\epsilon_0 m_e)} \quad (3.1)$$

To a good approximation, $f_{pe} = 9000 \cdot \sqrt{n_e}$ Hz, where n_e is the electron density in cm^{-3} , such that a typical peak electron density in the ionosphere of approximately 10^6 cm^{-3} (i.e 10^{12} m^{-3}) results in $f_{pe} \leq 9 \text{ MHz}$.

In the context of the work described in this thesis, the irregularities responsible for the coherent scatter radar are amplified well above thermal levels by the action of plasma instabilities (Ruohoniemi et al, 2014). Since the work reported in the thesis only uses data from SuperDARN (discussed in section 2.7.2), we focus on the operations of the radars that form this network.

3.2 SuperDARN

SuperDARN is a network of HF coherent scatter radars (Greenwald et al., 1995; Chisham et al., 2007; Lester, 2013) which has been in operation for over twenty years. SuperDARN radars employ backscatter (coherent scatter) from high-latitude field aligned ionospheric irregularities (E and F regions of the ionosphere) as tracers of the bulk plasma motion under the influence of the convection electric field and, hence, as a diagnostic tool for the investigation of large scale magnetospheric-ionospheric coupling (Milan et al., 1997).

SuperDARN currently consists of 35 radars in the southern and northern hemispheres which are essentially identical in their technical design. The radars are listed in table 3.1 for the northern hemisphere and table 3.2 for the southern hemisphere. The radars often operate in pairs. Initially, radar fields of view were designed such that they overlapped such that coincident observations of the line of sight velocity could be combined to form 2-D velocity vectors perpendicular to the magnetic field. Subsequently, however with the advent of new analysis techniques, such as the so-called map potential technique (Ruohoniemi & Baker, 1998), radar pairs were co-located thereby expanding the coverage from an individual site. The combined fields of view cover extensive regions of both the northern and southern hemisphere (Chisham et al 2007). The fields of view of the northern and southern hemispheres of the radars are illustrated in Figure 3.1.

The SuperDARN method or technique is based on the refraction and scattering of high frequency (HF) radio signals within the ionosphere (Chisham et al., 2001). The two radars in this study operate over a frequency band that extends from 8 to 20 MHz and both use an electronically phased array of 16 log-periodic antennas for both transmission and reception (Greenwald et al, 1985). The radars normally sound 16 beams sequentially to

form a full 52° azimuth scan and normally run between 9 and 14 MHz, often changing their frequency between day and night. The beam can be moved to any one of the 16 directions by changing the phase distribution along the array. Variations in the frequencies between day and night give HF radars the ability to monitor the ionosphere in relation to changes in ionospheric conditions. Lower frequencies are used at night since this increases the amount of refraction through the F region where the ionization is depleted at this time (McWilliams, 2001).

A typical SuperDARN radar comprises two arrays of about 50-foot-tall towers log-periodic antennas, separated by a spacing of 15.24m. The spacing allows the radar beam to take up several azimuthal directions. One array, the main array, is used for both transmission and reception of the radar signals, while the other, a smaller interferometer array is used for reception only. Each antenna in the main array is driven by a 600 Watts solid state pulse transmitter which includes a Receive/Transmit (Rx/Tx) switch to allow for the antenna array to be used to both receive and transmit.

The interferometer array of 4 antennas separated from the main array by typically 100 m, and parallel to it has antennas similar to those in the main array, and is used to estimate the elevation angle of the arrival of backscattered radar signals (Milan et al., 1997a; Milan et al., 1997b). The elevation angle of incoming radio waves can be determined by measuring the phase difference between the antenna arrays and is important in identifying the HF propagation mode, i.e. whether the received signal is from the E region or F region. The antennas in each array are phased with relationship to one another to form an antenna pattern in which the maximum gain (beam position) has one of 16 azimuthal pointing directions separated by approximately 3.2° , distributed symmetrically about the radar boresites of -12° (i.e. west of north) and 30° (east of north) for the Finland and Iceland radars respectively (Milan et al., 1997b).

The two SuperDARN radars discussed in this study are located at Hankasalmi, Finland, which has been in operation since the beginning of March 1995 and the Pykkvibaer, Iceland, which commenced operation in mid-November 1995. Each system is a bistatic HF auroral radar system with a viewing area of $3 \times 10^6 \text{ km}^2$ approximately the size of Western Europe, and can achieve a spatial resolution of about $50 \times 50 \text{ km}$, similar to that described by Greenwald et al (1995).

Table 3.1 SuperDARN radars in the northern hemisphere

S/N	Radar Name	Geographic coordinates		Geomagnetic coordinates		No. of beams	No. of Range Gates	Radar Code name	Radar Scan direction
		Lat.(°)	Lon. (°)	Lat.(°)	Lon.(°)				
1	Adak Island East	51.88	-176.62	47.6	-113.0	22	110	ade	E
2	Adak Island West	51.88	-176.62	47.6	-113.0	22	110	adw	W
3	Blackstone	37.10	-77.95	48.2	-2.7	24	110	Bks	W
4	Christmas Valley East	43.27	-120.36	49.5	-58.3	24	75	Cve	E
5	Christmas Valley West	43.27	-120.36	49.5	-58.3	24	75	Cvw	W
6	Clyde River	70.49	-68.50	78.8	18.1	16	100	Cly	W
7	Fort Hays East	38.86	-99.39	48.9	-32.2	22	110	Fhe	E
8	Fort Hays West	38.86	-99.39	48.9	-32.2	22	110	Fhw	W
9	Goose Bay	53.32	-60.46	61.1	22.9	16	100	Gbr	E
10	Hankasalmi	62.32	26.61	59.1	104.5	16	75	Han	W
11	Hokkaido	43.54	143.61	37.3	-144.9	16	110	Hok	E
12	Hokkaido West	43.54	143.61	37.3	-144.9	16	110	Hkw	W
13	Inuvik	68.414	-133.772	71.5	-85.1	16	100	Inv	E
14	Kapuska sing	49.39	-82.32	60.2	-8.3	16	100	Kap	W
15	King Salmon	58.68	-156.65	57.5	-99.1	16	75	Ksr	W

16	Kodiak	57.62	-152.19	57.5	-94.9	16	75	Kod	E
17	Longyearbyen	78.153	16.074			16	110	lyr	
18	Pykkvibaer	63.77	-20.54	64.6	67.3	16	75	Pyk	E
19	Prince George	53.98	-122.59	59.6	-64.3	16	100	Pgr	W
20	Rankin Inlet	62.82	-93.11	72.6	-26.4	16	100	Rkn	W
21	Saskatoon	52.16	-106.53	60.9	-43.8	16	75	Sas	E
*22	Schefferville	54.8	-66.80	63.7	14.9	16	75	Sch	W
23	Stokkseyri	63.86	-22.02	64.9	66.1	16	75	Sto	W
24	Wallops Island	37.93	-75.47	48.7	0.8	24	110	Wal	E

*radar not in operation

Table 3.2 SuperDARN radars in the southern hemisphere

S/N	Radar Name	Geographic coordinates		Geomagnetic coordinates		No. of beams	No. of Range Gates	Radar Code name	Radar Scan direction
		Lat.(°)	Lon. (°)	Lat.(°)	Lon.(°)				
1	Buckland park	-34.62	138.46	-46.2	-146.1	22	110	bpk	E
2	Dome C	-75.09	123.35	-88.9	54.6	16	75	dce	
*3	Falkland Islands	-51.83	-58.98	-39.0	9.9	16	75	fir	E
4	Halley	-75.52	-26.63	-62.1	29.3	16	75	hal	E
5	Kerguelen	-49.22	70.14	-58.7	122.7	16	75	ker	W
6	McMurdo	-77.88	166.73	-80.0	-33.3	16	75	mcm	E

7	SANAE	-71.68	-2.85	-61.8	43.7	16	75	san	W
8	South Pole Station	-89.995	118.291	-74.3	18.5	16	75	sps	
9	Syowa East	-69.00	39.58	-66.5	72.2	16	75	sye	E
10	Syowa South	-69.00	39.58	-66.5	72.2	16	75	sys	W
11	Tiger	-43.40	147.20	-54.8	-133.2	16	75	tig	W
12	Unwin	-46.51	168.38	-54.4	-106.2	16	75	unw	W
13	Zhongshan	-69.38	76.38	-74.9	97.2	16	75	zho	E

*radar not in operation

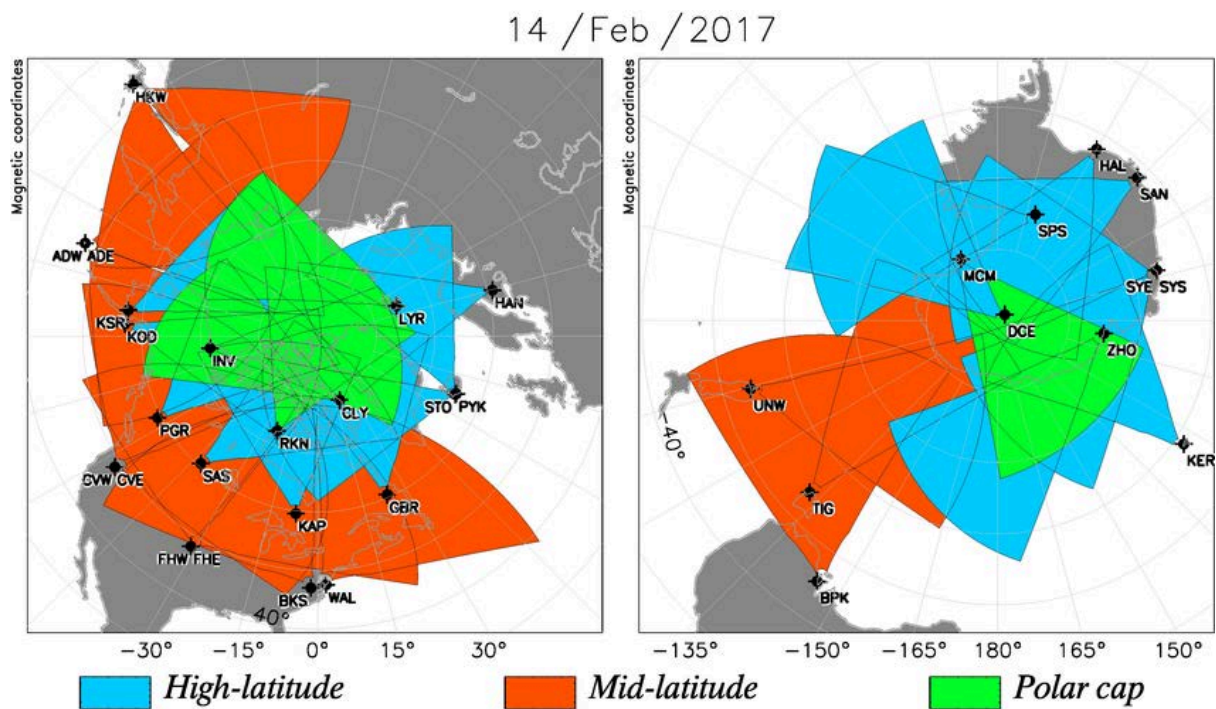


Figure 3.1 Fields-of-view of SuperDARN Radars in the Northern and Southern Hemispheres (The left panel is the Northern hemisphere; the right panel is the Southern hemisphere). Created from the Virginia Tech (VT-SuperDARN) using the Radar Field-ofView Tool

The SuperDARN radars operate in a number of different modes depending on the scientific objectives or goals to be achieved. However, the radars do operate a standard or

common mode for at least 50% of the time in each month. Other modes are either allocated as special time (up to 20% of each month) or discretionary time (up to 30% of each month). If high time resolution data are required, a SuperDARN radar can scan the beam sequentially during discretionary modes by returning to a selected beam or beams position after every other beam resulting in better time resolution along a particular beam. SuperDARN radar pairs are synchronised to perform a complete scan with the dwell time on each generated beam depending on the resolution required. When the radars are in common modes, they are synchronised to perform a complete scan, full beam sweeps for every two minutes with a dwell time of 7 s on each beam or 1 minute with a dwell time of 3s on each beam. Also when a higher temporal resolution is required, the radars are synchronised to perform a complete scan for every 1 minute during fast common modes with a dwell time of 3s on each beam.

3.3 Pulse sequence

SuperDARN radars are multi-pulse radars, they transmit pulses in a sequence rather than continuously. The multi-pulse sequence is used to cover the search area and enable the signals to track moving targets. The targets view SuperDARN radars as bistatic radars in a way that it appears as if the transmitter and the receiver antennas are at different locations, hence the transmitted pulses are not received simultaneously. SuperDARN radars make use of a seven-pulse sequence pattern (0, 9, 12, 20, 22, 26, 27) illustrated in Figure 3.3 using 100 ms transmission window for the full sequence with the radar switching to receiver mode after each pulse transmission. The duration for each transmitted pulse is normally 300 microseconds (μs) producing a range length or range cell of 45km.

The radars receive the transmitted pulse i.e the scattered signal after each pulse is transmitted by switching to receiver mode to receive the scattered signal which has a delay time or “lag” time τ in the pulse transmission. The time taken for the first pulse transmitted which is referred to as the time to the first range is set to t_0 , and represents the time over which the transmitted radar beam does not hit any scattering irregularities nor returned to the radar. The time to the first range is of the order of 1200 μs and corresponds to 180 km range, or distance, in the atmosphere. The scattered signals received by the radars are binned into 75 range gates along each beam giving a total of 75 x 16 range cells if all the 16 beams are used. During the normal mode of operation it takes about 2400 μs for pulses

to return from the furthest range gates such that the range (ground range) to the furthest gate is 3550km.

Since the delay time between pulse transmission and the measurement of the first echoes is used to determine the lag or distance to the first range, the separation of the first pulse by a large time lag with respect to the time lags of other pulses in the sequence from other pulses reduces the possible contamination of the zero-lag correlation pulse with itself. Hence, the second pulse in the pulse code is normally 9 x the unit time of the radar auto correlation function (ACF). SuperDARN transmitted pulses are separated by integral multiples of a unit pulse separation which is normally set to τ . The analysis of the radar returned signal is carried out and processed after which ACF for individual range cells as a function of the lag time is carried out for the targets.

The ACF is fitted with a mathematical function that uses signal power, Doppler shift and spectral width as parameters. The phase difference between the real and the imaginary parts of the computed autocorrelation function (ACF) of each of the pairs of radar pulses which are separated by increasing lag times are plotted for each lag time. The Doppler frequency is calculated from the gradient of the phase lag graph which can be used to determine the Doppler velocity. There is a decorrelation of the ACF with increasing lag as the time separation of the returned signals increases leading to a decay of the amplitude of the ACF with increasing lag time which is used to determine the spectral width. The parameters that yield the best fit are then stored in FITACF files as received power, Doppler velocity, signal to noise ratio and spectral width for that range. A typical daytime backscatter plot is illustrated in range time intensity plot by figure 3.2. It is such backscatter data illustrated that the statistical study in chapter 4, 5 and chapter 6 of this thesis are carried out.

The multi-pulse sequence is usually repeated 70 times at each beam for the 7s dwell time, producing 70 ACF's which are processed by integrating and averaging the ACF's to increase the signal to noise ratio for greater accuracy. Similarly, for a 3s dwell time the multi-pulse sequence might be repeated 30 times at each beam position resulting in 30 ACF's.

SuperDARN multi- pulse sequence pattern illustrated in Figure 3.3 has corresponding integer number of lags with unique lags for all integral multiples of the lag times except the missing lags, 16τ , 19τ , 21τ , 23τ , 24τ , 25τ . The missing lags are connected to the fact that the receiver is always turned off when the radars are transmitting.

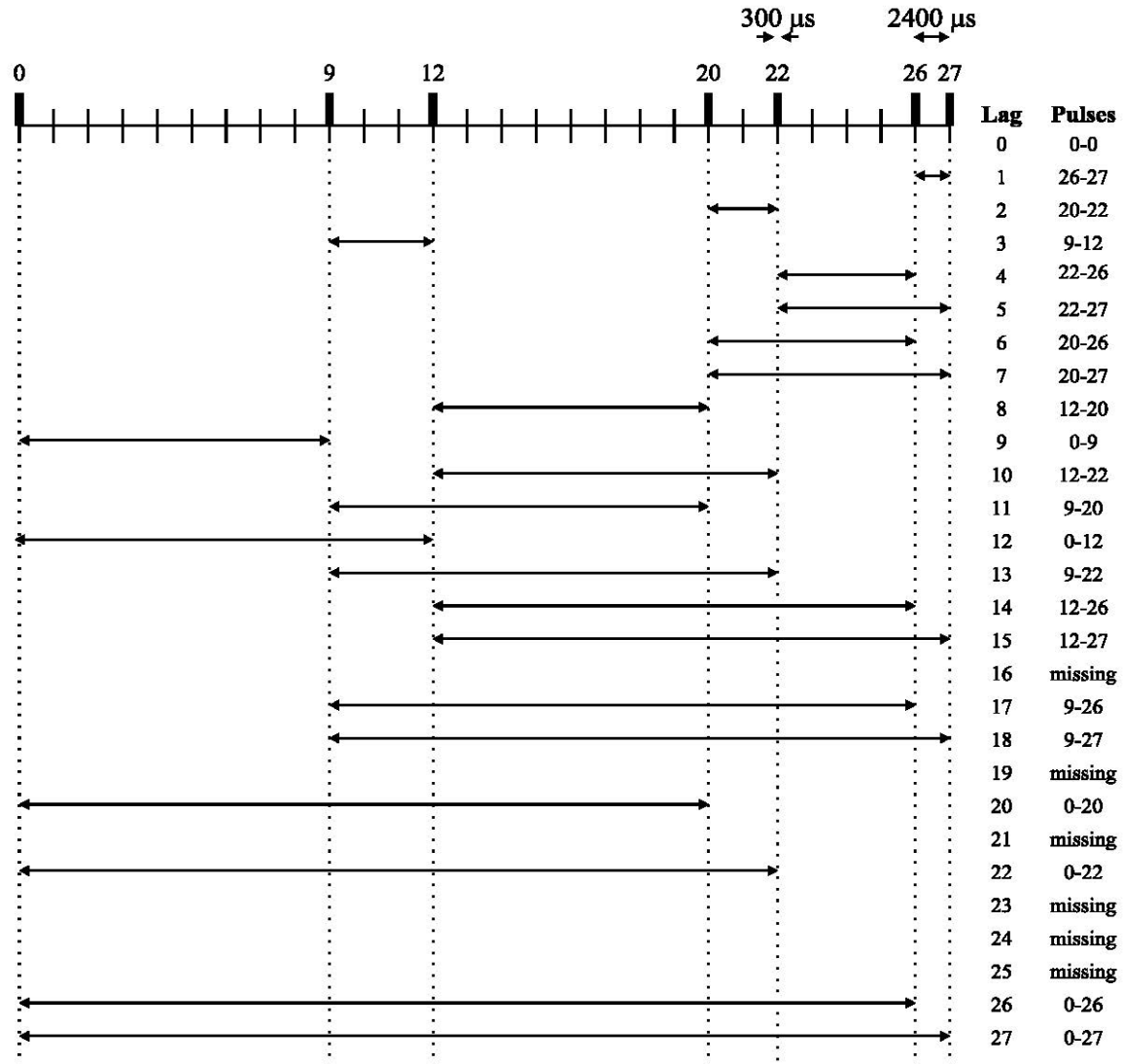


Figure 3.3: Schematic representation of SuperDARN radar seven-pulse sequence for normal operation mode. From McWilliams 2001

3.4 Data from Spacecraft Instruments

In this thesis data from spacecraft were also used in addition to data from SuperDARN radars. Solar wind data which includes information such as the solar wind velocity, density, pressure and the interplanetary magnetic field strength and orientation used in this

thesis were provided by The Advanced Composition Explorer (ACE) satellite which was launched in August 1997 as solar wind upstream monitor. The ACE satellite provides comprehensive upstream solar wind and IMF analysis. The spacecraft was designed by John Hopkins University Applied Physics Laboratory (JHU/APL) and is located near the L1 Lagrangian point, about 221 RE upstream of the Earth which is on the Sun-Earth line. The upstream solar wind and IMF (Interplanetary Magnetic Field) conditions are measured using the Magnetic Field Experiment (MAG) (16-s), the Solar Wind Electron, Proton and the Alpha Monitor (SWEPAM) (64-s) instruments (McComas et al., 1998; Smith et al., 1998; Stone et al., 1998).

The instruments on-board the Advanced Composition Explorer (ACE) measured the interplanetary parameters such as the plasma speed (v_p), the density, the pressure and the three GSM components of the IMF (B_x , B_y , B_z) used in this thesis upstream of the Earth (Stone et al., 1998).

3.5 Magnetic Indices

The measure of magnetic activity on the Earth's surface and in space is described by different magnetic indices (McPherron, 1995). These magnetic indices are derived from ground-based magnetometers. The main indices used here are the so called Auroral indices i.e. AU, AL and AE and a ring current index, the SymH.

Davis and Sugiura, (1966) monitored the global electrojet activity by observing the deviations made by ionospheric currents with the H component of the magnetic field. From their observations, indices known as the Auroral Electrojet indices based on the data from the magnetometers installed in many parts of the auroral zone were generated. These indices were firstly introduced by Davis and Sugiura in 1966 to measure the flow of the auroral electrojet currents in the auroral region, the high-latitude region of the Earth's ionosphere (Mayud, 1980). These indices are AE, AU, AL and AO. The specific Auroral Electrojet indices that are used in this thesis are the AE, AL, AU. The traces of the H component arranged in universal time measured from the stations is used to define the upper and lower envelopes with such upper and lower envelopes define as the AU (U for 'upper') and AL (L for 'lower') indices (Mayud, 1980). The AE index corresponds to the difference between AU and AL (AU-AL) and it is a measure of the overall horizontal current strength and depends on the maximum eastward and westward electrojet currents (Mayud, 1980). Figure 3.4 illustrates the plot of AU and AL indices showing signature of

substorm with an increase in AU from the background level and decrease in AL from the background level.

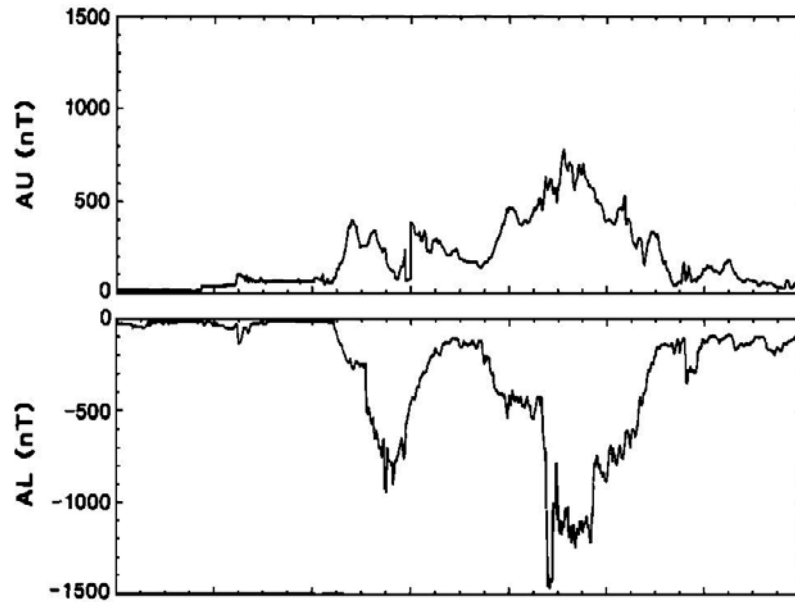


Figure 3.4 Top panel showing AU index and bottom panel showing AL index (adapted from McPherron and Manka, 1985)

The SYM-H index is calculated from ground-based magnetic stations on a monthly basis using the data of the 5 international quiet days are used for that month; the original data of the international 5 quiet days of the month that include the Sq and geomagnetic main field are averaged every minute and fitted by spline functions to give the monthly background field which is then subtracted to obtain the monthly disturbance field at 1-min intervals (Iyemori, 1990). Iyemori (1990) noted that these calculations were followed by a coordinate transformation to a magnetic dipole system, with the tacit assumption that the ring current flows parallel to the dipole equatorial plane after which the six station average of the longitudinal symmetric magnetic field component is calculated from the averages of the disturbance component at each minute and the SYM-H computed by making latitudinal corrections which involves division by the average value of the cosines of the dipole latitude.

3.6 Coordinate Systems

Different coordinate systems are used when taking into consideration different phenomena in Solar- Terrestrial relations such as plasma motion, geomagnetic disturbances, aurora events, ionospheric currents and variations due to their organization with respect to the Earth's magnetic field. The coordinate systems used in this thesis are discussed below.

3.6.1 Geocentric Solar Ecliptic Coordinates (GSE)

Geocentric solar ecliptic coordinates (GSE) are a non-magnetic coordinates system oriented around the ecliptic plane. The X - axis of GSE coordinates has the same x axis as Geocentric Solar magnetic Coordinates (GSM), and is in the positive direction towards the Sun with GSM- X equals zero at the centre of the Earth. The Y -axis of GSE coordinates is in the ecliptic plane, positive in the opposite direction to the Earth's motion around the Sun, and the Z axis completes the right handed system. In GSE coordinates, the dipole axis moves in three dimensions (Laundal and Richmond, 2016).

3.6.2 Geocentric Solar Magnetic Coordinates (GSM)

The Geocentric Solar Magnetic coordinates is used when studying the Sun's influence on the geomagnetic field at high altitudes regions controlled by the solar wind and the interplanetary magnetic field (IMF) (Laundal and Richmond, 2016). The GSM X -axis points from the origin of the Earth (the centre) to the Sun, and the GSM- Y axis direction is perpendicular to the magnetic dipole axis and the Earth-Sun line and positive towards the dusk, the Z -axis direction is perpendicular to the X -axis and it lies in the plane containing the Earth-Sun line (X -axis) and the Earth's dipole moment axis, and completes a right-handed system. Figure 3.5 illustrates the GSM coordinate systems, the x and z axes are in green. The GSM x axis is along \mathbf{s} , and the z axis intersects the sunlight terminator (the dark side of the Earth is *shaded*). The GSM xz plane is spanned by the vectors \mathbf{m} (along the dipole axis) and \mathbf{s} (pointing to the Sun). The base vectors of the GSM coordinates are written in equations below:

$$\mathbf{X}_{gsm} = \hat{\mathbf{S}} \quad (3.2)$$

$$\mathbf{Y}_{gsm} = \frac{\mathbf{M} \times \mathbf{X}_{gsm}}{\|\mathbf{M} \times \mathbf{X}_{gsm}\|} \quad (3.3)$$

$$\mathbf{z}_{gsm} = \mathbf{X}_{gsm} \times \mathbf{Y}_{gsm} \quad (3.4)$$

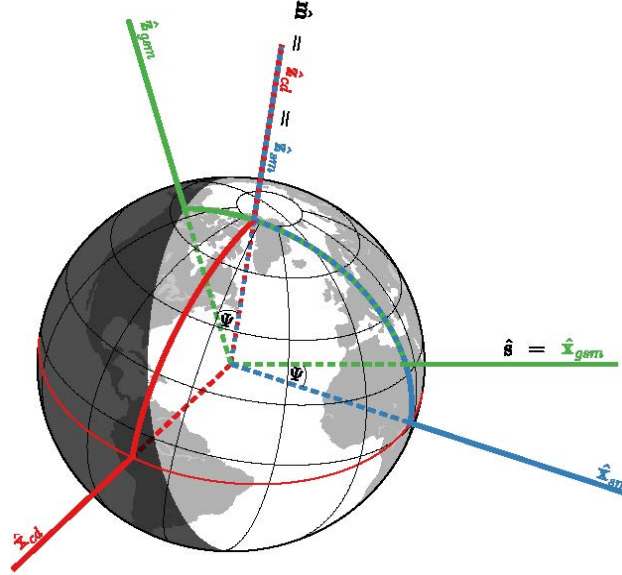


Fig. 3.5 Orthographic plot illustrating the GSM coordinate systems, the x and z axes in green. The GSM x axis is along \mathbf{s} , and the z axis intersects the sunlight terminator (the dark side of the Earth is *shaded*). The GSM xz plane is spanned by the vectors \mathbf{m} (along the dipole axis) and \mathbf{s} (pointing to the Sun). GSM coordinates depends on \mathbf{s} , which changes with the subsolar point. Taken from Laundal and Richmond, 2016.

3.6.3 Magnetic Local Time (MLT)

In this thesis, data in Magnetic Local Time (MLT) time-scales were used in addition to the data in Universal Time (UT). The Magnetic Local time is used to specify the location of a point on the Earth's surface relative to the Earth's magnetic pole, it is similar to geographic longitude with the exception that the lines of constant magnetic local time join the two magnetic poles rather than geographic poles. The use of magnetic local time to organize data and models with respect to the position of the Sun instead of magnetic longitude has been identified to be appropriate (Vegard, 1912). The equation of the Magnetic Local time used in this thesis is written in equation 3.5 below where φ is the magnetic longitude of the point in question and UT is the universal time also specified in hours.

$$\text{MLT}_1 = (\varphi / 15 + \text{UT}) - 4.73 \quad (3.5)$$

Instrumentation & Data Sources

The total number of hours in the Magnetic Local Time (MLT) reference frame is 24 hours similar to the total hours of Universal Time (UT), the 12th hour (noon) points toward the Sun, and 24th (midnight) points away from the Sun.

Chapter 4

Backscatter Occurrence Over the life time of SuperDARN

4.1 Introduction

This chapter describes the statistical analysis of the occurrence of ionospheric and ground backscatter using twenty years, i.e. nearly two complete solar cycles, of SuperDARN data, specifically data from Hankasalmi and Pykkvibaer. Previous statistical studies of the occurrence of backscatter, both ionospheric and ground scatter observed by the SuperDARN radars have utilised limited data sets or subsets of data that do not span more than a few years (e.g., Milan et al., 1997b; Ruohoniemi and Greenwald, 1997; Ballatore et al., 2000; Parkinson et al., 2003; Koustov et al., 2004; Carter and Makarevich 2010; Carter et al., 2011; Kumar et al., 2011; Kane et al., 2012; Ghezelbash et al., 2014) or, when extended further, for example over a solar cycle, have been limited to F region echoes (Ghezelbash et al., 2014; Koustov et al., 2004; Kane et al., 2012), near-range gates (Kumar et al., 2011) and sometimes to E region echoes only (Carter & Makarevich, 2010; Carter et al., 2012). Detailed discussion of previous work is found in chapter 2.

4.2 Instrumentation

Data from the two SuperDARN (Super Dual Auroral Radar Network, (Greenwald et al., 1995; Chisham et al., 2007)) coherent radars located at Hankasalmi (62.3°N, 26.6°E) in Finland and the other at Pykkvibaer (63.8°N, 20.5°W) in Iceland, which have both been in operation for over twenty years, are used in this analysis. The field-of-view of the two radars are shown in Figure 4.1. Long term statistical studies on the occurrence of ionospheric backscatter and ground backscatter of the whole data set, the total field of view of the two SuperDARN radars, which extends from 1996-2015 spanning nearly two full solar cycles are used in this analysis making the study unique from other previous studies.

4.3 Data

In order to determine the solar cycle variation, the seasonal variation, and the diurnal variation in the backscatter data the data for the total field of view for both Hankasalmi and Pykkvibaer radars were binned into ionospheric backscatter and ground backscatter using

the standard criterion for SuperDARN data. Only data when the radars were in normal scan mode (Greenwald et al. 1995, Lester, 2013) are used in this analysis.

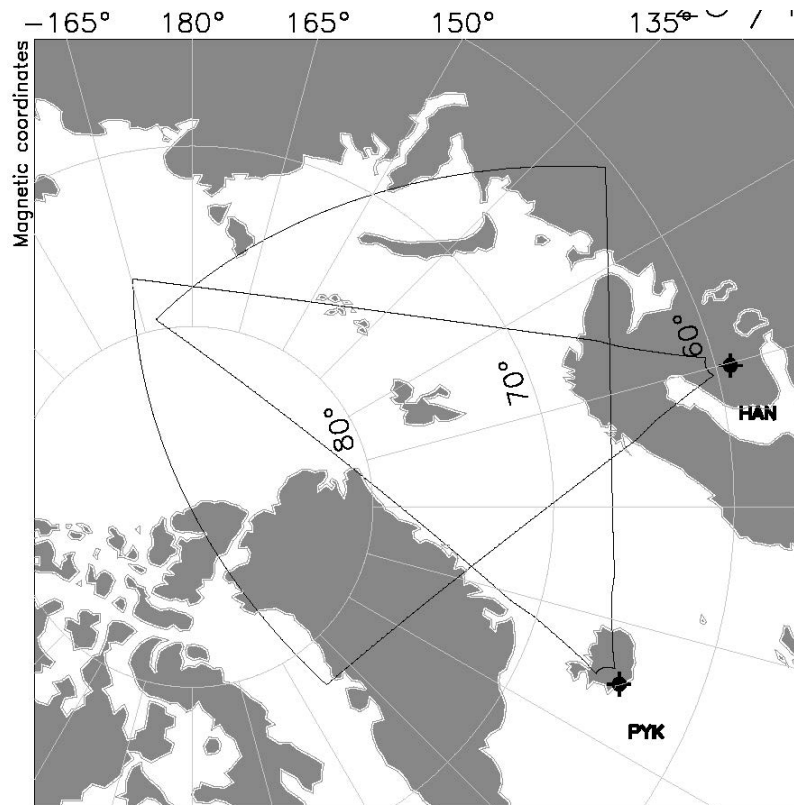


Figure 4.1 Radar field of view of Hankasalmi (62.3°N , 26.6°E) and Pykkvibaer (63.8°N , 20.5°W) (<http://superdarn.org/tiki-index.php?page=radarFoV>)

In this chapter we investigate the diurnal monthly occurrence of ionospheric and ground scatter. The hourly percentage occurrence within the Hankasalmi and Pykkvibaer radar fields-of-view for the full period of interest is calculated. The ground scatter and ionospheric scatter percentage occurrence rate is calculated as a ratio of the number of recorded echoes in the total field of view to the total number of observations in the total field of view over each month. The ratios were averaged for each hour of observations and in 1 hour universal time bins. We first present the monthly mean percentage occurrence of ionospheric and ground backscatter for the total field of view for both Hankasalmi and Pykkvibaer radars. This is then followed by the hourly percentage occurrence of ionospheric and ground backscatter for the total field of view for the two radars.

In addition to the percentage occurrence of ground and ionospheric backscatter from the two SuperDARN radars data, the latter part of the chapter also includes sunspot data. The Sunspot number R was introduced by Rudolph Wolf in 1948 to find the average length of a solar cycle by organising the daily observations of sunspots, and they are also used by solar physicists to determine the nature of the solar cycle (Richards and Rogers, 2013). The sunspot number is characterized by its variability as much as its regularity and the sunspot data used here are the quarterly mean of sunspots from 1996 - 2015.

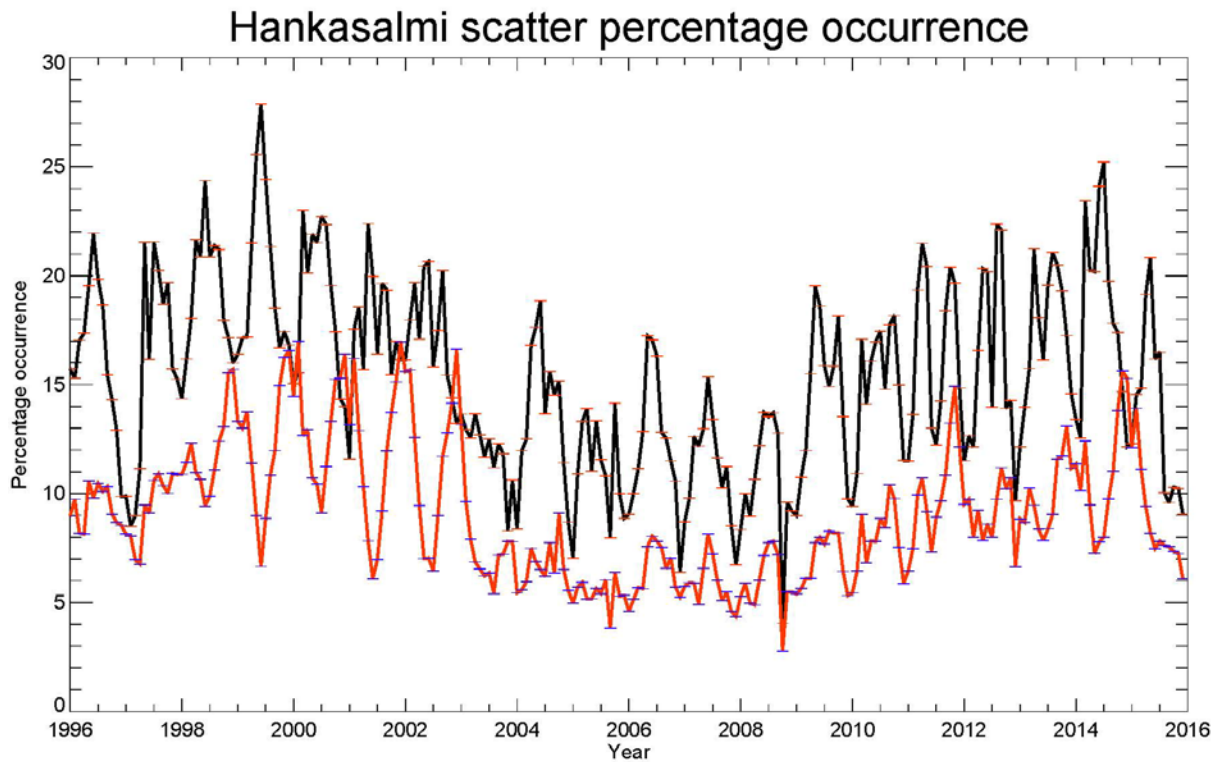
4.4 Monthly mean statistics of backscatter

The monthly mean percentage of ionospheric backscatter and ground backscatter is taken by averaging the hourly percentage occurrence of backscatter for each month and plotting the data as a function of year. The ionospheric and ground backscatter monthly mean occurrence for Hankasalmi and Pykkvibaer are presented in Figure 4.2a and Figure 4.2b respectively, the red line with blue error bars in each plot represents the monthly mean percentage occurrence of ionospheric backscatter while the black line with red error bars represents the monthly mean percentage occurrence of ground scatter. The error bars represent the standard error on the mean of the distribution for each monthly value.

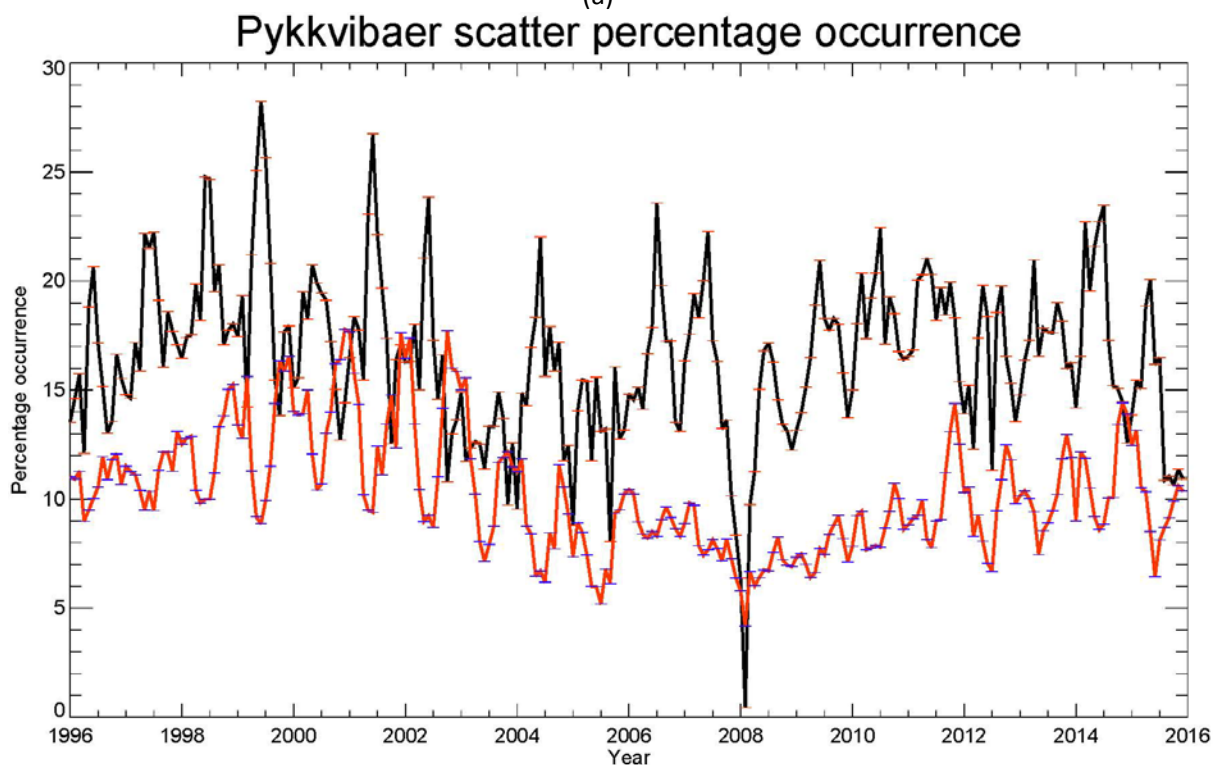
4.4.1 Ionospheric backscatter

The monthly mean percentage occurrence of ionospheric backscatter at Hankasalmi (red) peaks during solar maximum, with a maximum value of 16%, with a minimum of about 5% during solar minimum years, 2006 - 2009 (Figure 4.2a). During the solar maximum of cycle 23 (2000-2002), Hankasalmi data typically exhibit an overall larger occurrence of ionospheric backscatter than at the maximum of solar cycle 24 (2012-2013), although the peak levels are similar, 16% in 2000 – 2002 and 14% in 2012-2013. Figure 4.2a also demonstrates that the occurrence of ionospheric backscatter during the solar minimum between cycles 22 and 23 (1997) is larger than during the solar minimum between cycles 23 and 24 (2005-2009). It should be noted that the data during the first of these two minima is limited to just one year, while the second is extended over a period of 4 years.

We note that there is also a significant seasonal variation in the occurrence of ionospheric scatter at Hankasalmi during solar cycle 23 between 1998 and 2004. During this time the ionospheric scatter occurrence peaks during the winter months, while the occurrence minimum occurs during the summer.



(a)



(b)

Figure 4.2a and b illustrates monthly mean percentage occurrence of ionospheric (red) backscatter with error bar (blue) and ground (black) backscatter with error bar (red). The monthly mean percentage of ionospheric backscatter and ground backscatter is taken by averaging the hourly percentage occurrence of backscatter for each month and plotting the data as a function of year from 1996 – 2015. The percentage occurrence of both ionospheric and ground backscatter is plotted on the y axis and year is plotted on the x axis **(a)** Hankasalmi radar; **(b)** Pykkvibaer radar.

As discussed later this is in antiphase to the occurrence of ground scatter in 1998 – 2002 and in phase from 2002 – 2012 with the antiphase effects returning back around 2013.

It is also noticeable that this seasonal variation is not as clear during solar minimum nor the increasing phase of the current solar maximum, reoccurring only in 2014 and 2015, i.e. close to solar maximum. We return to the seasonal variation later in this section.

The monthly mean percentage occurrence of ionospheric scatter within the Pykkvibaer radar field –of-view for the full period of interest is presented in Figure 4.2b in the same format as in Figure 4.2a. In general, the monthly mean percentage occurrence of ionospheric backscatter at Pykkvibaer behaves in a very similar fashion to that for the Hankasalmi radar. Peaks in the occurrence of ionospheric scatter occur during the two solar maxima periods with a minimum in the occurrence during the extended solar minimum of 2006 - 2009. Also, Pykkvibaer data exhibit a larger occurrence of ionospheric backscatter during the solar maximum of cycle 23 than in the solar maximum of cycle 24, although again the actual peaks in occurrence are similar, 17% in cycle 23 and 14% in cycle 24. There is again a seasonal variation in the occurrence of ionospheric backscatter at Pykkvibaer which in this case lasts until 2006 which is longer than at Hankasalmi, and there is evidence for the return of the seasonal variation earlier in the current solar cycle than at Hankasalmi.

4.4.2 Ground backscatter

Moving to the ground backscatter occurrence for Hankasalmi (black in Figure 4.2a) we note that this is almost exclusively greater than the ionospheric backscatter occurrence. Hankasalmi ground scatter peaks at 28% in 1999 and in 2014 at 25%. Similar to ionospheric scatter, it is also noticed that ground scatter data occurrence during the solar maximum of cycle 23 is on average higher than the maximum of solar cycle 24. A solar cycle dependence of ground backscatter is also noticed, again peaking during solar maximum. There is also a seasonal variation in ground scatter but on this occasion the peak occurs at a different time within each year than the ionospheric scatter. Indeed, as mentioned previously, the two are effectively in antiphase when the seasonal variation is present at Hankasalmi in some of the years and in phase in some other years.

The occurrence of ground scatter in Pykkvibaer (black in Figure 4.2b) shows a similar pattern to that of Hankasalmi. The difference between the peak and minimum in occurrence throughout the interval is perhaps smaller than at Hankasalmi, while there does

appear to be significantly more variability than at Hankasalmi. There is also a significant dip in scatter occurrence in early 2008, which appears to be real, i.e. it is not an instrumental effect. Another prominent difference is that ground scatter and ionospheric scatter occurrence in Pykkvibaer appears to be in anti-phase throughout the period investigated unlike the pattern in Hankasalmi.

4.4.3 Solar Cycle Variation Summary

Our analysis has shown that the maximum occurrence of ionospheric backscatter occurs during the solar cycle maximum while minimum occurrence of ionospheric backscatter occurs during the solar cycle minimum. The maximum occurrence feature of ionospheric backscatter during solar maximum was seen during the two solar cycle maxima that occurred during the period investigated and the pattern is recorded by the two SuperDARN radars. Likewise, the minimum in occurrence of ionospheric backscatter during an extended solar minimum as well as the end of the previous minimum was seen in both SuperDARN radars. It is observed from the analysis that maximum occurrence of ionospheric backscatter during solar cycle 23 maximum is much higher in comparison with the solar cycle 24 maximum.

Although there is limited coverage of the solar maximum period between cycles 22 and 23, the minimum occurrence of ionospheric backscatter during that period is higher than the minimum occurrence of ionospheric backscatter during solar cycle 23/24 minimum. The observation of maximum occurrence of ionospheric backscatter during the two solar maxima might be due to the higher occurrence of ionospheric irregularities due to enhanced electric fields in the high latitude ionosphere and an increase in geomagnetic activity. The minimum occurrence in ionospheric backscatter during the two cycle minima might be due to a lower occurrence of ionospheric irregularities due to the general decrease in geomagnetic activity.

Similar to the pattern of occurrence of ionospheric backscatter, the analysis showed that the maximum occurrence of ground backscatter occurs during the two-solar cycle maxima, while the minimum occurrence was observed during the two-solar cycle minima. Also, it is noticed that the overall peak in occurrence of ground backscatter was recorded during cycle 23 maximum while an overall minimum in occurrence of ground scatter is seen in during the solar cycle 23/24 minimum.

4.5 Hourly-mean percentage occurrence statistics

We now move to the hourly mean percentage occurrence of ionospheric and ground backscatter shown in Figure 4.3 and 4.4 respectively. Here the data are plotted as a function of UT (x axis) and year (y axis), with year starting at the bottom of the figure and increasing up the y axis. The percentage occurrence is colour coded. Also, the quarterly mean sunspot number is plotted on the right side of the hourly mean percentage occurrence of backscatter to illustrate the solar cycle. The ionospheric backscatter occurrence with the quarterly mean of sunspots numbers for Hankasalmi and Pykkvibaer are presented in panels a and b, respectively, of Figure 4.3 while the ground backscatter for Hankasalmi and Pykkvibaer are presented in panels c and d, respectively.

4.5.1 Diurnal Variation of Ionospheric Scatter

The solar cycle variation of ionospheric backscatter described earlier is evident at both Hankasalmi and Pykkvibaer (Figure 4.3a and 4.3b). Looking at the diurnal variation at Hankasalmi of the ionospheric scatter occurrence, the peak occurrence during the two solar maximum periods occurs at night time, i.e. between 0 and 5 UT and 20 and 24 UT. Note that the centre of the Hankasalmi field of view is located at a local time which is approximately one hour ahead of UT. However, at solar minimum, between 2004 and 2009, there is evidence for a seasonal effect. At some times of the year the peak occurrence is at night e.g. 2004 and 2006 while at other times it occurs during the day e.g. 2005 and 2007. This seasonal occurrence is investigated further later in the chapter.

Although, similarities exist in the solar cycle dependence of the occurrence of ionospheric backscatter in the two radars, the solar cycle features for ionospheric scatter occurrence observed in the Pykkvibaer radar are somewhat different from that observed in Hankasalmi radar. The high occurrence rate of ionospheric scatter during solar cycle 23 maximum is seen to appear only around night time and evening time in Pykkvibaer radar unlike in Hankasalmi radar where it appears throughout most of the day with little exception. Also, the minimum percentage occurrence in ionospheric backscatter at Pykkvibaer during the solar cycle minimum occurs during day time only, whereas it is seen to appear in both day time and night time in Hankasalmi radar. It is evident however, that there exist similarities in the high occurrence rate feature in ionospheric scatter pattern in both radars. It can be seen from the Hankasalmi plot in Figure 4.3a that the diurnal variation in the occurrence of

ionospheric backscatter over the period is not constant. For instance, there are months (January and February) with peak occurrence of ionospheric scatter at daytime and months (e.g May, July and August) with a dip in occurrence of ionospheric backscatter at daytime. Also, we notice there are months (e.g May, July and August) with peak occurrence of ionospheric scatter at nighttime and months (February, September) with a minimum occurrence at nighttime. Thus, the occurrences of ionospheric backscatter over the period investigated shows a seasonal dependence of the diurnal variation.

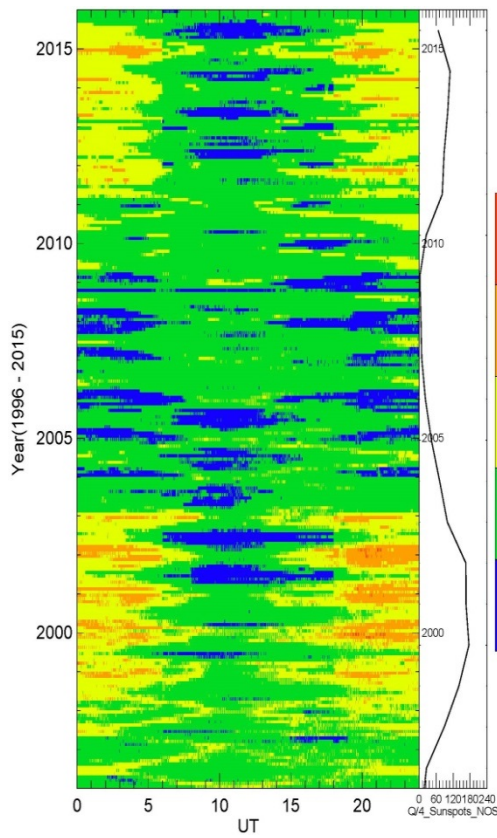


Figure 4.3a

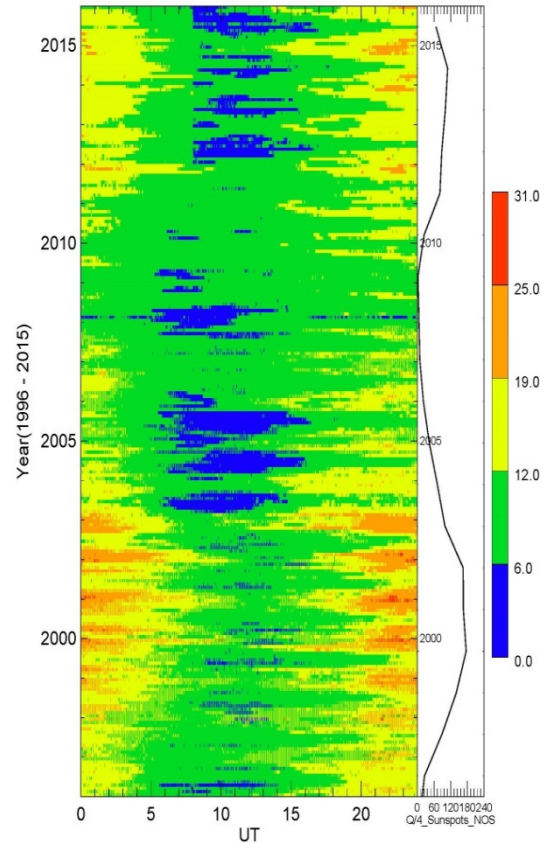


Figure 4.3b

Figure 4.3: Hourly percentage occurrence of ionospheric backscatter as a function of UT (x axis) for the total field-of-view from 1996 to 2015 (y axis). The ionospheric scatter percentage occurrence rate is calculated as a ratio of the number of recorded echoes in the total field of view to the total number of observations in the total field of view over each month from 1996 to 2015. The ratios were averaged for each hour of observations and in 1 hour universal time bins; (*panel a*) Hankasalmi; (*panel b*) Pykkvibaer.

The diurnal variation at Pykkvibaer is much the same as that at Hankasalmi. Note that the centre of the Pykkvibaer field of view is about 2 hours to the west of Hankasalmi and therefore the local time is one hour behind UT. Throughout the period shown the night

time peak occurrence appears reasonably stable for both solar maximum and solar minimum which differs from that at Hankasalmi during the solar minimum years of 2004 to 2009.

4.5.2 Ground backscatter Hourly-mean percentage occurrence statistics

The ground scatter percentage occurrence data for Hankasalmi and Pykkvibaer radars are presented in Figure 4.4a and 4.4b respectively. Similar to the ionospheric backscatter and following the monthly mean occurrence, evidence of the solar cycle dependence of ground backscatter is seen at both radars. The diurnal variation indicates a clear peak in occurrence during daylight hours, for both radars, with the peak in UT being displaced by a couple of hours at Pykkvibaer. There is also clear evidence that high levels of ground scatter can be found at certain times of the year, e.g. during June. The pattern of ground scatter occurrence percentage in Pykkvibaer radar follows the same trend as that of ground scatter occurrence in Hankasalmi radar. Unlike the ionospheric backscatter seasonal dependence of diurnal variation, it is noticed that the diurnal variation in the occurrence of ground backscatter over the period is constant, the two radars exhibit no seasonal dependence of diurnal variation in ground scatter which is evident in Figure 4.4a and 4.4b. From the two figures, we noticed that there exists a peak in the occurrence of ground scatter at daytime in all the months with a minimum in occurrence at nighttime.

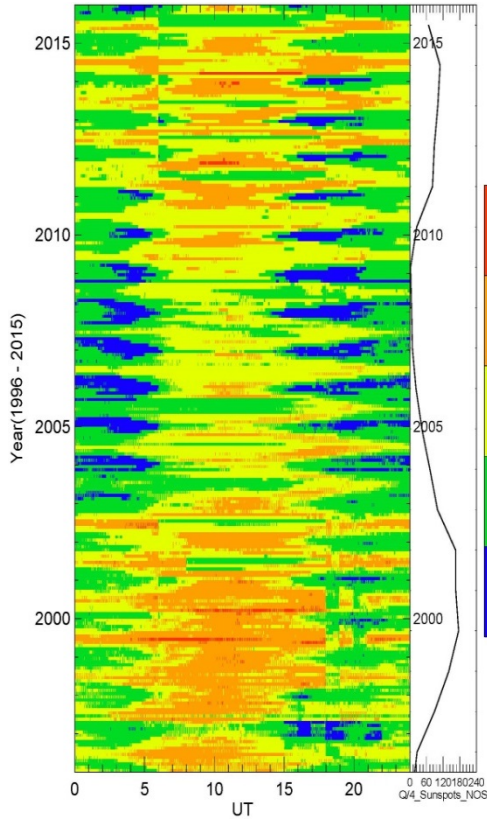


Figure 4.4a

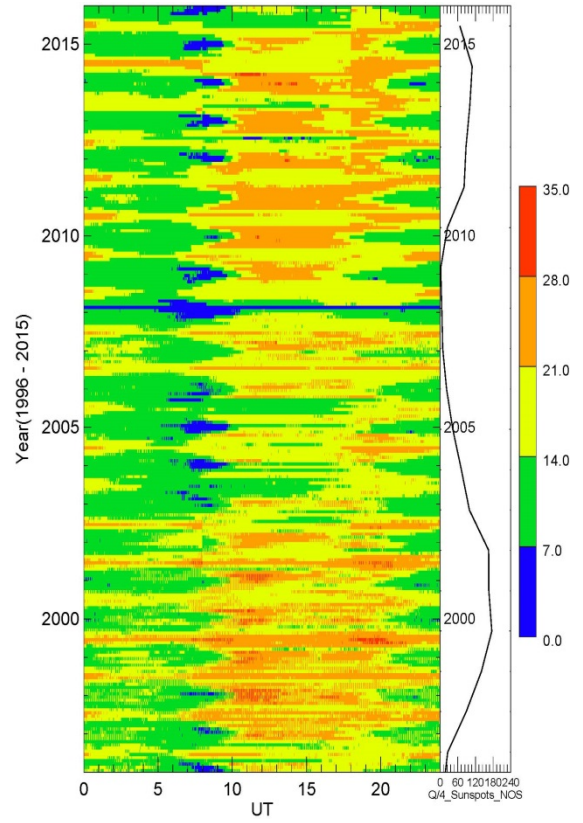


Figure 4.4b

Figure 4.4: Hourly percentage occurrence of ground backscatter as a function of UT for the total field-of-view. The ground scatter percentage occurrence rate is calculated as a ratio of the number of recorded echoes in the total field of view to the total number of observations in the total field of view over each month from 1996 to 2015. The ratios were averaged for each hour of observations and in 1 hour universal time bins; (*panel a*) Hankasalmi; (*panel b*) Pykkvibaer

4.6 Diurnal and Seasonal Variations

As indicated in the previous sections, the variation in the occurrence of ionospheric backscatter at Hankasalmi is not constant throughout the solar cycle. To investigate this seasonal dependence further throughout the solar cycle, a slightly different approach from that used in the above analysis is adopted. This approach can also be used to determine if the occurrence of backscatter varies as a result of the propagation conditions over the solar cycles or due to the presence of ionospheric irregularities. In this section, two months of data are selected as representative of the two extremes of the diurnal occurrence of scatter, June representing northern summer and December representing northern winter. The result of the Hankasalmi ionospheric occurrence for June and December are presented in Figure 4.5a and b, respectively, while Figure 4.6a and b presents the Pykkvibaer ionospheric scatter occurrence for June and December, respectively.

Comparison of panels a and b of Figure 4.5, allows us to illustrate how the diurnal variation in ionospheric scatter differs in June from December. The diurnal variation for June shown in Figure 4.5a for Hankasalmi radar displays a broad maximum in the occurrence of ionospheric backscatter at night time, i.e. between 0 to 05 UT and 20 – 24 UT and a broad minimum in occurrence during the daytime. This diurnal variation in June is effectively the same throughout the period of interest and displays no change during the solar cycle.

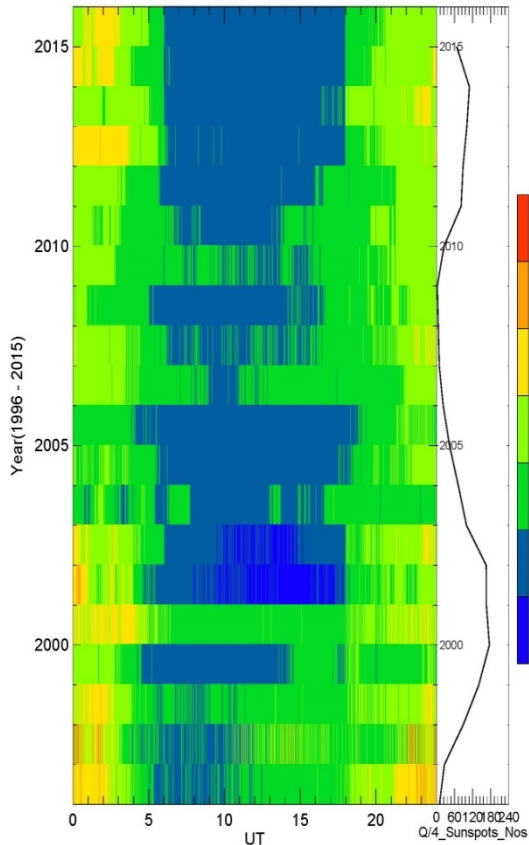


Figure 4.5a

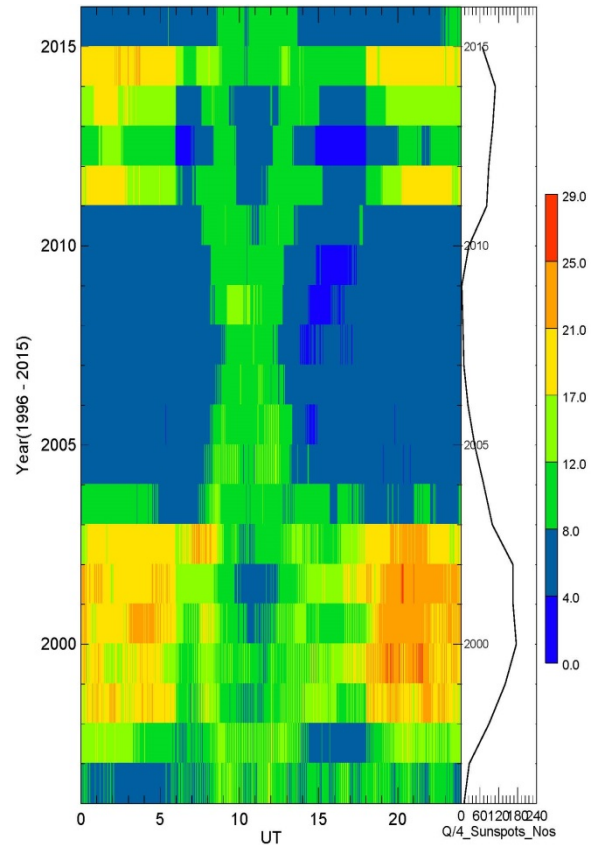


Figure 4.5b

Figure 4.5: Seasonal variation of percentage occurrence of ionospheric backscatter during the month of June and December as a function of UT for Hankasalmi radar. The panel on the left is for the month of June and the panel on the right is for the month of December. The ionospheric scatter percentage occurrence rate is calculated as a ratio of the number of recorded echoes in the total field of view to the total number of observations in the total field of view for each season (June and December) over each month from 1996 to 2015. The ratios were averaged for each hour of observations and in 1 hour universal time bins.

During the month of December a broad maximum in occurrence of ionospheric backscatter in the night time is noticed again during solar maximum of cycle 23. Note that this peak in

occurrence in December is longer than that in June. However, during the extended minimum between cycles 23 and 24, the peak in occurrence seems to occur more often during the daytime rather than at night (between 2005 and 2010) while returning to the same local time variation with a peak at night as cycle 24 approaches its maximum, from 2011 onwards. We again note that the peak occurrence as solar cycle 24 maximum approaches is lower than that in solar cycle 23. There is also evidence during the previous minimum (1996) that a peak in occurrence is seen during the day, and that in 2015 the peak occurrence in December also occurs during the daytime.

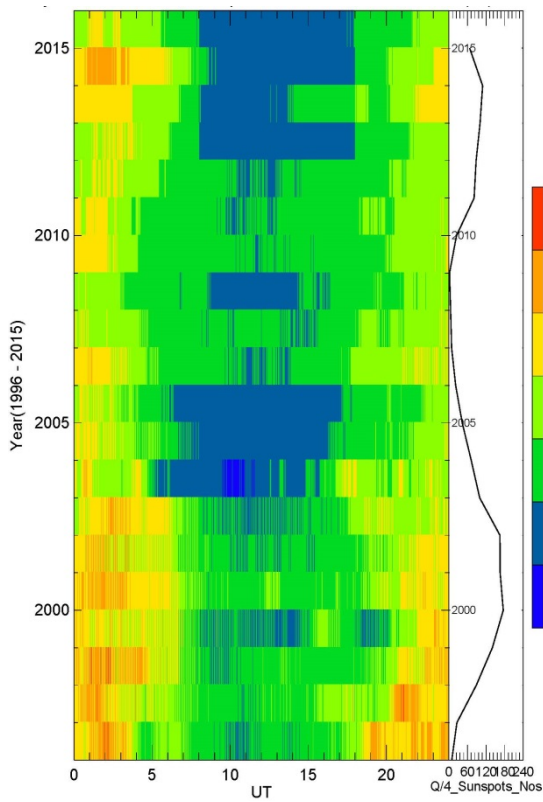


Figure 4.6a

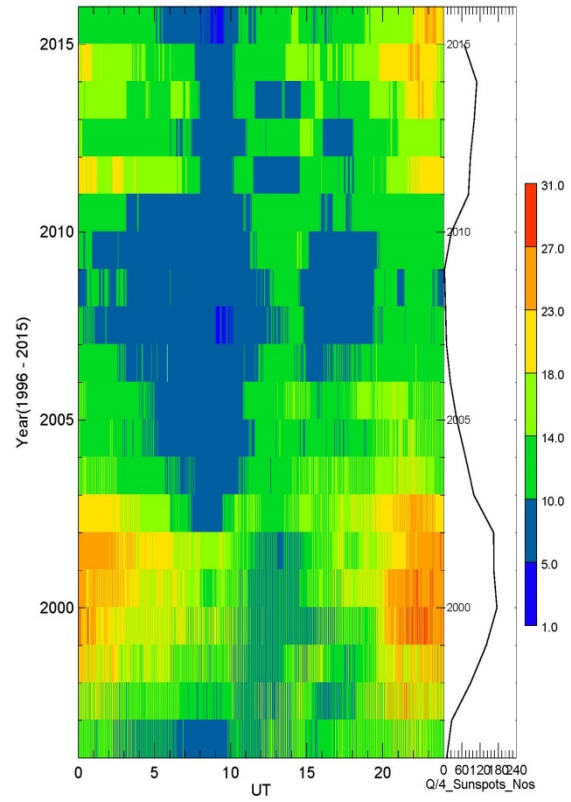


Figure 4.6b

Figure 4.6: Seasonal variation of percentage occurrence of ionospheric backscatter during the month of June and December as a function of UT for Pykkvibaer radar. The panel on the left is for the month of June and the panel on the right is for the month of December. The ionospheric scatter percentage occurrence rate is calculated as a ratio of the number of recorded echoes in the total field of view to the total number of observations in the total field of view for each season (June and December) over each month from 1996 to 2015. The ratios were averaged for each hour of observations and in 1 hour universal time bins.

By contrast, the diurnal variation in the occurrence of ionospheric scatter at the Pykkvibaer radar (Figure 4.6a, b) for June and December, respectively, displays a consistent pattern

with season. Figure 4.5a shows the percentage occurrence data for June for Pykkvibaer. Here the diurnal variation has a peak in occurrence during the night time and a minimum during the day time 05- 15 UT throughout the period irrespective of phase of solar cycle, similar to Hankasalmi. The lower occurrence rate of ionospheric scatter noticed at Hankasalmi in June during solar minimum is also present at Pykkvibaer. Furthermore, this diurnal variation across the two seasons is consistent in Pykkvibaer data.

The diurnal variation during December at Pykkvibaer is, however different from that displayed in December at Hankasalmi. The peak in occurrence at day time seen during solar minimum of cycle 24 (2005-2008) during December in Hankasalmi is not present in Pykkvibaer.

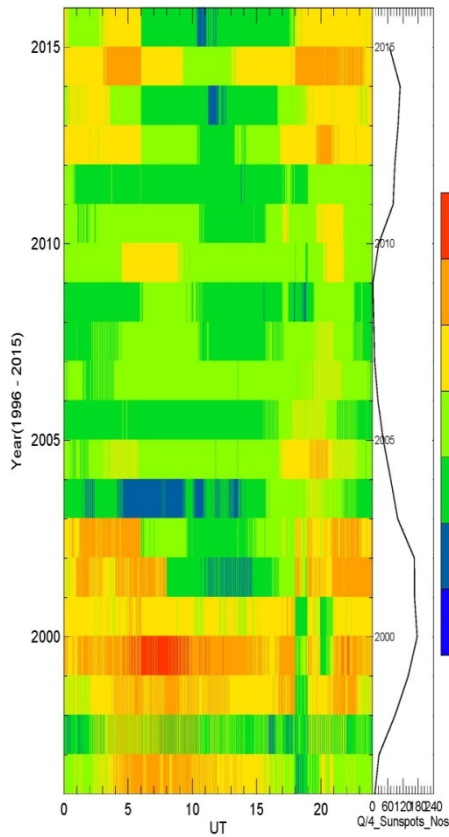


Figure 4.7a

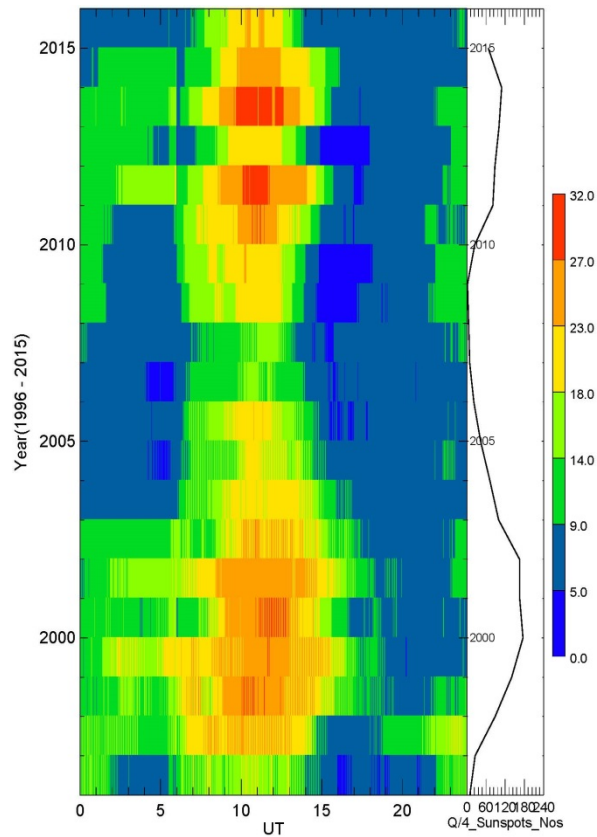


Figure 4.7b

Figure 4.7: Seasonal variation of percentage occurrence of ground backscatter during the month of June and December as a function of UT for Hankasalmi radar. The panel on the left is for the month of June and the panel on the right is for the month of December. The ground scatter percentage occurrence rate is calculated as a ratio of the number of recorded echoes in the total field of view to the total number of observations in the total field of view for each season (June and December) over each month from 1996 to 2015. The ratios were averaged for each hour of observations and in 1 hour universal time bins.

Again the broad maximum in occurrence at night at Pykkvibaer is higher as the maximum of solar cycle 23 compared with the minimum between 23 and 24 and again as we approach the maximum of cycle 24.

The ground scatter percentage occurrences for Hankasalmi and Pykkvibaer for the same months are presented in Figure 4.7 and 4.8 respectively. The diurnal variation of ground scatter occurrence rate for Hankasalmi radar also exhibits both solar cycle and seasonal dependences. Similar to the ionospheric scatter, we illustrate this by starting with the month of June (Figure 4.7a). The occurrence of ground scatter for Hankasalmi appears to be seen throughout the day and minimum in occurrence at nighttime in the month of June seems to be evident while we noticed peak in occurrence rate during day time in both solar minimum and maximum of cycle's 23.

Unlike the month of June, we notice that during December ground scatter has a very clear maximum occurrence rate during the daytime in both solar cycles and a minimum in the occurrence rate is noticed during nighttime. This well-defined peak occurs between 06 00 and 15 00 UT. The solar cycle variation is clear with the maximum occurrence peaking during sunspot maximum years. In addition, there is a higher occurrence rate of ground scatter at night during solar maximum.

Pykkvibaer exhibits a similar pattern in the diurnal variation and the seasonal dependence in ground scatter occurrence (Figure 4.8). During June the peak in occurrence often occurs at night and there is no clearly repeatable pattern. December shows a different pattern from June and as for Hankasalmi there is a well-defined day time peak, a clear solar cycle variation and a low level of ground scatter at night during solar minimum years.

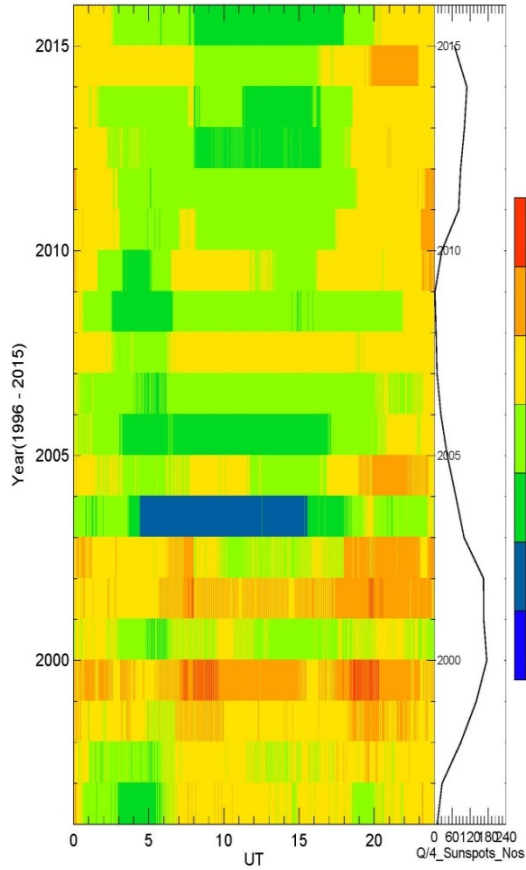


Figure 4.8a

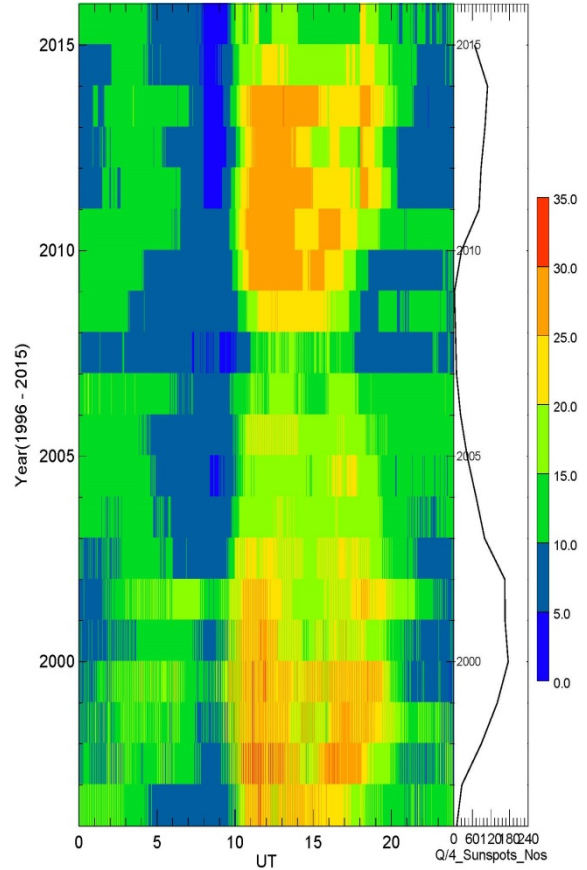


Figure 4.8b

Figure 4.8: Seasonal variation of percentage occurrence of ground backscatter during the month of June and December as a function of UT for Pykkvibaer radar. The panel on the left is for the month of June and the panel on the right is for the month of December. The ground scatter percentage occurrence rate is calculated as a ratio of the number of recorded echoes in the total field of view to the total number of observations in the total field of view for each season (June and December) over each month from 1996 to 2015. The ratios were averaged for each hour of observations and in 1 hour universal time bins.

4.7 Discussion

Long term statistical studies of the occurrence of backscatter (ionospheric and ground backscatters) observed by the SuperDARN (Hankasalmi and Pykkvibaer) radars for a time interval spanning almost two complete solar cycles (1996-2013) have been investigated. Two approaches were used in the study in an attempt to identify solar cycle variations, seasonal dependences and diurnal variations. The focus of the first part was the monthly mean percentage occurrence of ionospheric and ground backscatter for the total field of view of both radars and the second part is the hourly percentage occurrence of ground and ionospheric backscatter for the total field-of-view for both radars. The results obtained in the study are:

- (i) The occurrence of ground scatter tends to be larger than the occurrence of ionospheric scatter.
- (ii) The observed solar cycle variation indicates those scatter occurrence peaks at solar maximum and is a minimum at solar minimum with a ratio of 3:1 in occurrence rate and there is evidence that the recent solar minimum is lower than the previous.
- (iii) There is clear evidence during solar maximum of an annual variation in both ionospheric scatter and ground scatter. This annual variation is present for a longer period in solar cycle 23 than solar cycle 24. In addition, it is noticed that in solar cycle 24 it is not clear, in particular at Hankasalmi, and also it appears to stop earlier at Hankasalmi than at Pykkvibaer.
- (iv) This annual variation in ground scatter and ionospheric scatter is in antiphase.
- (v) Comparing the diurnal variation of ionospheric scatter in the month of June and December, it is noticed that ionospheric scatter peaks at night for June in all years but only during solar maximum in December. In December the peak in occurrence is seen at night for solar maximum and in day during solar minimum at Hankasalmi and less clear at Pykkvibaer.
- (vi) Comparing the diurnal variation of ground scatter in the month of June and December, it is noticed that ground scatter peaks in the day in December at both Hankasalmi and Pykkvibaer radars but there is no clear diurnal variation in June.

We now discuss each of these points in turn.

4.7.1 Solar cycle dependence of backscatter

Our analysis has shown that the occurrence of ground backscatter is much larger than the occurrence of ionospheric backscatter during the solar cycles. The larger occurrence of ground backscatter was seen during the two solar cycle maxima and solar cycle minima that occurred during the twenty year period investigated. This feature is evident in both Hankasalmi and Pykkvibaer radars. This feature of larger occurrence of ground scatter is attributed to propagation conditions which is a requirement for ground scatter occurrence which is the most likely explanation that favours the observations. On the other hand, the occurrence of ionospheric scatter requires both propagation conditions and a highly

structured ionosphere for the production of irregularities. Also, a solar cycle effect is observed in ground scatter. It is noticed that during solar maximum, peak in occurrence of ground scatter is evident during the two-solar cycle maxima, while the minimum in occurrence is seen during solar minimum. It is important to point out that it appears there is no comprehensive long term study on the occurrence rate of ground scatter. The study on ground scatter carried out by Ponomarenko et al. (2010) has only utilised a limited data set focusing on seasonal and diurnal variations.

Our analysis has shown that the maximum occurrence of ionospheric backscatter occurs during the solar cycle maximum while minimum occurrence of ionospheric backscatter occurs during the solar cycle minimum. The maximum occurrence feature of ionospheric backscatter during solar maximum was seen during the two solar cycle maxima that occurred during the period investigated and the pattern is recorded by the two SuperDARN radars. In the study carried out by Milan et al. (1997b), they anticipated an increase in the occurrence of ionospheric backscatter resulting from an increase in ionospheric irregularities towards solar maximum due to an increase in geomagnetic activity. This is in agreement with our result. Also, this feature of maximum occurrence of ionospheric scatter during sunspot maximum was observed in the study carried out by Ruohoniemi and Greenwald (1997) on the backscatter occurrence rate at Goose Bay radar. Although, the data set used in that study spans only half of the solar cycle, which is less than the data set used in the present study and that their method of analysis differs from the method used in this study, one of their major conclusions from the study by Ruohoniemi and Greenwald (1997) was that during solar maximum, backscatter occurs more than during solar minimum. In another study on HF radar F region backscatter occurrence in the midnight sector carried out by Koustov et al. (2004), they also confirm the increase in the occurrence rate of ionospheric backscatter during solar maximum for all the radars investigated. Koustov et al. (2004) attributed the significant increase in the occurrence of backscatter to increase in the occurrence of strong electric fields which is associated with an increase in the occurrence of ionospheric plasma density gradients during solar maximum due to the Sun's dynamism and activeness resulting in increase in magnetic activity around sunspot maximum.

Likewise, the minimum in occurrence of ionospheric backscatter during an extended solar minimum as well as the end of the previous minimum was seen in both SuperDARN radars. The minimum occurrence of ionospheric scatter during solar minimum appears to be due to a lower occurrence of ionospheric irregularities which is related to a lower solar

EUV. Our analysis also shows that the occurrence of ionospheric scatter appears to reach a dip around the extended solar minimum of solar cycle 23/24. Solomon et al, (2011) noted that the occurrence level of solar EUV during the extended solar minimum (2007-2009) was lower than the previous solar minima which seems to be in agreement with our observation of a dip occurrence of ionospheric backscatter during solar minimum of cycle 23/24 in comparison to the minimum occurrence during solar minimum of cycle 22/23. In another study carried out by Klenzing et al., (2013), they noted that during the extended solar minima that ionospheric irregularities are also observed to be significantly different during the extreme solar minimum which might be due to the unprecedented nature of the solar minimum of solar cycle 23 since the space age (Russell et al., 2010). Similarly, Didkovsky et al., (2010) shows that the solar EUV irradiance was lower than the previous solar minimum by using space-based measurements. Also, we noticed that the minimum occurrence in ionospheric backscatter which appears during the solar minimum of cycle 23/24 for Pykkvibaer radar is lower than the occurrence level seen at Hankasalmi radar. This feature is seen in both ionospheric scatter and ground scatter.

Similarly, a long term statistical study of the latitude of the Heppner-Maynard Boundary (HMB) measured at midnight using the northern hemisphere Super Dual Auroral Radar Network (SuperDARN) carried out by Imber et al. (2013) also shows that there is solar cycle effects in both the number of data points per map produced in the study and the total number of maps.

Comparing the occurrence rate of backscatter during solar maximum to occurrence rate during solar minimum during the period of interest, we noticed occurrence rate of ration 3:1. This rate of occurrence is also reported by Imber at al. (2013). Imber et al. (2013) observed that there is 3:1 more data points observed during northern hemisphere winter than during the summer.

4.7.2 Annual dependences of backscatter

There is clear evidence of an annual variation in both ionospheric scatter and ground scatter. This annual variation is present for a longer period in solar cycle 23 than solar cycle 24. It is noticed that during solar minimum, between 2004 and 2009, the seasonal effect is pronounced. The question is why is the annual variation in solar cycle 23 different from that of cycle 24 and what is the cause of the difference in peak in the year? In the study carried out by Koustov et al. (2004) on six SuperDARN radars, they observed a

seasonal variation in the occurrence of midnight backscatter for most of the radars investigated. They noted that Hankasalmi and Pykkvibaer radars show significant winter-summer contrasts even though both radars have overlapping field of view and exhibit significant summer increase in ground scatter that makes the detection of ionospheric backscatter impossible. This contrast in seasonal variation was attributed to radar geographical location. The rate of occurrence of backscatter within a particular fields of view depends on factors such as the opacity of the D and E regions to radio signals and the availability of F region plasma irregularities required to produce backscatter. Hence, these factors are responsible for variability in the rate of occurrence of backscatter.

A distinct feature is noticed in the annual variation of ionospheric and ground backscatter in the two radars. This feature is the difference in the phase pattern. At Hankasalmi, it is noticed that there are times that ground scatter is in out of phase with ionospheric scatter and there are times both are in phase. However, ground scatter and ionospheric scatter are seen to be in phase at Pykkvibaer.

4.7.3 Diurnal variations of backscatter

The diurnal variations of the occurrence of ionospheric backscatter display variation in solar cycle and seasonal dependences during the month of June in Hankasalmi. The occurrence of ionospheric backscatter maximises in the night time sector during solar maximum and minimum occurrence rate at daytime sector. We noticed that there is a similarity in the features of occurrence of ionospheric scatter during the month of June displayed by the two radars. It is observed that occurrence of ionospheric scatter peaks at night for June in all years in both Hankasalmi and Pykkvibaer radars. This result is in contrast with the result of Ghezelbash et al. (2014). The study of Ghezelbash et al. (2014) shows that during years of low solar activity, the occurrence of backscatter show a clear peak. Also, it is noticed that there are times of the year that the peak in occurrence is seen at night e.g. 2004 and 2006 while at other times it occurs during the day e.g. 2005 and 2007. An important question is why the difference in peak in occurrence? Ghezelbash et al. (2014) observed peak in occurrence at night time in RKN radar. This peak in occurrence at night can hardly be linked to the illumination effect of the sun.

We also note that for solar cycle 24 maximum, a peak returns at night time. The peak in occurrence rate during solar maximum is consistent with the study carried out by Koustov et al. (2004) that shows nighttime maxima towards the solar cycle maximum. A larger

occurrence rate of ionospheric backscatter in the day time sector during solar minimum and lower occurrence rate at nighttime sector during solar minimum is seen in Hankasalmi radar. The diurnal variation pattern of the occurrence of ionospheric scatters for Pykkvibaer during June appears to show peak in occurrence of ionospheric scatter throughout all the years investigated. The pattern is less clear in Pykkvibaer radar during December.

However, during the month of December, the winter month, the two radars exhibit distinct features. It is observed that the occurrence of ionospheric scatter peaks at night in December only during solar maximum in Hankasalmi radar while it is less clear in Pykkvibaer radar. A minimum occurrence of ionospheric backscatter in the night time during the two-solar minima is recorded in Hankasalmi radar in the month of December. This result is in contrast with the result of Ghezelbash et al. (2014). The study of Ghezelbash et al. (2014) shows that during years of low solar activity, occurrence of backscatter show clear peak near noon during winter, near dusk and dawn during equinoxes and near midnight during summer time. The difference in the occurrence of ionospheric backscatter features for the two radars might be due to geographical reasons rather than propagation conditions (Milan et al., 1997b). It is important to point out that ionospheric backscatter occurrence seems to be much lower in June than in the other month for both radars.

The ground scatter occurrence for the two radars exhibits similar trends in occurrence for the months investigated. There is no clear diurnal variation in the occurrence of ground scatter in Hankasalmi and Pykkvibaer radars during the summer month, June. However, clear evidence of diurnal variation in the occurrence of ground scatter during the winter month, December, in both radars is noticed. A peak in the occurrence of ground scatter during day time is noticed in the month of December. This peak in the occurrence of ground scatter seen during the daytime might be due to sufficiency in ionospheric refraction to reflect the radar ray back to the ground. These features are noticed in the two radars.

4.8 Summary

Long term statistical studies of the occurrence of backscatter (ionospheric and ground scatter) observed by the SuperDARN (Hankasalmi and Pykkvibaer) radars for a time interval spanning approximately two-solar cycles (1996-2015) were carried out. The data

used is the whole data e.g., Milan et al., 1997b; Ruohoniemi and Greenwald, 1997; Ballatore et al., 2000; Parkinson et al., 2003; Koustov et al., 2004; Carter and Makarevich set when the two radars were in common mode covering the total field of view of the radars. In the past, studies on the occurrence of SuperDARN radar backscatter have being limited to few data sets, data spanning few years, specific beam or selected beams on the radar or on E-region backscatter or F region backscatter.

In this study, the diurnal variation, seasonal and solar cycle dependences of ionospheric and ground backscatter using SuperDARN radars for a time interval spanning approximately two-solar cycle (1996-2015) has been observed. The key new results obtained in the study are, (i) the occurrence of ground scatter tends to be larger than the occurrence of ionospheric scatter, (ii) the solar cycle variation observed indicates that scatter occurrence peaks in solar maximum and is a minimum in solar minimum which appears to be in ratio 3:1 and there is evidence that the recent solar minimum is lower than the previous, (iii) there is clear evidence during solar maximum of an annual variations in both ionospheric scatter and ground scatter, (iv) this annual variation is present for a longer period in solar cycle 23 than solar cycle 24, (v) ground scatter and ionospheric scatter are in out of phase in Pykkvibaer while in Hankasalmi there are times they are in phase and times they are out of phase, (vi) in addition, it is noticed that in solar cycle 24 it is not clear in particular in Hankasalmi and also it stops earlier at Hankasalmi than at Pykkvibaer.

Chapter 5

Long term spatial variation of the ionosphere with SuperDARN radar data

5.1 Introduction

The focus of the previous chapter was on the statistical analysis of the occurrence of ionospheric and ground backscatter using the percentage of occurrence of scatter in the radar field of view. The discussion centred on the monthly mean percentage occurrence of ionospheric and ground backscatter for both Hankasalmi and Pykkvibaer radars and the hourly percentage occurrence of ionospheric and ground backscatter for the total field of view for the two radars.

We now move to a study which seeks to understand the results from Chapter 4 in terms of radar range. This allows us to investigate the propagation mode responsible in particular for ionospheric scatter.

5.2 Instrument and Data selection

This chapter reports a study of the backscatter variation as a function of ground range using data from Hankasalmi (62.3°N, 26.6°E) and Pykkvibaer (63.8°N, 20.5°W), both of which have been in operation for over twenty years. Three of the sixteen beams are selected from each radar. They are beam 1, 9 and 14 from the Hankasalmi radar and beam 1, 7 and beam 14 from the Pykkvibaer radar. The analysis used in this chapter consists of the point occupancy statistics of ionospheric backscatter and ground backscatter to investigate the occurrence of both types of scatter as a function of range gates. The backscatter data used are from 1996-2015 spanning nearly two full solar cycles. The data are binned in two universal time (UT) hour bins for each beam and the point occupancy as a function of range (75 range gates) versus UT for each of the radars generated. Universal time is used here as it is close to the local time for the central beam of Hankasalmi. Furthermore in certain cases notably beam 14 of Pykkvibaer, the local time varies with range and hence UT is a simple way of ordering the data. Four months out of the twelve months data are analysed in each year for the full 20 year interval investigation and these

were selected to represent the four seasons to reduce the data being shown. The selected months are March (Spring Equinox), June (Summer Solstice), September (Autumn Equinox) and December (Winter Solstice).

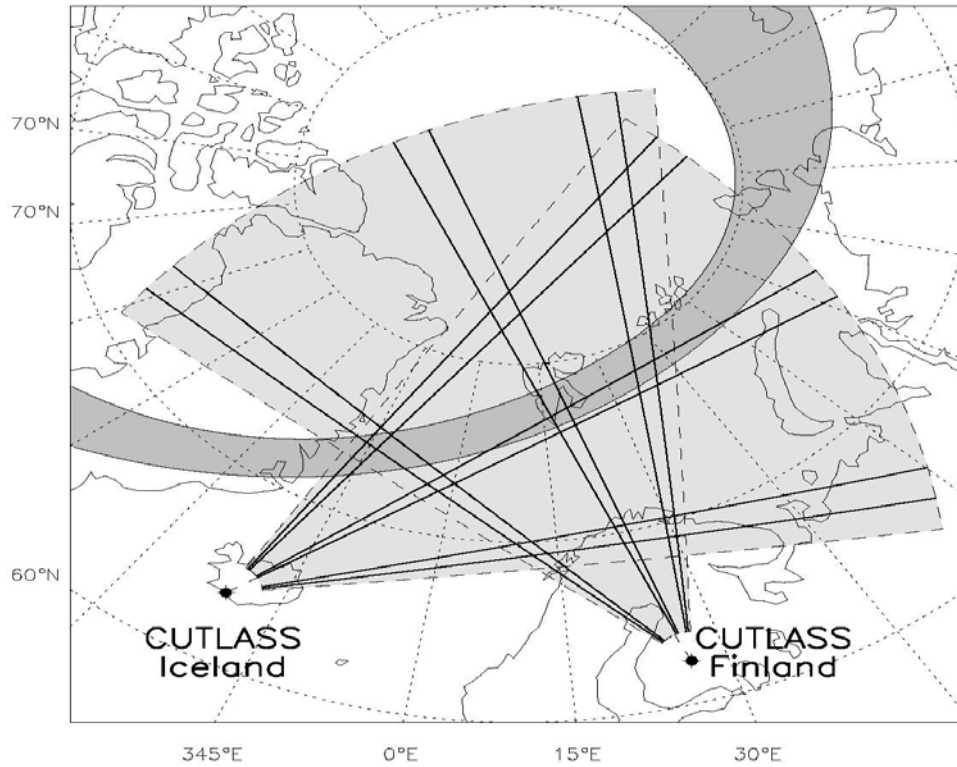


Figure 5.1 Illustration of the selected beams within the field of view of Hankasalmi (62.3°N, 26.6°E) and Pykkvibaer (63.8°N, 20.5°W) (1, 9 and 14 for the Finland and 1, 7 and 14 for Iceland radars respectively) (courtesy, S.E. Milan)

The range gates (75 range gates) can be considered simplistically in three categories. These three categories are defined as near range gates 0-20, mid-range gates, between 21-40, and far range gates corresponding to gates 41-75. This categorisation is employed in the interpretation of the data and is designed to help to identify the type of propagation pattern in the range gates, where near ranges will typically be $\frac{1}{2}$ hop propagation, mid-range represents 1 hop and $1\frac{1}{2}$ hop, while far ranges will be dominated by $1\frac{1}{2}$ hop or possibly multi-hop. The point occupancy as a function of range versus UT is colour coded in each of the following figures. It should be borne in mind that we have used different colour scales for the ionospheric backscatter and the ground scatter.

Two different methods are employed in the presentation of the results in this chapter. The first method is the comparison of the ionospheric backscatter data from the central beam of

each of the radars, beam 9 of Hankasalmi and beam 7 of Pykkvibaer as well as a similar comparison of the ground backscatter data from the central beam of each of the radars. Each of the selected months representing seasons is discussed in section 5.3 and section 5.4 for ground and ionospheric scatter, respectively. The second approach is the comparison of the three selected beams relative to each other for the Hankasalmi and Pykkvibaer radars which is discussed in section 5.7 this latter approach is to investigate if there are significant variations with azimuth within each field of view.

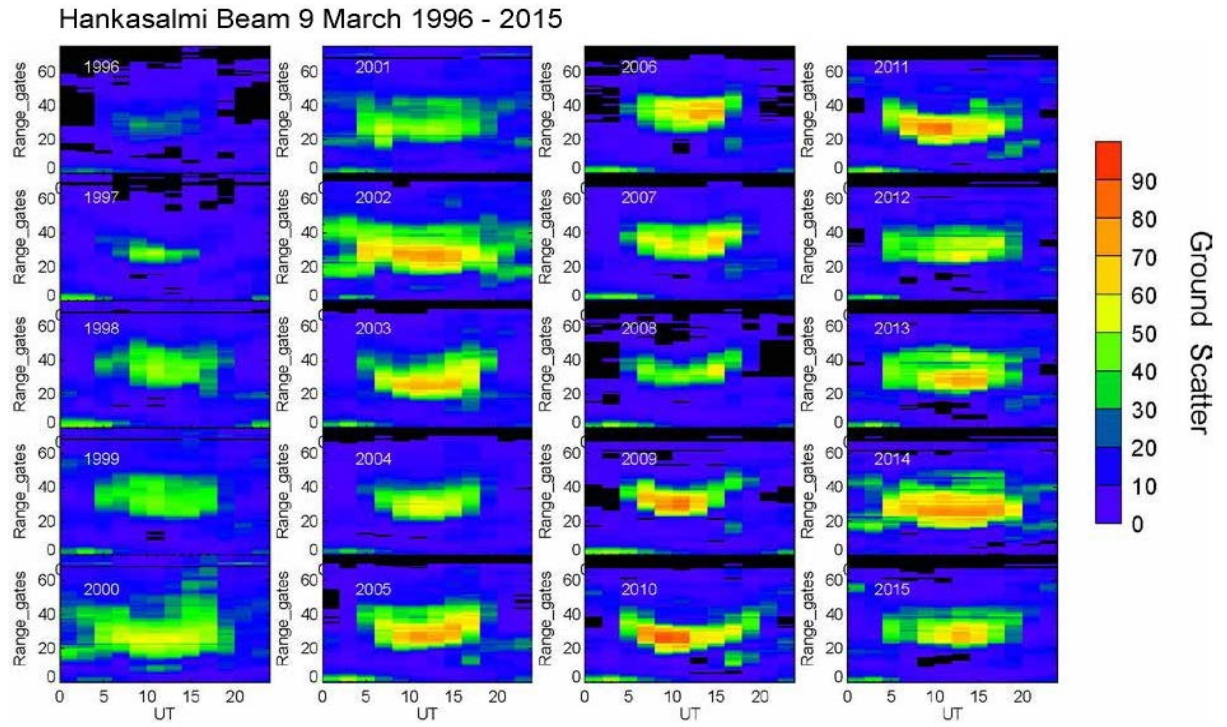
5.3 Ground backscatter point occupancy statistics

Figure 5.2a presents the point occupancy of ground backscatter data as a function of range versus universal time for beam 9 of the Hankasalmi radar and Figure 5.2b presents the point occupancy of ground backscatter data for beam 7 of the Pykkvibaer radar for the month of March. Each of these figures follows the same format as those for ionospheric scatter presented in the previous section but note the colour scale is different.

The point occupancy statistics for Hankasalmi during the month of March presented in Figure 5.2 show that there is virtually no occurrence of ground scatter at far ranges, range gates > 41 . At mid-ranges, ground scatter is seen around 06 – 18 UT and is present almost throughout the year investigated except in 1996 and 1997. The point occupancy statistics of ground backscatter occurrences in Pykkvibaer radar shown in Figure 5.2b follow the same trends as that of Hankasalmi, although shifted to later UT.

Figure 5.3 presents the point occupancy of the ground backscatter for beam 9 of the Hankasalmi radar for June. The point occupancy statistics for Hankasalmi during June show that there is very little occurrences of ground scatter at far ranges, range gates > 41 almost throughout the years investigated. Ground backscatter is noticed to almost disappear in 2003 which mirrors the near-disappearance of ionospheric scatter as well compared to other years. At mid-ranges, ground scatter is seen around 06 – 18 UT and is present almost throughout the year investigated except in 1996 and 2003. Ground backscatter is observed to occur at 0-5 range gates and is seen to be present for almost the whole of the day in some of the years and might probably be a mixture of meteor scatter, E region backscatter, and polar mesospheric summer echoes (PMSE).

a)



b)

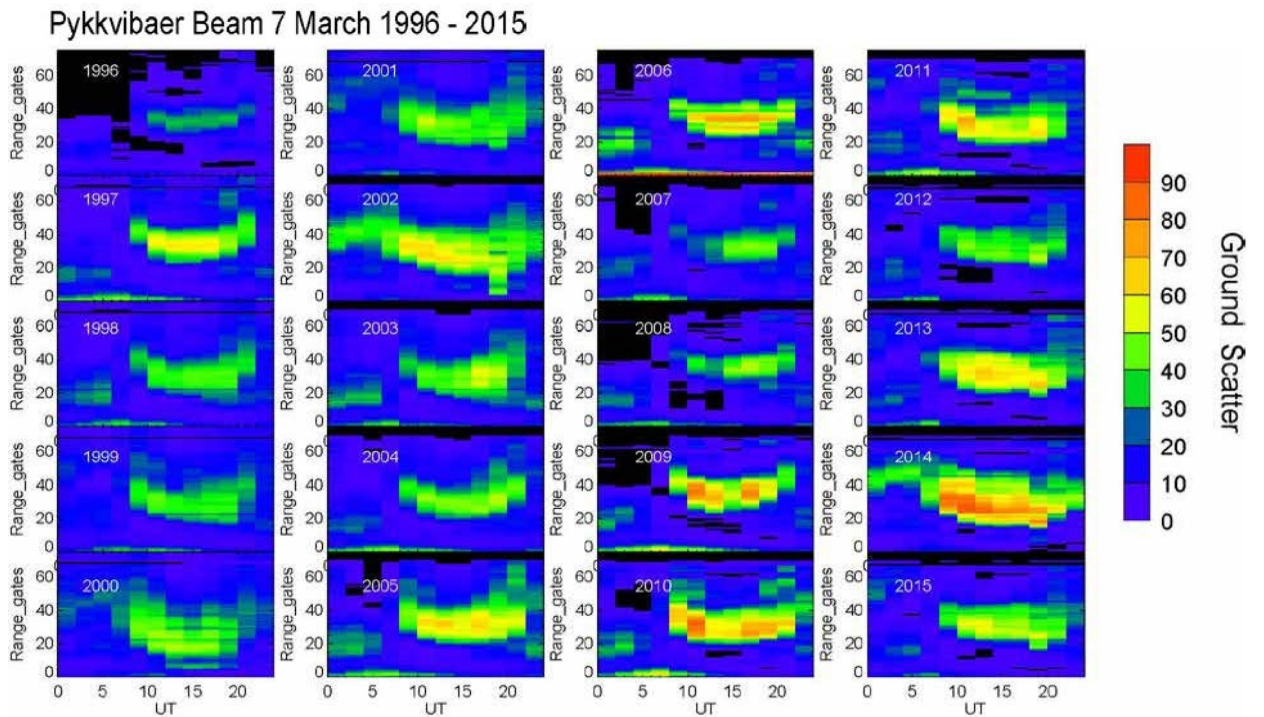
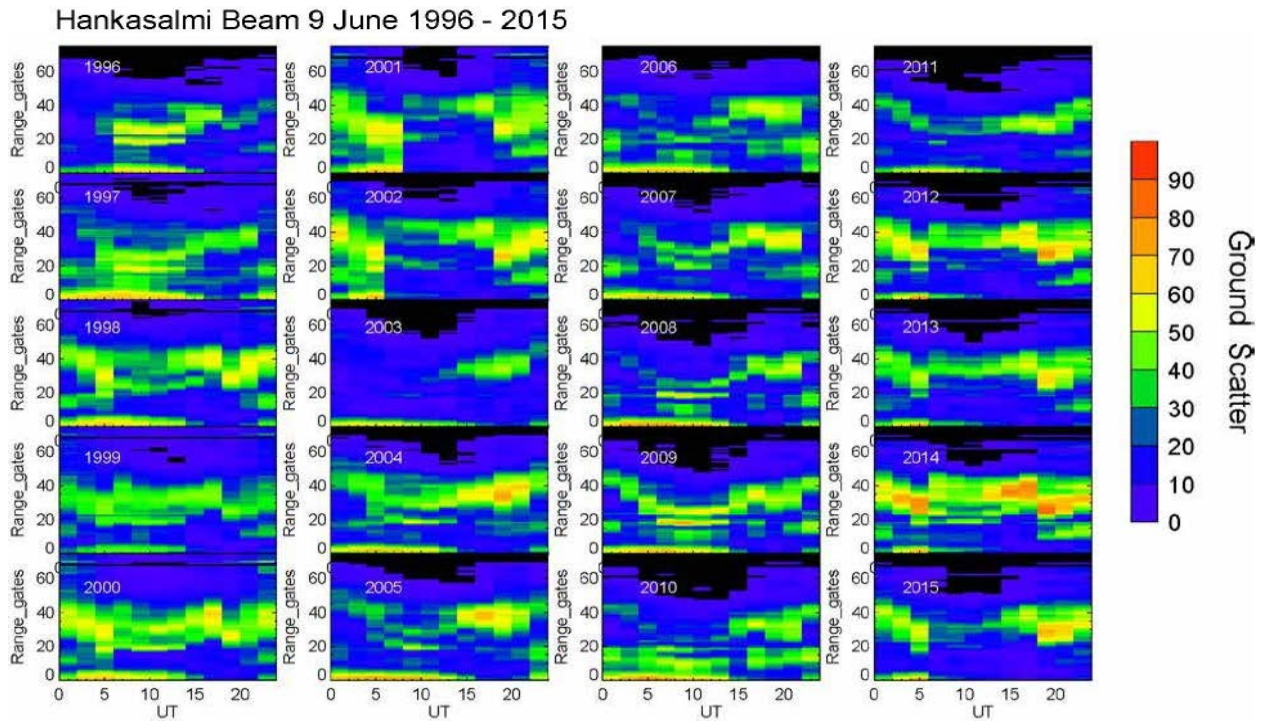


Figure 5.2 shows the point occupancy statistics of ground backscatter (colour coded) of Hankasalmi and Pykkvibaer radars for the month of March (spring) from 1996 - 2015. The data are binned in two universal (UT) hour bins for each beam with the point occupancy as a function of range (75 range gates) gates (y axis) versus UT (x axis). The range gates are categorised into three; 0-20, mid-range gates, between 21-40, and far range gates corresponding to gates 41-75. Panel a) is Hankasalmi (Finland radar) beam 9, Panel b) is Pykkvibaer (Iceland radar) beam 7.

a)



b)

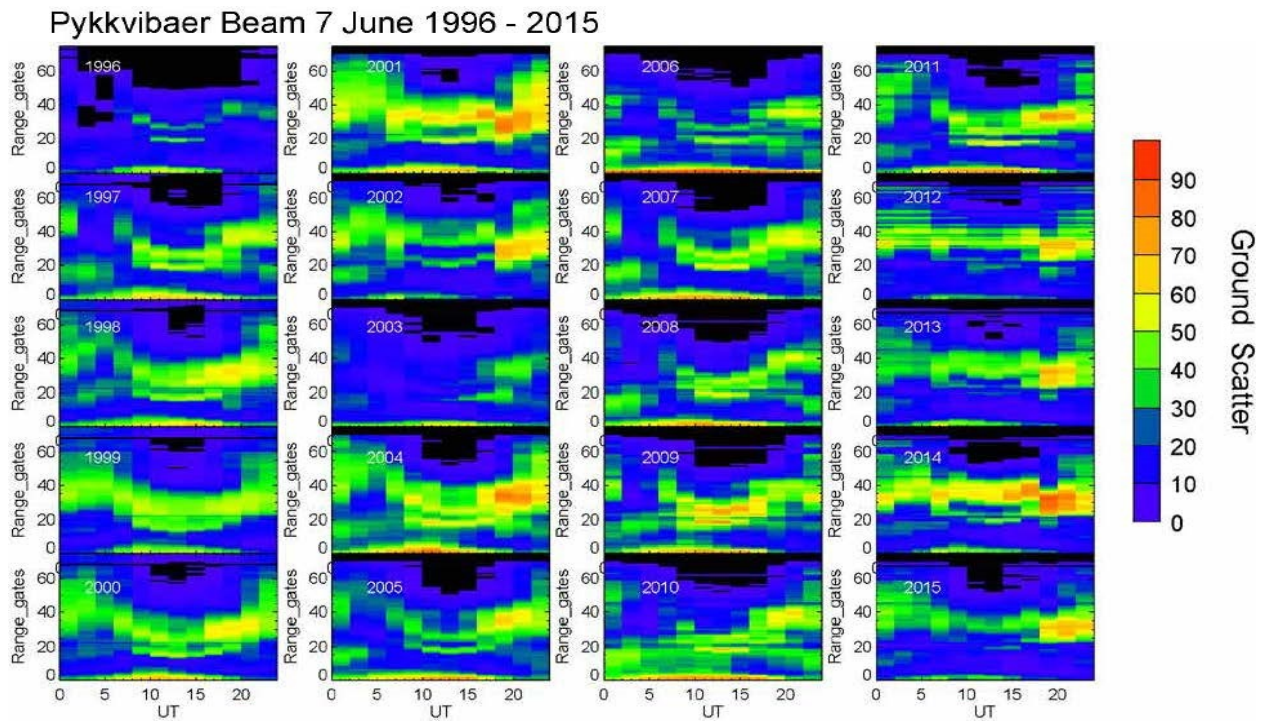


Figure 5.3 shows the point occupancy statistics of ground backscatter (colour coded) of Hankasalmi and Pykkvibaer radars for the month of June (summer) from 1996 - 2015. The data are binned in two universal (UT) hour bins for each beam with the point occupancy as a function of range (75 range gates) gates (y axis) versus UT (x axis). The range gates are categorised into three; 0-20, mid-range gates, between 21-40, and far range gates corresponding to gates 41-75. Panel a) is Hankasalmi (Finland radar) beam 9, Panel b) is Pykkvibaer (Iceland radar) beam 7.

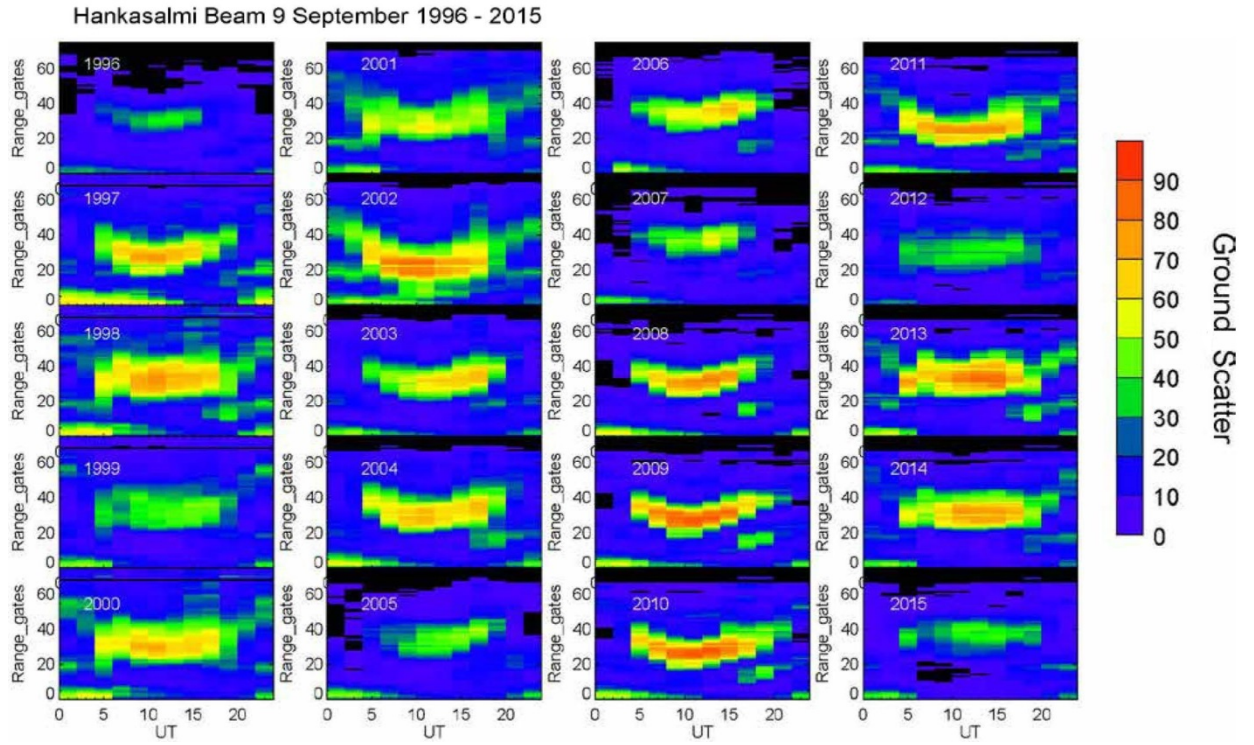
However, in contrast to the point occupancy statistics of ground backscatter occurrence in the Hankasalmi radar, ground scatter occurrence in the Pykkvibaer radar shown in Figure 5.3b appears to be somewhat different. The Pykkvibaer radar records low occurrence of ground scatter in 1996 when compared with Hankasalmi radar. The occurrence of far range ground backscatter is seen at Pykkvibaer radar during nighttime. This feature is seen around solar maximum even though evidence of the feature is seen in 2004. This is not the case for Hankasalmi radar. Mid-range gates occurrence of ground scatter is seen at Pykkvibaer during daytime in almost all the years investigated except in 2003 when occurrence of ground scatter almost disappear. The occurrence of ground scatter at very near range gates (0-5) is seen to be present throughout the years during daytime around 05 – 18 UT at Pykkvibaer.

Figures 5.4a and Figure 5.4b presents the point occupancy statistics as a function of range versus universal time for ground scatter data for beam 9 of Hankasalmi radar and beam 7 of Pykkvibaer radar, respectively, for September. Ground scatter point occupancy statistics for Hankasalmi during September (Equinox) are noticed to have similar features to those from March. There is virtually no occurrence of ground scatter at far ranges, range gates > 41. At mid-ranges, ground scatter is seen around 06 – 18 UT and it is present almost throughout the year investigated. It is noticed that very little ground scatter at mid-range gates is seen in 1996. Also, a gradual decline in the occurrence of ground scatter close to solar minimum (2005) is noticed and a re-appearance of increase in the occurrence rate in 2008 is seen. The point occupancy statistics of ground backscatter occurrences in Pykkvibaer radar shown in Figure 5.4b follow the same trends as that of Hankasalmi.

There is characteristic change in the location of ground scatter during the day, this occurrence of scatter starts at the further ranges and move closer to the radar as the solar zenith angle decreases. This is an effect due to increasing density.

Also, the occurrence of ground scatter exceeds 70% in most of the months and years. However, the occurrence typically reduces at sunspot maximum to 50% and occasionally at individual months at sunspot maximum e.g. June 2003.

a)



b)

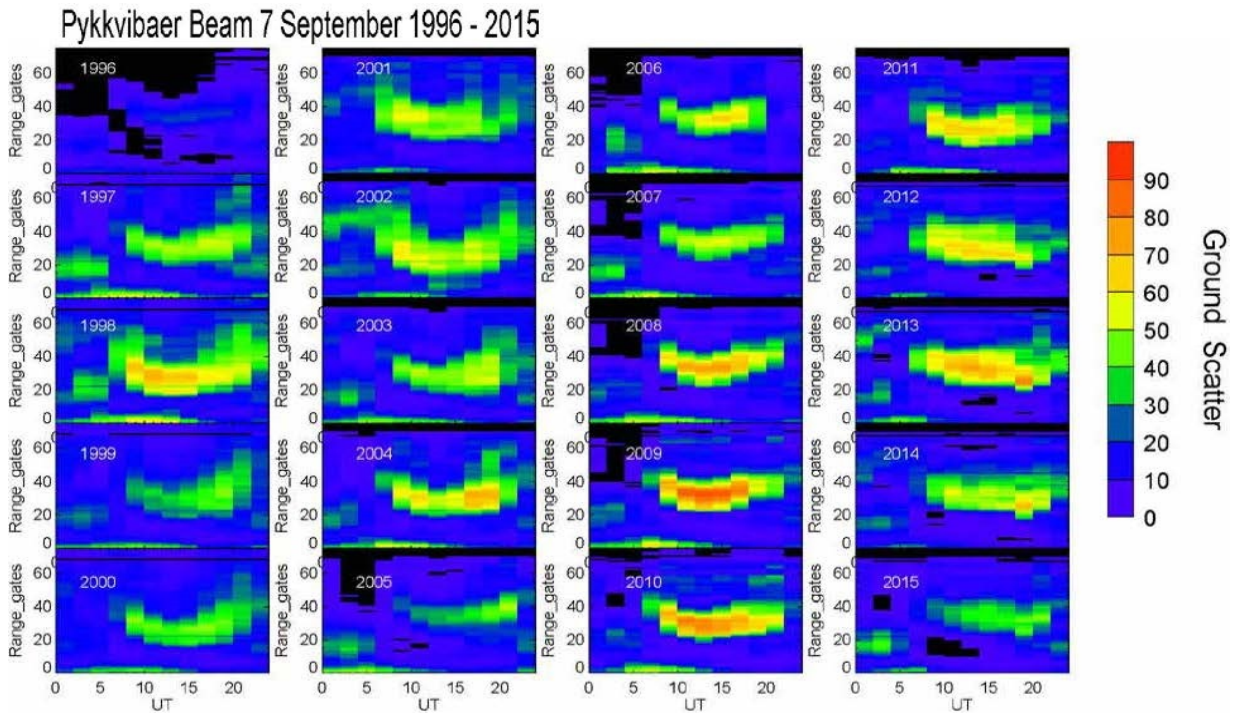


Figure 5.4 shows the point occupancy statistics of ground backscatter (colour coded) of Hankasalmi and Pykkvibaer radars for the month of September (autumn) from 1996 - 2015. The data are binned in two universal (UT) hour bins for each beam with the point occupancy as a function of range (75 range gates) gates (y axis) versus UT (x axis). The range gates are categorised into three; 0-20, mid-range gates, between 21-40, and far range gates corresponding to gates 41-75. Panel a) is Hankasalmi (Finland radar) beam 9, Panel b) is Pykkvibaer (Iceland radar) beam 7.

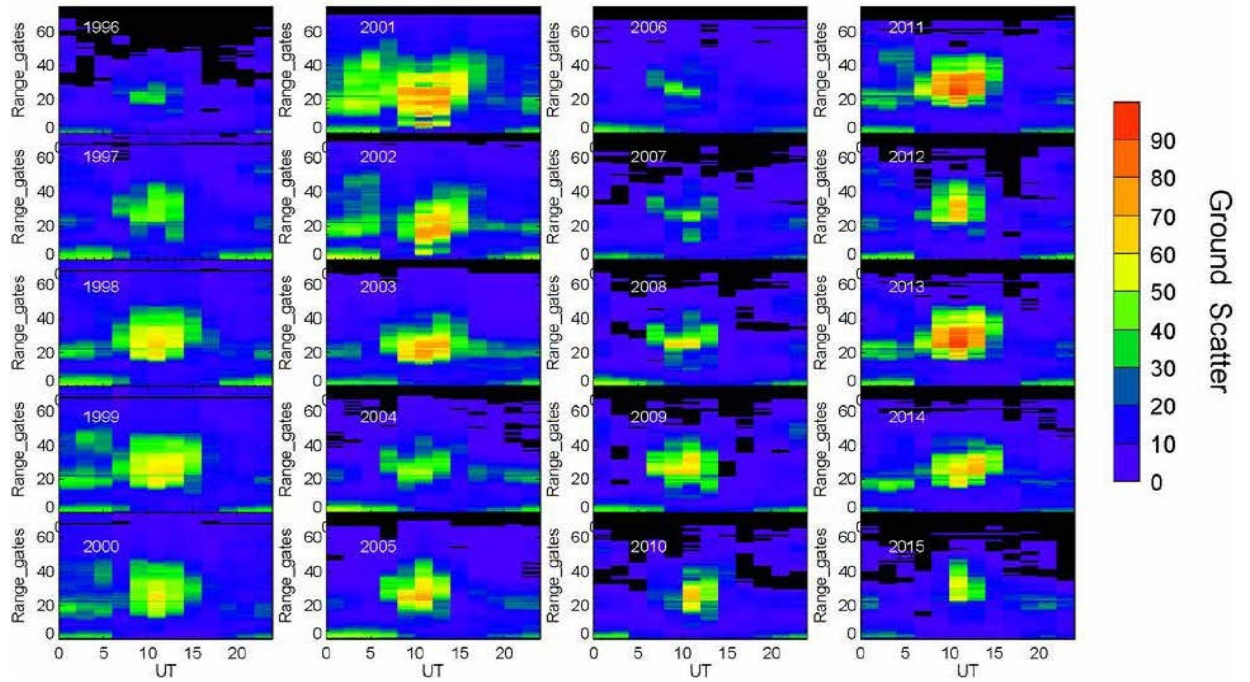
Figures 5.5a and Figure 5.5b presents the point occupancy statistics as a function of range versus universal time for ground scatter data for beam 9 of Hankasalmi radar and beam 7 of Pykkvibaer radar, respectively, December from 1996-2015.

Figure 5.5a shows that there is virtually no occurrence of ground scatter at far ranges, range gates > 41 . At mid-ranges, occurrence of ground scatter is noticed to occur predominantly during daytime (06 – 14 UT). It is noticed that during 1996, very little occurrence of ground backscatter is seen to occur at mid-range gates. However, as we approach the solar maximum of cycle 23, we noticed an enhancement in the occurrence of ground scatter during day time at mid-ranges. As we approach the solar minimum of cycle 23/24, the intensity in occurrence of ground backscatter at mid-range gates declines. This is evident in the figure from 2004 to 2009. In 2001, the occurrence of ground scatter at a longer duration is evident. The enhancement in the occurrence of ground backscatter at mid-range gates during day time re-appears in 2011-2015. The mid-range ground scatter is solar cycle dependent. Also, it is noticed that near range ground scatter at range gates 0-5 is seen to be present throughout the years investigated at pre-noon and post noon sectors.

Ground backscatter occurrence in Pykkvibaer presented in Figure 5.5b follows the same trends as that of Hankasalmi which agrees with the observation of Milan et al (1997b) even though the occurrence in Pykkvibaer tends to be much higher than in Hankasalmi. It is typically shorter lived during the day and no apparent change in range with time.

a)

Hankasalmi Beam 9 December 1996 - 2015



b)

Pykkvibaer Beam 7 December 1996 - 2015

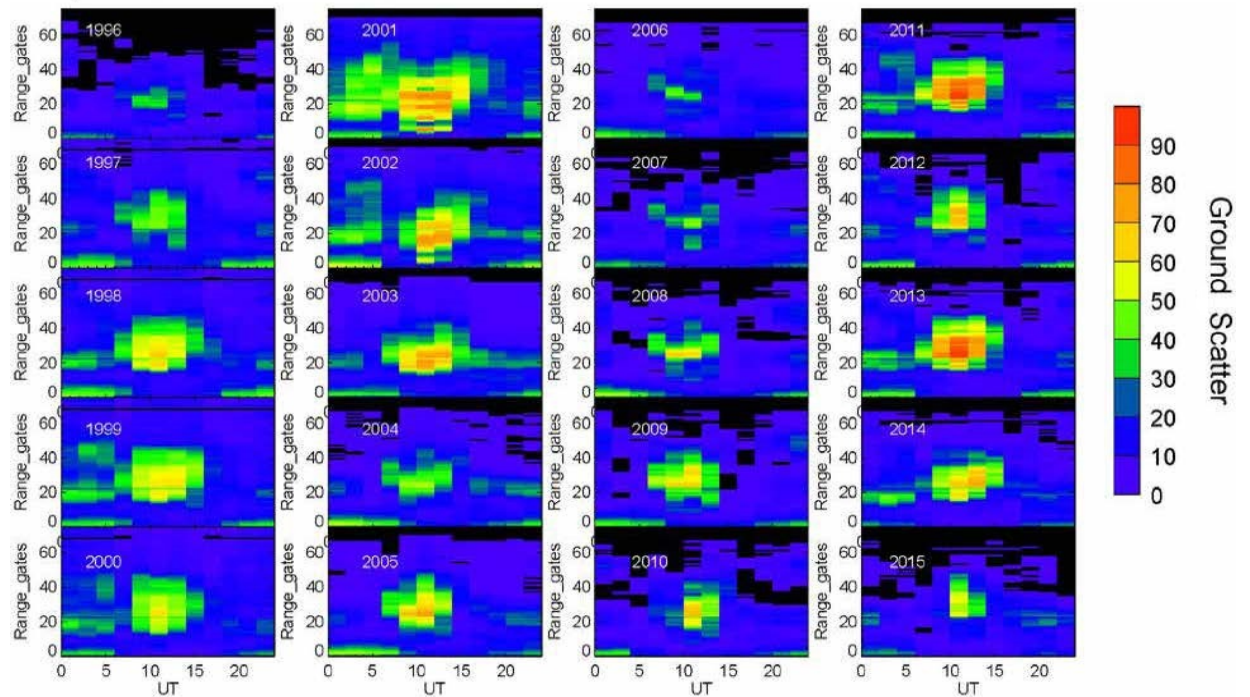


Figure 5.5 shows the point occupancy statistics of ground backscatter (colour coded) of Hankasalmi and Pykkvibaer radars for the month of December (winter) from 1996 - 2015. The data are binned in two universal (UT) hour bins for each beam and the point occupancy as a function of range (75 range gates) gates (y axis) versus UT (x axis). The range gates are categorised into three; 0-20, mid-range gates, between 21-40, and far range gates corresponding to gates 41-75. Panel a) is Hankasalmi (Finland radar) beam 9, Panel b) is Pykkvibaer (Iceland radar) beam 7.

5.4 Ionospheric backscatter point occupancy statistics

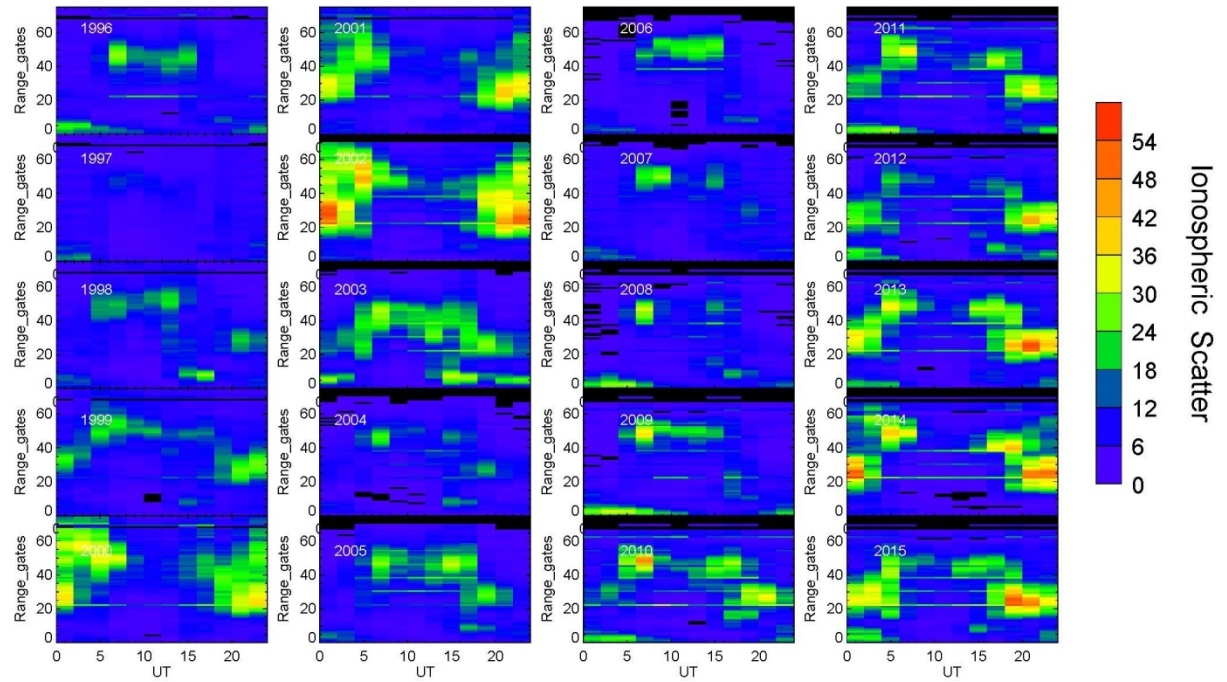
Figure 5.6a presents the point occupancy of ionospheric backscatter data as a function of range versus universal time for beam 9 of the Hankasalmi radar and Figure 5.6b presents the point occupancy of ionospheric backscatter data for beam 7 of the Pykkvibaer radar for the month of March. Figure 5.6a consists of four columns, each with 5 panels representing data from one year. Each panel presents the percentage occurrence, or the point occupancy, as a function of UT and range gate. The first panel represents the first year, 1996, in the case of the first column, and the bottom panel the most recent, 2015 in the case of the last column. The point occupancy is colour coded according to the scale on the right hand side. The format for Figure 5.6b which presents the point occupancy from Pykkvibaer beam 7 is the same as Figure 5.6a.

The point occupancy statistics for Hankasalmi during the month of March presented in Figure 5.6 show that the occurrence of ionospheric scatter at far ranges, range gates > 41 is solar cycle dependent. For the years 1996, 1998, and 2004-2009 inclusive, the far range ionospheric scatter occurs predominantly during the daytime (05 – 16 UT) at Hankasalmi. During these years, ionospheric scatter occurs rarely at other universal times, apart from very near ranges which are likely to be related to meteor scatter or possibly E-region scatter. These years are representatives of solar minimum and the early, rising or late, declining phases of the solar cycle. Close to solar maximum years, far range scatter is typically seen only at nighttime, between 00 – 05 UT and 16 UT. At mid ranges, i.e. between range gates 20 – 40, ionospheric scatter is observed around 00 UT to 06 UT and around 18 UT to 24 UT. This effect is seen only for years close to solar maximum, 1999 – 2003 and 2010 – 2015, i.e during more active conditions. Otherwise, there is very little ionospheric scatter at mid-ranges while at near ranges, range gates < 20 , ionospheric scatter occurs to some extent throughout the solar cycle and is typically close to the radar. This is probably E-region scatter but probably includes some meteor scatter, at very near ranges and possibly F-region scatter at the further ranges.

The point occupancy data of ionospheric backscatter for Pykkvibaer radar is shown in Figure 5.6b. Figure 5.6b shows that the occurrence of ionospheric scatter at far ranges, i.e. range gates > 40 , is seen only in the post noon sector. It is seen at solar maximum years, but appears not to be present during solar minimum and especially it is not seen during the extended solar minimum (2007, 2008 and to a lesser extent 2009).

a)

Hankasalmi Beam 9 March 1996 - 2015



b)

Pykkvibaer Beam 7 March 1996 - 2015

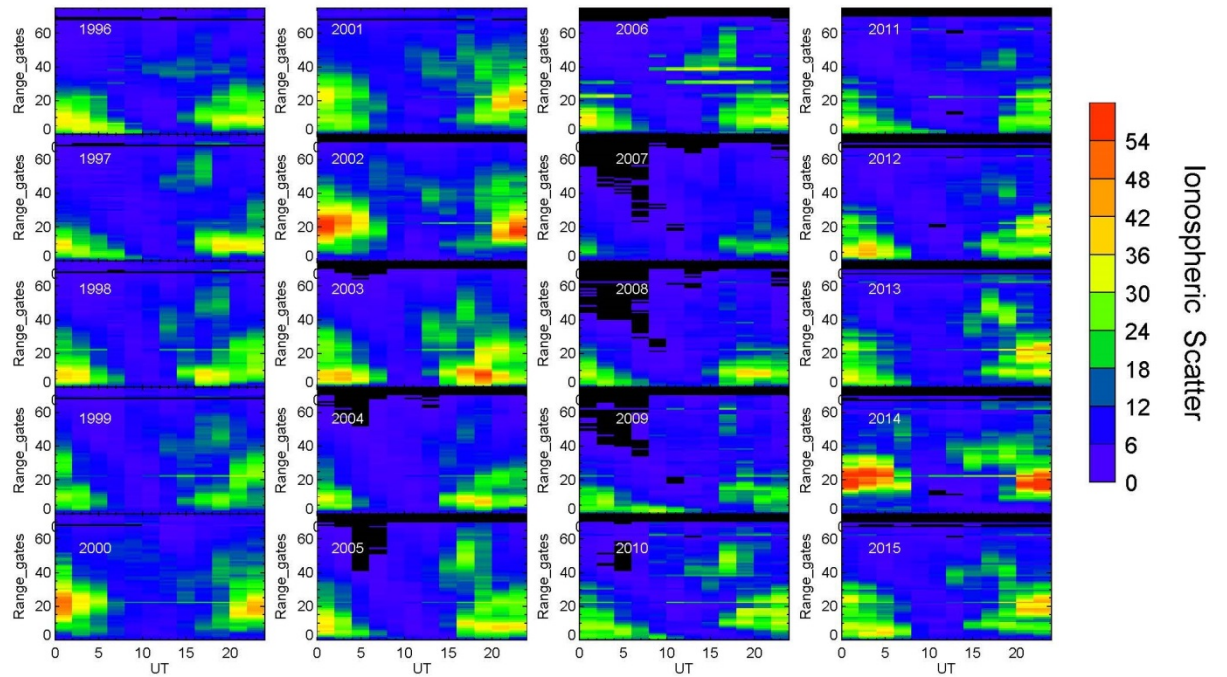


Figure 5.6 shows the point occupancy statistics of ionospheric backscatter (colour coded) of Hankasalmi and Pykkvibaer radars for the month of March (spring) from 1996 - 2015. The data are binned in two universal (UT) hour bins for each beam and the point occupancy as a function of range (75 range gates) gates (y axis) versus UT (x axis). The range gates are categorised into three; 0-20, mid-range gates, between 21-40, and far range gates corresponding to gates 41-75. Panel a) is Hankasalmi (Finland radar) beam 9, Panel b) is Pykkvibaer (Iceland radar) beam 7.

A striking feature of the occurrence of ionospheric backscatter at far range gates at Pykkvibaer is that it is seen only around 12 UT and 18 UT unlike that seen at Hankasalmi

radar where ionospheric scatter is seen at far range gates at both flanks of pre-noon and post noon sector.

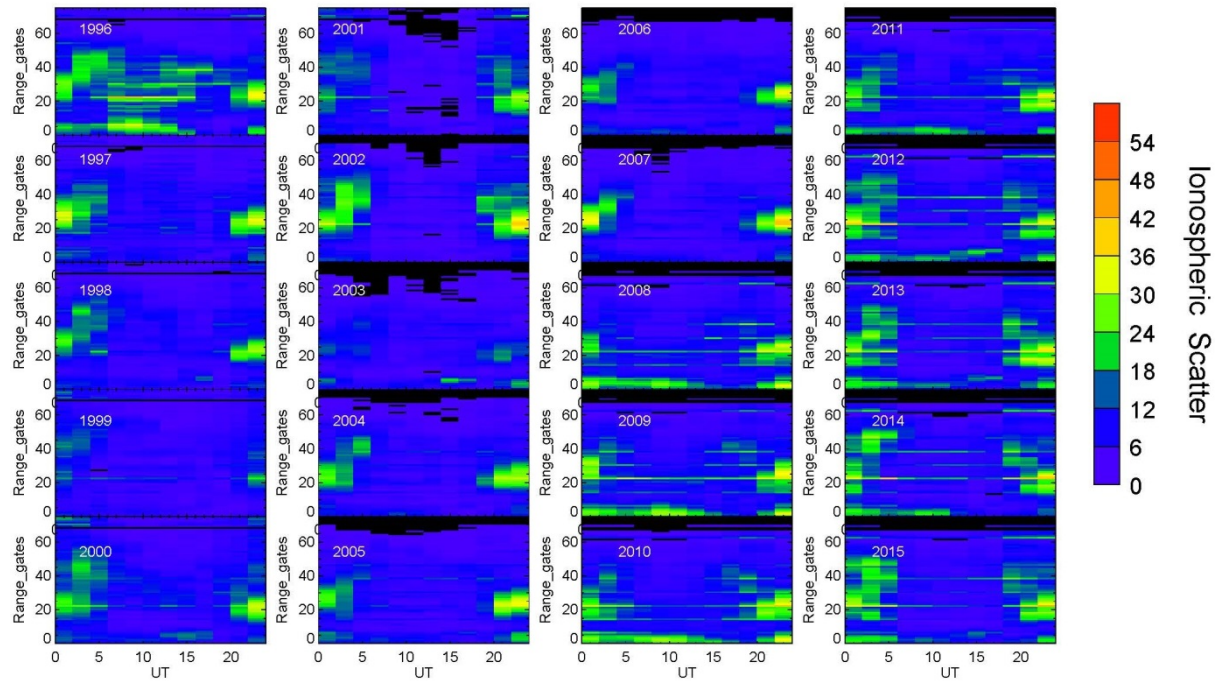
At mid-ranges, i.e. between range gates 20 – 40, ionospheric scatter is observed at Pykkvibaer predominantly around 00 UT to 06 UT and around 16 UT to 24 UT. Occurrence at mid-range gates shows a solar cycle variation, where the scatter occurs predominantly during solar cycle maximum and tends to disappear during solar cycle minimum similar to ionospheric scatter seen at far range gates. Unlike the occurrence percentage seen at Hankasalmi, ionospheric backscatter seen at mid-range gates in Pykkvibaer is much higher. Ionospheric scatter observed at near ranges, range gates < 20 is seen around 00 - 06 UT and around 18 - 24 UT, pre-noon and post noon. The pattern of ionospheric scatter seen does not show any clear solar cycle dependence. Also, there are times when very little ionospheric scatter is seen during the day around 06 – 14 UT.

The point occupancy statistics for Hankasalmi during the month of June are presented in Figure 5.7a. The figure shows that the occurrence of ionospheric scatter is seen primarily at far range gates during nighttime only except in 1996 when far range ionospheric scatter is seen during daytime. At far ranges, range gates > 40, ionospheric backscatter during the nighttime is seen only during 2000, 2001, and 2002, 2012-2015. These years are years of close to the relevant sunspot maximum indicating that far range ionospheric scatter shows some solar cycle dependency. Unlike the far range ionospheric scatter seen during March at daytime, the far range ionospheric scatter seen in June occurs during nighttime. Similar to ionospheric scatter seen at far range gates, the mid-range ionospheric scatter, range gates > 20 is seen at nighttime throughout the period investigated. Mid-range ionospheric scatter does not show any solar cycle dependence. The occurrence of ionospheric scatter at near range gates is seen during solar cycle maximum and is predominantly observed around 00-06 UT and around 18 - 24 UT. However, at range gates 0-5, occurrence of ionospheric backscatter appears to be seen throughout the day.

Figure 5.7b presents the point occupancy of ionospheric scatter during June for Pykkvibaer. The figure shows virtually no occurrence of ionospheric scatter at far ranges during the period investigated. Also, no occurrence of ionospheric scatter at mid-range gates is seen in Pykkvibaer during the period. Occurrence of ionospheric scatter is seen predominantly at near range gates. The near range ionospheric scatter is seen throughout the years investigated and it is seen at same UT as in Hankasalmi.

a)

Hankasalmi Beam 9 June 1996 - 2015



b)

Pykkvibaer Beam 7 June 1996 - 2015

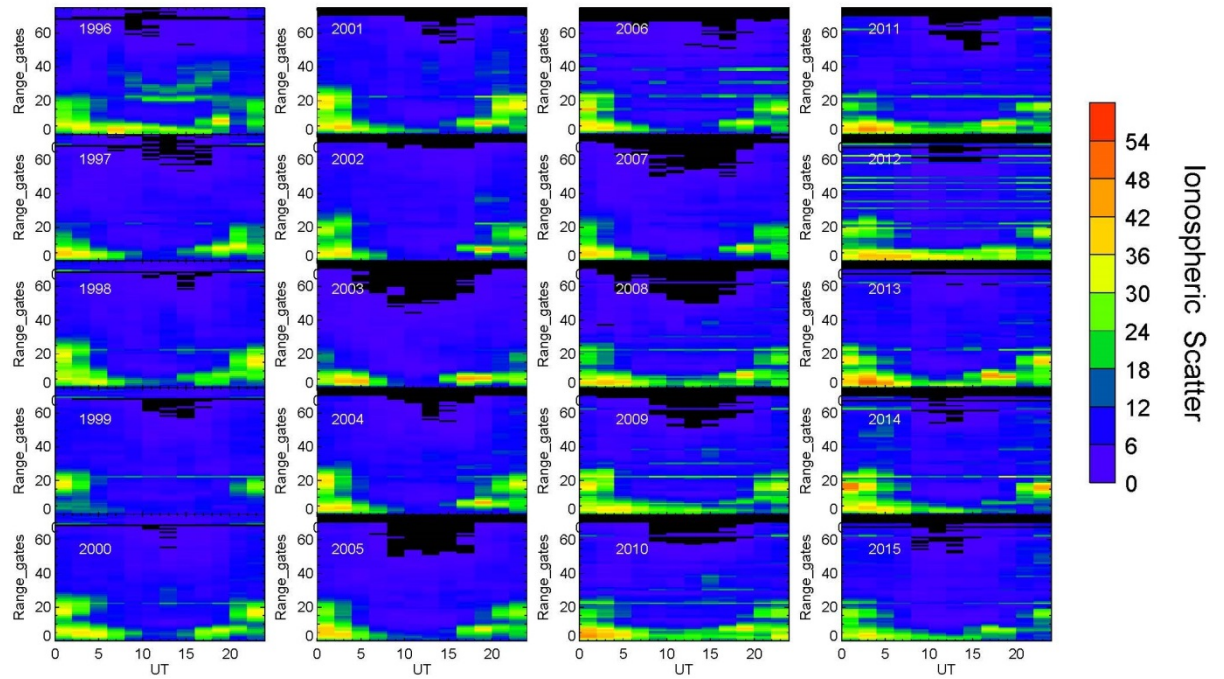


Figure 5.7 shows the point occupancy statistics of ionospheric backscatter (colour coded) of Hankasalmi and Pykkvibaer radars for the month of June (summer) from 1996 - 2015. The data are binned in two universal (UT) hour bins for each beam and the point occupancy as a function of range (75 range gates) gates (y axis) versus UT (x axis). The range gates are categorised into three; 0-20, mid-range gates, between 21-40, and far range gates corresponding to gates 41-75. Panel a) is Hankasalmi (Finland radar) beam 9, Panel b) is Pykkvibaer (Iceland radar) beam 7.

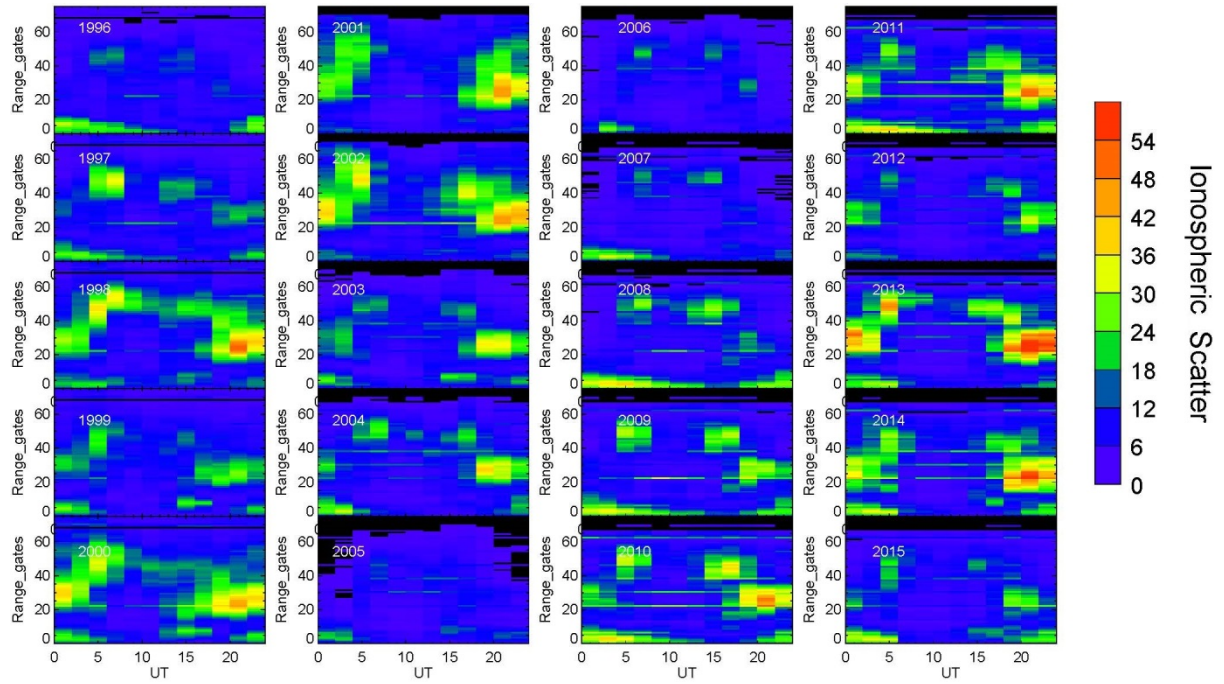
The point occupancy plot for the month of September for Hankasalmi radar is presented in Figure 5.8a. It can be seen from the figure that the pattern of ionospheric backscatter seen is similar to the pattern seen during March. However, there are years that the occurrence pattern of ionospheric scatter is different. During 2002, far range ionospheric scatter is seen at daytime in September which is not seen in March. Also, during September, the occurrence of ionospheric scatter during 2005 appears not to be present in all the range gates but in March 2005, daytime far range ionospheric scatter is seen.

For the point occupancy for the month of September for Pykkvibaer radar data, the occurrence pattern of ionospheric scatter is similar to the pattern during March. There are few years with variations in occurrence of ionospheric scatter in September compared to March. During 2005, far range ionospheric scatter is seen at post noon sector in March which is not seen in September. Also, it appears the occurrence of ionospheric scatter during September is higher than during March.

The point occupancy statistics of ionospheric backscatter for the Hankasalmi radar during December (winter month) is presented in Figure 5.9a. During, 1996-1997 ionospheric backscatter is seen to occur more at far ranges, range gates >40 around 08 UT and 10 UT. As we approach the solar maximum of solar cycle 23 (1998-2000), the occurrence pattern of ionospheric backscatter appears to differ from that of the previous years. During 1998-2000, a higher occurrence of ionospheric scatter appears to be recorded at far range gates around 08 – 14 UT day time. In 2001 far range ionospheric scatter is seen to occur throughout the day. Comparing the solar cycle 22/23 minimum with the solar cycle 23/24 minimum which spans through 2006-2009, we noticed that the daytime feature of occurrence of ionospheric backscatter during day time at far range gates is present but not as pronounced in 2006 – 2009 as in the period 1996-1997. At mid-ranges, occurrence of ionospheric scatter is seen at nighttime in 1997 – 2003 and it does not return until 2011. Although after 2003, we also noticed that there is absence of occurrence of ionospheric backscatter at mid-range gates. This disappearance of ionospheric backscatter occurrence at mid-ranges is noticed from 2004-2010. The range gates and the time of the day at which ionospheric backscatter occurs in 2003-2010 is somewhat similar to that of 1996-1997.

a)

Hankasalmi Beam 9 September 1996 - 2015



b)

Pykkvibaer Beam 7 September 1996 - 2015

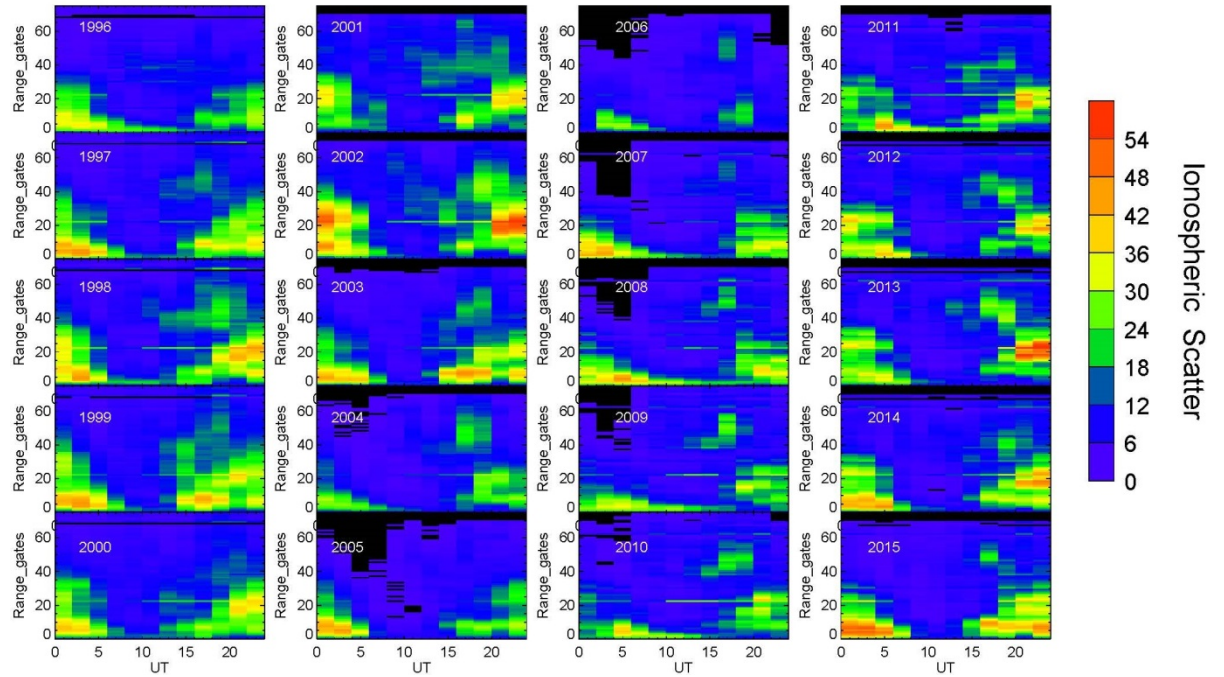
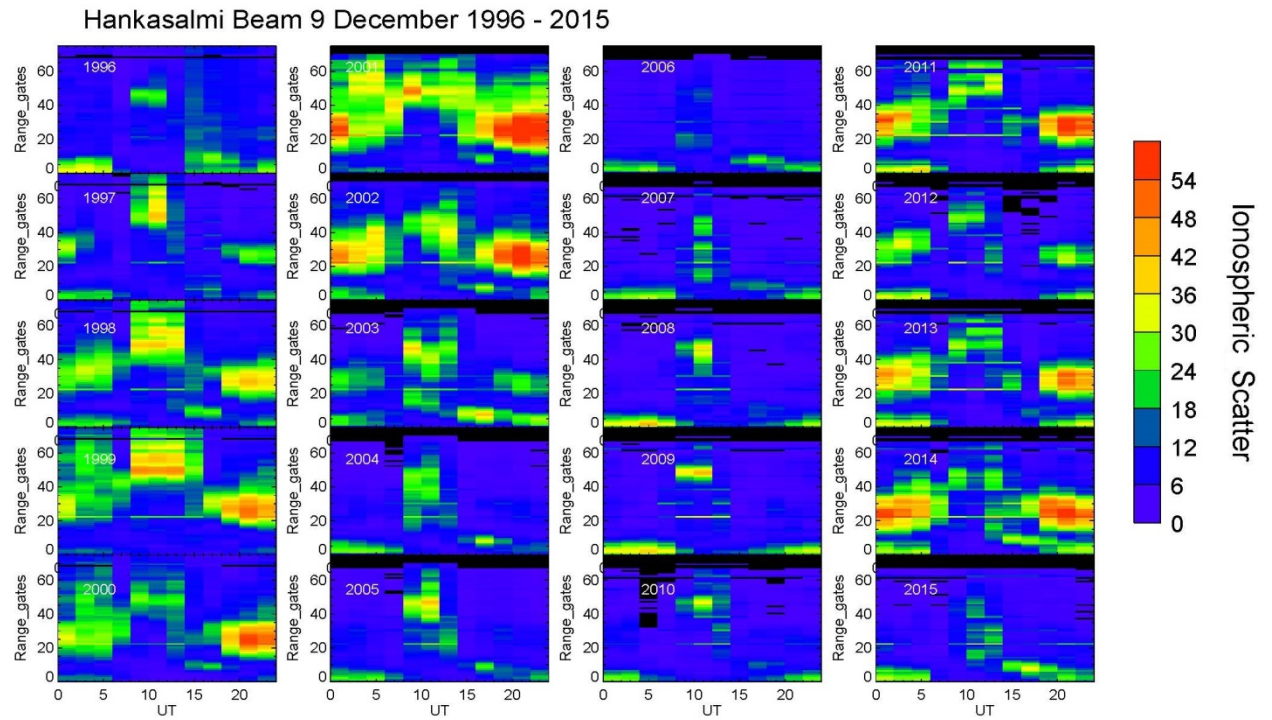


Figure 5.8 shows the point occupancy statistics of ionospheric backscatter (colour coded) of Hankasalmi and Pykkvibaer radars for the month of September (autumn) from 1996 - 2015. The data are binned in two universal (UT) hour bins for each beam and the point occupancy as a function of range (75 range gates) gates (y axis) versus UT (x axis). The range gates are categorised into three; 0-20, mid-range gates, between 21-40, and far range gates corresponding to gates 41-75. Panel a) is Hankasalmi (Finland radar) beam 9, Panel b) is Pykkvibaer (Iceland radar) beam 7.

a)



b)

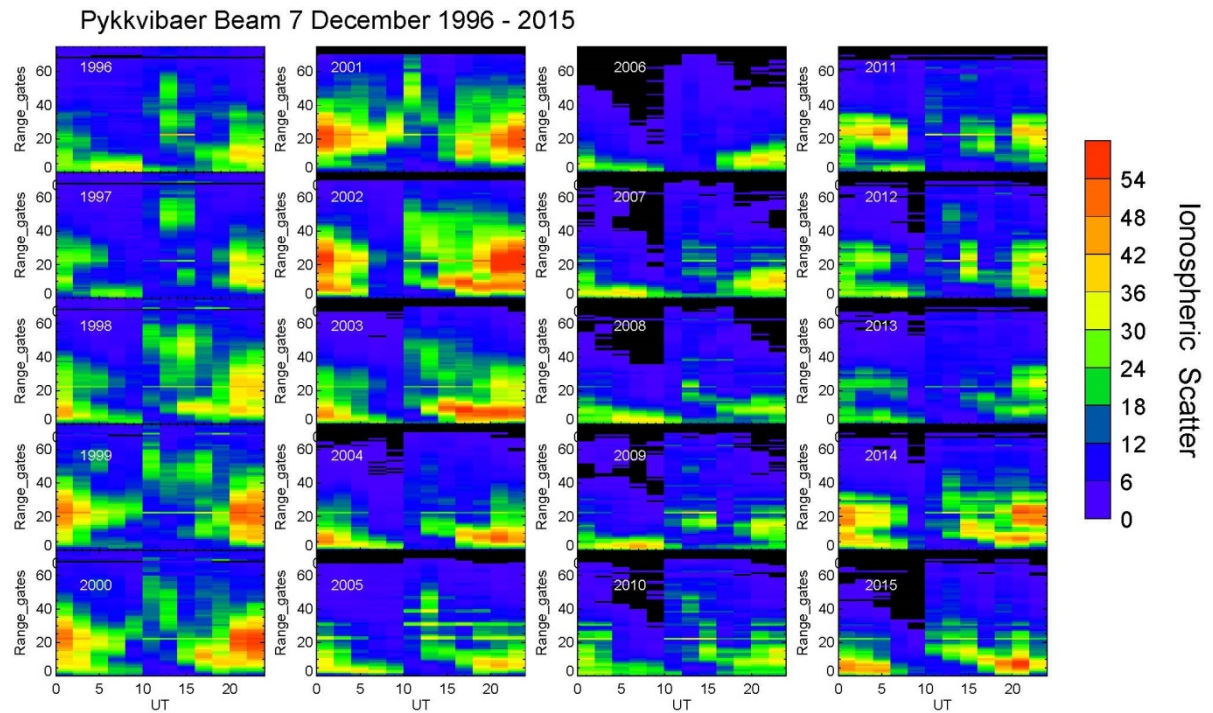


Figure 5.9 shows the point occupancy statistics of ionospheric backscatter (colour coded) of Hankasalmi and Pykkvibaer radars for the month of December (winter) from 1996 - 2015. The data are binned in two universal (UT) hour bins for each beam and the point occupancy as a function of range (75 range gates) gates (y axis) versus UT (x axis). The range gates are categorised into three; 0-20, mid-range gates, between 21-40, and far range gates corresponding to gates 41-75. Panel a) is Hankasalmi (Finland radar) beam 9, Panel b) is Pykkvibaer (Iceland radar) beam 7.

It is noticed that the occurrence of ionospheric backscatter in all range gates seen throughout the day reappears in 2011-2013 though at different range gates. The occurrence of ionospheric backscatter is seen to occur at far ranges during day time around 08 UT to 14 UT while at mid-range gates occurrence of ionospheric backscatter is seen to occur during night time in addition to the occurrence of very little ionospheric backscatter seen at very near range gates during night time. This trend is similar to that observed around the solar maximum of cycle 23 (2000-2002) although there is low scatter at far ranges. From figure 5.5b, it is noticed that the time of day, the range and the year at which ionospheric backscatter occurs in Pykkvibaer is somewhat different from that of Hankasalmi. Occurrence of ionospheric backscatter in Pykkvibaer is seen to be present in almost all the range gates from 1996 to 2005 while it is seen to be present at near range gates from 2006-2008. In addition, it is noticed in Figure 5.9b that the occurrence of ionospheric backscatter at near ranges in Pykkvibaer occurs during night time universal time throughout the period investigated.

5.5 Summary

The point occupancy statistics of ionospheric backscatter and ground backscatter to investigate the occurrence of both types of scatter as a function of range gates spanning nearly two full solar cycles from the central beam of each of the radars, beam 9 of Hankasalmi and beam 7 of Pykkvibaer has been investigated. The results obtained are as follows:

- i. The time of the day at which ground scatter occurs displays a consistent pattern in all the seasons
- ii. The occurrence of ground scatter is noticed to occur predominantly during daytime (06 – 14 UT) at mid-range gates in both radars showing solar cycle variation during March, September and December
- iii. Ground scatter and ionospheric scatter exhibits solar cycle variation
- iv. Solar cycle variation in the occurrence of ground scatter during June is seen to occur at far range gates at Pykkvibaer during nighttime.
- v. diurnal variation in the occurrence of ionospheric scatter is fairly mixed
- vi. There are times when ionospheric scatter is seen at daytime and times when it is seen at nighttime

- vii. Annual variation in the occurrence of ground scatter peaks during summer and reduce in winter
- viii. During solar maximum, occurrence of ground scatter and ionospheric scatter are seen to be more pronounced than during solar minimum
- ix. occurrence of ionospheric scatter displays mixed seasonal variation
- x. solar cycle variation of occurrence of far range ionospheric scatter is seen in March and September
- xi. .During solar maximum, far range ionospheric scatter is seen at nighttime between 00 – 05 UT and 16 UT and mid-range ionospheric scatter is seen around 00 UT to 06 UT and around 18 UT to 24 UT during solar maximum
- xii. The occurrence of near range ionospheric scatter throughout the solar cycle is also evident in Hankasalmi.
- xiii. Occurrence of ionospheric scatter at far ranges is seen only in the post noon sector at solar maximum years
- xiv. the pattern of ionospheric scatter seen at Pykkvibaer is different

5.6 Point occupancy as a function of radar azimuth

The focus of this section is to compare the point occupancy statistics of both the ionospheric and ground backscatter received by the selected beams in both the Hankasalmi radar and Pykkvibaer radar to investigate the effect of the radar look direction on point occupancy. The three beams selected from Hankasalmi radar are beam 1, 9 and beam 14 while the selected beams from Pykkvibaer radar are beam 1, 7 and beam 14 respectively. This approach is to investigate if there are significant variations with azimuth within each field of view by understanding the spatial distribution of ionospheric backscatter and ground backscatter with respect to the location of the selected beams. We have limited this analysis to comparing a central beam with two of the extreme beams, although we have not chosen the beams at the edges of the field of view as the antenna beam pattern is at its worst there. The first presentation will be the point occupancy of the selected beams of Hankasalmi radar for both ionospheric and ground backscatter followed by the presentation of the point occupancy statistics of the selected beams of Pykkvibaer radar.

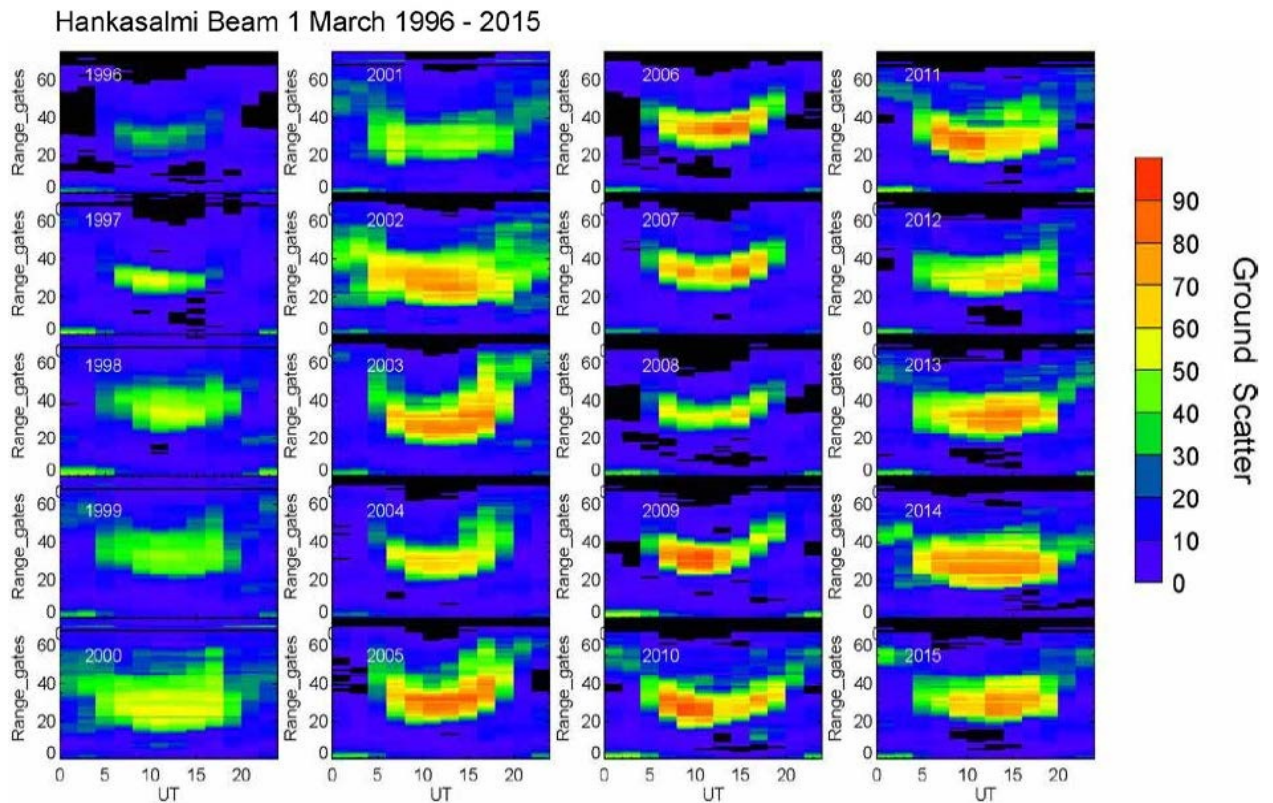
The figures presented in this section for both radars are only those where the point occupancy pattern is distinct or different from the occurrence pattern of the other two

beams or presented as an example of other months. The figures of the two beams with similarity in the occurrence pattern are presented in the Appendix.

5.6.1 Hankasalmi ground backscatter

The point occupancy of ground scatter during the month of March is presented in Figure 5.10 for beam 1, 14. Figure 5.10 show that the occurrence of ground scatter at far ranges, range gates > 41 appears to be present in only a few years on all beams. The pattern of occurrence of ground scatter is much the same on all beams. There is no evidence of significant difference in the pattern of ground scatter on all the beams. The occurrence level of ground scatter on beam 1 (Figure 5.10a) appears to be higher than the occurrence level seen in beam 9 (Figure 5.2a) and beam 14 (Figure 5.10b) which tends to record the same level of in occurrence. Each of the four months seems to show the same effect in all the three beams. Beam 1, 9 and 14 of the month of March is presented as an example of the four months. Other Figures for the other months not presented here are presented in the Appendix 1.

a)



b)

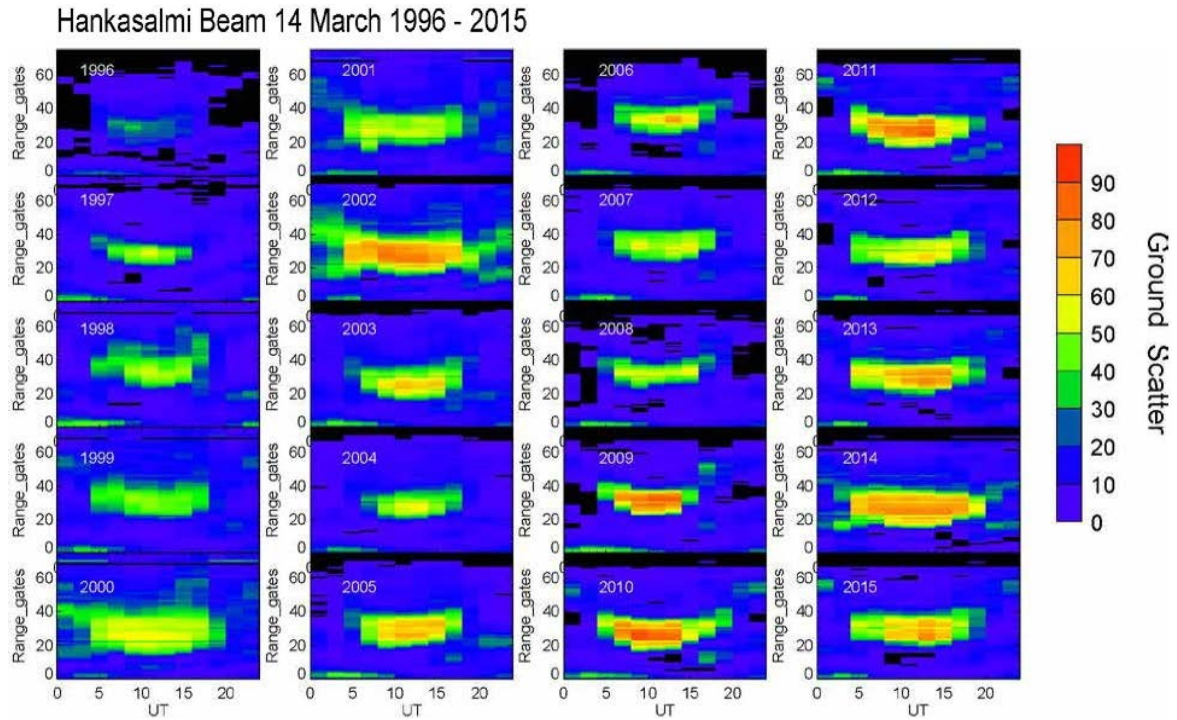


Figure 5.10 shows the point occupancy statistics of ground backscatter (colour coded) of Hankasalmi (Finland radar) beam 1 (**panel a**) & 14 (**panel b**) for the month of March (spring) from 1996 - 2015. The data are binned in two universal (UT) hour bins for each beam and the point occupancy as a function of range (75 range gates) gates (y axis) versus UT (x axis). The range gates are categorised into three; 0-20, mid-range gates, between 21-40, and far range gates corresponding to gates 41-75.

5.6.2 Hankasalmi ionospheric backscatter

The point occupancy of ionospheric scatter during the month of March for beam 1 is presented in Figure 5.11. Figure 5.11 shows that the diurnal variation in the occurrence of ionospheric scatter with range for beam 1 is similar to that of beam 9 (Figure 5.6a) and beam 14 (Figure A2.1). Similarly, it is noticed that the solar cycle variation in the occurrence of ionospheric scatter seen in beam 9 shows the same trend in beam 1 and beam 14.

The major difference in the occurrence pattern of ionospheric backscatter in the three beams is seen in the general level of scatter. The scatter level for beam 1 is typically less than seen in beam 9 and beam 14, which are both similar. Examples of the difference in scatter level include firstly, the lower level (lack) of ionospheric scatter during the day in 2006 and 2007 in beam 1. Secondly, it is noticed that there is lack of post noon ionospheric scatter in beam 1 at mid-range gates, while post noon ionospheric scatter at mid-range gates is seen in beam 9 and beam 14 almost throughout the years investigated.

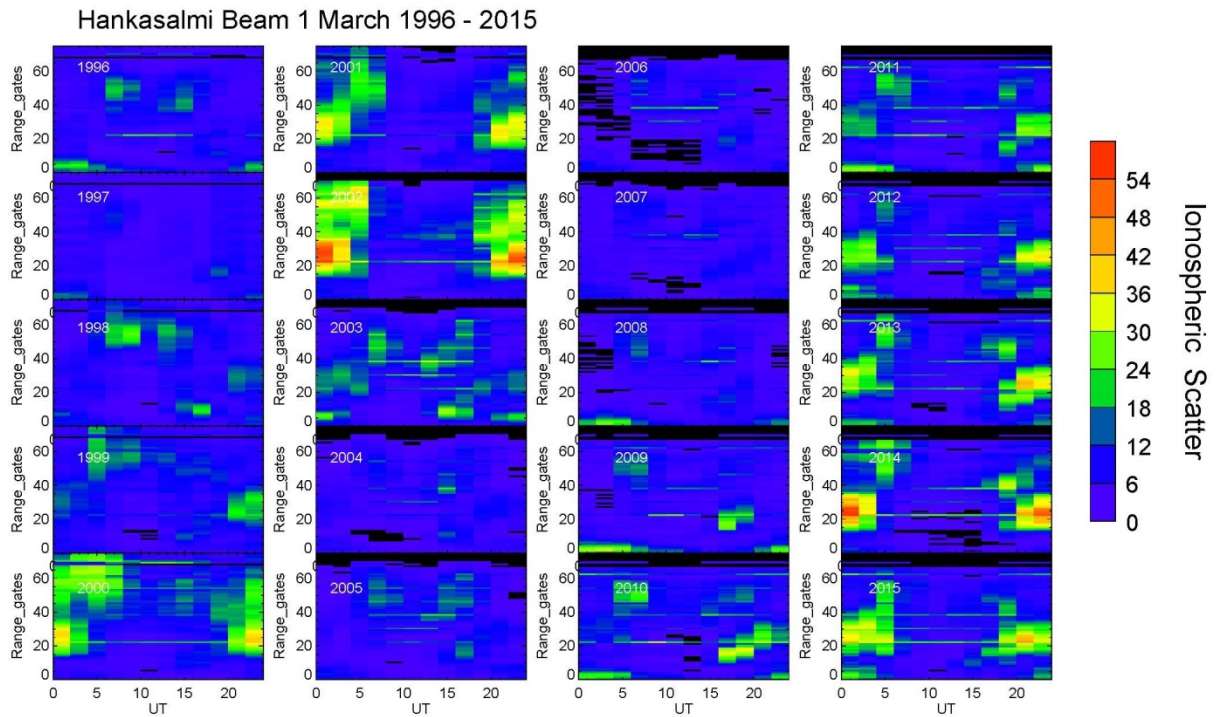


Figure 5.11 shows the point occupancy statistics of ionospheric backscatter (colour coded) of Hankasalmi (Finland radar) beam 1 for the month of March (spring) from 1996 - 2015. The data are binned in two universal (UT) hour bins for each beam and the point occupancy as a function of range (75 range gates) gates (y axis) versus UT (x axis). The range gates are categorised into three; 0-20, mid-range gates, between 21-40, and far range gates corresponding to gates 41-75.

The level of ionospheric scatter seen in beam 1, 9 and 14 point occupancy plot during June (Figure A2.2a, Figure 5.7a & Figure A2.2b) respectively, September (Figure A2.3a Figure 5.8a & Figure A2.3b) and December (Figure A2.4a Figure 5.9a & Figure A2.4b) respectively is similar to the pattern seen in the month of March with beam 1 recording lower level of scatter than beam 9 and 14.

5.6.3 Pykkvibaer ground backscatter

The point occupancy statistics during the month of March is presented in Figure 5.13 for beam 1. The figure shows that the pattern of occurrence of ground scatter is much the same on all beams. There is no evidence of significant difference in the pattern of ground scatter on all the beams. The diurnal variation seen on beam 1 is similar to the diurnal variation of ground scatter on beam 7 (Figure 5.2b) and beam 14 (Figure A.13). In addition, there is no significant difference in the seasonal variation on all the beams. The occurrence level of ground scatter on beam 1 appears to be lower than the occurrence level seen in beam 7 and beam 14 which tends to record higher level in occurrence of ground scatter.

Each of the four months seems to show the same effect in all the three beams. Beam 1, 7 and 14 of the month of March is presented as an example of the four months. Other Figures for the other months not presented here are presented in the Appendix 1.

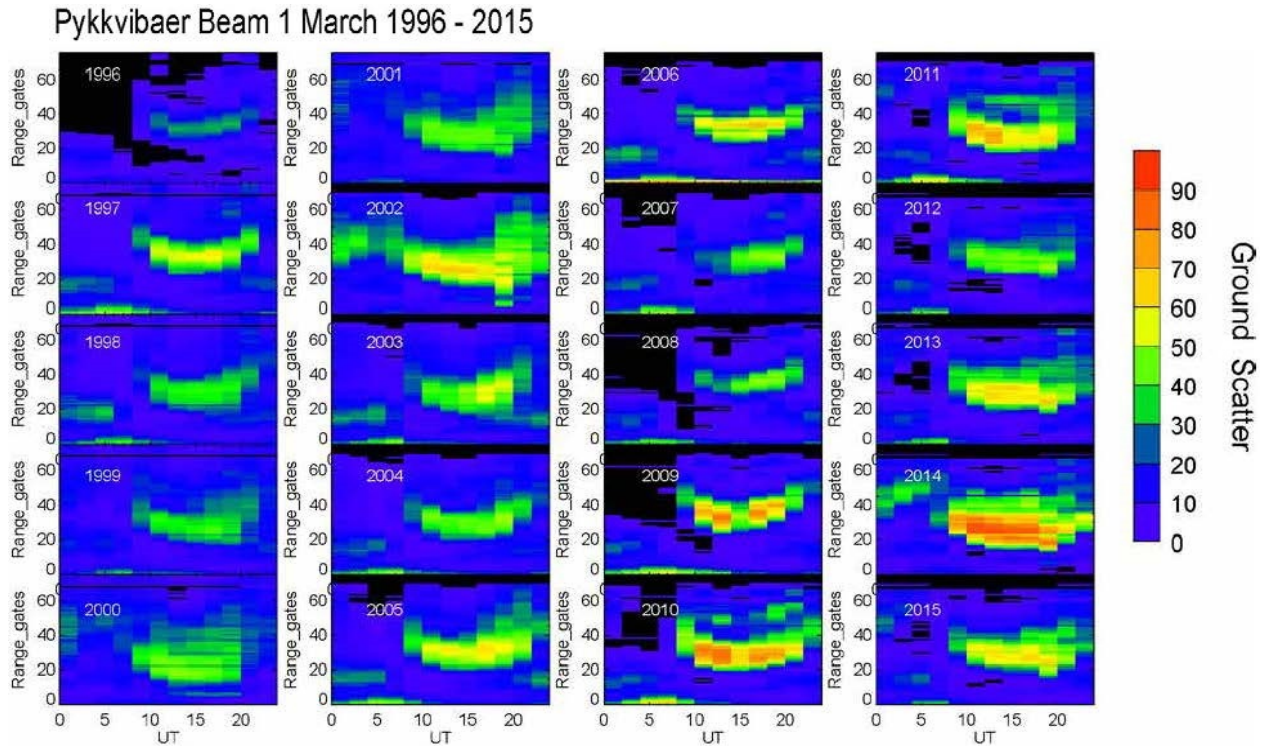


Figure 5.12 shows the point occupancy statistics of ground backscatter (colour coded) of Pykkvibaer (Iceland radar) beam 1 for the month of March (spring) from 1996 - 2015. The data are binned in two universal (UT) hour bins for each beam and the point occupancy as a function of range (75 range gates) gates (y axis) versus UT (x axis). The range gates are categorised into three; 0-20, mid-range gates, between 21-40, and far range gates corresponding to gates 41-75.

5.6.4 Pykkvibaer ionospheric backscatter

The point occupancy of ionospheric scatter for Pykkvibaer radar during the month of March is presented in Figure 5.13 for beam 14. Figure 5.13 show that the pattern of occurrence of ionospheric backscatter is much the same on all beams. The diurnal variation of ionospheric scatter in beam 1 is similar to the diurnal variation of ionospheric scatter on beam 7 and beam 14. Similarly, the seasonal variation is similar on all the beams. One important difference that is noticed on the three beams is the higher occurrence level of ionospheric scatter is seen on beam 1 (Figure 5.13) and beam 7 (Figure 5.6b) than on beam

14 (Figure A2.5). Also, it is noticed that beam 14 does not seem to record far range gates ionospheric scatter at gates >40 but this feature is seen to be present on beam 1 and beam 7. The occurrence level of ionospheric scatter on beam 1 appears to be higher than the occurrence level seen in beam 9 and beam 14 which tends to record same level of in occurrence.

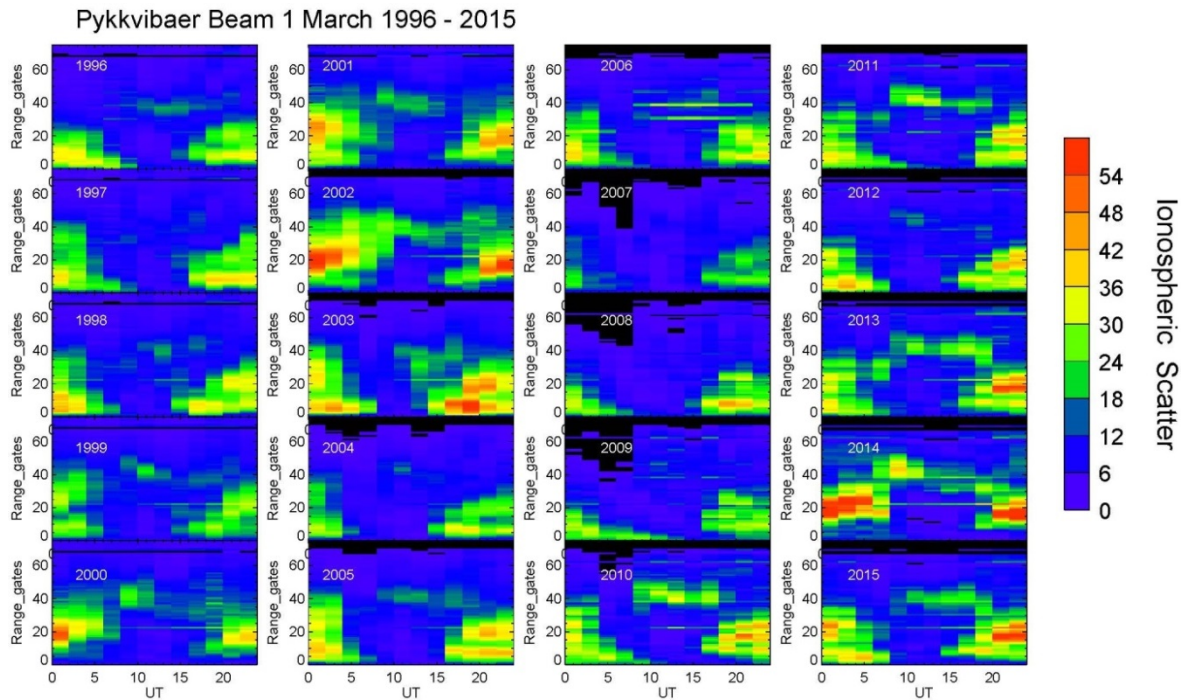


Figure 5.13 shows the point occupancy statistics of ionospheric backscatter (colour coded) of Pykkvibaer (Iceland radar) beam 1 for the month of March (spring) from 1996 - 2015. The data are binned in two universal (UT) hour bins for each beam and the point occupancy as a function of range (75 range gates) gates (y axis) versus UT (x axis). The range gates are categorised into three; 0-20, mid-range gates, between 21-40, and far range gates corresponding to gates 41-75.

The level of ionospheric scatter seen in beam 1, 7 and 14 point occupancy plots during the June (Figure A2.6a, Figure 5.7b & Figure A2.6b), September (Figure A2.7a, Figure 5.8b & Figure A2.7b) and December (Figure A2.8a; Figure 5.9b & Figure A2.8b) in Pykkvibaer are similar to the pattern seen in March with beam 14 recording lower level of scatter than beam 7 and 14.

5.7 Summary

The point occupancy statistics of ionospheric backscatter and ground backscatter to compare the occurrence of both types of scatter as a function of range gates spanning

nearly two full solar cycles received in both the Hankasalmi radar and Pykkvibaer radar to investigate the effect of the radar look direction on point occupancy has been investigated. The results obtained in the study are:

:

- (i) The occurrence of ground scatter in Pykkvibaer tends to be lower in beam 1 than beam 7 and 14 in March
- (ii) The pattern of ground scatter in Pykkvibaer seen in June, September and December is similar to that seen in March in Pykkvibaer
- (iii) The occurrence of ground scatter in Hankasalmi tends to be higher in beam 1 than beam 9 and 14 in March
- (iv) The pattern of ground scatter in Hankasalmi seen in June, September and December is similar to that seen in March
- (v) The occurrence of ionospheric scatter in Pykkvibaer tends to be higher in beam 1 than beam 7 and 14 in March
- (vi) The occurrence of ionospheric scatter in Pykkvibaer tends to be lower in beam 14 than in the other two beams
- (vii) The pattern of ionospheric scatter in Pykkvibaer seen in June, September and December is similar to that seen in March
- (viii) The occurrence of ionospheric scatter in Hankasalmi tends to be lower in beam 1 than beam 9 and 14 in March
- (ix) The pattern of ionospheric scatter in Hankasalmi seen in June, September and December is similar to that seen in March
- (x) Comparing the diurnal variation of ground scatter in the month of June and December, it is noticed that ground scatter peaks in the day in December at both Hankasalmi and Pykkvibaer radars but there is no clear diurnal variation in June.

5.8 Discussion

Long term spatial studies of the occurrence of backscatter (ionospheric and ground backscatters) observed by the SuperDARN (Hankasalmi and Pykkvibaer) radars for a time interval spanning almost two complete solar cycles (1996-2015) have been investigated. The focus of the present study is on the point occupancy as a function of range for

backscatter which was analysed in order to establish whether the variations in occurrence of backscatter are due to radar signal propagation conditions such as operational frequency, ionospheric densities or due to formation of ionospheric irregularities.

The two radars used in this study were operated at frequencies which changed during three time intervals, (00 - 06 UT), (06 - 18 UT) and (18 - 24 UT). Table 5.1 presents the Hankasalmi radar operating frequency during each day of the year investigated, while Table 5.2 presents that of Pykkvibaer radar. For Hankasalmi radar, the radar stepped through four frequency bands (10 MHz, 11 MHz, 12 MHz and 13 MHz) while the Pykkvibaer radar stepped through two frequency bands (10 MHz and 12 MHz).

The frequency of operation of Pykkvibaer radar shows that at 00-06 UT and 18-24 UT there is no frequency change throughout the period. However, during 2001, 2002, 2012 and 2013 at 06-18 UT the radar operated at 12MHz and the comparison shows that at the boundaries it indicates there is no functional change. Similarly, the frequency of operation of Hankasalmi radar shows that at 00-06 UT and 18-24 UT is similar to Pykkvibaer in that only two operating frequency bands, 10 MHz and 11 MHz during each day of the year in all the years investigated. It is noticed that the occurrence of ground backscatter decreases as frequency increases in both radars. The decrease in ground backscatter is due to the decrease in the refraction which is insufficient for ionospheric reflection to occur. Similarly, it is noticed that occurrence of ionospheric backscatter decreases with increasing frequency during in all the four seasons. This decrease in occurrence of ionospheric backscatter with increase in frequency recorded by Hankasalmi radar is similar to that observed by Pykkvibaer radar. We noticed that the operational frequency for Pykkvibaer radar illustrated in Table 5.2 in 1996-2000 was around 10 MHz throughout the day of the year. During 2001-2002 the operational frequency for 00-08 UT and 18-24 UT was 10 MHz, while the frequency from 08-18 UT it was around 12 MHz. The operational frequency for the years 2003-2011 was 10 MHz throughout the time of day of the years while the operational frequency for the year 2012-2013 is similar to that of 2001-2002 period, i.e. 10 MHz for 00-08 UT and 18-24 UT and 12 MHz for 08-18 UT. We noticed that the maximum occurrence of ionospheric backscatter appears not to have direct dependence on the increase in operating frequency of the radar.

The next section discusses solar cycle variation in ground scatter and ionospheric scatter and the seasonal variation seen is discussed further.

Table 5.1: Frequency of operation of Hankasalmi radar

Frequency of Operation (MHz)	00 – 06 UT	06 – 18 UT	18 -24 UT
10	1996, 1997, 1998, 1999, 2000, 2001, 2002, 2008, 2009, 2010, 2011, 2012, 2013	1996, 1997, 2008, 2010, 2011	1996, 1997, 1998, 1999, 2000, 2001, 2002, 2008, 2009, 2010, 2011, 2012, 2013, 2014, 2015
11	2003, 2004, 2005, 2006, 2007	2003, 2004, 2005, 2006, 2007	2003, 2004, 2005, 2006, 2007
12	nill	1998, 1999, 2000, 2012, 2013, 2014, 2015	nill
13	nill	2001, 2002	nill

Table 5.2: Frequency of operation of Pykkvibaer radar

Frequency of Operation (MHz)	00 – 06 UT	06 – 18 UT	18 -24 UT
10	1996, 1997, 1998, 1999, 2000, 2001, 2002, 2003, 2004, 2005, 2006, 2007, 2008, 2009, 2010, 2011, 2012, 2013, 2014, 2015	1996, 1997, 1998, 1999, 2000, 2003, 2004, 2005, 2006, 2007, 2008, 2009, 2010, 2011	1996, 1997, 1998, 1999, 2000, 2001, 2002, 2003, 2004, 2005, 2006, 2007, 2008, 2009, 2010, 2011, 2012, 2013, 2014, 2015
12	nill	2001, 2002, 2012, 2013	nill

5.8.1 Solar cycle dependences of backscatter

The present analysis has showed that the point occupancy plot of the analysis showed that maximum occurrence of ground backscatter occurs during the two-solar cycle maxima and minimum occurrence was observed during the two-solar cycle minima. It is also noticed that overall peak in occurrence of ground backscatter was recorded during cycle 23 maximum while overall minimum in occurrence of ground scatter is seen in during the solar cycle 23/24 minimum. The dependence of ground scatter occurrence on the radar's frequency of operation appears to be similar to that observed for ionospheric backscatter for both radars. Hence, the occurrence of ionospheric backscatter and ground scatter does not seem to increase due to increase in frequency of operation rather increase or decrease in rates of occurrence of ionospheric and ground backscatter might be due to some other factors.

Similarly, the ionospheric backscatter occurs at far ranges in the day time sector during both solar maxima and solar minima in the Hankasalmi radar during winter months while occurrence at mid and near ranges are observed in the Pykkvibaer radar at night time sector of both solar maxima and during solar minimum of cycle 23/24 occurrence of ionospheric backscatter is seen to occur more at near-ranges. Hankasalmi records more far range backscatter which is likely to be $1 \frac{1}{2}$ hop F-region scatters while Pykkvibaer records more of mid-range, probably $\frac{1}{2}$ hop F region backscatter and near-range backscatter probably $\frac{1}{2}$ hop E-region scatter. We noticed that the occurrence of ionospheric scatter at far range gates and mid-range gates exhibit a solar cycle dependence. The point occupancy plot shows that the Pykkvibaer radar records a higher occurrence of near range ionospheric backscatter than the Hankasalmi radar in all the years investigated. The contrast in the occurrence rate of ionospheric scatter observed by the two radars throughout the interval confirms the results of a previous study by Milan et al., (1997b) based on 18 months of data, which also show that the Pykkvibaer radar observed more near range E region backscatter than the Hankasalmi radar as a consequence of its zonal look-direction and higher magnetic latitude.

Ghezelbash et al (2014) considered data for 2000-2002 & 2008-2010 and reported that the overall echo (ionospheric) occurrence for Hankasalmi radar is larger on the dawnside than on the duskside although, the present analysis shows that the occurrence of ionospheric

scatter for the Hankasalmi radar displays peak occurrence of backscatter during solar minimum at the day time sector and a minimum at night time sector in all of the seasons except summer. This seems to be in agreement to the observation reported by Ghezelbash et al (2014). This might be due to the fact that Ghezelbash et al (2014) computed backscatter occurrence data for beam 5 and 6 of Hankasalmi radar while we also make use of total field-of-view data set for the occurrence rate and beam 9 of Hankasalmi radar for the point occupancy as a function of range data.

The point occupancy statistics show that the occurrence of ionospheric backscatter decreases as the frequency of operation during the day is increased in most of the years investigated. Occurrence of Ionospheric scatter is seen to reduce in 2006-2007 when the radar operated at higher frequency (11 MHz) compared to 1996, 2011 when the radar operating frequency was lower (10 MHz). Ionospheric backscatter point occupancy falls to a very lower level in all the range gates and time of day at Hankasalmi in 1997 compared to that of 1996 when the radar operated at the same frequency band (10 MHz (00-06 UT, 06-18 UT and 18-24 UT)) . However, the higher occurrence rate in ionospheric backscatter point occupancy is noted in 2000 compared to 1998 and 1999 when the radars operated at the same frequency bands (10 MHz (00-06 UT and 18-24 UT), 12 MHz (06-18 UT)) as illustrated in Table 1. Also, the increase in the daytime frequency of operation in 2001-2002 to 13MHz does not appear to have had any effect on the rate of occurrence of ionospheric backscatter point occupancy compared to 2000.

During the solar minimum of cycle 23/24 (2003-2007) the occurrence of ionospheric backscatter point occupancy fell to a near zero level at mid-range and far range gates at nighttime despite the increase in the operational frequency during nighttime from 10 MHz in previous years (1996-2002) to 11 MHz in 200-2007. This total disappearance in the occurrence of ionospheric backscatter point occupancy at both mid and far ranges was also observed in 1996 and 1997. Similarly, comparing the occurrence rate of ionospheric scatter point occupancy for 2008-2011 when the frequency of operation of Hankasalmi radar was 10 MHz with 1996 when it operated with the same frequency, there was a higher occurrence rate in 1996 than 2008-2011, while in 1997 there was a lower occurrence rate than 2008-2011. Reduction in the occurrence rate of ionospheric backscatter point occupancy with increase in frequency during day time is noticed in 2012-2013 in comparison with years when the radar operated at lower frequency (< 12 MHz) than 12 MHz it operated during day time during the two years (2012-2013). This decrease in

occurrence of ionospheric backscatter with increase in frequency recorded by Hankasalmi radar is similar to that observed by Pykkvibaer radar. We noticed that the operational frequency for Pykkvibaer radar illustrated in Table 2 in 1996-2000 was around 10 MHz throughout the day of the year. During 2001-2002 the operational frequency for 00-08 UT and 18-24 UT was 10 MHz, while the frequency from 08-18 UT it was around 12 MHz. The operational frequency for the years 2003-2011 was 10 MHz throughout the time of day of the years while the operational frequency for the year 2012-2013 is similar to that of 2001-2002 period, i.e. 10 MHz for 00-08 UT and 18-24 UT and 12 MHz for 08-18 UT.

5.8.2 Seasonal dependences of backscatter

The ground scatter occurrence for the two radars exhibit similar trends in occurrence for the months investigated with the exception of the month of June. The daytime ground scatter seen during summer month, June, is a consequence of propagation via E region. Minimum occurrence of ground backscatter is noticed in the night time sector in all the years investigated for the month of March, June and September. This minimum in occurrence of ground backscatter is seen to occur in both solar minima and solar maxima. However, peak occurrence of ground scatter during day time is noticed in the month of December. These features are noticed in the two radars. The seasonal variation displayed by ground backscatter is a consequence of the ionization of the E and F regions due to variability in the illumination. It is pertinent to point out that during the extended solar minimum of solar cycle 23/24, Solomon et al, (2011) noted that that solar EUV during the period (2007-2009) was lower than previous solar minima which seems to be in tandem with our observation of lower minimum occurrence of ionospheric backscatter during solar minimum of cycle 23/24 in comparison to the minimum occurrence during solar minimum of cycle 22/23. Also, it is noticed that the minimum occurrence in ionospheric backscatter which appears during the solar cycle minimum for Pykkvibaer radar has a distinct feature from that of Hankasalmi radar.

The occurrence of ionospheric backscatter during the month of March, September and December for the two radars exhibits distinct features during the two solar minima and during the solar maxima while having similarities in trend for the month of June. A minimum occurrence of ionospheric backscatter in the night time during the two-solar minima is recorded in Hankasalmi radar in the month of March, September and December,

even though Hankasalmi data display a different pattern during the solar cycle 22/23 minimum (1996) having higher occurrence of ionospheric backscatter during daytime than during nighttime. The minimum in occurrence of ionospheric backscatter during solar minima is recorded during the daytime in Pykkvibaer throughout the four seasons or months with the exception of December which exhibit the minimum occurrence during solar minima feature for a shorter period in daytime in comparison to other months. Maximum occurrence of ionospheric backscatter in the night time during the two-solar minima is recorded in Hankasalmi radar in all the months investigated. The overall peak in occurrence of ionospheric backscatter is much higher in solar cycle 23 maximum in comparison to solar cycle 24 maximum. This trend is also true for the Pykkvibaer data. It is important to point out that ionospheric backscatter occurrence seems to be much lower in June than in other months for both radars. Our observation of the variation in the location and occurrence of backscatter in season is in agreement with the findings from the work of Milan et al., (1997). In addition, it is also noticed that ionospheric backscatter was observed to be present at near ranges in the midnight universal time sector during summer months while being observed to occur most frequently at far ranges during winter and equinoctial months. The two radars exhibit less variability in the occurrence of backscatter around similar period.

Ruohoniemi and Greenwald (1997) study on scatter occurrence statistics of the Goose Bay SuperDARN radar which focused primarily on F region scatter observed that the scatter occurrence level was low in summer in both noon and afternoon sectors while the occurrence rate during winter shows high level in both noon and afternoon sectors. The above observation can be said to be somewhat similar to what is observed in both Hankasalmi and Pykkvibaer radars for the month of June (summer). However, the high level occurrence in the noon and afternoon sectors observed by Ruohoniemi and Greenwald (1997) during winter month seems not to be the case for the Pykkvibaer radar during the winter period but does for the Hankasalmi radar. Pykkvibaer radar exhibit low level of occurrence of ionospheric backscatter during day time throughout the period investigated. This difference in the observation might be due to geographic location of the radars.

The observation of Koustov et al. (2004) that there was an increase in the midnight echo occurrence as the solar cycle approaches its maximum with no significant increase in noon

sector observations seems to be in agreement with our observation of backscatter occurrence in the point occupancy analysis with the exception that we notice that as we approach the solar maximum backscatter occurrence also increase during day time in Hankasalmi point occupancy analysis.

5.9 Conclusion

We have carried out long term statistical studies of the occurrence of backscatter (ionospheric and ground scatter) observed by the SuperDARN (Hankasalmi and Pykkvibaer) radars for a time interval spanning approximately two-solar cycles (1996-2015). In this study, we have obtained diurnal, seasonal and solar cycle dependences of ionospheric and ground backscatter using SuperDARN radars for a time interval spanning approximately two-solar cycle (1996-2013). It is noted that the point occupancy as a function of range versus time are discussed. The key new results obtained in the study are, (i) Ionospheric backscatter is prominent at far ranges at local day during solar cycle 23 than solar cycle 24, (ii) Mid-range ionospheric scatter occurs at night-time in June (summer) during the entire period, (iii) ground scatter occurrence at both mid-range and a near-range gate is more in June than other months, (iv) Hankasalmi's beam 1 records less ionospheric backscatter than beam 9 and beam 14 in almost all the seasons investigated (v) Hankasalmi's beam 1 records more ionospheric backscatter than beam 9 and beam 14 in almost all the seasons investigated (vi) ground scatter occurs at mid-ranges around local mid-day and mirror the far-range ionospheric scatter occurrence, (vii) in contrast to Milan et al (1997) occurrences tends to be higher in Pykkvibaer than in Hankasalmi, the difference in observation might be due to the number of range gates investigated (viii) Pykkvibaer's beam 1 records more ionospheric backscatter than beam 7 which records more than beam 14.

Chapter 6

Effects of energy drivers on occurrence of backscatter.

6.1 Introduction

In the previous chapters, we have reported investigations on the long term temporal and spatial variations of ionospheric and ground backscatter using data from two SuperDARN (Hankasalmi and Pykkvibaer) radars for a time interval spanning approximately two-solar cycles (1996-2015). In chapter 5, we discussed the occurrence of ionospheric backscatter and ground backscatter and how it varies with ground distance by studying the diurnal variation of backscatter and the range gates at which both ionospheric backscatter and ground backscatter are observed.

In addition to the solar cycle, seasonal and diurnal variability, the occurrence of ionospheric and ground backscatter reported in the previous chapters are controlled by events or activities relating to solar terrestrial interactions. The major drivers directly affecting the occurrence of ionospheric scatter and ground scatter and those having indirect effects on the occurrence of both scatters over a long term have, as yet, not been undertaken.

In this chapter, we report a statistical analysis to parameterize the occurrence rate of ionospheric backscatter from 1996 to 2015 as a function of the upstream solar wind drivers and magnetic indices. In addition, the study in this chapter investigates the impact of solar cycle variability on the impact of the drivers on the occurrence of backscatter seen during the four seasons in four different sectors of magnetic local time of both ionospheric scatter and ground scatter. The goal of this chapter is to identify which of the parameters, seasonal and local time for which such a parameterization can be used as a predictive tool for now cast and forecast purposes of the occurrence of ionospheric scatter.

6.2 Data

For this study of the effects of upstream solar wind drivers and magnetic activity, the percentage occurrence for the total field of view for both Hankasalmi and Pykkvibaer radars from January 1996 to January 2016 have again been used. The backscatter data were characterized as ionospheric backscatter using the standard criteria for SuperDARN data.

Also, in this study, upstream solar wind data from the 1 minute high-resolution OMNI database were employed as well as a number of magnetic indices. In this study, the variations of ionospheric scatter with five parameters are analysed and presented in this chapter. The five parameters are the solar wind dynamic pressure, two components of the interplanetary magnetic field in the geocentric solar magnetic (GSM) coordinates (IMF Bz and IMF By), and the two magnetic indices, AE, and AU.

Ionospheric scatter data are sorted according to each of the parameters mentioned above. In the selection of the data, data for 61 days centred on the equinoxes and solstices have been identified to represent each of the four seasons, Spring, Summer Solstice, Autumn and Winter Solstice. In addition, the data were sorted into four Magnetic Local Time (MLT) sectors. The sorting of the data into MLT sectors was done using equation (3.4) discussed in chapter three section 3.6.3 of this thesis. The four MLT sectors are dawn (03 - 09 MLT), noon (09 - 15 MLT), dusk (15 - 21 MLT) and midnight (21 - 03 MLT).

In order to investigate the effect of the solar wind drivers and magnetic indices, it is also important to take into account the fact that there is both a solar cycle variation and a seasonal variation in the percentage occurrence of ionospheric backscatter. This is illustrated perfectly by a comparison of Figure 6.1a and Figure 6.1b. In the figure, there are four panels representing each of the four MLT sectors, with dawn on the top left, noon at the top right, dusk at the bottom left and the midnight at the bottom right. In each of the panels, the percentage occurrence of ionospheric scatter is presented as a function of Bz (x axis) in bins of 1 nT centred on the integer value of nT and year (y axis). Figure 6.1a presents data for winter and Figure 6.1b presents data for summer.

In Figure 6.1a we clearly see the solar cycle variations, with more scatter during sunspot maximum and less scatter during sunspot minimum. This is particularly clear for the dusk and midnight MLT sectors. Using the same colour scale for summer (Figure 6.1b), however, we see that although the seasonal variation is obvious, i.e., much less scatter in summer, any solar cycle variation is obscured. Furthermore, it is difficult for both winter and summer to determine how the occurrence of scatter varies as a function of Bz.

Hankasalmi Ionospheric scatter against Bz(GSM) (Winter Solstice)

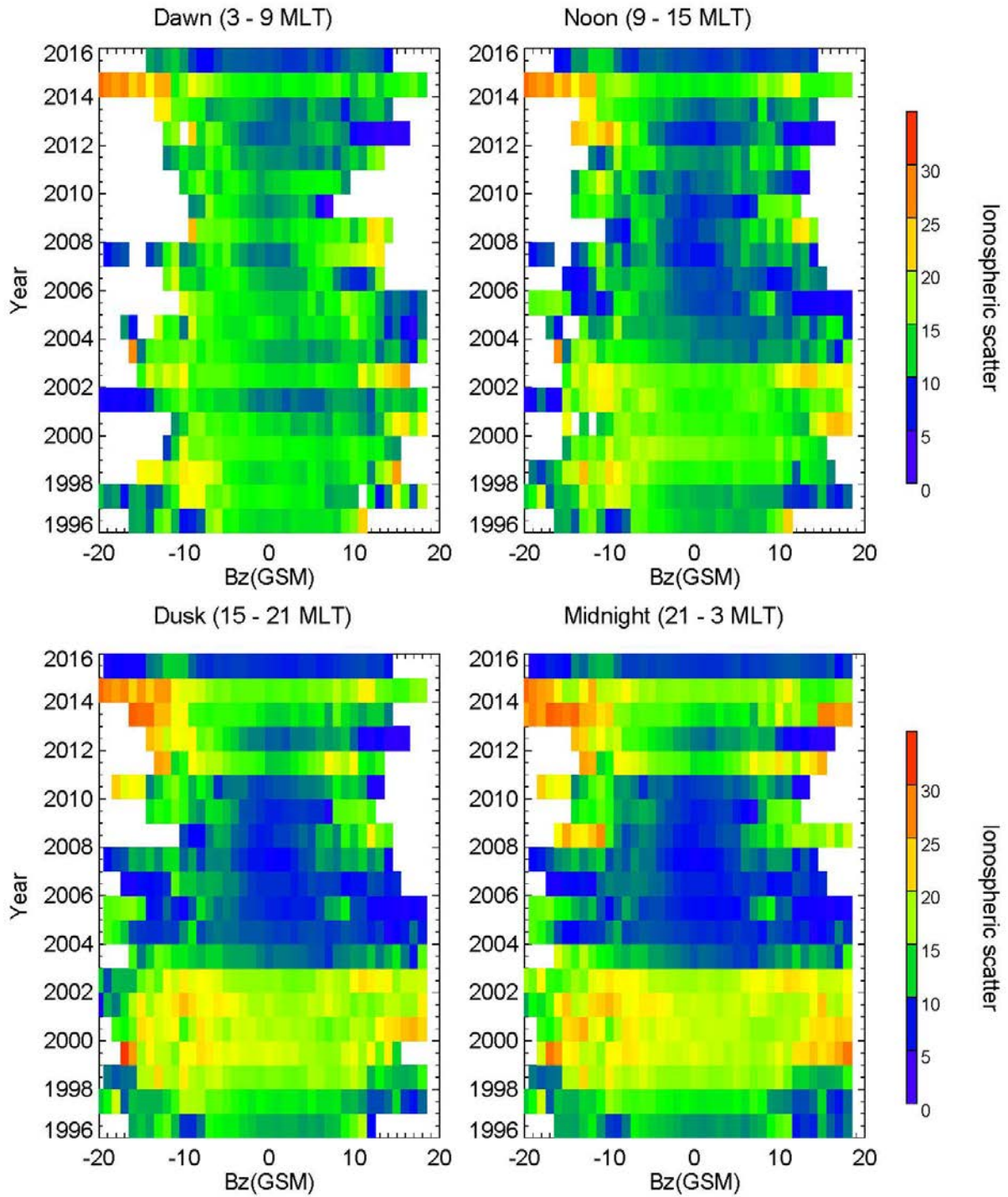


Figure 6.1a. Not-normalised percentage occurrence of ionospheric scatter as a function of Bz (nT) from 1996 to 2015 sorted by MLT sectors for Winter season showing solar cycle variation. The top left panel shows the dawn (03-09 MLT) sector, the right upper panel shows the noon (09-15 MLT) sector, the left lower panel shows the dusk (15-21 MLT) and the right lower panel shows the midnight (21-03 MLT) sector.

Hankasalmi Ionospheric scatter against Bz(GSM) (Summer Solstice)

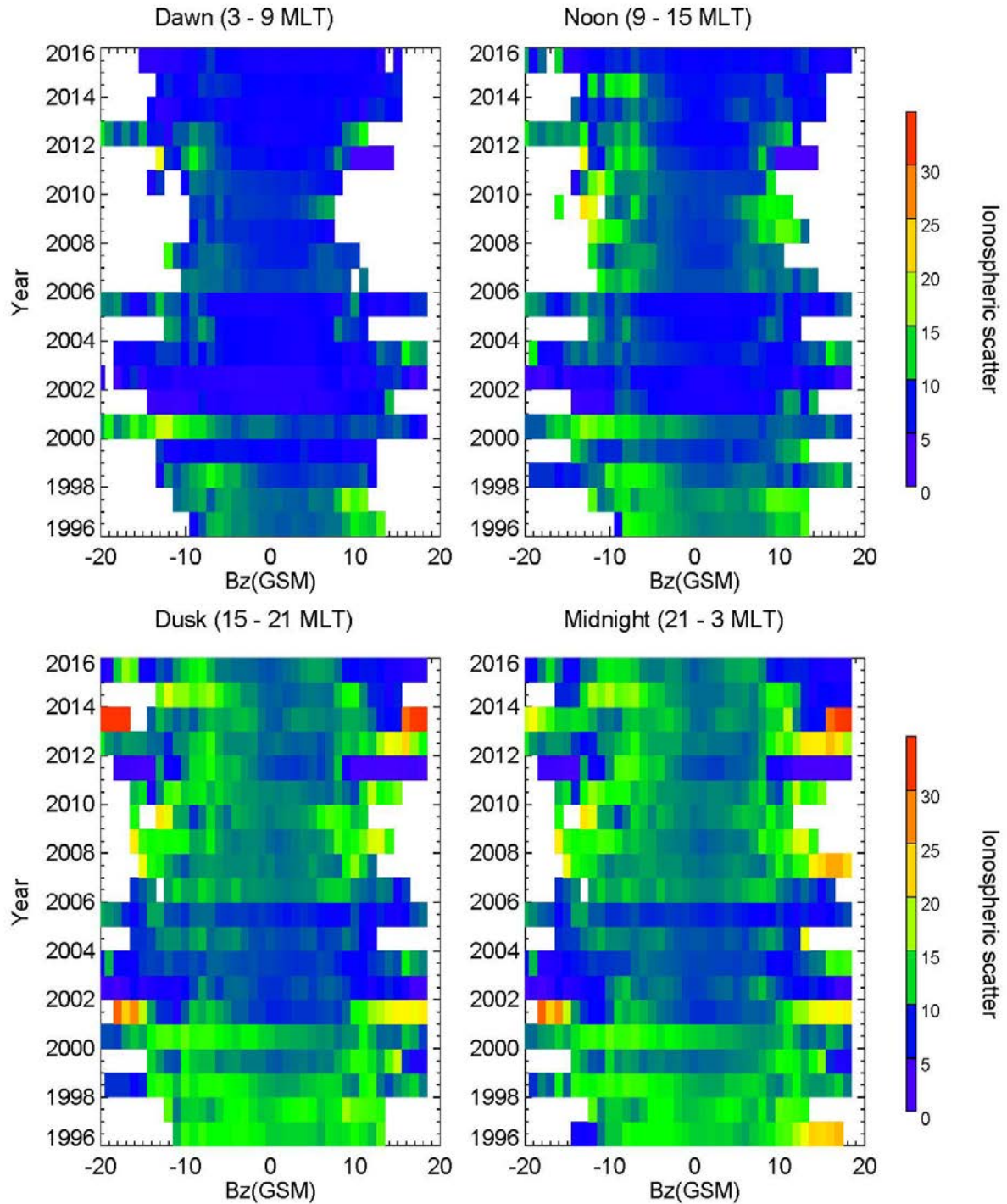


Figure 6.1b. Not-normalised percentage occurrence of ionospheric scatter as a function of Bz (nT) from 1996 to 2015 sorted by MLT sectors for summer season. The top left panel shows the dawn (03-09 MLT) sector, the right upper panel shows the noon (09-15 MLT) sector, the left lower panel shows the dusk (15-21 MLT) and the right lower panel shows the midnight (21-03 MLT) sector.

To overcome these difficulties we take a different approach and normalise the percentage occurrence for each year to that at a specific value of the parameter. The normalization, reducing the measurement, is carried out by transforming the data vector into a new vector such that the length is equal to unity, and the process therefore reduces the percentage occurrence to a standard scale. For B_z , we choose that value of normalization to be $B_z = -0.5$ to 0.5 nT.

The subsequent plots are shown in Figure 6.2a for winter and 6.2b for summer. The format of the plot is as before, simply the data plotted are the normalised percentage occurrence of ionospheric scatter as a function of B_z and year. The key difference now, however is that we see the change for each year in percentage occurrence as a function of B_z . Interestingly for winter, the largest effect appears to be for the period 2003-2013 encompassing the declining phase of solar cycle 23, the sunspot minimum between cycle 23 and 24 and the ascending phase of cycle 24. This effect is predominantly in the dusk and midnight sector. For summer, however, this is not as clear (Figure 6.2b). Now there is a more consistent variation of normalised scatter occurrence where for higher magnitudes of negative B_z , proportionally more scatter is observed. It is also the case for both winter and summer that, in general, for large values of positive B_z (> 8 nT) more scatter is observed.

Having demonstrated the ability of this approach, we now move to a detailed discussion of the effect of a number of solar wind parameters and magnetic activity on the occurrence of ionospheric scatter for Hankasalmi and Pykkvibaer.

6.3 Occurrence of Ionospheric backscatter as a function of upstream solar wind drivers

The upstream drivers presented in this chapter are the solar wind dynamic pressure, the IMF B_y , the IMF B_z components and the clock angle. The percentage occurrences of ionospheric scatter as a function of the four parameters are presented. Each figure presents the corresponding MLT sectors for each season and the figure is organized according to the MLT sectors as follows; the left upper panel presents the dawn (03-09 MLT) sector, the right upper panel presents the noon (09-15 MLT) sector, the left lower panel presents the dusk (15-21 MLT) and the right lower panel presents the midnight (21-03 MLT).

Hankasalmi Ionospheric scatter against Bz(GSM) (Winter Solstice)

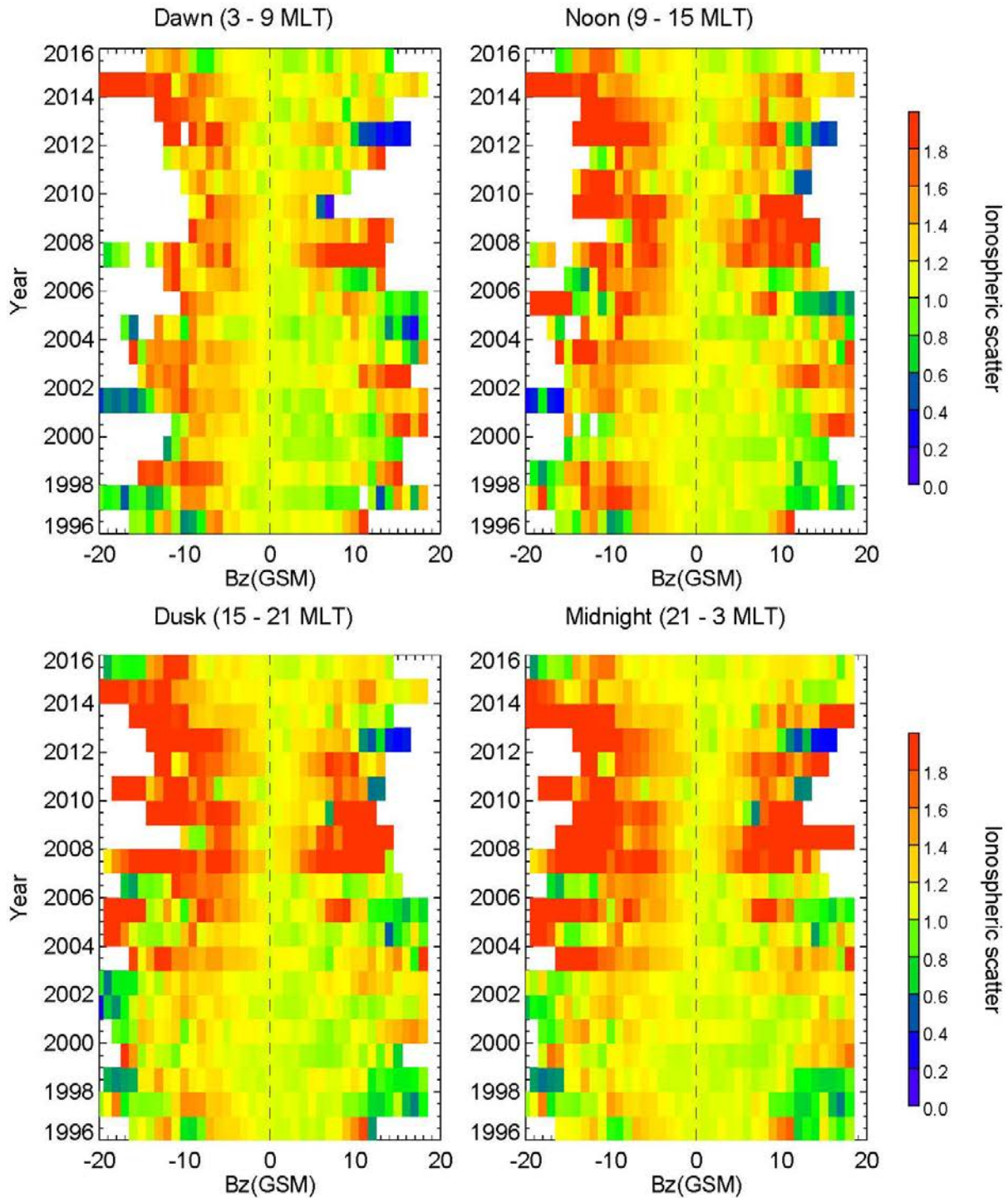


Figure 6.2a. Normalised percentage occurrence of ionospheric scatter as a function of Bz (nT) from 1996 to 2015 sorted by MLT sectors for winter season. The dashed black line indicates the point of normalisation. The top left panel shows the dawn (03-09 MLT) sector, the right upper panel shows the noon (09-15 MLT) sector, the left lower panel shows the dusk (15-21 MLT) and the right lower panel shows the midnight (21-03 MLT) sector.

Hankasalmi Ionospheric scatter against Bz(GSM) (Summer Solstice)

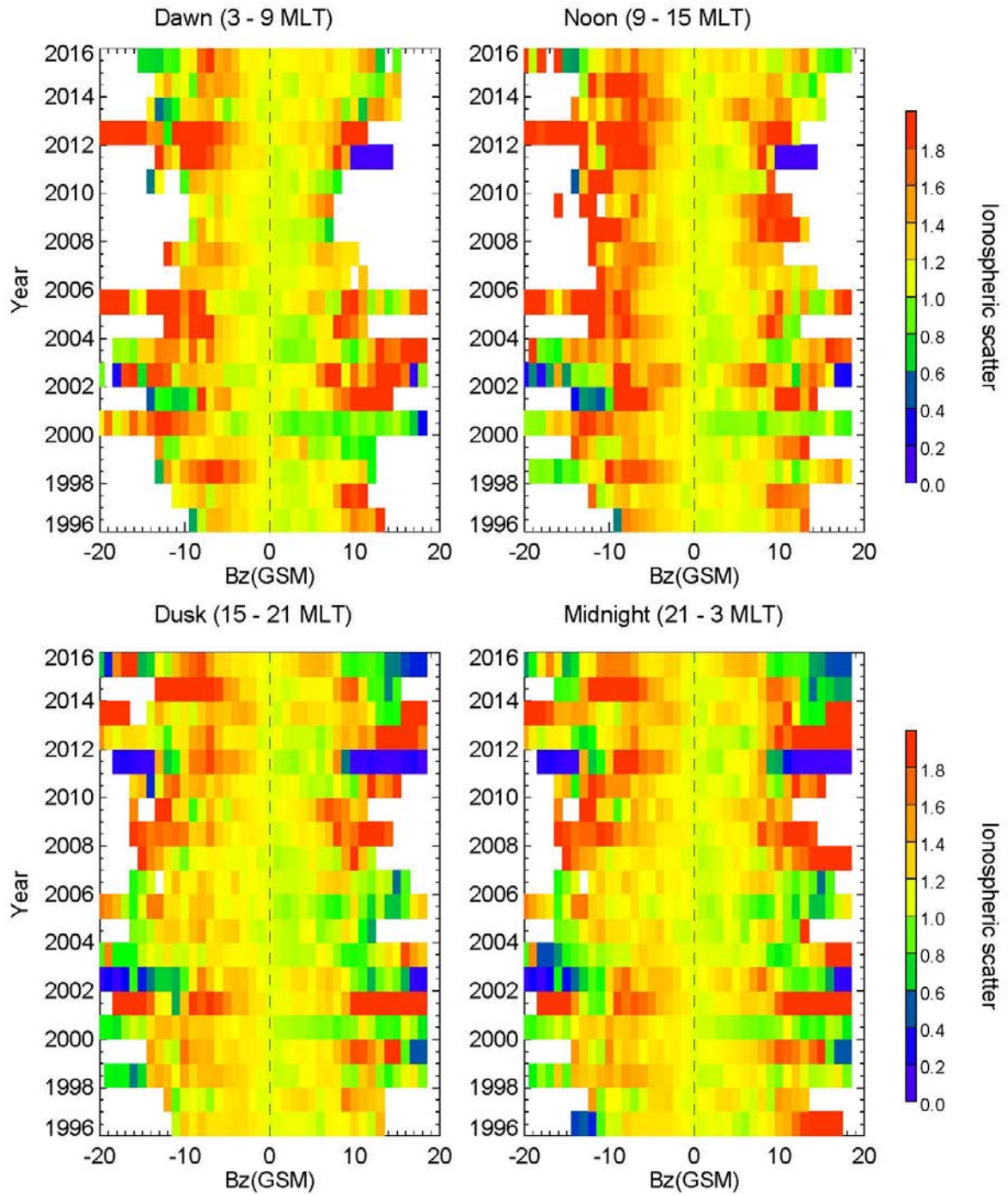


Figure 6.2b. Normalised percentage occurrence of ionospheric scatter as a function of Bz (nT) from 1996 to 2015 sorted by MLT sectors for summer season. The dashed black line indicates the point of normalisation. The top left panel shows the dawn (03-09 MLT) sector, the right upper panel shows the noon (09-15 MLT) sector, the left lower panel shows the dusk (15-21 MLT) and the right lower panel shows the midnight (21-03 MLT) sector.

Figure 6.3a, presents the ionospheric scatter data as a function of solar wind dynamic pressure p for each MLT sector for spring, summer (Figure A3.1a), autumn (Figure A3.1b) and winter (Figure A3.1c). During spring, a considerable effect is seen around 2003 – 2013 in the dusk and midnight sectors. It is noticed that for low values of solar wind dynamic pressure around 0 – 2 nPa, the bins are mostly green, hence, the occurrence of ionospheric scatter around is lower than at other values. For higher values of pressure (> 10 nPa), more scatter is observed while the other two MLT sectors does not show any clear effects. It is noticed that this is noticed for all seasons and MLTs, the dawn and the noon sector is seen to be mostly affected.

The percentage occurrence of ionospheric scatter as a function of B_z for each MLT sectors for Hankasalmi radar are shown in Figure 6.2a (winter), Figure 6.2b (summer) and Figure 6.4 (spring) Figure A3.2 for autumn, again starting with spring. The figure shows that there is a clear increase of greater than 20% more scatter than the value of 0 nT for all MLT sectors. The value where this change occurs is of order -4 nT, although it is seasonal and MLT dependant with dawn, noon and to a lesser extent dusk quite clear but less so again in the midnight sector. This does seem consistent for all seasons but in winter, the midnight sector does demonstrate a clear change at 2 - 4 nT.

A well-defined cut off for B_z negative throughout the solar cycle on the nightside (dayside) around 4 nT is noticed. The distribution pattern in the spring season is much the same as the distribution pattern seen in summer. However, in autumn we see a much higher value of scatter at B_z positive at nightside which might be due to selection effects. This feature disappears during solar maximum. For B_z negative, the distribution during winter season looks different from other three seasons investigated. The higher value of scatter than normal seems to disappear in winter at nightside during solar maximum which might be due to more scatter in general. Also, the solar minimum effect is seen during winter.

For B_z positive, it is noticed that there are regions where enhanced scatter is seen and regions of reduced scatter which might be due to sparse data when compared with the value at 0 nT, in some of the bins. It is noticed that during spring and autumn there is clear evidence in dawn and noon sector for enhanced scatter for B_z . During, there is no distinct pattern in the four sectors. However winter shows the clearest demonstration of occurrence at sunspot minimum in all MLT sectors.

Hankasalmi Ionospheric scatter against Pressure (Spring)

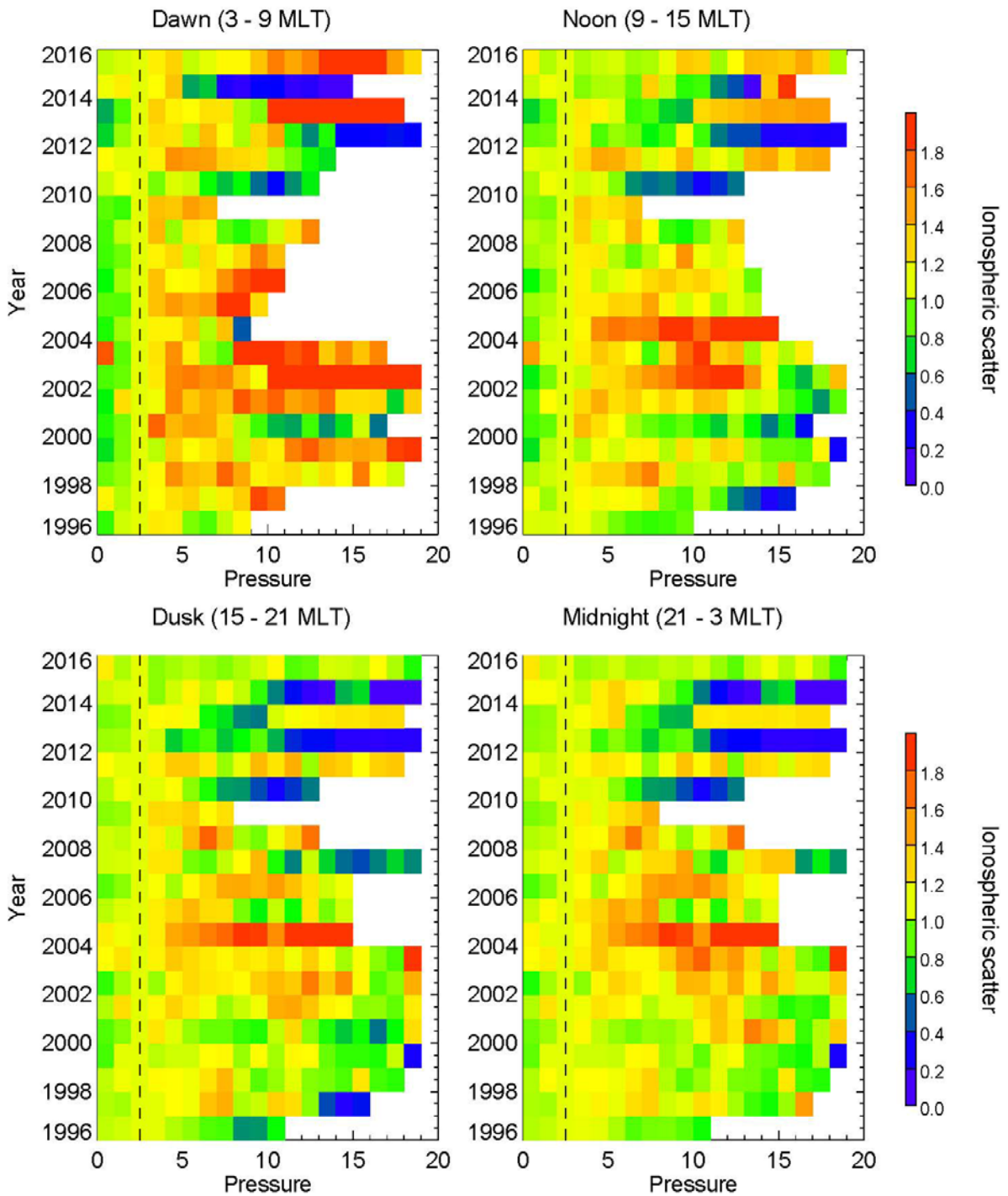


Figure 6.3. Normalised percentage occurrence of ionospheric scatter as a function of Pressure from 1996 to 2015 sorted by MLT sectors for Spring (Equinox) season. The dashed black line indicates the point of normalisation. The top left panel shows the dawn (03-09 MLT) sector, the right upper panel shows the noon (09-15 MLT) sector, the left lower panel shows the dusk (15-21 MLT) and the right lower panel shows the midnight (21-03 MLT) sector.

Hankasalmi Ionospheric scatter against Bz(GSM) (Spring)

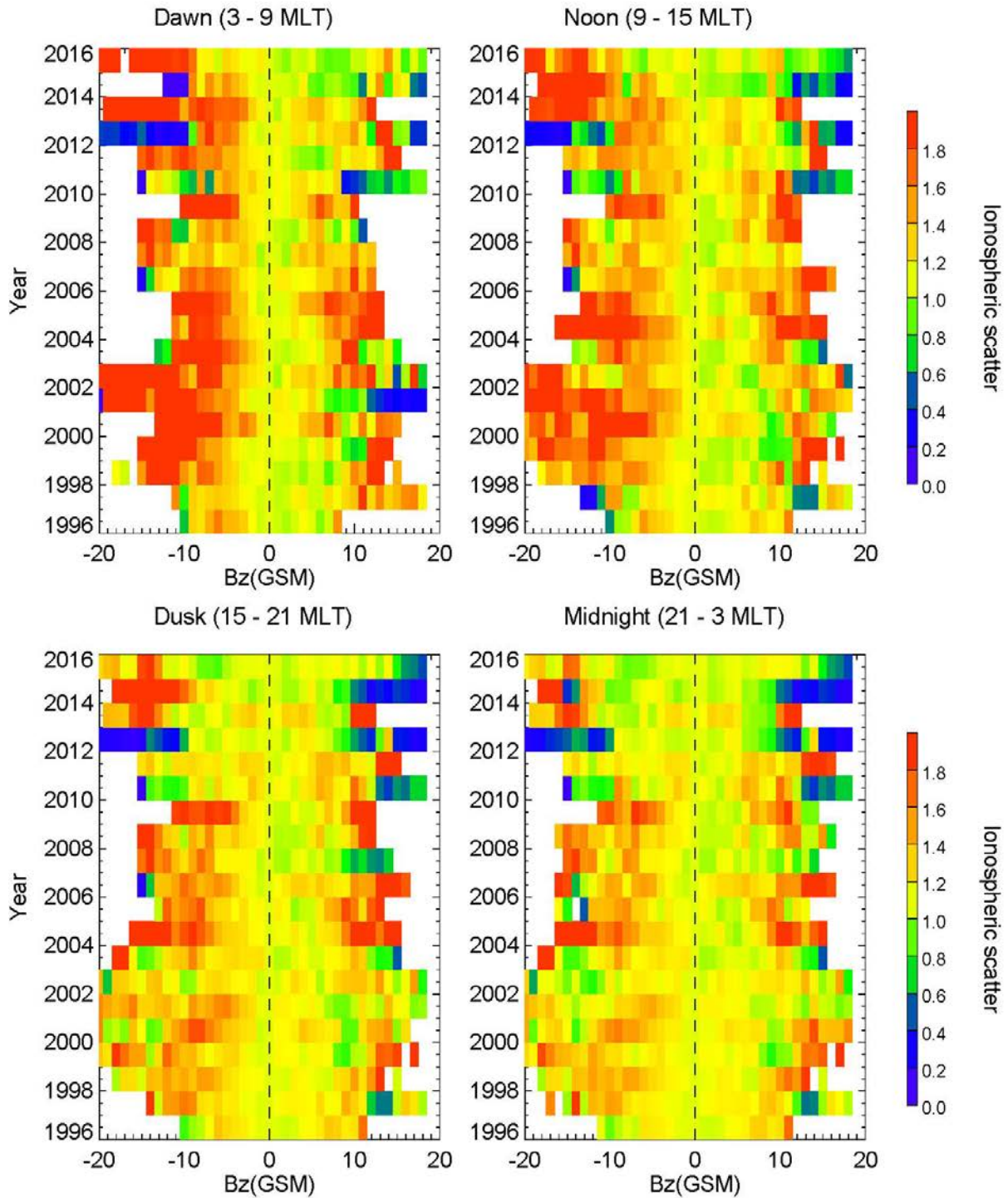


Figure 6.4. Normalised percentage occurrence of ionospheric scatter as a function of Bz (nT) from 1996 to 2015 sorted by MLT sectors for spring season. The dashed black line indicates the point of normalisation. The top left panel shows the dawn (03-09 MLT) sector, the right upper panel shows the noon (09-15 MLT) sector, the left lower panel shows the dusk (15-21 MLT) and the right lower panel shows the midnight (21-03 MLT) sector.

The normalised ionospheric scatter data as a function of B_y for each MLT sector for Hankasalmi radar are shown in Figure 6.5 (spring), Figure A3.3a (summer), Figure A3.3b (autumn), Figure A3.3a (winter). The figure illustrates that generally for larger positive and negative values of B_y , it is noticed that higher percentage scatter is seen than at 0 nT. It is noticed that this feature is not consistent though at all MLT and seasons. Also, it is noticed that there is no evidence of an asymmetry due to B_y in the occurrence percentage of ionospheric scatter. However during winter, it is noticed that there is large changes in the percentage occurrence during sunspot minimum and the ascending phase of the solar cycle.

Hankasalmi Ionospheric scatter against By(GSM) (Spring)

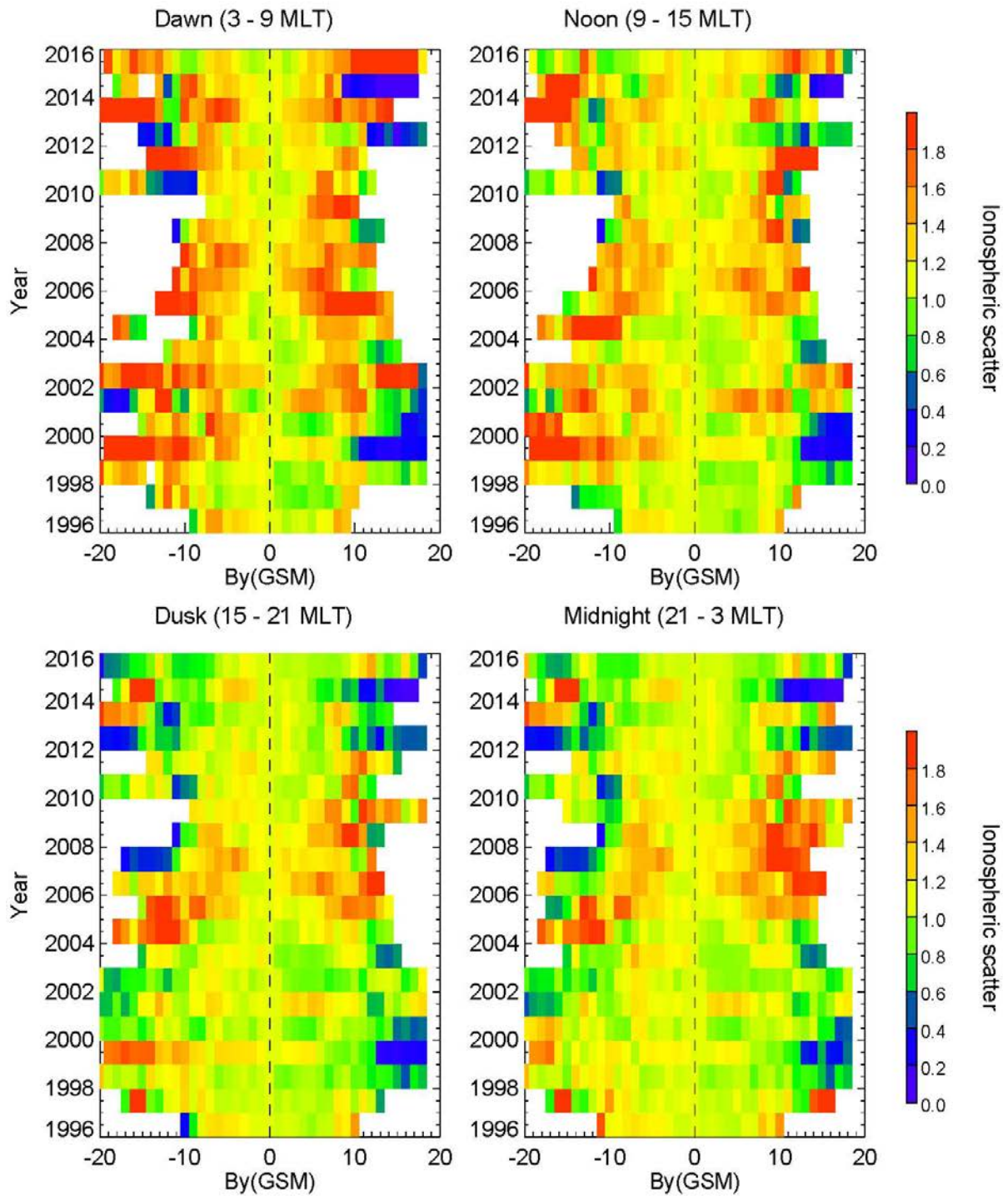


Figure 6.5. Normalised percentage occurrence of ionospheric scatter as a function of By (nT) from 1996 to 2015 sorted by MLT sectors for spring season. The dashed black line indicates the point of normalisation. The top left panel shows the dawn (03-09 MLT) sector, the right upper panel shows the noon (09-15 MLT) sector, the left lower panel shows the dusk (15-21 MLT) and the right lower panel shows the midnight (21-03 MLT) sector.

Figure 6.6a, presents the ionospheric scatter data as a function of pressure for spring sector and Figure A3.4a (summer), Figure A3.4b (autumn), Figure A3.4a (winter) for the other MLT sectors at Pykkviaber. The distribution pattern seen appears to be similar to the pattern seen in Hankasalmi data. During spring, a considerable effect is seen around 2003 – 2013 in the dusk and midnight sectors. It is noticed that the percentage occurrence of ionospheric scatter is almost always less than value at 3 nPa the bins are mostly green, hence, the occurrence of ionospheric scatter around is lower than at other values. For higher values of pressure (> 10 nPa), more scatter is observed while the other two MLT sectors does not show any clear effects. It is noticed that this is noticed for all seasons and MLTs, the dawn and the noon sector is seen to be mostly affected.

The normalised ionospheric scatter data as a function of Bz for Pykkvibaer radar for spring MLT sector is shown in Figure 6.7 and for summer, autumn and winter are shown in Figure A3.5a (summer), Figure A3.5b (autumn), Figure A3.5a (winter). The scatter distribution illustrates that during spring there seems to be a clear change of about 20% occurrence of scatter than the normal at Bz negative while no clear effect at Bz positive. There is a well-defined cut off for Bz negative throughout the solar cycle on the nightside (dayside) around 4 nT for spring. The distribution pattern in summer and autumn seasons appears to be similar to the pattern seen during spring. However, it is noticed that the distribution during the winter season looks different from the other three seasons investigated. The features (cut-offs) above disappears during solar maximum during winter which might be due to more scatter in general on the nightside. For the Bz positive, it is noticed that there are regions where enhanced scatter is seen and regions of reduced scatter which might be due to limited amount of data, sparse data. Similar to the observation of occurrence of scatter as a function of Bz in Hankasalmi, it is noticed that more scatter is observed at higher values of negative Bz.

The normalised ionospheric scatter data as a function of By for spring MLT sector is shown in Figure 6.8 and for the other three MLT sectors for Pykkvibaer radar are shown in Figure A3.6a (summer), Figure A3.6b (autumn), Figure A3.6a (winter). The distribution of ionospheric scatter illustrates that there seems to be no clear solar cycle variation during spring in the entire local time sectors for By negative and By positive. This pattern seems to be seen in summer and autumn however, during winter, evidence of solar cycle variation is seen at both By positive and By negative flanks.

Pykkvibaer Ionospheric scatter against Pressure (Spring)

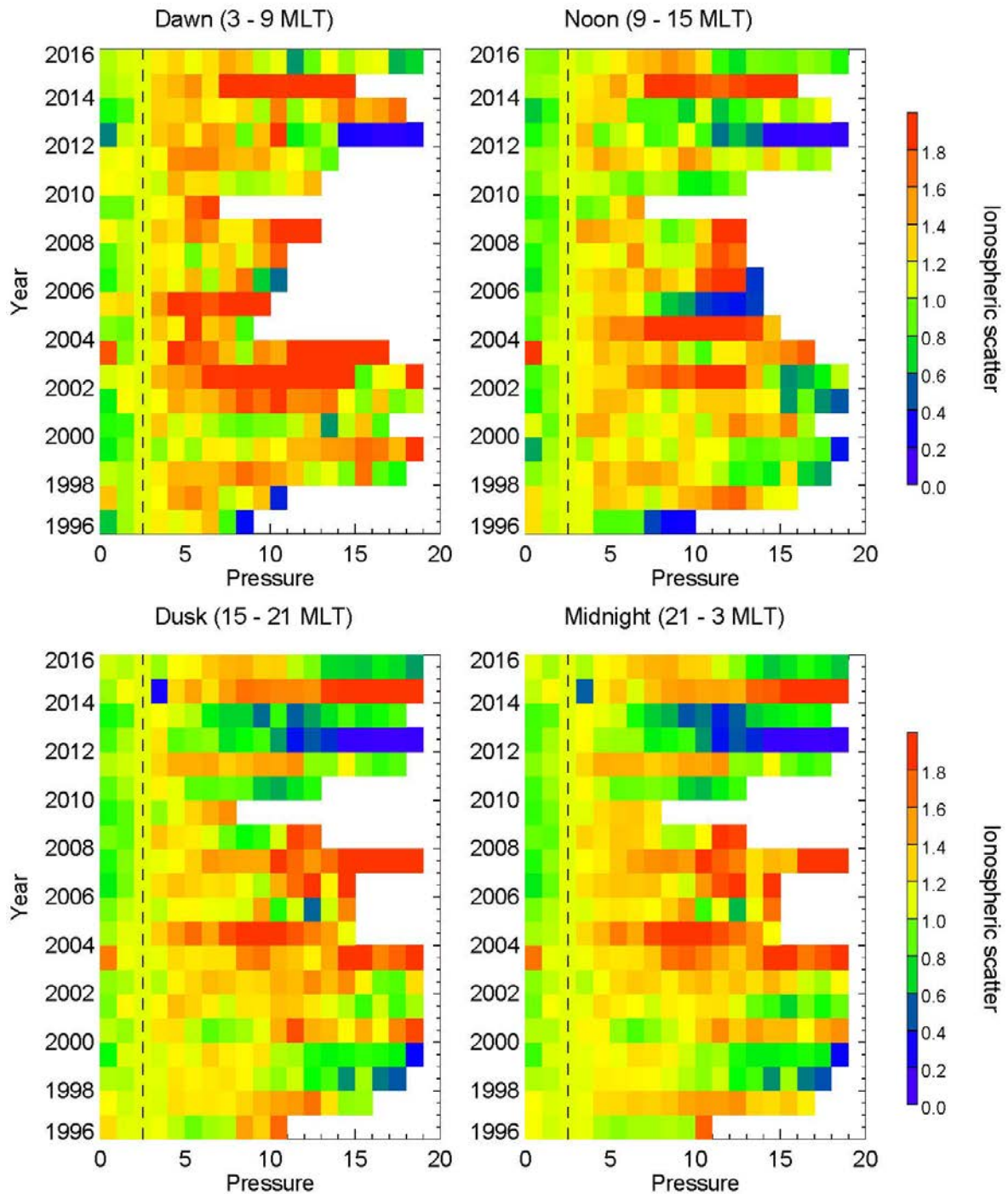


Figure 6.6. Normalised percentage occurrence of ionospheric scatter as a function of Pressure (nT) from 1996 to 2015 sorted by MLT sectors for spring season. The dashed black line indicates the point of normalisation. The top left panel shows the dawn (03-09 MLT) sector, the right upper panel shows the noon (09-15 MLT) sector, the left lower panel shows the dusk (15-21 MLT) and the right lower panel shows the midnight (21-03 MLT) sector.

Pykkvibaer Ionospheric scatter against Bz(GSM) (Spring)

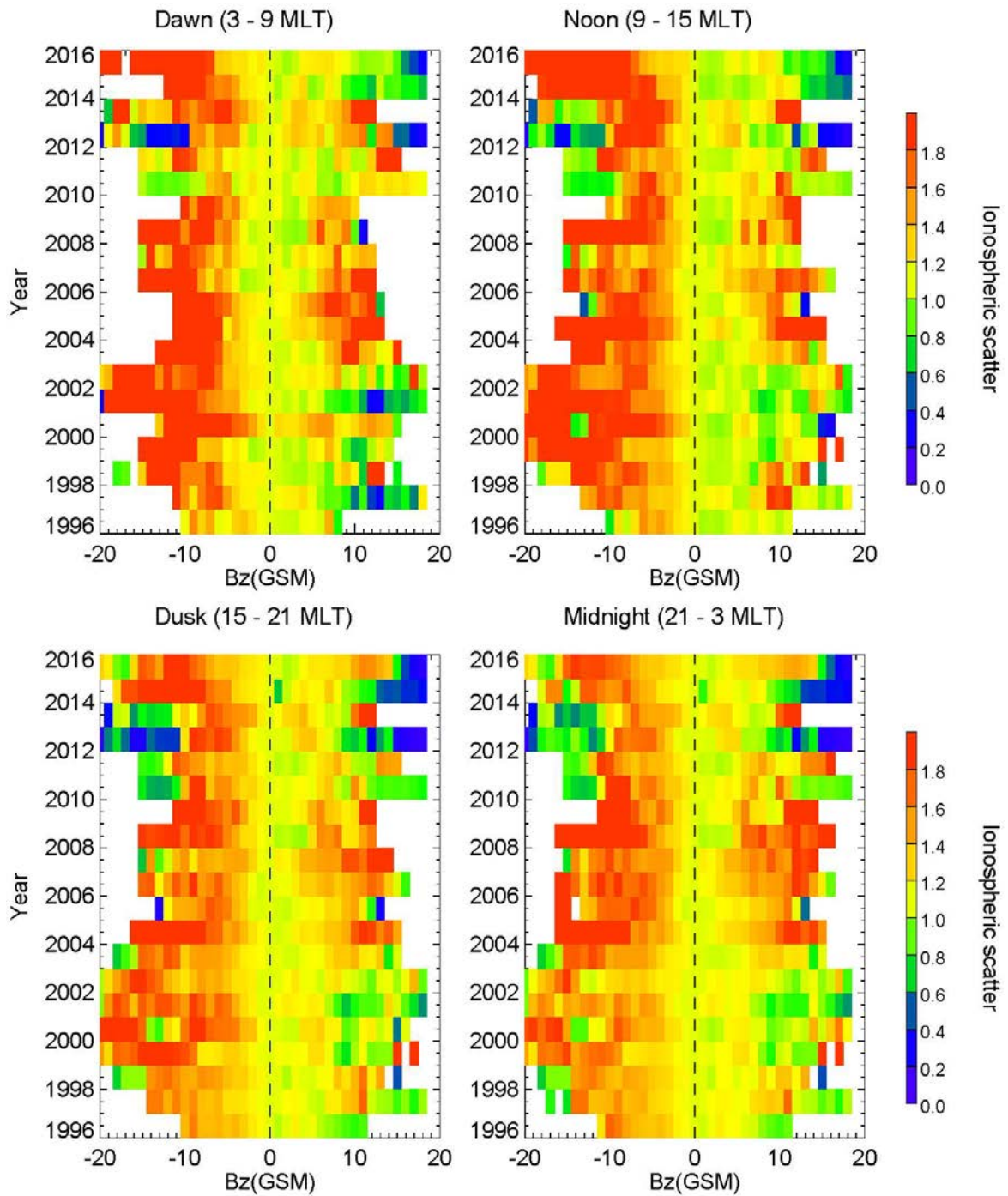


Figure 6.7. Normalised percentage occurrence of ionospheric scatter as a function of Bz from 1996 to 2015 sorted by MLT sectors for Spring (Equinox) season. The dashed black line indicates the point of normalisation. The top left panel shows the dawn (03-09 MLT) sector, the right upper panel shows the noon (09-15 MLT) sector, the left lower panel shows the dusk (15-21 MLT) and the right lower panel shows the midnight (21-03 MLT) sector.

Pykkvibaer Ionospheric scatter against By(GSM) (Spring)

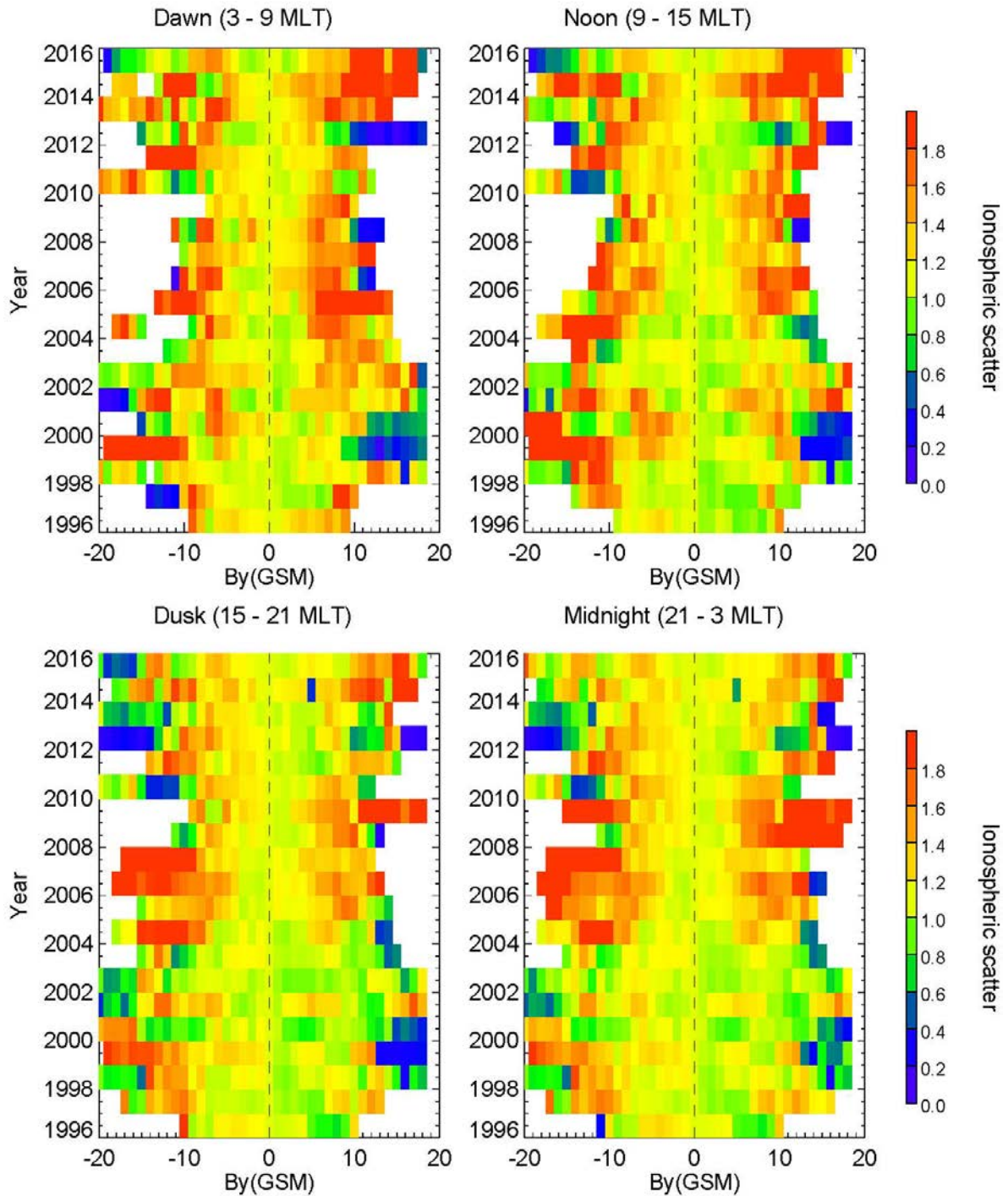


Figure 6.8. Normalised percentage occurrence of ionospheric scatter as a function of By from 1996 to 2015 sorted by MLT sectors for Spring (Equinox) season. The dashed black line indicates the point of normalisation. The top left panel shows the dawn (03-09 MLT) sector, the right upper panel shows the noon (09-15 MLT) sector, the left lower panel shows the dusk (15-21 MLT) and the right lower panel shows the midnight (21-03 MLT) sector.

6.4 Summary

- i. The normalised statistics on the distribution of ionospheric scatter data as a function of solar wind parameters for Hankasalmi and Pykkvinbaer radars for the four MLT sectors has been carried out
- ii. Generally there is more scatter in all seasons and MLT sectors which is particularly clear in summer
- iii. All seems to have a bigger impact in dawn and noon sector and at sunspot minimum (dusk and midnight)

6.5 Occurrence of Ionospheric backscatter as a function of magnetic indices

The normalised ionospheric scatter data as a function of AU for spring MLT sector is shown in Figure 6.9 and for the other three MLT sectors for Hankasalmi radar are shown in Figure A3.7a (summer), Figure A3.7b (autumn), Figure A3.7a (winter). The scatter distribution illustrates that there is more scatter as it becomes more disturbed giving the ionosphere a structured ionosphere. There is no clear evidence for MLT and seasonal impact in the percentage occurrence of ionospheric scatter.

Hankasalmi Ionospheric scatter against AU (Spring)

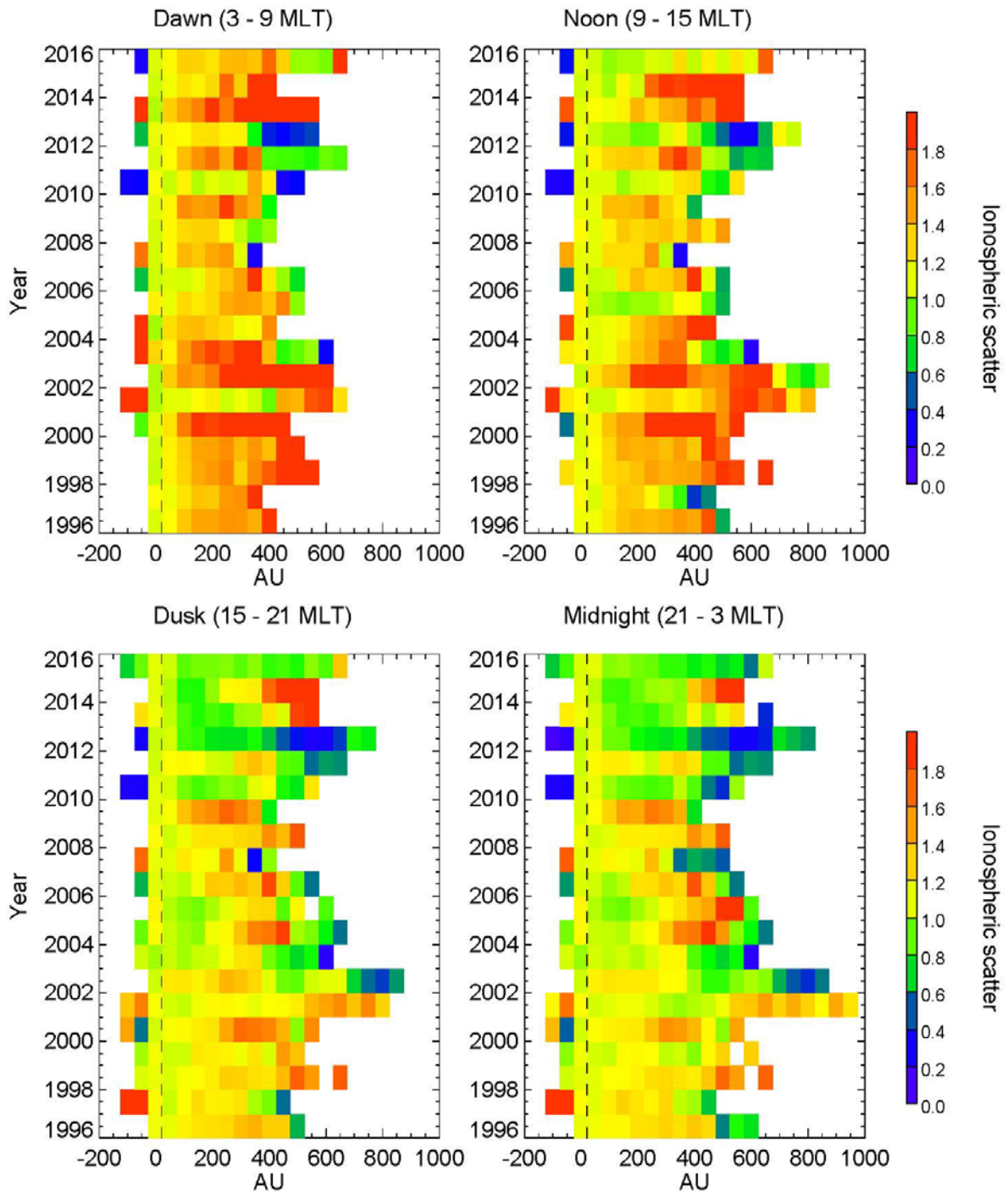


Figure 6.9. Normalised percentage occurrence of ionospheric scatter as a function of AU from 1996 to 2015 sorted by MLT sectors for Spring (Equinox) season. The dashed black line indicates the point of normalisation. The top left panel shows the dawn (03-09 MLT) sector, the right upper panel shows the noon (09-15 MLT) sector, the left lower panel shows the dusk (15-21 MLT) and the right lower panel shows the midnight (21-03 MLT) sector.

Figure 6.10 shows the normalised ionospheric scatter as a function of AE for spring MLT sector is shown in Figure 6.10 and for the other three MLT sectors for Hankasalmi radar are shown in Figure A3.8a (summer), Figure A3.8b (autumn), Figure A3.8a (winter). The distribution pattern shown in Figure 6.11 illustrates that during spring there is no clear solar cycle variation in the entire MLT sectors. This pattern is also seen in summer. However, in the autumn we see a much higher value of normalised occurrence AE in the nightside, it appears we have more scatter. The distribution during the winter season looks different from other three seasons investigated. During winter season in the dusk sector and the midnight sector it appears the distribution levels out during solar maximum of cycle 23 and during solar minimum, higher occurrence of ionospheric scatter is seen an indication of solar cycle variation at the two local time sectors.

Figure 6.11 shows the normalised percentage occurrence of ionospheric scatter data as a function of AU for spring MLT sector and for the other three MLT sectors for are shown in Figure A3.9a (summer), Figure A3.9b (autumn), Figure A3.9a (winter) for Pykkvibaer radar. It is seen from the figure that during spring the distributions shows no clear solar cycle effect. The scatter distribution pattern seen during spring is similar to the pattern seen during, summer and autumn. However, scatter distribution shows that there is a clear solar cycle variation during winter season in the dusk sector and the midnight sectors.

Hankasalmi Ionospheric scatter against AE (Spring)

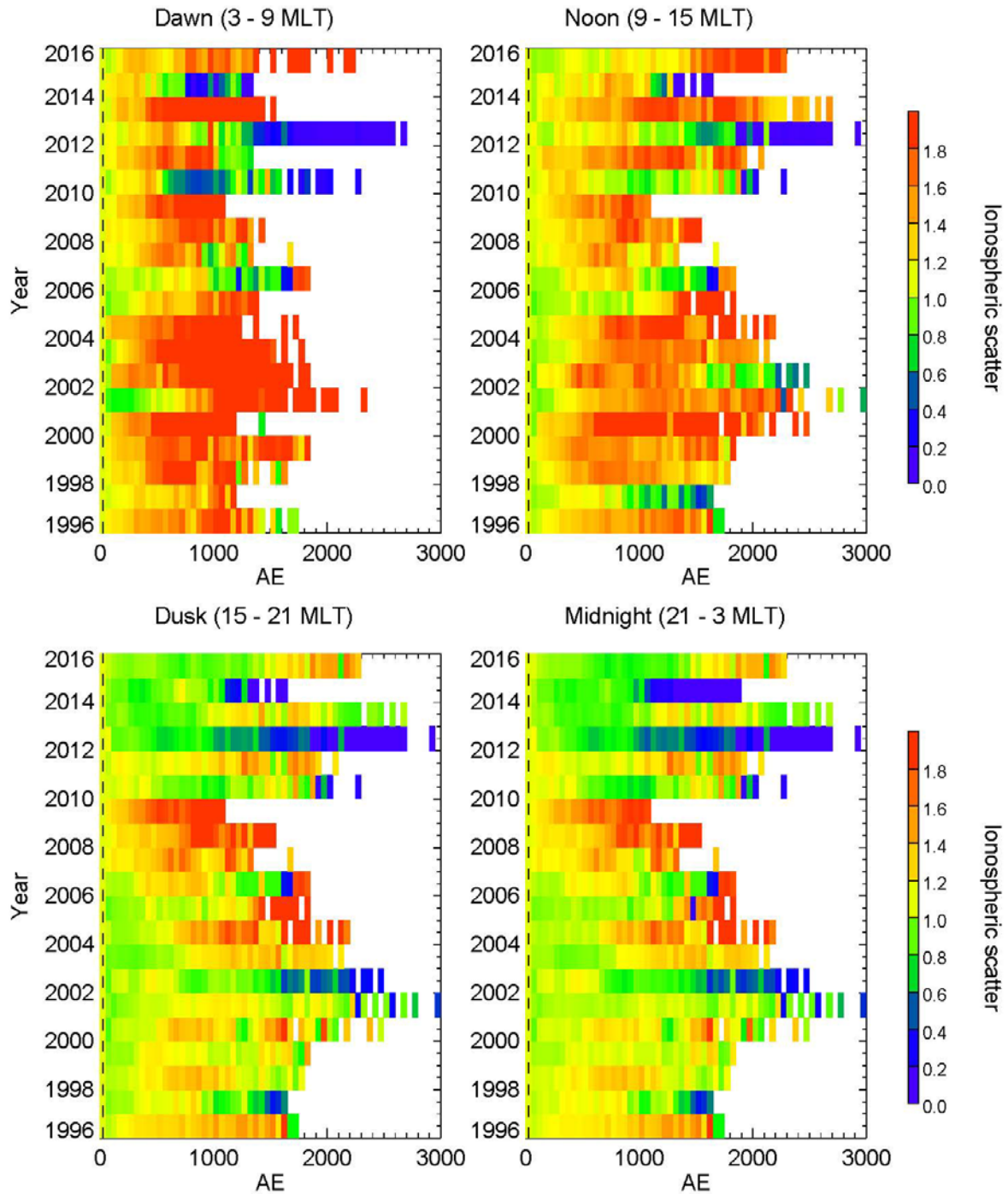


Figure 6.10. Normalised percentage occurrence of ionospheric scatter as a function of AE from 1996 to 2015 sorted by MLT sectors for Spring (Equinox) season. The dashed black line indicates the point of normalisation. The top left panel shows the dawn (03-09 MLT) sector, the right upper panel shows the noon (09-15 MLT) sector, the left lower panel shows the dusk (15-21 MLT) and the right lower panel shows the midnight (21-03 MLT) sector.

Pykkvibaer Ionospheric scatter against AU (Spring)

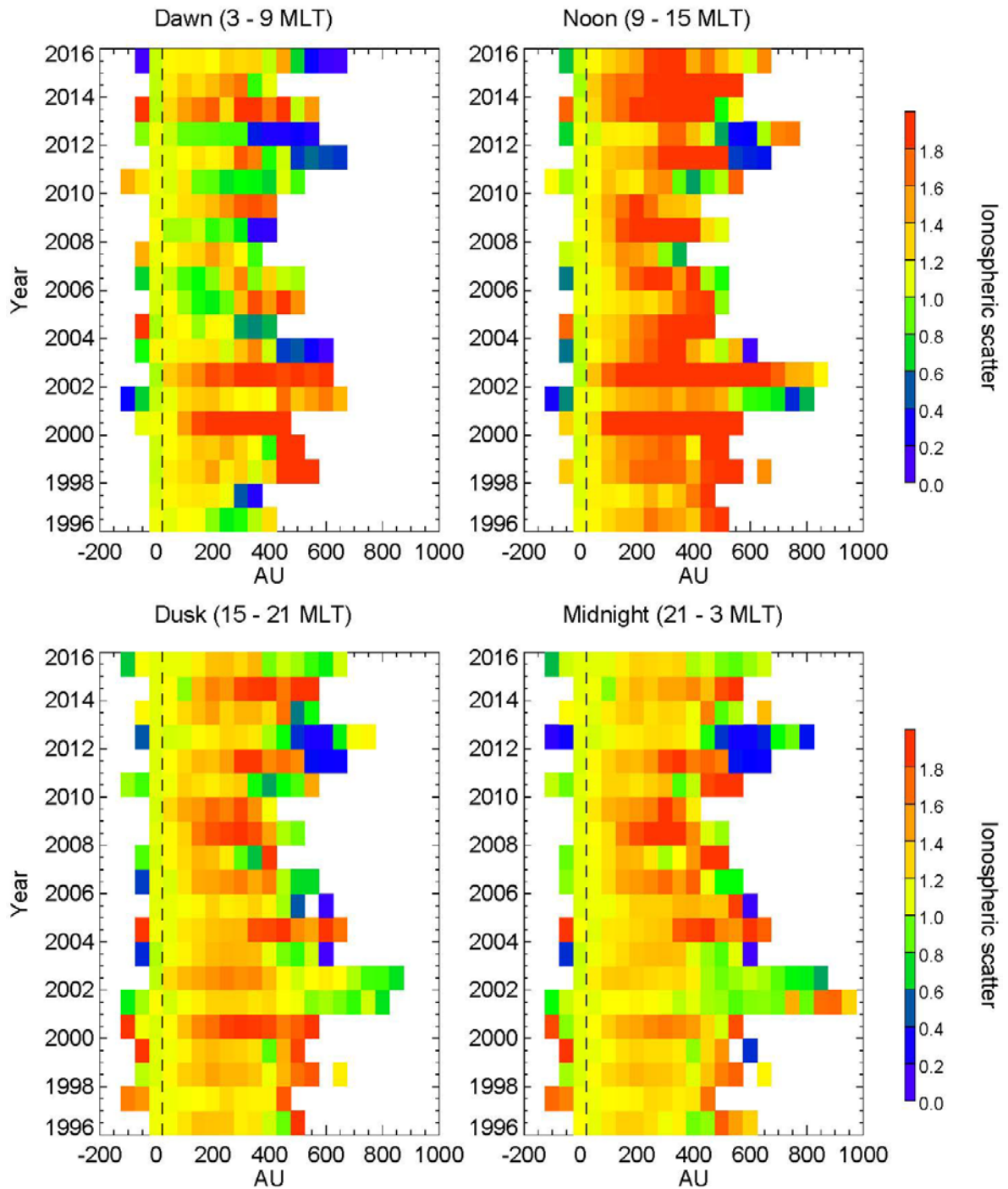


Figure 6.11. Normalised percentage occurrence of ionospheric scatter as a function of AU from 1996 to 2015 sorted by MLT sectors for Spring (Equinox) season. The dashed black line indicates the point of normalisation. The top left panel shows the dawn (03-09 MLT) sector, the right upper panel shows the noon (09-15 MLT) sector, the left lower panel shows the dusk (15-21 MLT) and the right lower panel shows the midnight (21-03 MLT) sector.

The normalised ionospheric scatter as a function of AE for spring MLT sector is shown in Figure 6.12 and for the other three MLT sectors for are shown in Figure A3.10a (summer), Figure A3.10b (autumn), Figure A3.910c (winter). The distribution pattern shows that during spring there is no clear solar cycle variation in the entire MLT sectors. This pattern is also noticed during summer. However, in autumn it is noticed that a much higher value of normalised occurrence AE is seen at nightside, which appears to be due to the presence of more scatter. The distribution during winter season looks different from other three seasons investigated. During winter season at the dusk sector and the midnight sector it appears the distribution level out during solar maximum of cycle 23 and during solar minimum, higher occurrence of ionospheric scatter is seen an indication of solar cycle variation at the two local time sectors.

Pykkvibaer Ionospheric scatter against AE (Spring)

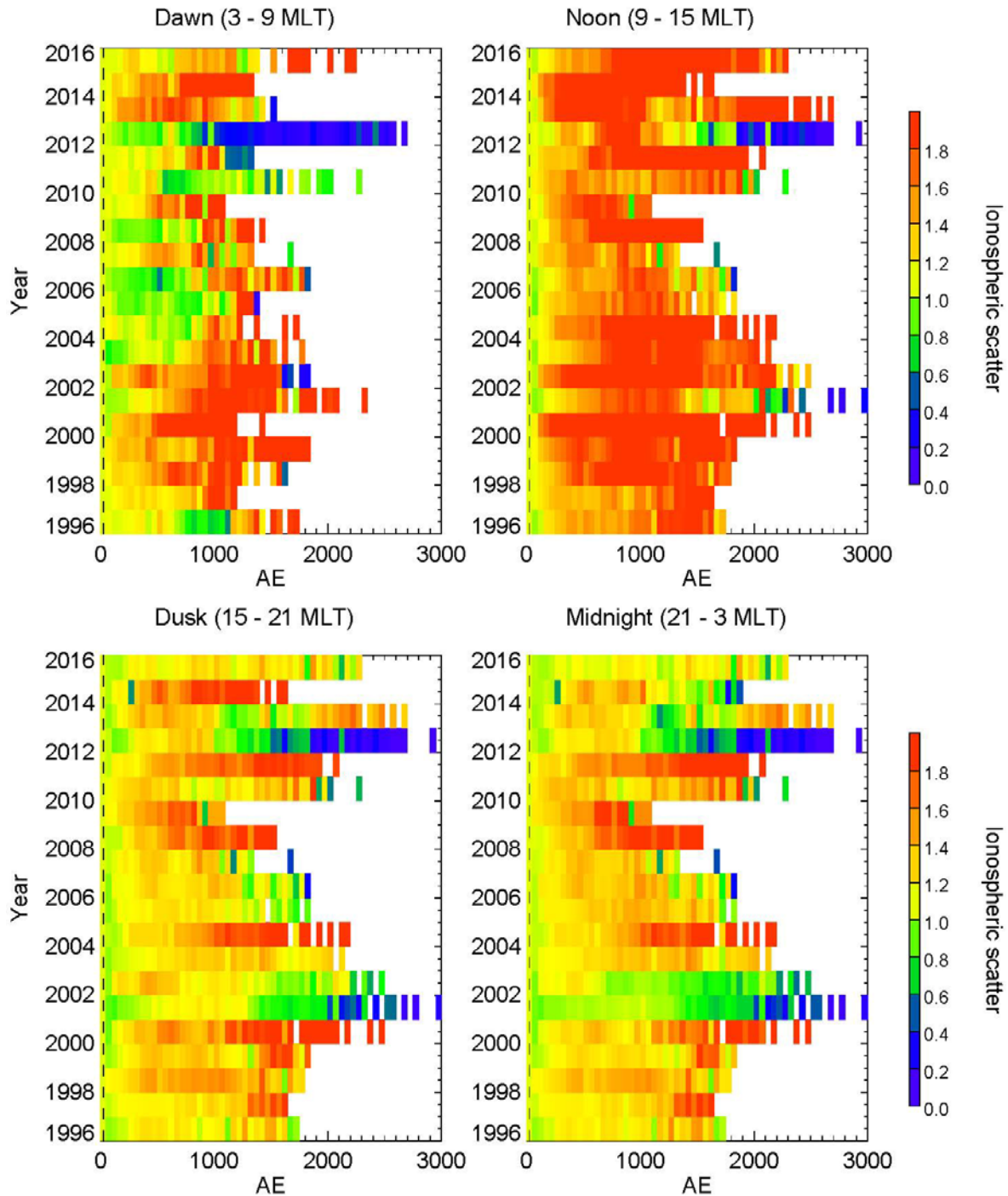


Figure 6.12. Normalised percentage occurrence of ionospheric scatter as a function of AE from 1996 to 2015 sorted by MLT sectors for Spring (Equinox) season. The dashed black line indicates the point of normalisation. The top left panel shows the dawn (03-09 MLT) sector, the right upper panel shows the noon (09-15 MLT) sector, the left lower panel shows the dusk (15-21 MLT) and the right lower panel shows the midnight (21-03 MLT) sector.

6.6 Summary

- i. It is noticed that there is more scatter as the ionosphere becomes more disturbed
- ii. There is no obvious evidence for MLT and seasonal impact

6.7 Discussion

Previous studies that have investigated the effects of solar wind parameters or IMF parameters or effects of magnetic indices on the occurrence rate of ionospheric scatter, have investigated the effects of one or a few parameters with a limited data set spanning few years, or less than a complete solar cycle or have restricted their study to either F region backscatter or E region backscatter. The study presented in this chapter is a statistical analysis to parameterize the occurrence rate of ionospheric backscatter from 1996 to 2015 as a function of the upstream drivers and the downstream drivers. In addition, the study investigated the impact of solar cycles and the impact of the drivers on the occurrence of backscatter seen during the four seasons in each of the four sectors of the magnetic local time of both ionospheric scatter and ground scatter and the relationship between occurrence of ionospheric scatter and clock angle. One of the major goals of this chapter is to identify which of the parameters, the season and the local time that such parameterization can be used as a predictive tool for now cast and forecast purposes.

Ruohoniemi and Greenwald (1997) carried out a 6-year study on scatter occurrence statistics of the Goose Bay SuperDARN radar focusing primarily on F region scatter using a subset of the Goose Bay radar data archive for the 6-year period from 1988 to 1993 which corresponds to the solar cycle maximum of solar cycle 22. One of the key results is that they found that HF backscatter occurrence level was low in summer in both noon and afternoon sectors while the occurrence rates during winter shows a high level in both noon and afternoon sectors. The present study has also shown that the occurrence level during summer is lower in almost all the four MLT sectors than in the winter which is seen in the non-normalised plot of ionospheric scatter as a function of B_z and ionospheric scatter as a function of clock angle. This effect is attributed to suppression of density gradients by intense summer photoionization by Ruohoniemi and Greenwald (1997).

In the work of Ballatore et al. (2000) on the influence of the interplanetary medium on SuperDARN ionospheric scatter occurrence, a two-year data set from 1997 to 1998 from the six northern hemisphere radars operating at the time of their study was used. Ballatore et al.

(2000) demonstrated the dependence of HF scatter occurrence on the Magnetic Local Time (MLT), the magnetic latitude and the local season. In addition, they concluded that the occurrence of scatter is seasonally dependent and generally higher during winter. This result is in agreement with our observation with respect to the occurrence of ionospheric scatter and certain parameters. However, the time range of maximum occurrence of ionospheric scatter observed by Ballatore et al. (2000) during summer and winter is in contrast with most of our observations. They noted that during summer the time is at about 00:00-03:00 MLT while during winter, the time range is in the afternoon sector, from 15:00 to 18:00 MLT. Our result shows that it is at about 15:00 to 21:00 and 21:00 to 03:00 for winter and at about 21:00 to 03:00 in summer. In addition, they also found that the interplanetary parameter which influences the daily modulation of ionospheric scatter occurrence is the interplanetary electric field.

A study of the seasonal variation of midnight F region echo occurrence was carried out by Koustov et al., (2004) using a data set of a half-solar cycle duration and data from the meridional beams of the Hankasalmi, Pykkvibaer, Saskatoon, Kodiak, Halley and Syowa East radars were selected. Koustov et al., (2004) observed enhancements of backscatter occurrence during the summer in Hankasalmi for the years near the solar cycle minimum. The result from the study is in contrast to the result of the present study. The difference in the result might be due to the fact that the present study utilised a large data set covering the total field of view of Hankasalmi radar while the study carried out by Koustov et al. (2004) have utilised limited data set.

The statistical study of the diurnal variations of the E-region ionospheric backscatter occurrence was carried out by Carter and Makarevich. This study focussed on scatter only from near range gates ($r \leq 765$ km) of the field of view of the two radars located at Bruny Island, Tasmania, Australia for a 2-year (2004-2006) period dataset and ground scatter data were excluded. Carter and Makarevich (2009) observed a similarity in the pattern of the daily occurrence of E-region scatter for most of the radars investigated during low geomagnetic activity. In addition, they noted that the structures of most of the E-region backscatter were diffuse echoes and demonstrated the existence of the relationship between ion precipitation and E-region backscatter.

Kane et al., (2012) analysed the quiet time coherent backscatter in the F region of the ionosphere observed by the Tasman International Geospace Environment radar to determine the trends and the controlling factors in the occurrence of ionospheric echoes. Kane et al.,

(2012) observed that the solar cycle effects in the daytime occurrence are much weaker as compared to those during the night. Also, they reported the control of the occurrence of backscatter in the F region by the electrical conductance of the ionosphere and the electron density of the F region.

Makarevich et al., (2012) carried out an investigation of the IMF control and magnetic conjugacy of the E region backscatter with data from a conjugate pair of radars in the SuperDARN array in conjunction with the ACE IMF measurements. In the study, a data set spanning 1 year period from January–December 2000 near the peak of the solar cycle 23 from Pykkvibaer in Iceland and Syowa East in Antarctica within the E region FOV of each of the radars were used. The results from the study shows that IMF Bz effects dominate and that occurrence of scatter increases strongly when Bz becomes more negative and the By effects 2 times weaker and manifest differently for negative and positive Bz. The increase in occurrence of ionospheric scatter when Bz becomes more negative observed by Makarevich (2012) appears to be in agreement with the study carried out in this chapter.

In a separate study, Ghezelbash et al. (2014) studied the variations in the occurrence rates of F region echoes with special focus on the Saskatoon SuperDARN radar data for 1994 – 2012 illustrated in Figure 2.11. The findings from their study include repetitive patterns of ionospheric backscatter occurrence in both months and MLT. The present study also shows that repetitive pattern in season and MLT on the occurrence of ionospheric backscatter. Also, Ghezelbash et al. (2012) observed changes in the pattern of occurrence of ionospheric backscatter during solar cycle maximum in comparison with the pattern during solar cycle minimum conditions. The above observation is in tandem with our result. However, there exist contrast in the result of Ghezeelbash et al (2012) to the result of the present study. Also, the conclusion from their studies indicates that a maximum occurrence of echoes during winter noon hours at solar cycle minimum, maximum echo occurrence in equinoctial dusk/dawn hours and summer mid- night hours during solar cycle minimum and observation of echoes during nighttime for all seasons during solar cycle maximum conditions, the latter having more extended periods of time during the winter than summer. In addition they noticed that the occurrence of ionospheric backscatter during nighttime increases by a factor of 3 towards the solar cycle maximum while there was no significant change in the the nearnoon echo occurrence for summer and fall equinox.

In another study, Lamarche et al. (2015) carried out a statistical analysis of ionospheric backscatter observed by SuperDARN McMurdo Antarctica (MCM) station radar of the polar F region using 4 year data set to investigate the role of solar wind and illumination in production of small-scale F region plasma irregularities. In the analysis, four months were chosen as representatives of different seasons. The result of the investigation indicates that the occurrence of ionospheric backscatter detected by MCM shows that it is seen in wide and persistent bands in range which displays systematic changes with local time, season, and solar cycle. In addition, their observations indicate that solar illumination control of irregularity production is strong and not restricted to the nightside and that indirect solar wind control is also exerted by the IMF-dependent convection pattern, since the gradient-drift instability favours certain orientations between the plasma density gradients and convection velocity. Their analysis show enhancement in the occurrence of ionospheric backscatter for negative IMF B_y and B_z with higher occurrence for more negative IMF B_z . This result also agrees with our findings.

The investigation on other parameters are not presented in this thesis due to the fact that the occurrence of ionospheric backscatter as a function of each of the parameters shows very little variability apart from the clock angle which shows clear enhancement in the occurrence of ionospheric backscatter at $\pm 90^\circ$ when B_z turns negative. This observation with clock angle is seen in the B_z parameterization presented earlier in this chapter.

6.8 Conclusions

The study carried out in this chapter is on the parameterization of the occurrence rate of ionospheric backscatter from 1996 to 2015 as a function of the upstream drivers and the downstream drivers. The study investigated the impact of the drivers on the occurrence of backscatter in relation to solar cycle variation and magnetic local time during the four seasons of ionospheric scatter and the relationship between occurrence of ionospheric scatter and clock angle. One of the key results is that there is evidence of occurrence of ionospheric scatter for higher values of solar wind dynamic pressure. The result is unique because no one has investigated the relationship between the occurrence of ionospheric scatter and solar wind dynamic pressure. It is noticed that for scatter to occur pressure has to be higher. Most likely, the factor due to higher pressure being related to solar wind dynamic and IMF. Also, it is

noticed that there is more scatter on the dawn and dayside for negative B_z . B_z is expected to cause more reconnection and increase dynamics resulting in more structured ionosphere from which irregularities is produced. It also noticed that the winter sector demonstrates higher occurrence in sunspot minimum probably related to a mix of propagation and irregularities. Similarly, seasonal occurrence of ionospheric scatter is noticed. There is no evidence of asymmetry of B_y which is expected to cause asymmetry in convection cell in dawn and dusk sectors.

One of the major goals of this chapter is to identify which of the parameters, the season and the local time that such parameterization can be used as a predictive tool for now cast and forecast purposes.

Chapter 7

Conclusion and future work

7.1 Conclusion

The focus of this thesis was to investigate how Hf radar backscatter, both ionospheric and ground, varies over long term duration. Chapter 4 of this thesis presents a long term statistical study of the occurrence of ionospheric and ground backscatter in order to determine the solar cycle variation, the seasonal variation and the diurnal variation. In the study, twenty years, i.e. nearly two complete solar cycles of SuperDARN data, of the ionospheric scatter occurrence in the total field of view of Hankasalmi and Pykkvibaer radars were used. Two types of analysis were carried out in the study. The monthly mean percentage occurrence of ionospheric and ground backscatter for both Hankasalmi and Pykkvibaer radars was carried out. A solar cycle dependence in the occurrence of backscatter with an increase in ionospheric scatter during solar maximum, previously anticipated by Milan et al. (1997b), and higher occurrence of ground scatter than ionospheric scatter were observed in the monthly mean percentage occurrence statistics. Seasonal variations in the occurrence of ionospheric and ground scatter were observed in the statistics at Hankasalmi and Pykkvibaer. Also, the seasonal variations observed in ground scatter and ionospheric scatter were out of phase. A very important feature of the analysis is that sometimes ground scatter is seen to be in phase with ionospheric scatter and at other period in antiphase in Hankasalmi data while at Pykkvibaer, they are in antiphase in most of the times. The two radars were seen to behaved similarly for part of the cycle, while they behave differently in another part of the cycle.

The statistics above was then followed by the hourly percentage occurrence of ionospheric and ground backscatter for the total field of view of the two radars for the same period. This analysis was carried out to investigate the diurnal occurrence of ionospheric and ground scatter such that the result from the study can provide us with a good understanding of the ionosphere over a long term using SuperDARN data. It is observed that ionospheric scatter peaks at night during June in all years investigated but only during solar maximum in December. In December the peak in occurrence is seen at night for solar maximum and in

day during solar minimum at Hankasalmi, although a similar variation is less clear at Pykkvibaer. Also, the analysis shows that the ground scatter does not show any clear diurnal variation in June unlike December where peaks in the occurrence of ground scatter is seen in the day for both Hankasalmi and Pykkvibaer radars.

The study in Chapter 4 is followed with study in Chapter 5. Unlike the study in the previous chapter where data from the total field of view of Hankasalmi and Pykkvibaer radars were used, the study in Chapter 5 consisted of the point occupancy statistics of ionospheric backscatter and ground backscatter in three beams selected from each radar, though, the same period of investigation similar to that of Chapter 4 was considered. The goal of the chapter was to investigate the occurrence of both types of scatter as a function of range gate such that we can understand the propagation mode responsible for the occurrence of backscatter. In this study, it was found that occurrence of ionospheric backscatter is prominent at far ranges at local day during solar cycle 23 than solar cycle 24.

Also, the occurrence of ionospheric scatter at mid-range gates occurs at night-time in June (summer) during the entire period. Similar point occupancy statistics have been carried out by Milan et al. (1997b) using a limited data set identifying the occurrence of ionospheric backscatter at near ranges in the midnight local time sector during summer (June) which is in contrast to the result of this analysis where occurrence of ionospheric scatter is seen at mid-range gates. During winter and equinoctial months, ionospheric backscatter occurs most frequently at far ranges in the midday local time sector. In addition, the analysis in Chapter 5 shows that the occurrence of ground scatter seen at both mid-range and near-range gates is more in June than other months. Another striking feature in contrast to Milan et al (1997b) is that occurrence of backscatter tends to be higher in Pykkvibaer than in Hankasalmi, the difference in observation might be due to the number of range gates investigated.

The study carried out in Chapter 6 is on parameterization of occurrence of ionospheric backscatter as a function of both upstream drivers and downstream drivers in order to determine the solar cycle and local time variations in backscatter data for both Hankasalmi and Pykkvibaer radars. This is to enable us understand the parameter that can be used to predict and forecast the occurrence of ionospheric backscatter for both short and long term durations for predictive capability. In addition the relationship between the occurrence of ionospheric scatter and clock angle was carried out. The data set used in this study was from January 1996 to January 2016. The focus of the analysis was on the four seasons and the four Magnetic Local times (MLT). Lower occurrence of backscatter in summer than during winter

is a feature that is predominantly seen in the two radars which might be due to density gradients suppression by photoionization.

7.2 Future Work

The studies carried out in this thesis have utilised data set from two SuperDARN radars when the radar are in common mode of operation. It has been observed in chapter 4 that the occurrences of both ionospheric and ground scatter are solar cycle dependent. The work carried out in this chapter should extend to the next solar cycle to provide more detailed temporal variability.

The analysis carried out in chapter 5 show that the occurrence of ground scatter and ionospheric scatter in the three beams investigated appears to exhibit mirror pattern in both radars. This study could be carried further with analysis of the occurrence pattern in all the sixteen beams in each of the radar to provide more detailed analysis of spatial variability. Doing so may provide better understanding on the propagation mode of ionospheric scatter in the radars and may enhance future campaigns.

The study carried out in Chapter 6 was on the long term parameterization of the occurrence rate of ionospheric backscatter from 1996 to 2016 as a function of the upstream drivers and the downstream drivers. The solar cycle and local time variations of the occurrence of ionospheric scatter as a function of the drivers in the four sectors of the magnetic local time and during the four season's shows a remarkable result. The goal of the study is to use such parameterization as a predictive tool for now cast and forecast purposes. One of the key results from the study is that occurrence of backscatter was low in summer than during winter which might be due to density gradients suppression by photoionization. Previous studies carried out with data from other SuperDARN radars have utilised limited data set or have restrict their analysis to one or few parameters. It is suggested that the present result from Hankasalmi and Pykkvibaer radars should be compared with similar long term studies of other SuperDARN radars to adequately understand the global picture.

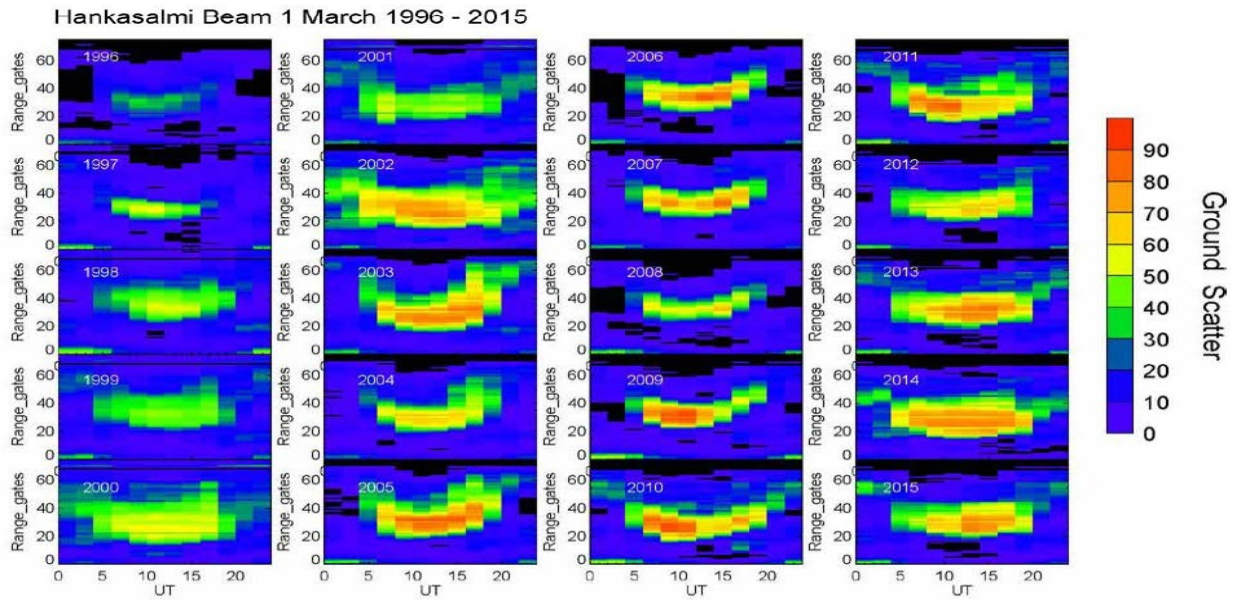
Also, the effect of backscatter from behind the radar was not carried out in this thesis hence, future work may investigate the effect of scatter from behind the two radars so as to ascertain their contribution to the temporal and spatial pattern of both ionospheric and ground backscatter.

One of the important future work the research carried out in this thesis has showed is the possibility to develop a multivariate time series model (forecasting/prediction tool) of ionospheric scatter and its drivers for space weather prediction using Neural Networks or similar artificial intelligence algorithm with SuperDARN data.

Another important future work proposed (draft paper to be submitted for publication) is a science campaign to equip the African sector of the magnetic equator of the ionosphere with network of radars similar in style and technicalities to the high-latitude SuperDARN radar network and array of magnetometers along the equatorial belt. These two proposed space physics instruments will be used to study this region of the equatorial ionosphere over a long interval of time, at least one solar cycle for simultaneous observations of both electric and magnetic variations over the African sector. The proposed projects will clearly improve our understanding of the dynamics of the equatorial ionosphere and our understanding of its role in balancing the large-scale ionospheric current system, and will contribute to our ability to adequately model ionospheric and plasmaspheric densities. It will also enhance our understanding of global ionospheric processes which will improve the space weather capabilities of the space science community.

Appendix 1

a)



b)

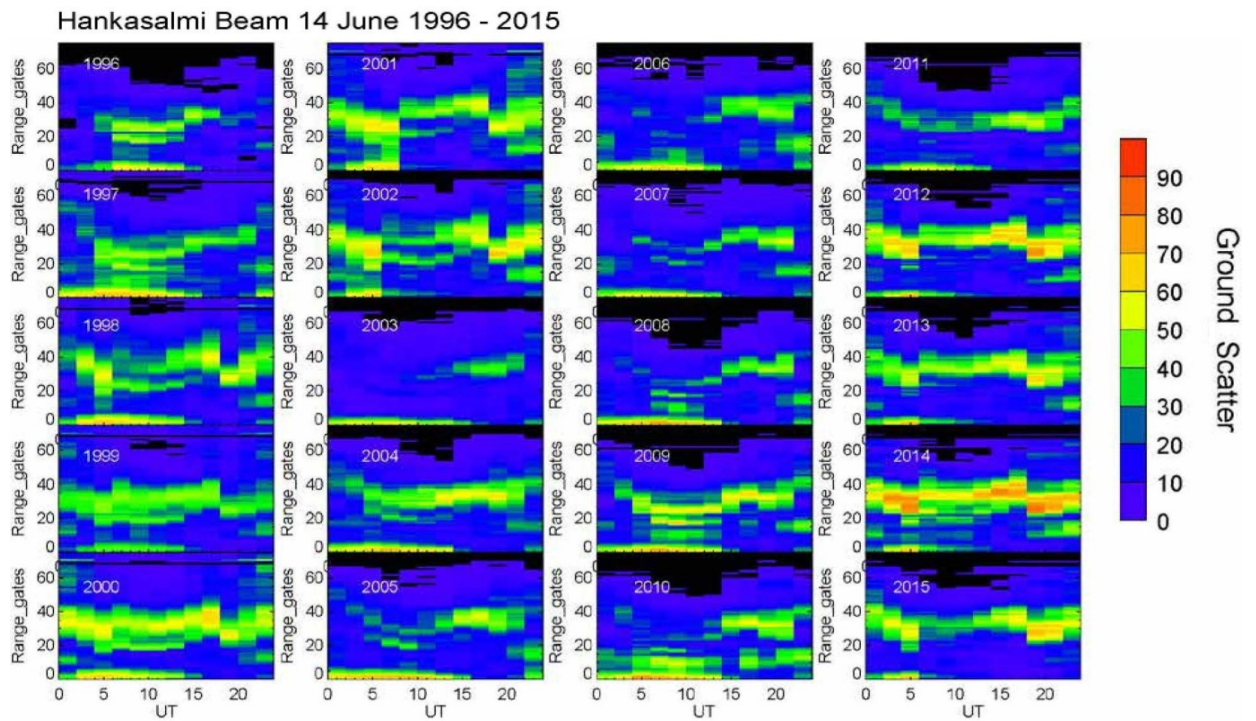
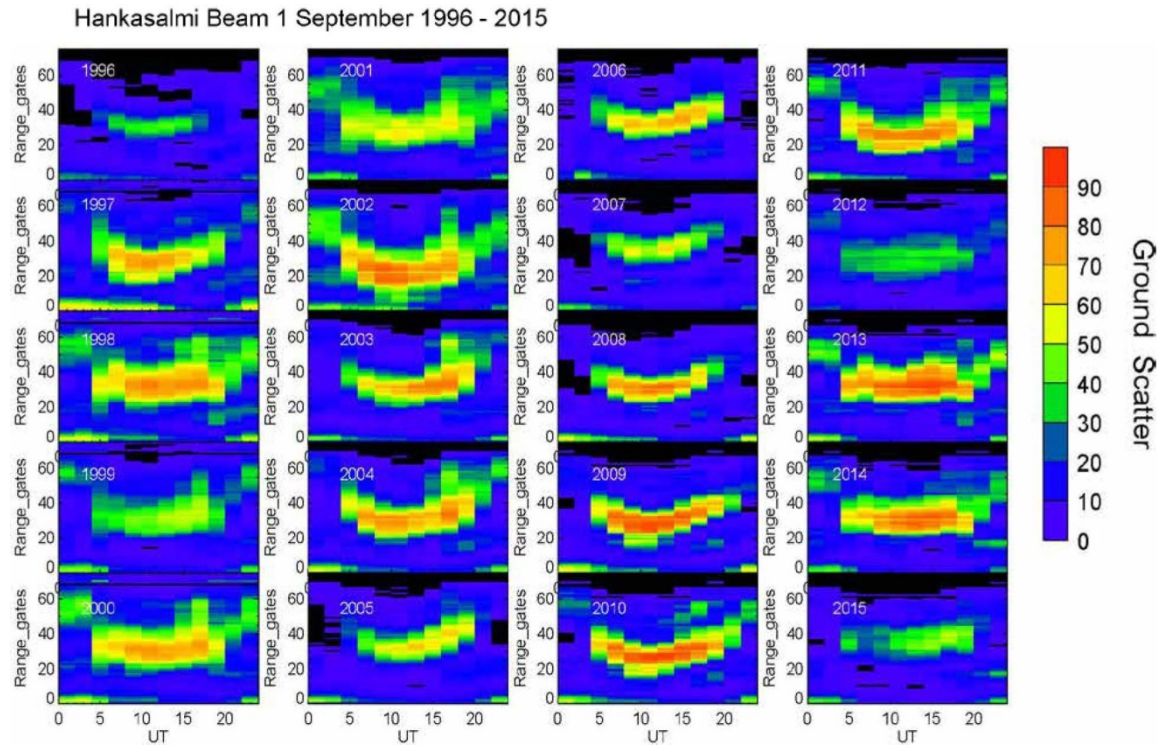


Figure A1.1 shows the point occupancy statistics of ground backscatter (colour coded) of Hankasalmi (Finland radar) beam 1 (**panel a**) & 14 (**panel b**) for the month of June (summer) from 1996 - 2015.

a)



b)

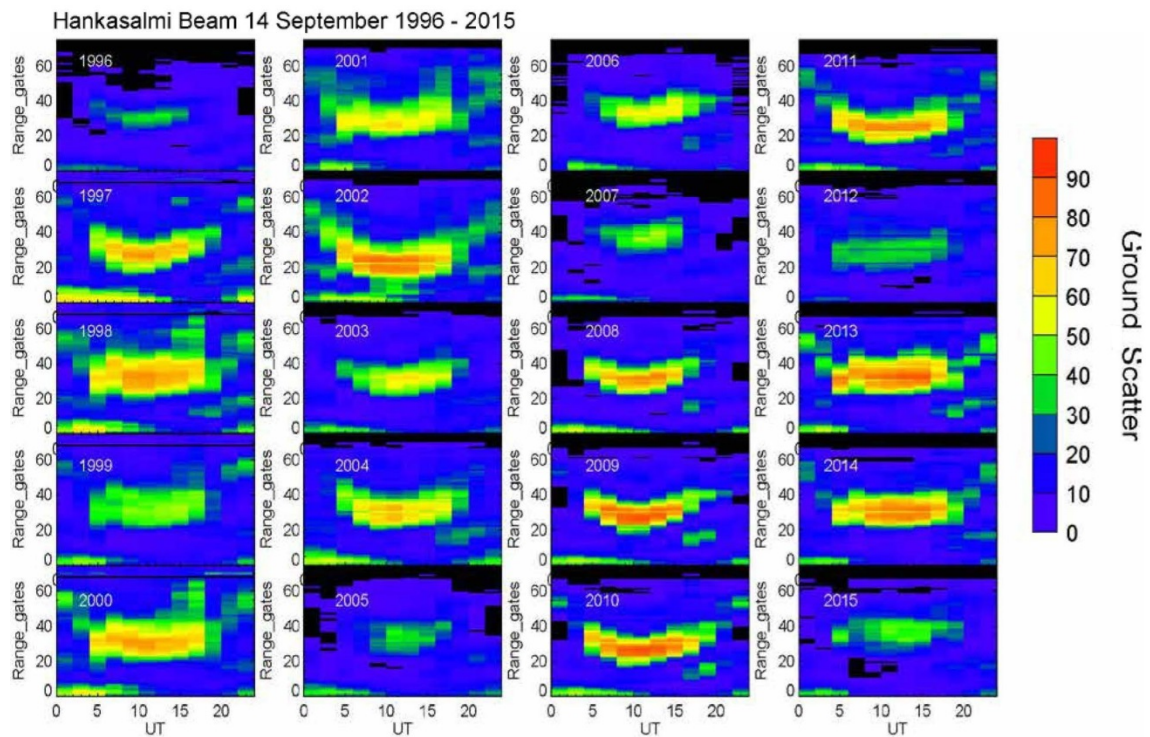
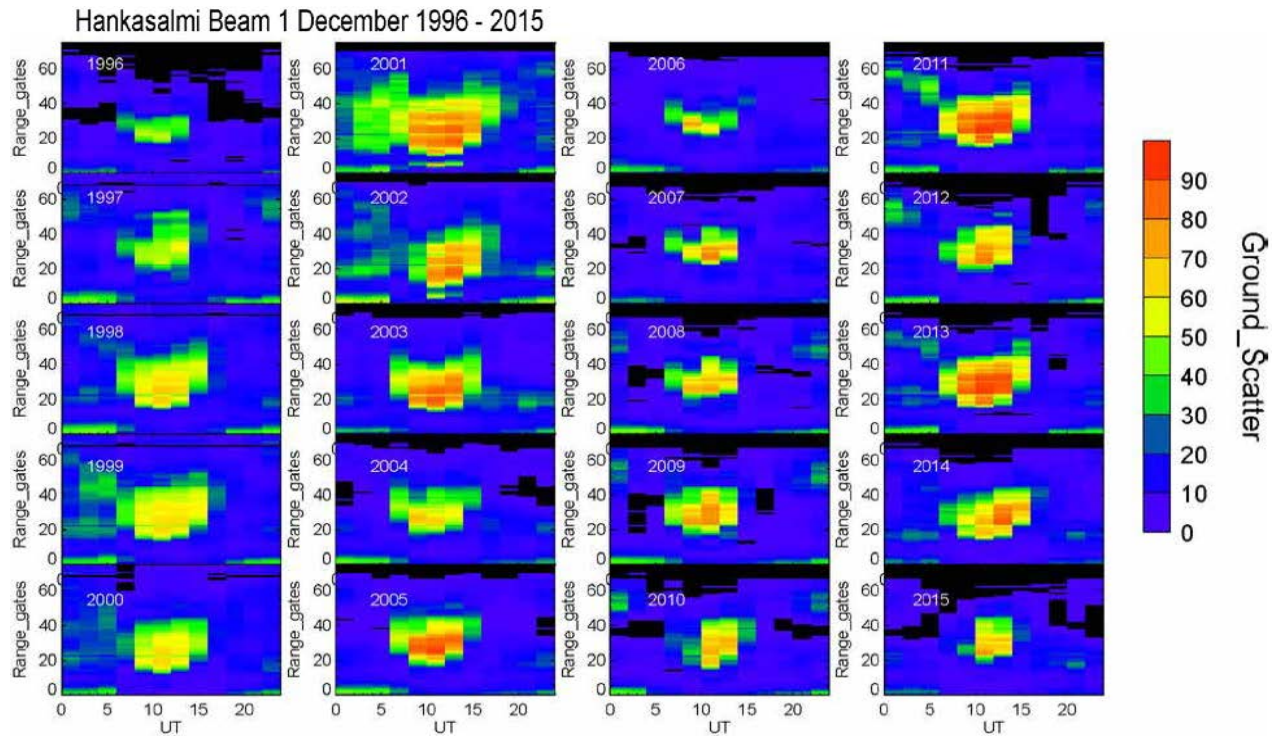


Figure A1.2 shows the point occupancy statistics of ground backscatter (colour coded) of Hankasalmi (Finland radar) beam 1 (**panel a**) & 14 (**panel b**) for the month of September (autumn) from 1996 – 2015

a)



b)

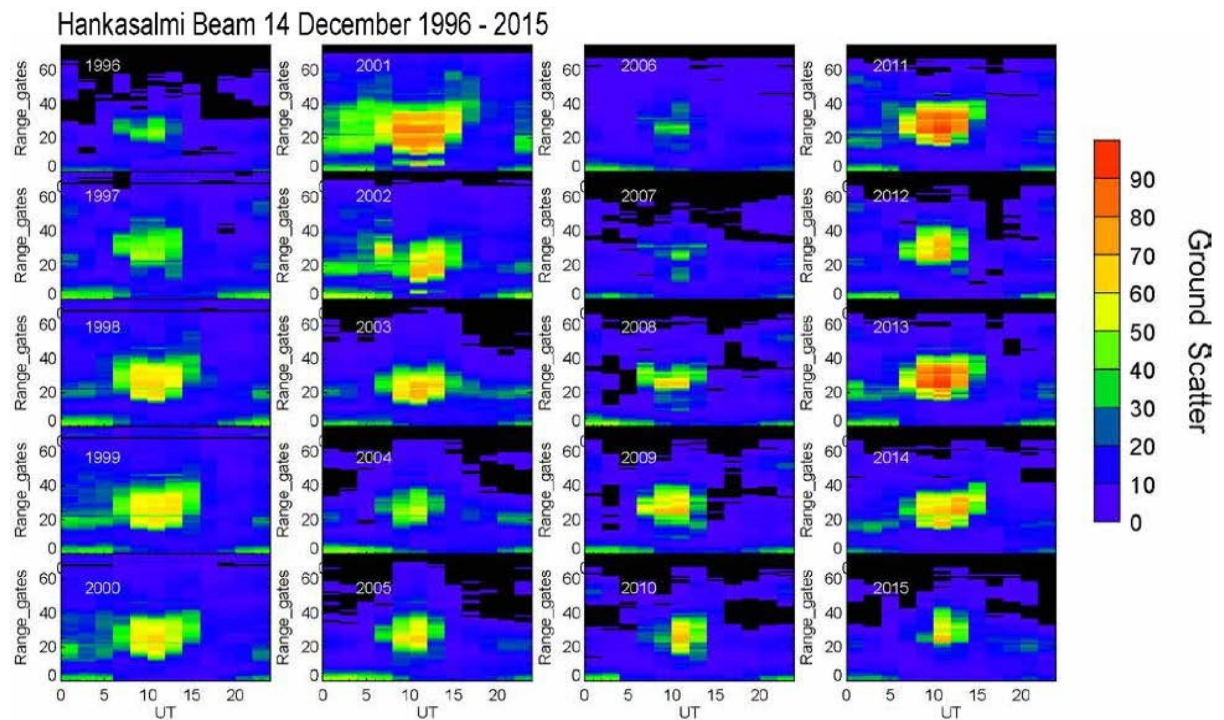


Figure A1.3 shows the point occupancy statistics of ground backscatter (colour coded) of Hankasalmi (Finland radar) beam 1 (**panel a**) & 14 (**panel b**) for the month of December (winter) from 1996 - 2015

a)

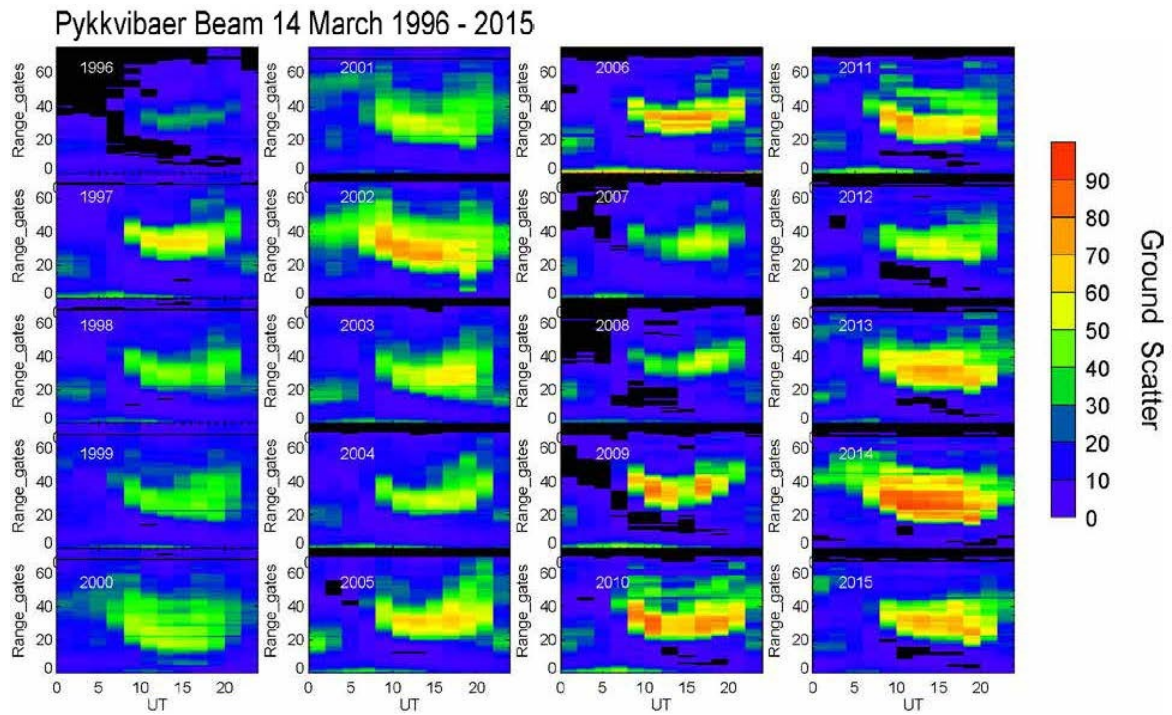
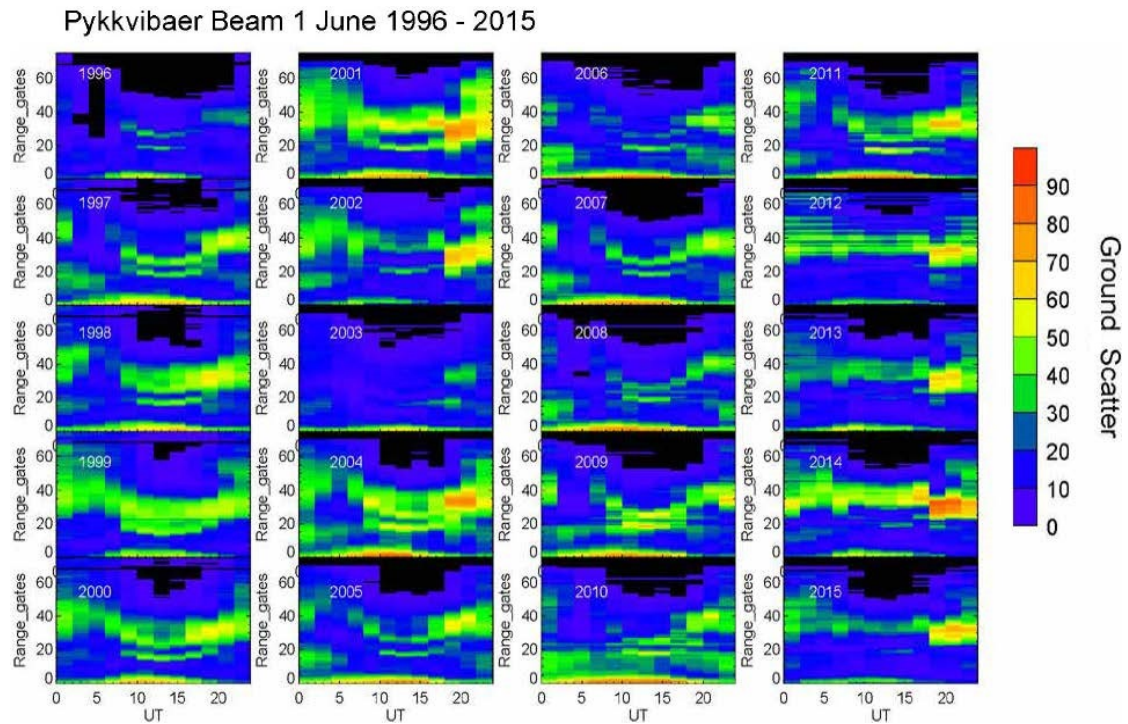


Figure A1.4 shows the point occupancy statistics of ground backscatter (colour coded) of Pykkvibaer (Iceland radar) 14 for the month of March (spring) from 1996 - 2015

a)



b)

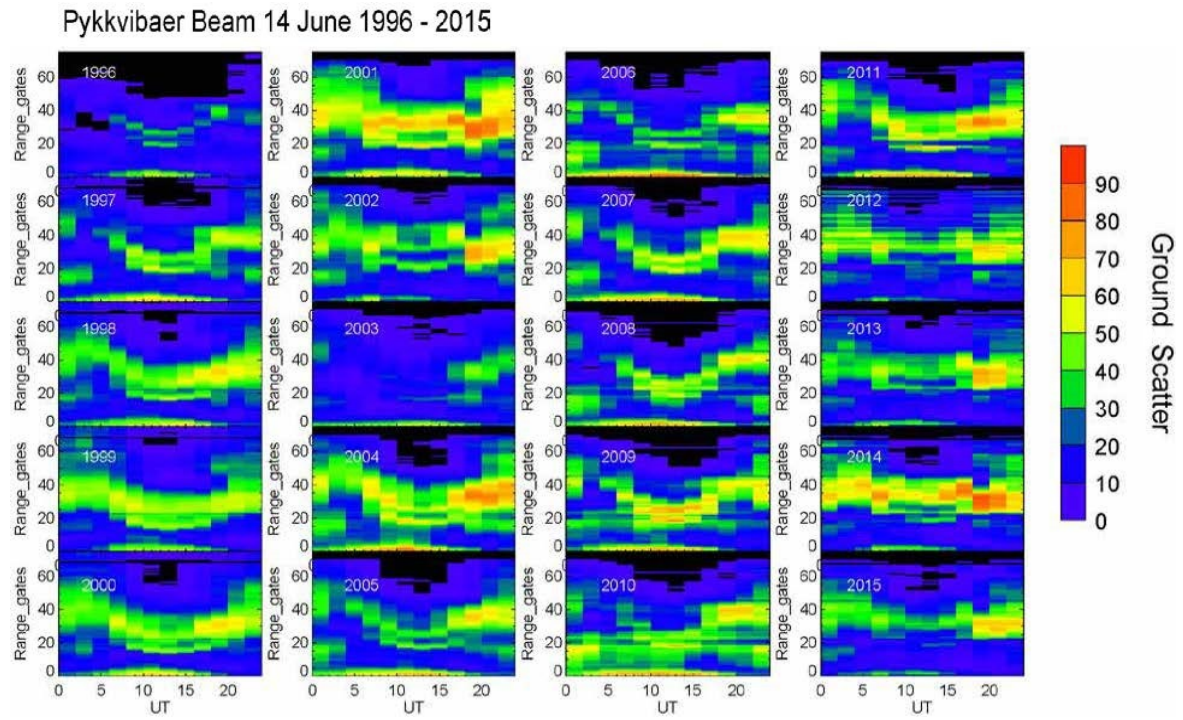
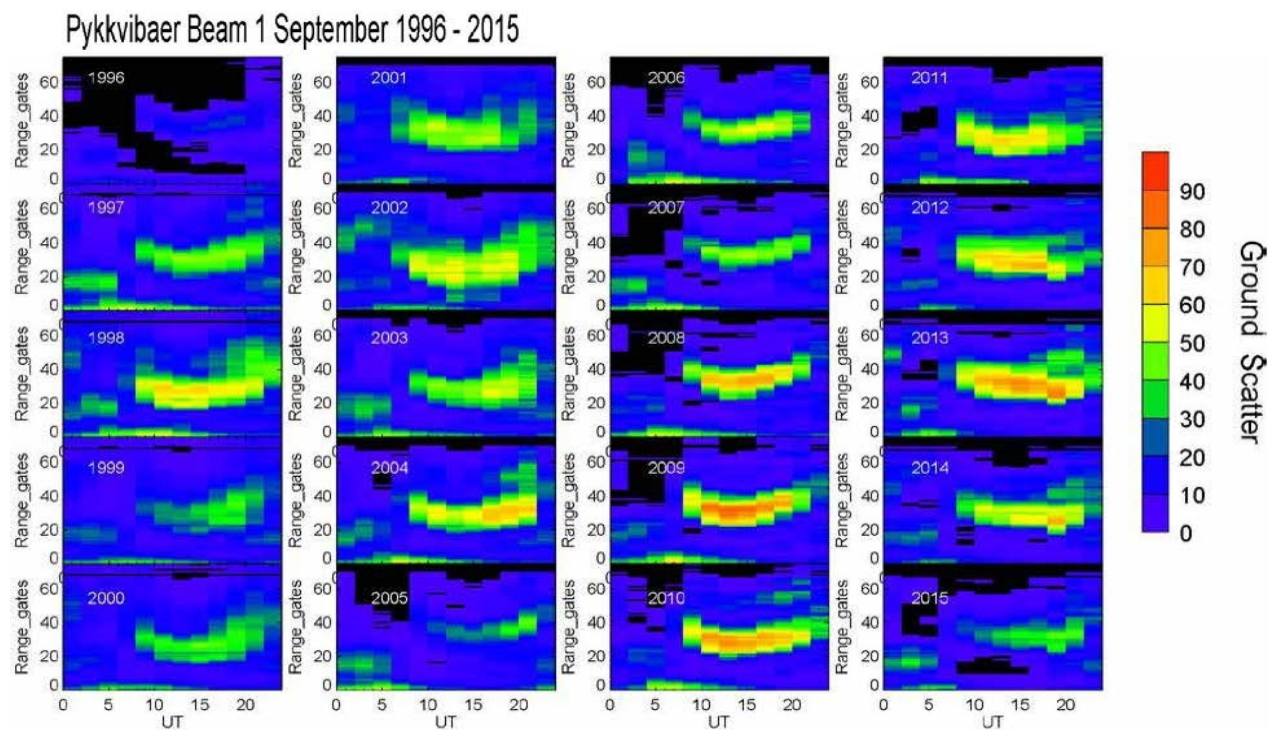


Figure A1.5 shows the point occupancy statistics of ground backscatter (colour coded) of Pykkvibaer (Iceland radar) beam 1 (**panel a**) & 14 (**panel b**) for the month of June (summer) from 1996 - 2015

a)



b)

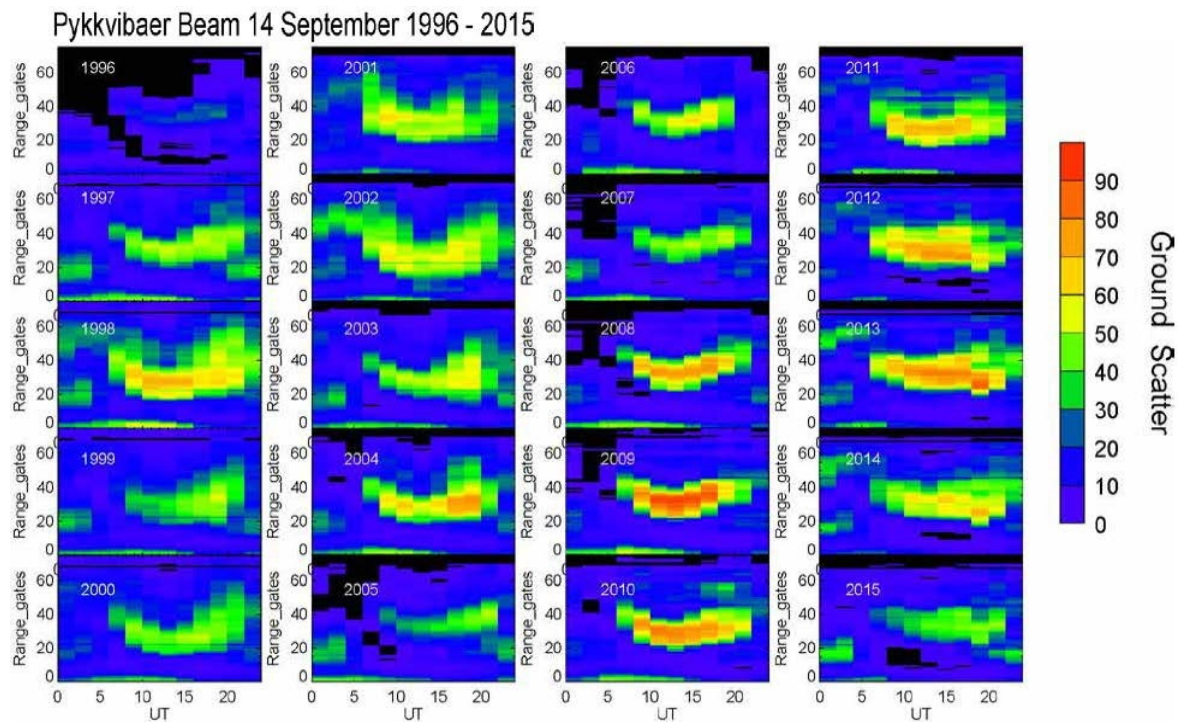
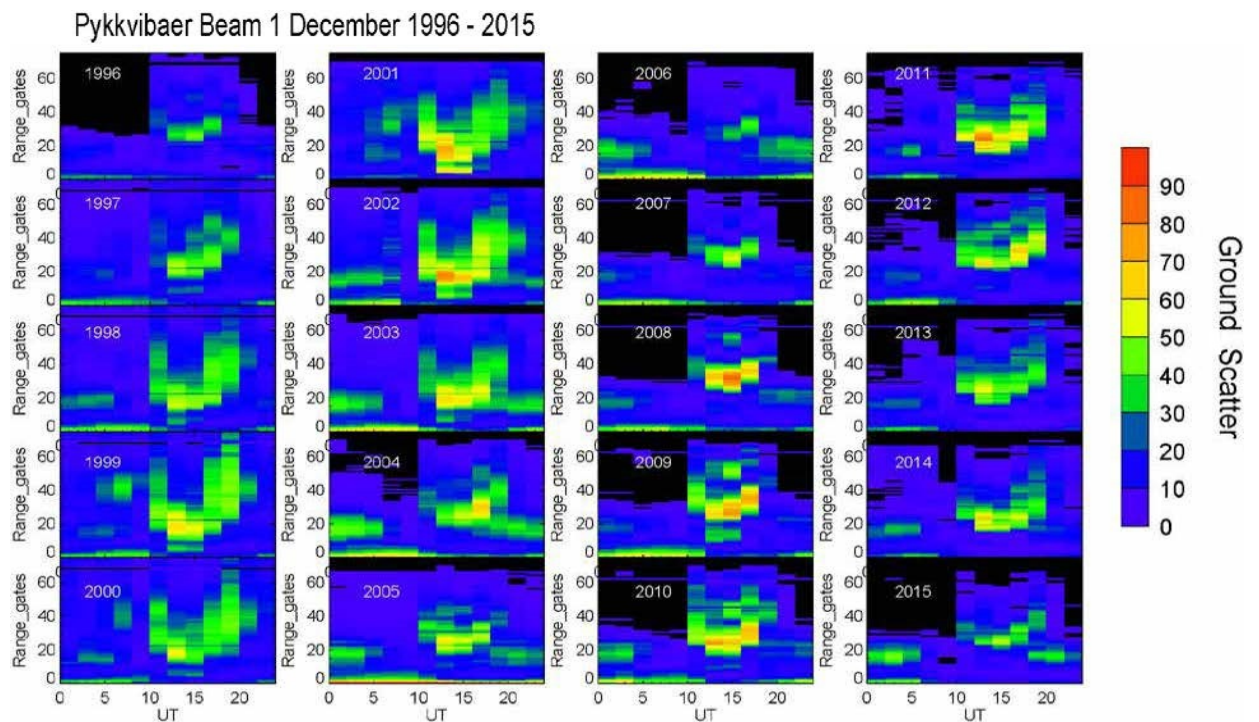


Figure A1.6 shows the point occupancy statistics of ground backscatter (colour coded) of Pykkvibaer (Iceland radar) beam 1 (**panel a**) & 14 (**panel b**) for the month of September (autumn) from 1996 - 2015

a)



b)

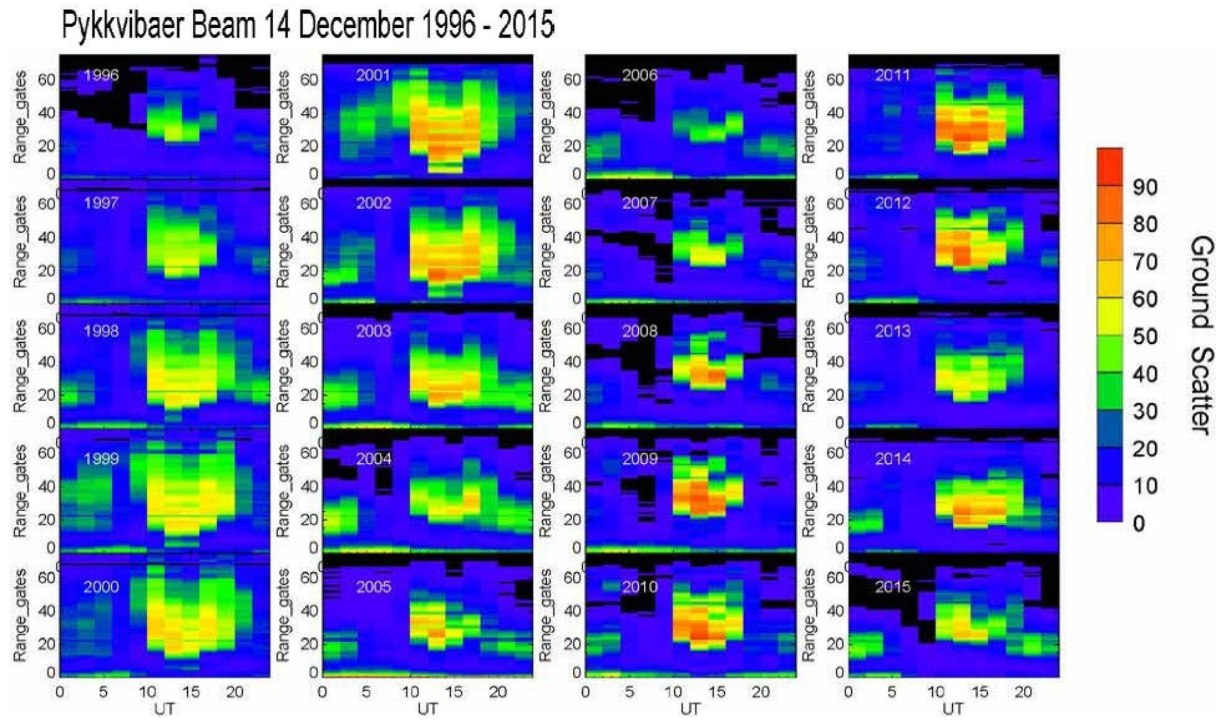


Figure A1.7 shows the point occupancy statistics of ground backscatter (colour coded) of Pykkvibaer (Iceland radar) beam 1 (**panel a**) & 14 (**panel b**) for the month of December (winter) from 1996 - 2015

Appendix 2

a)

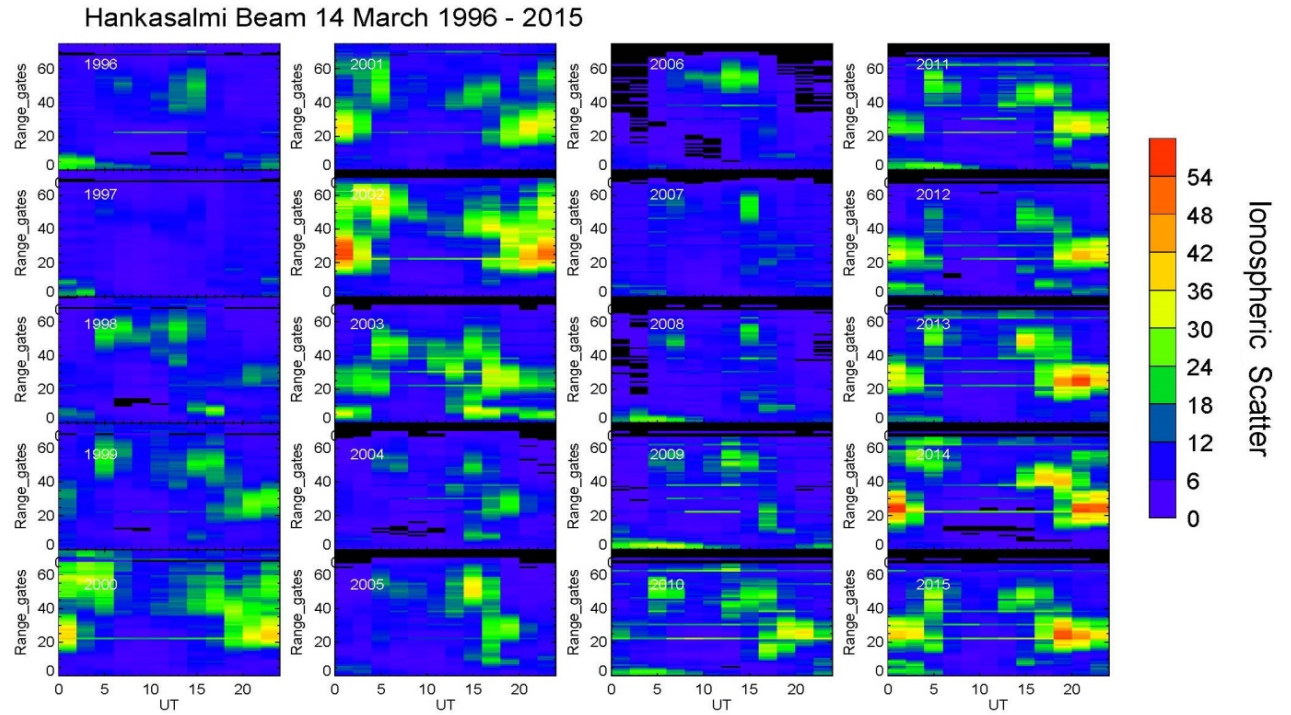
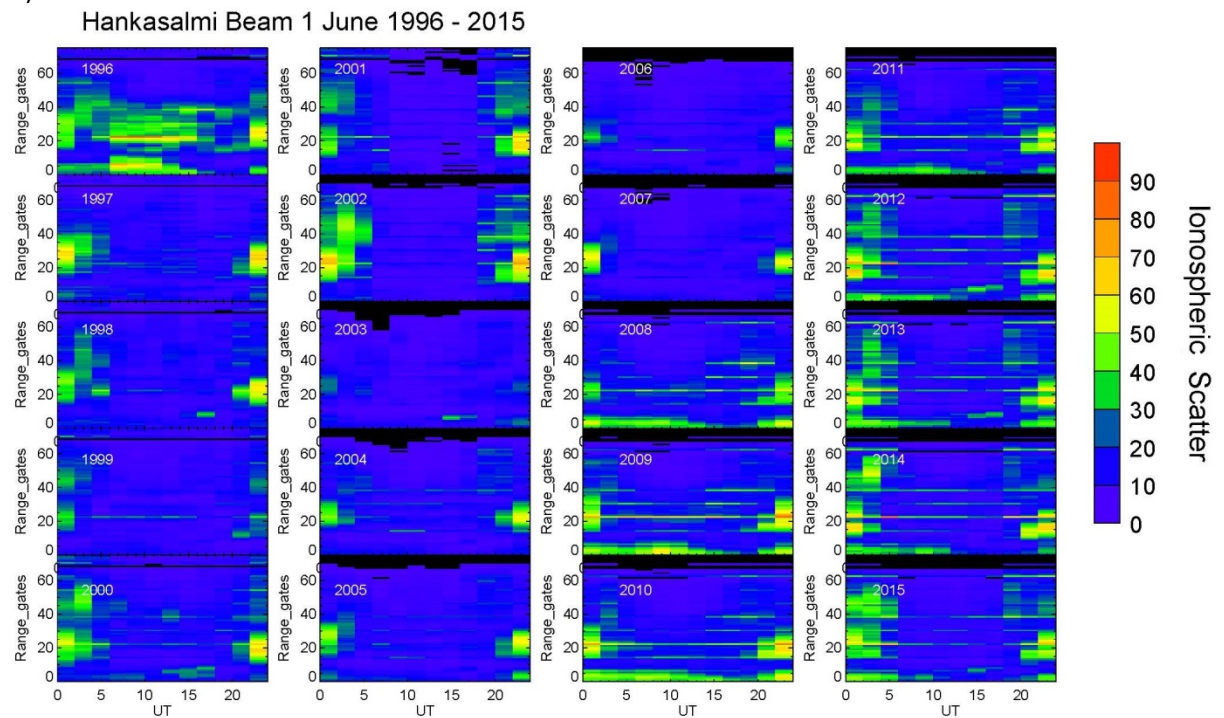


Figure A2.1 shows the point occupancy statistics of ionospheric backscatter (colour coded) of Hankasalmi (Finland radar) beam 14 for the month of March (spring) from 1996 – 2015

a)



b)

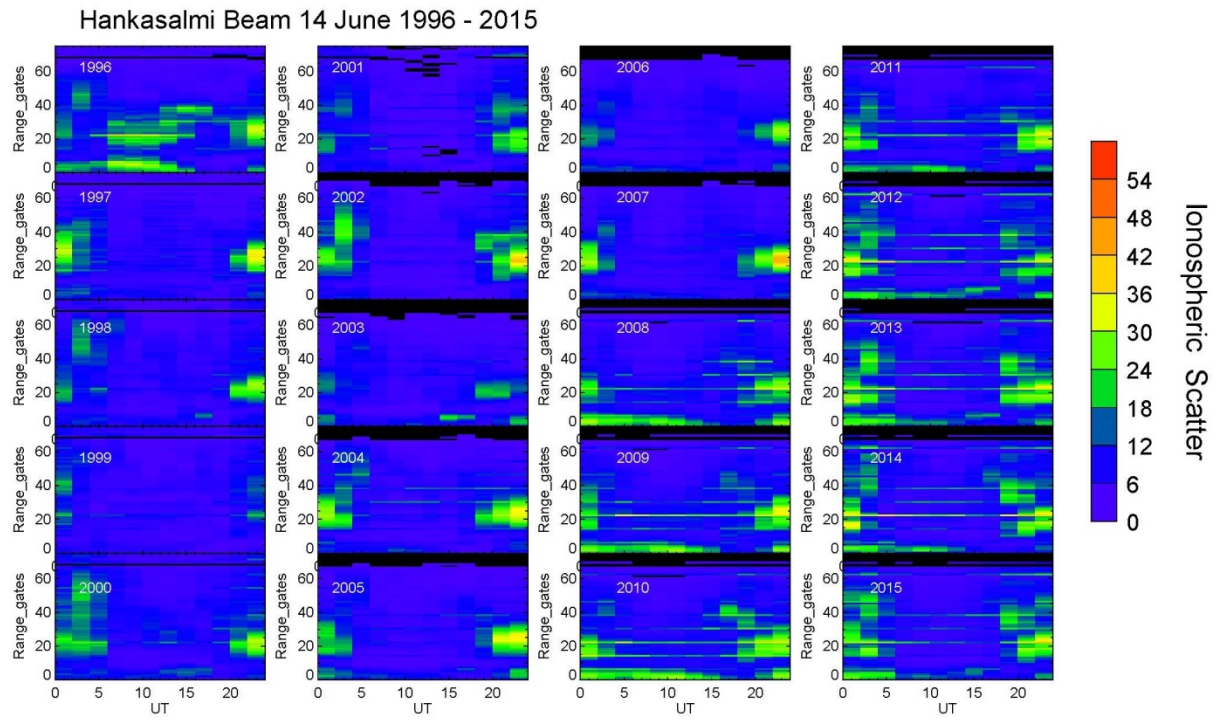
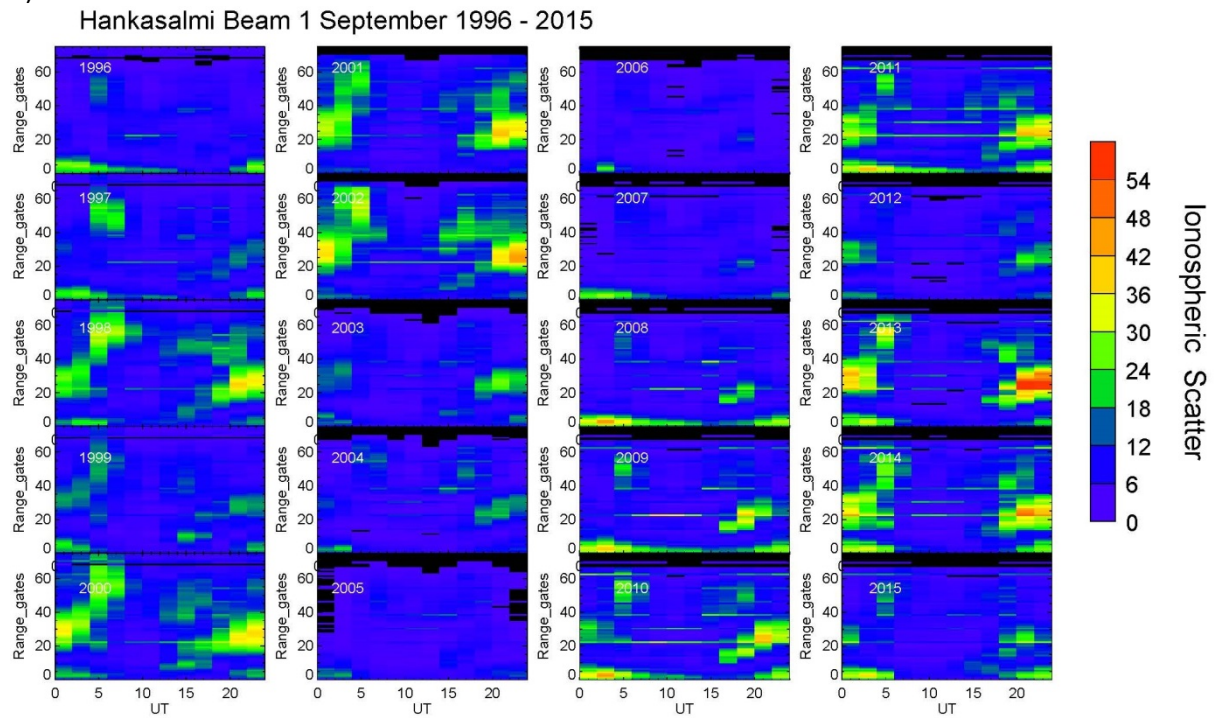


Figure A2.2 shows the point occupancy statistics of ionospheric backscatter (colour coded) of Hankasalmi (Finland radar) beam 1 (**panel a**) & 14 (**panel b**) for the month of June (summer) from 1996 - 2015.

a)



b)

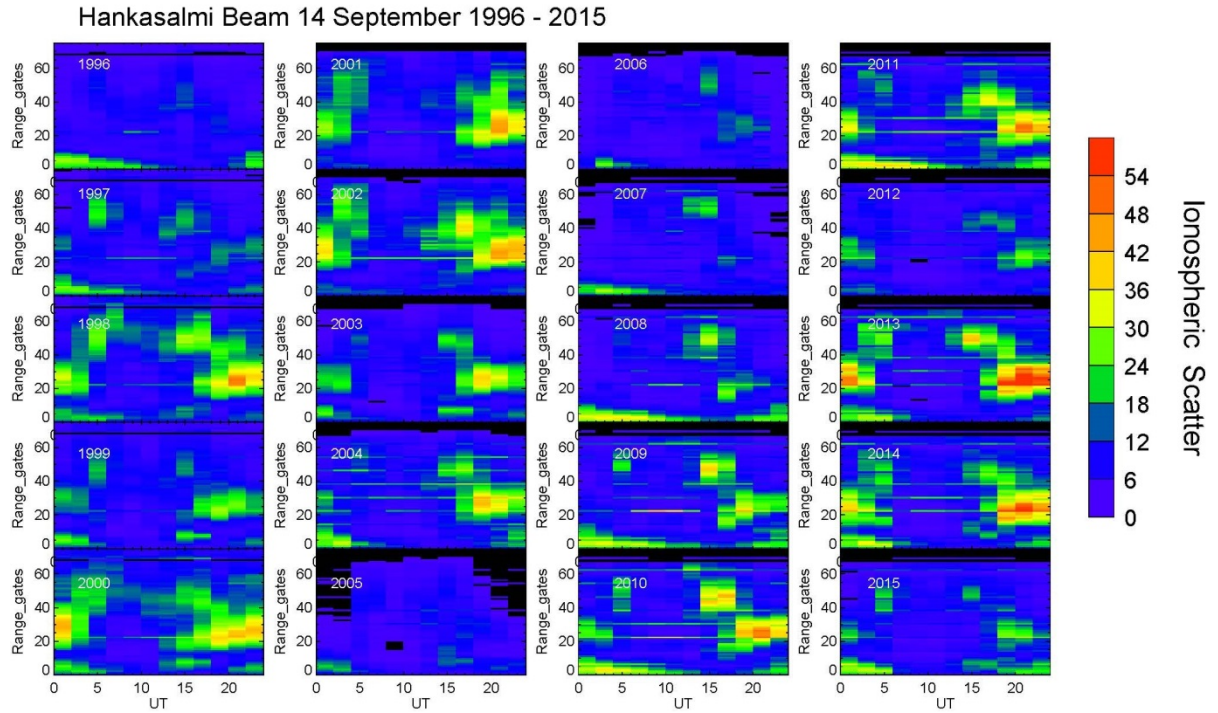
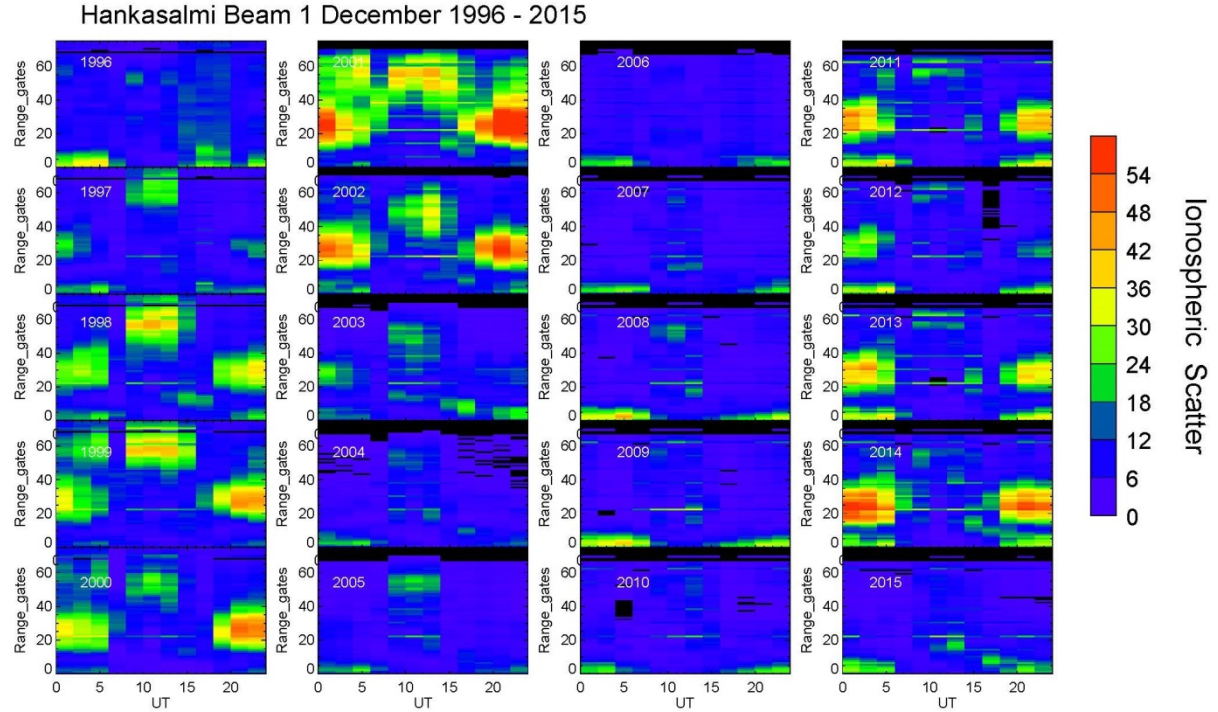


Figure A2.3 shows the point occupancy statistics of ionospheric backscatter (colour coded) of Hankasalmi (Finland radar) beam 1 (**panel a**) & 14 (**panel b**) for the month of September (autumn) from 1996 - 2015.

a)



b)

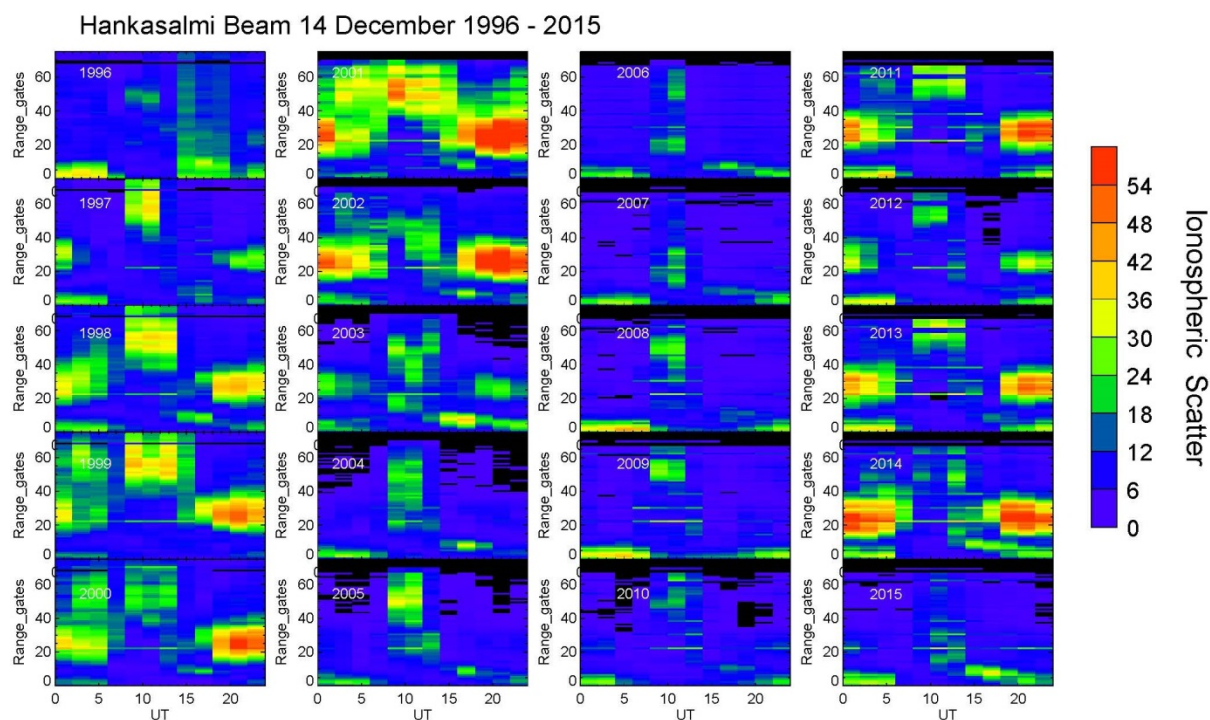


Figure A2.4 shows the point occupancy statistics of ionospheric backscatter (colour coded) of Hankasalmi (Finland radar) beam 1 (**panel a**) & 14 (**panel b**) for the month of December (winter) from 1996 - 2015.

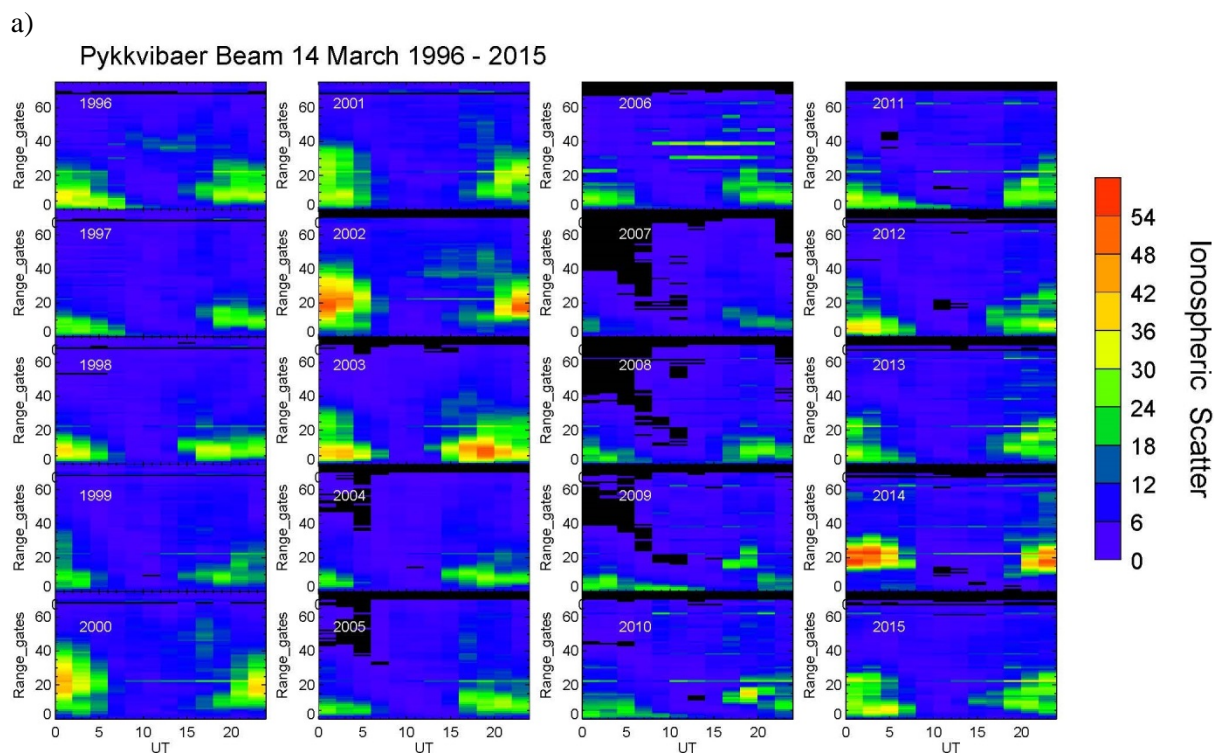


Figure A2.5 shows the point occupancy statistics of ionospheric backscatter (colour coded) of Hankasalmi (Finland radar) beam 14 for the month of March (spring) from 1996 - 2015.

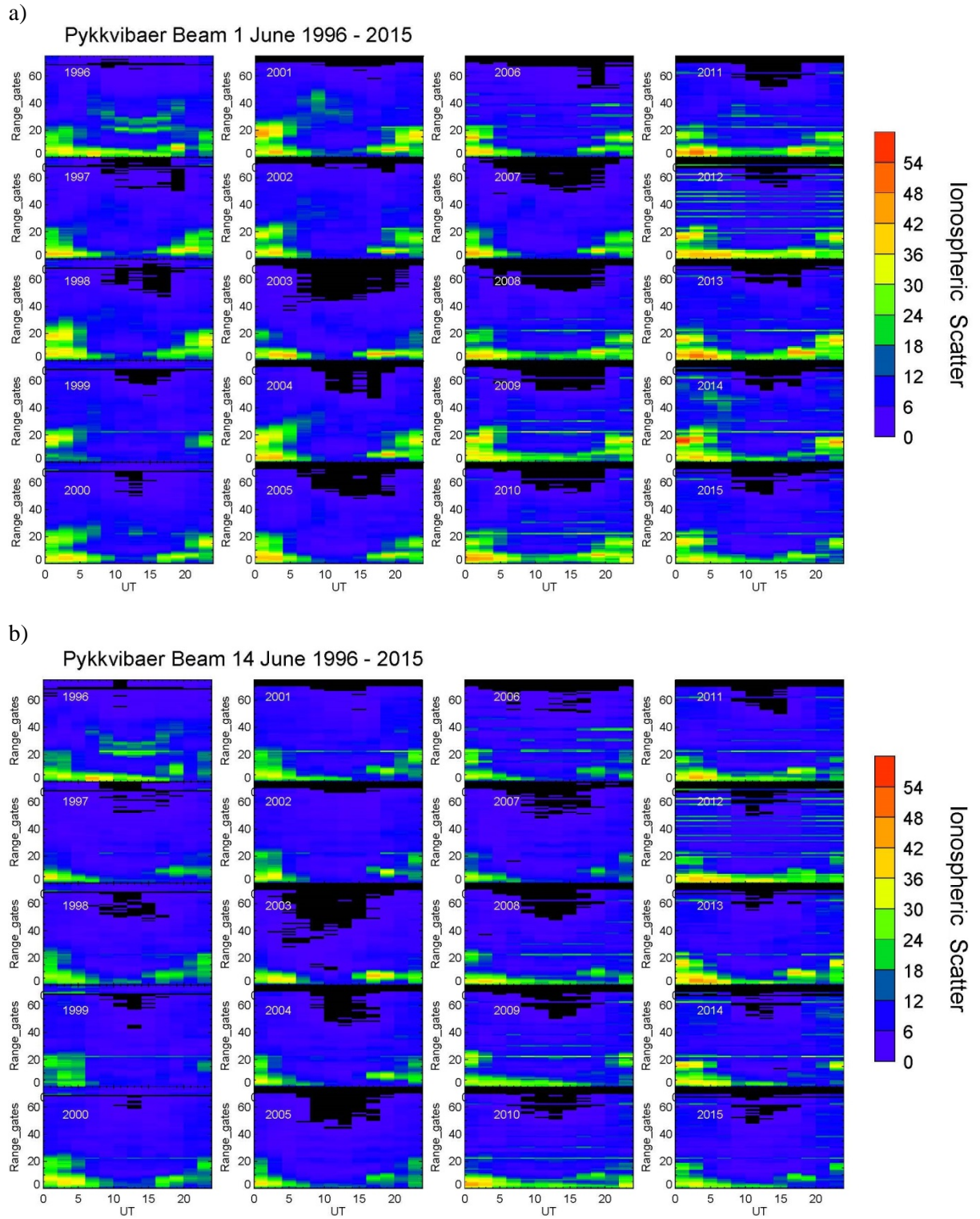
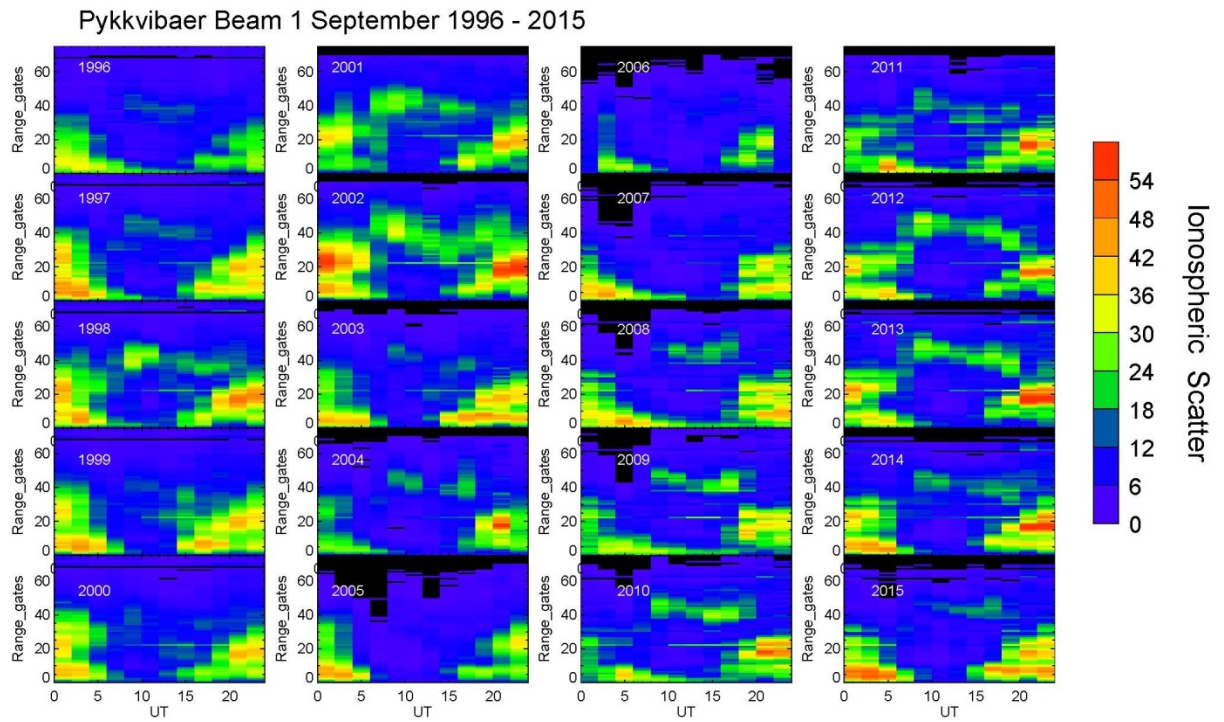


Figure A2.6 shows the point occupancy statistics of ionospheric backscatter (colour coded) of Hankasalmi (Finland radar) beam 1 (**panel a**) & 14 (**panel b**) for the month of June (summer) from 1996 - 2015.

a)



b)

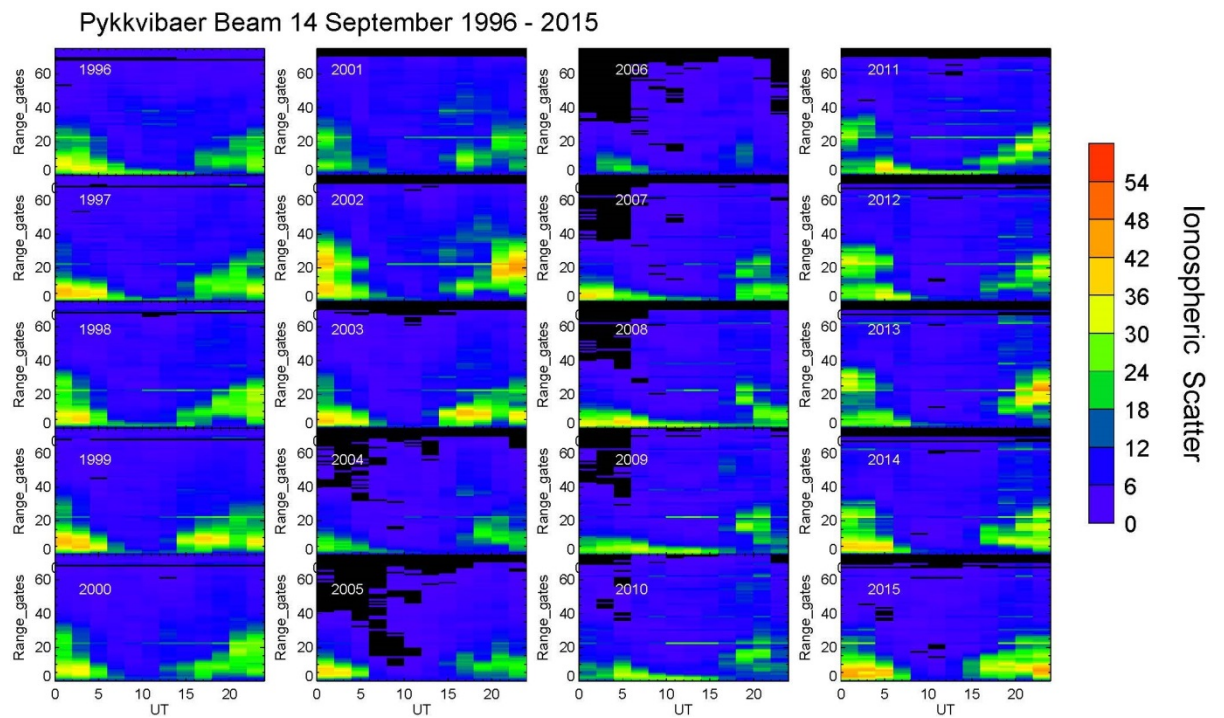


Figure A2.7 shows the point occupancy statistics of ionospheric backscatter (colour coded) of Hankasalmi (Finland radar) beam 1 (**panel a**) & 14 (**panel b**) for the month of September (autumn) from 1996 - 2015.

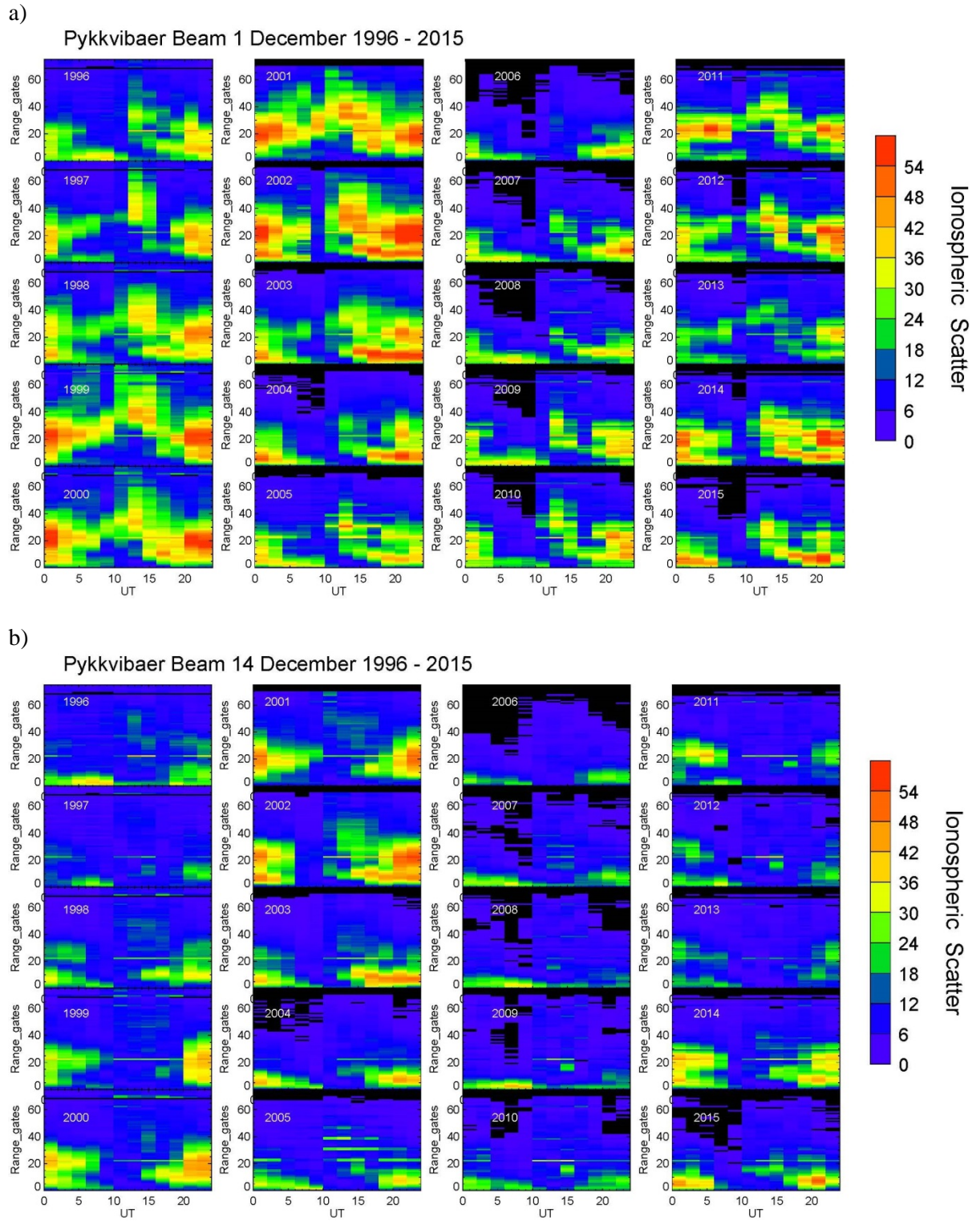


Figure A2.8 shows the point occupancy statistics of ionospheric backscatter (colour coded) of Hankasalmi (Finland radar) beam 1 (**panel a**) & 14 (**panel b**) for the month of December (winter) from 1996 - 2015.

Hankasalmi Ionospheric scatter against Pressure (Summer Solstice)

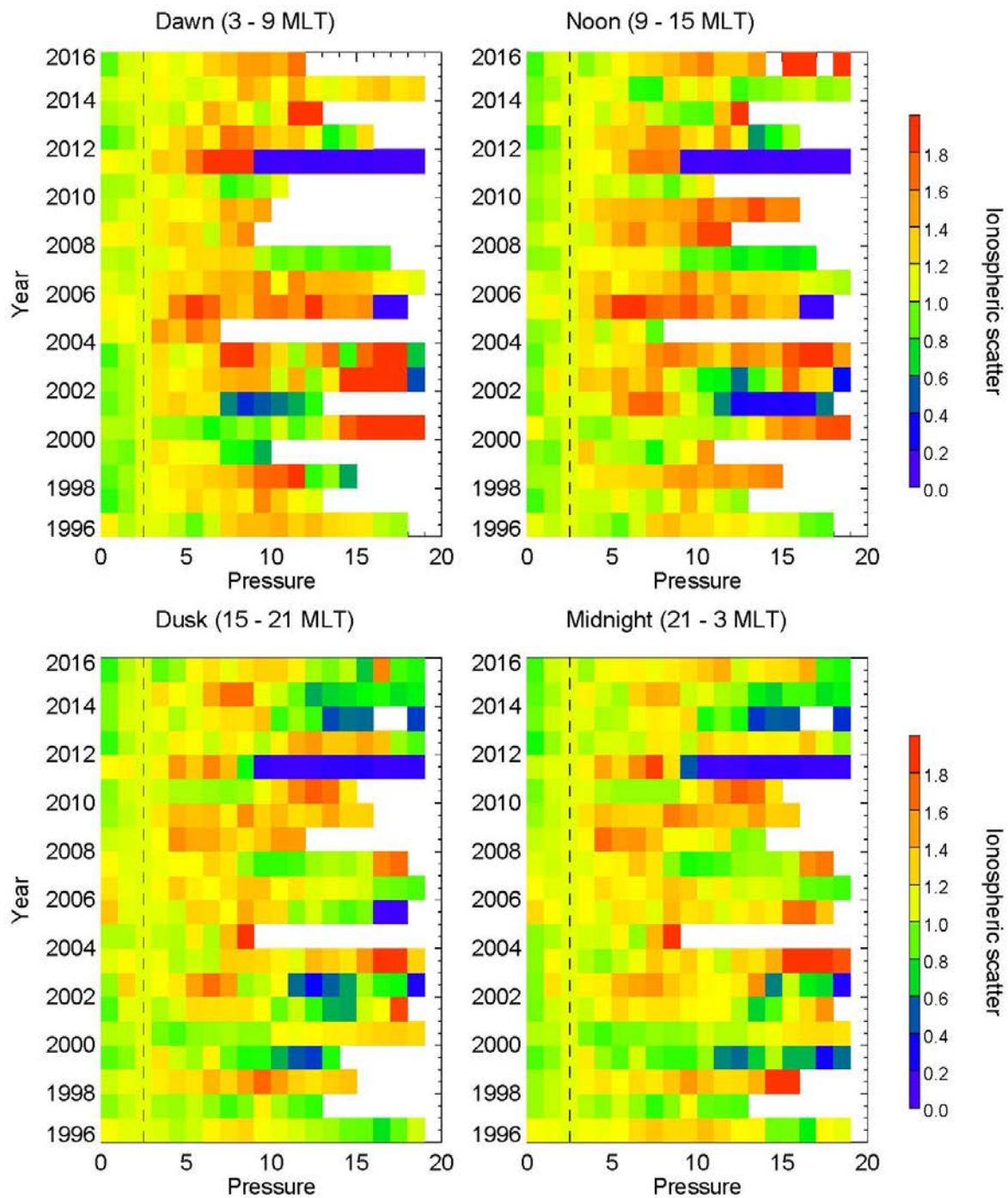


Figure A3.1a. Normalised percentage occurrence of ionospheric scatter as a function of Pressure from 1996 to 2015 sorted by MLT sectors for Summer season. The dashed black line indicates the point of normalisation. The top left panel shows the dawn (03-09 MLT) sector, the right upper panel shows the noon (09-15 MLT) sector, the left lower panel shows the dusk (15-21 MLT) and the right lower panel shows the midnight (21-03 MLT) sector.

Hankasalmi Ionospheric scatter against Pressure (Autumn)

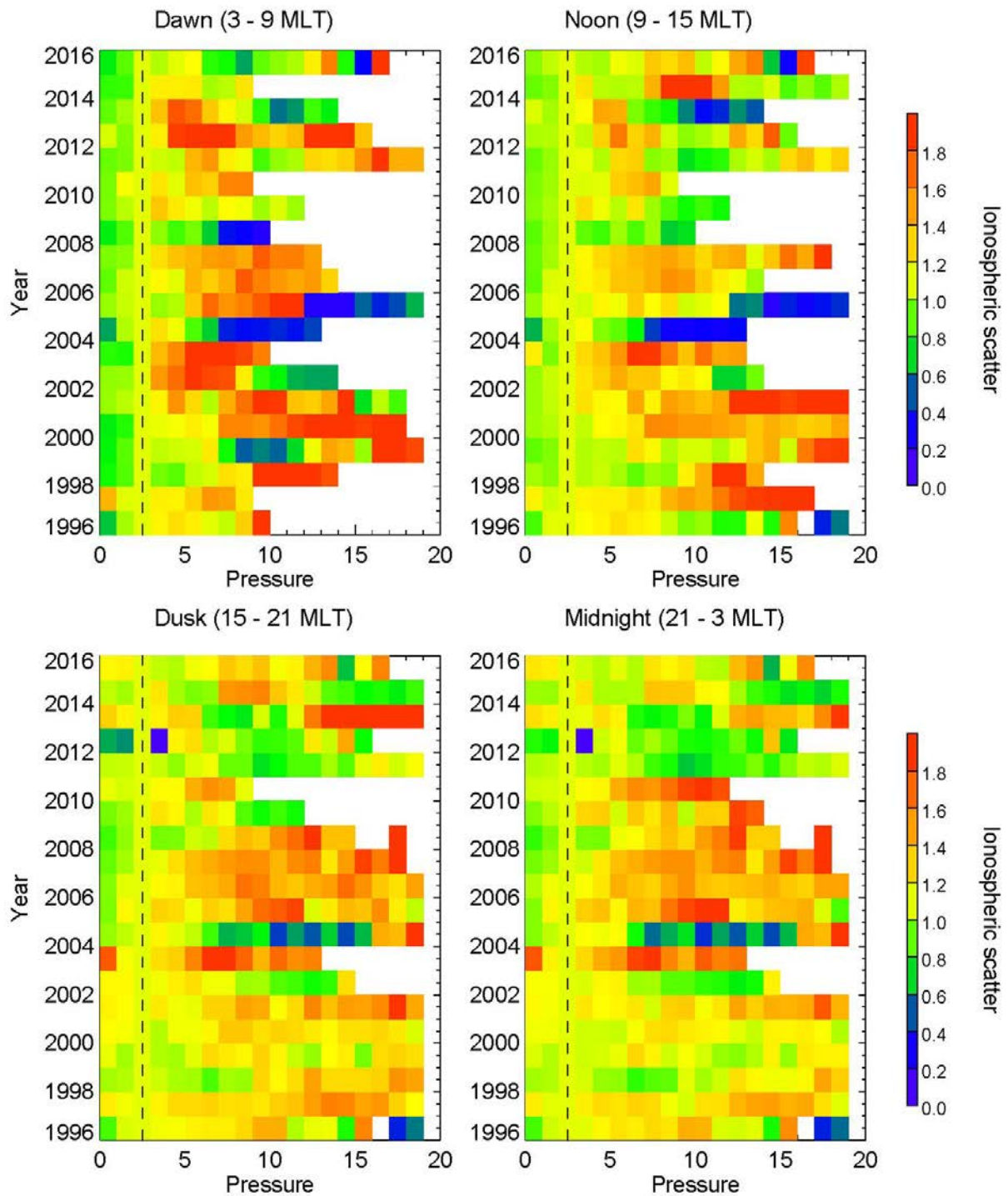


Figure A3.1b. Normalised percentage occurrence of ionospheric scatter as a function of Pressure from 1996 to 2015 sorted by MLT sectors for Autumn season. The dashed black line indicates the point of normalisation. The top left panel shows the dawn (03-09 MLT) sector, the right upper panel shows the noon (09-15 MLT) sector, the left lower panel shows the dusk (15-21 MLT) and the right lower panel shows the midnight (21-03 MLT) sector.

Hankasalmi Ionospheric scatter against Pressure (Winter Solstice)

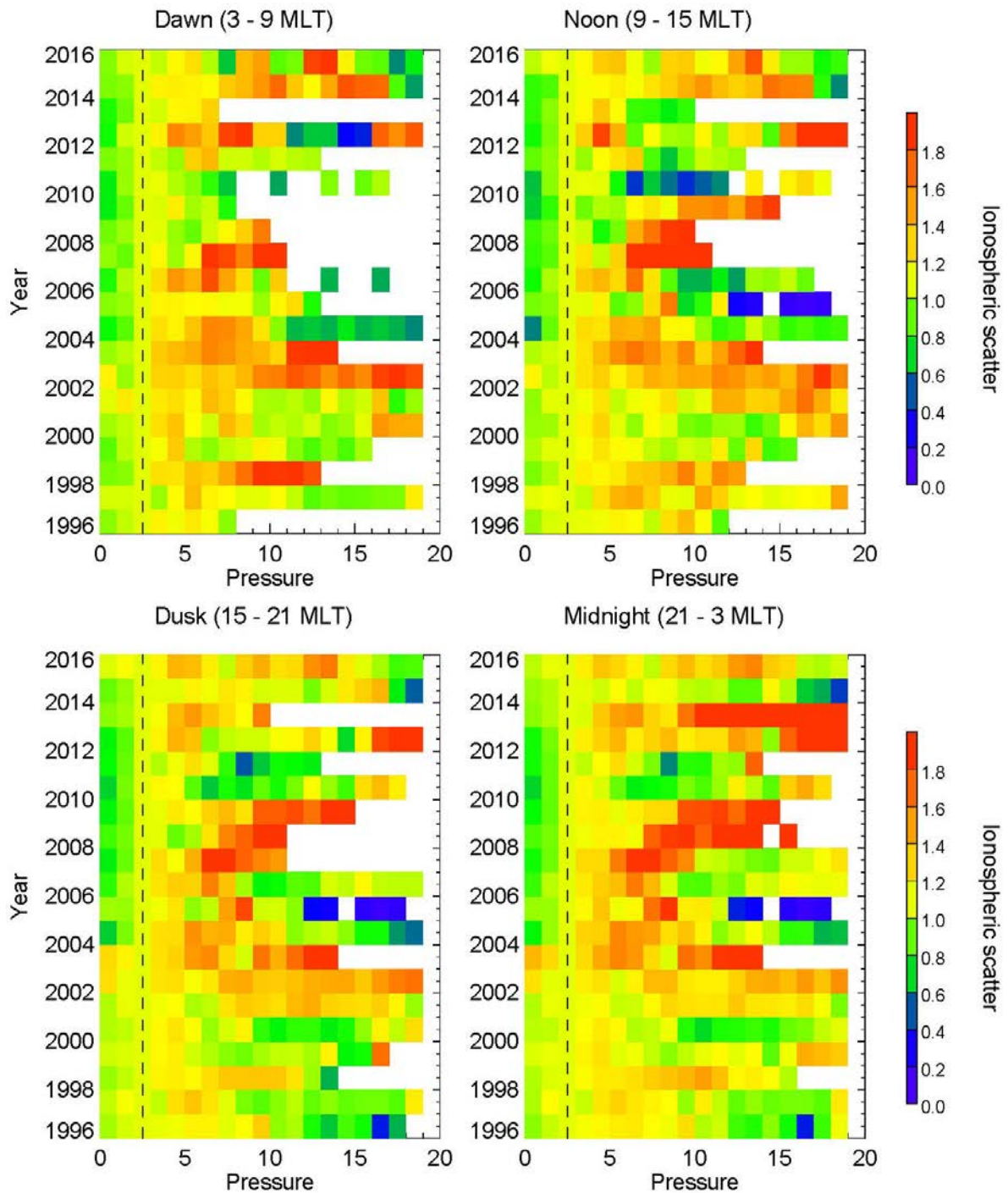


Figure A3.1c. Normalised percentage occurrence of ionospheric scatter as a function of Pressure from 1996 to 2015 sorted by MLT sectors for Winter (Solstice) season. The dashed black line indicates the point of normalisation. The top left panel shows the dawn (03-09 MLT) sector, the right upper panel shows the noon (09-15 MLT) sector, the left lower panel shows the dusk (15-21 MLT) and the right lower panel shows the midnight (21-03 MLT) sector.

Hankasalmi Ionospheric scatter against Bz(GSM) (Autumn)

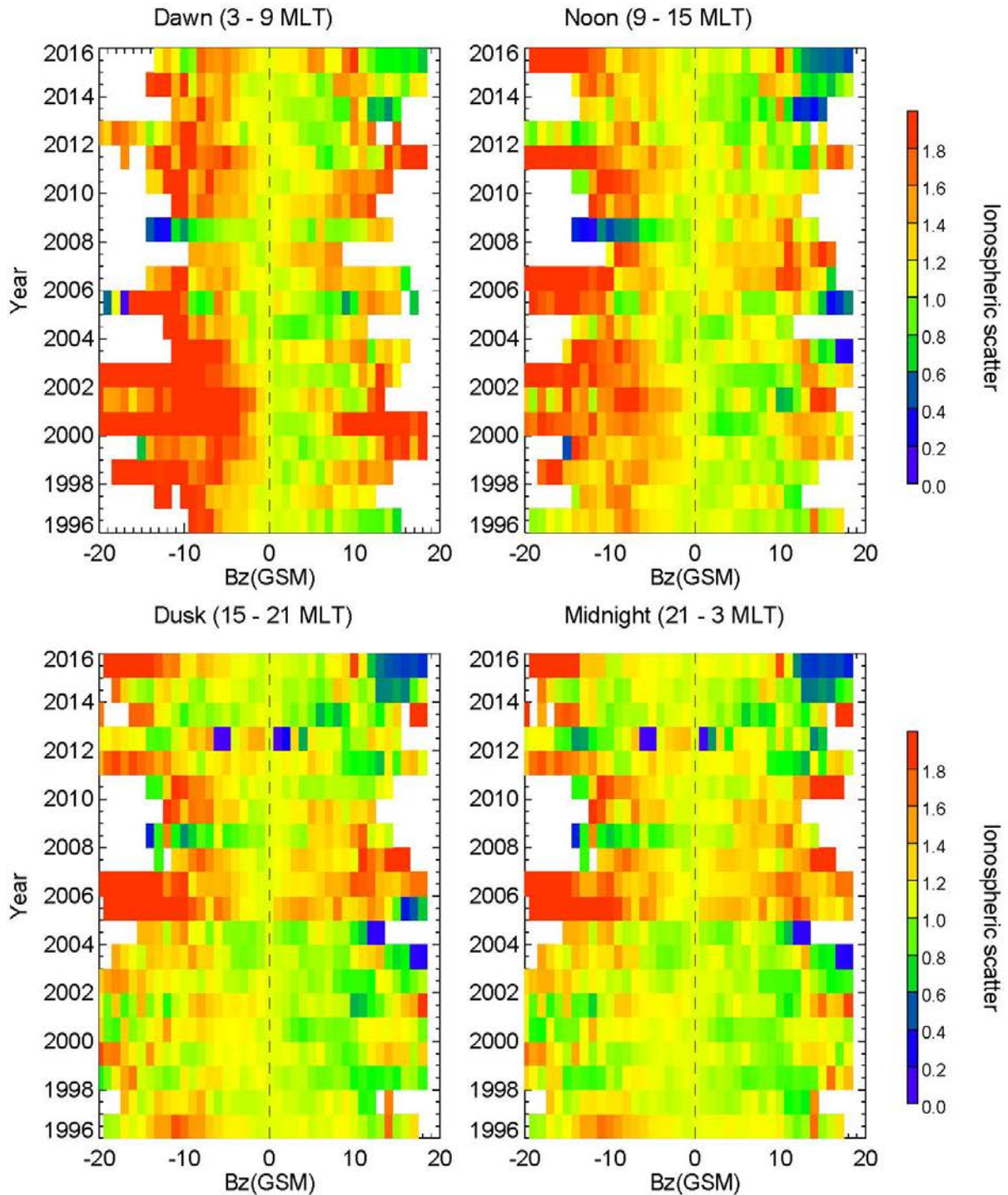


Figure A3.2. Normalised percentage occurrence of ionospheric scatter as a function of Bz (nT) from 1996 to 2015 sorted by MLT sectors for autumn season. The dashed black line indicates the point of normalisation. The top left panel shows the dawn (03-09 MLT) sector, the right upper panel shows the noon (09-15 MLT) sector, the left lower panel shows the dusk (15-21 MLT) and the right lower panel shows the midnight (21-03 MLT) sector.

Hankasalmi Ionospheric scatter against By(GSM) (Summer Solstice)

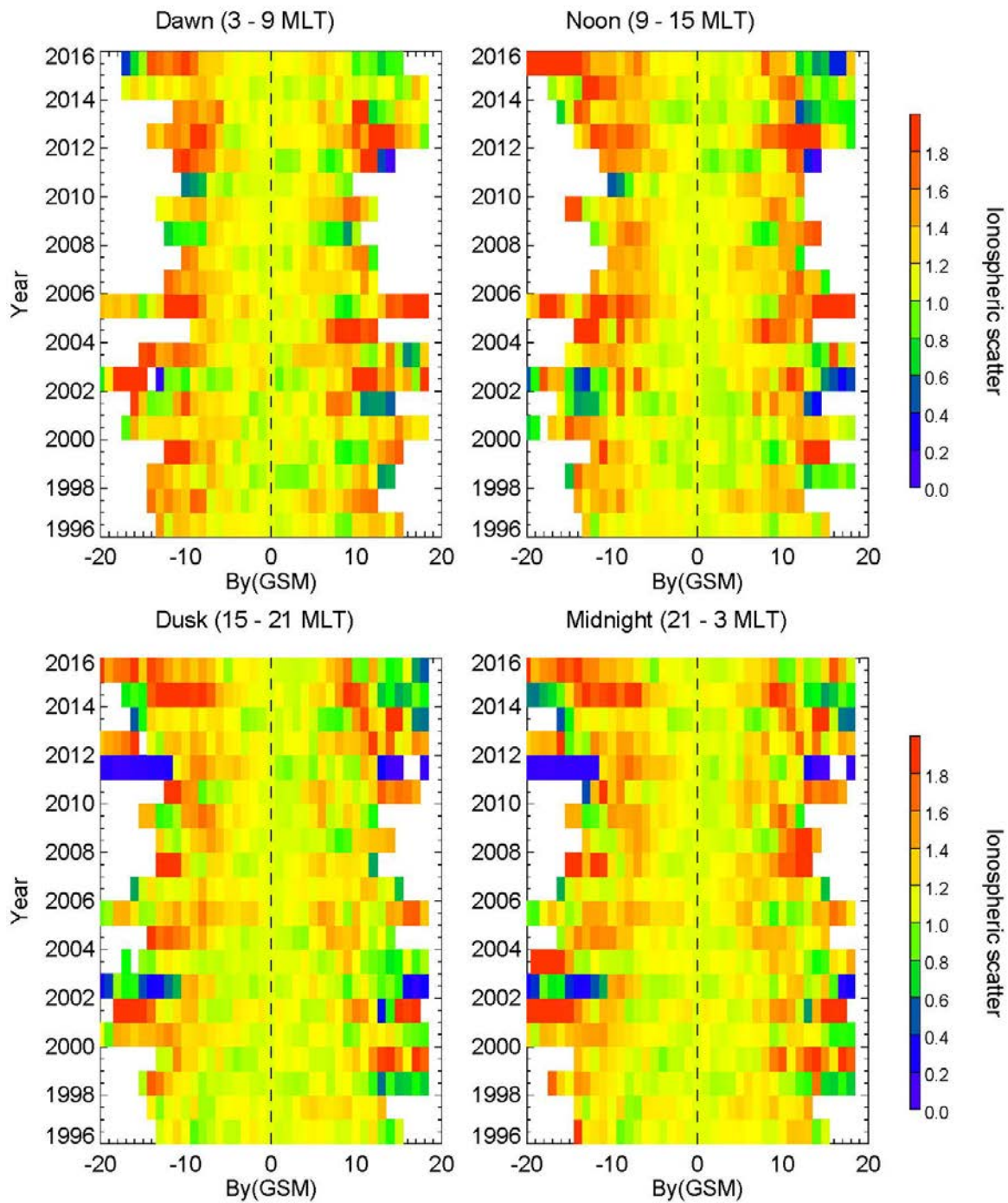


Figure A3.3a. Normalised percentage occurrence of ionospheric scatter as a function of By (nT) from 1996 to 2015 sorted by MLT sectors for summer season. The dashed black line indicates the point of normalisation. The top left panel shows the dawn (03-09 MLT) sector, the right upper panel shows the noon (09-15 MLT) sector, the left lower panel shows the dusk (15-21 MLT) and the right lower panel shows the midnight (21-03 MLT) sector.

Hankasalmi Ionospheric scatter against By(GSM) (Autumn)

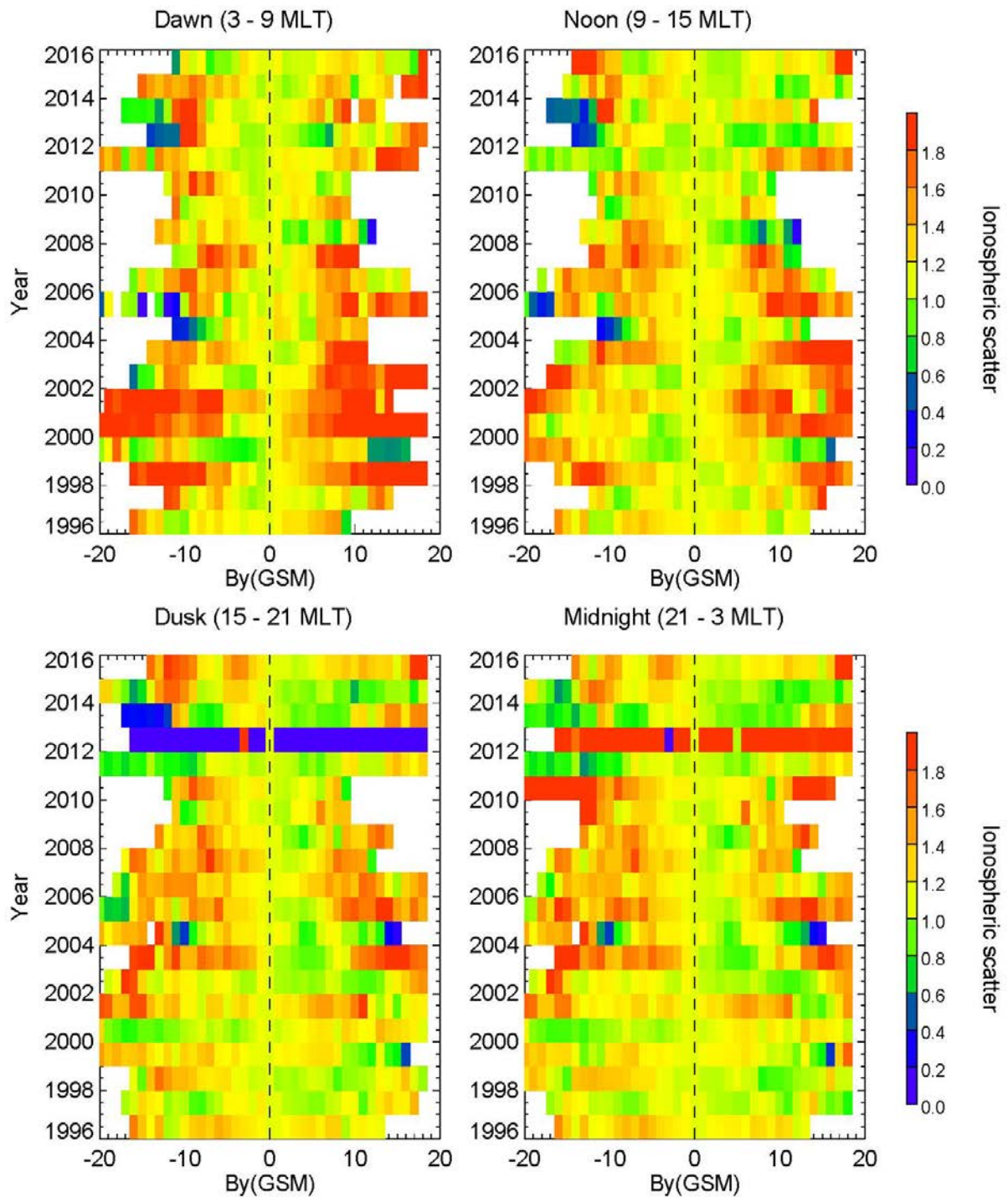


Figure A3.3b. Normalised percentage occurrence of ionospheric scatter as a function of By (nT) from 1996 to 2015 sorted by MLT sectors for autumn season. The dashed black line indicates the point of normalisation. The top left panel shows the dawn (03-09 MLT) sector, the right upper panel shows the noon (09-15 MLT) sector, the left lower panel shows the dusk (15-21 MLT) and the right lower panel shows the midnight (21-03 MLT) sector.

Hankasalmi Ionospheric scatter against By(GSM) (Winter Solstice)

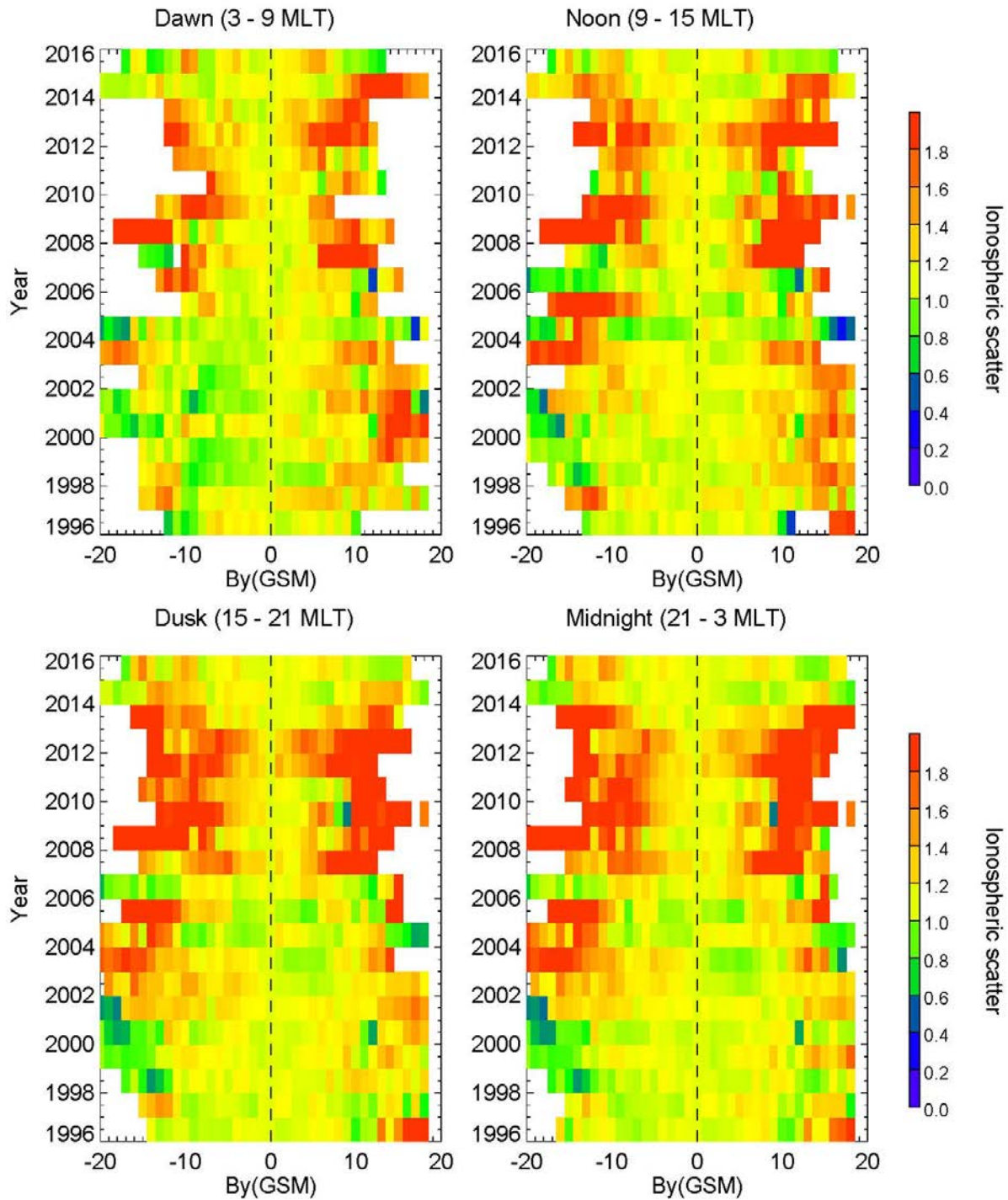


Figure A3.3c. Normalised percentage occurrence of ionospheric scatter as a function of By (nT) from 1996 to 2015 sorted by MLT sectors for winter season. The dashed black line indicates the point of normalisation. The top left panel shows the dawn (03-09 MLT) sector, the right upper panel shows the noon (09-15 MLT) sector, the left lower panel shows the dusk (15-21 MLT) and the right lower panel shows the midnight (21-03 MLT) sector.

Pykkvibaer Ionospheric scatter against Pressure (Summer Solstice)

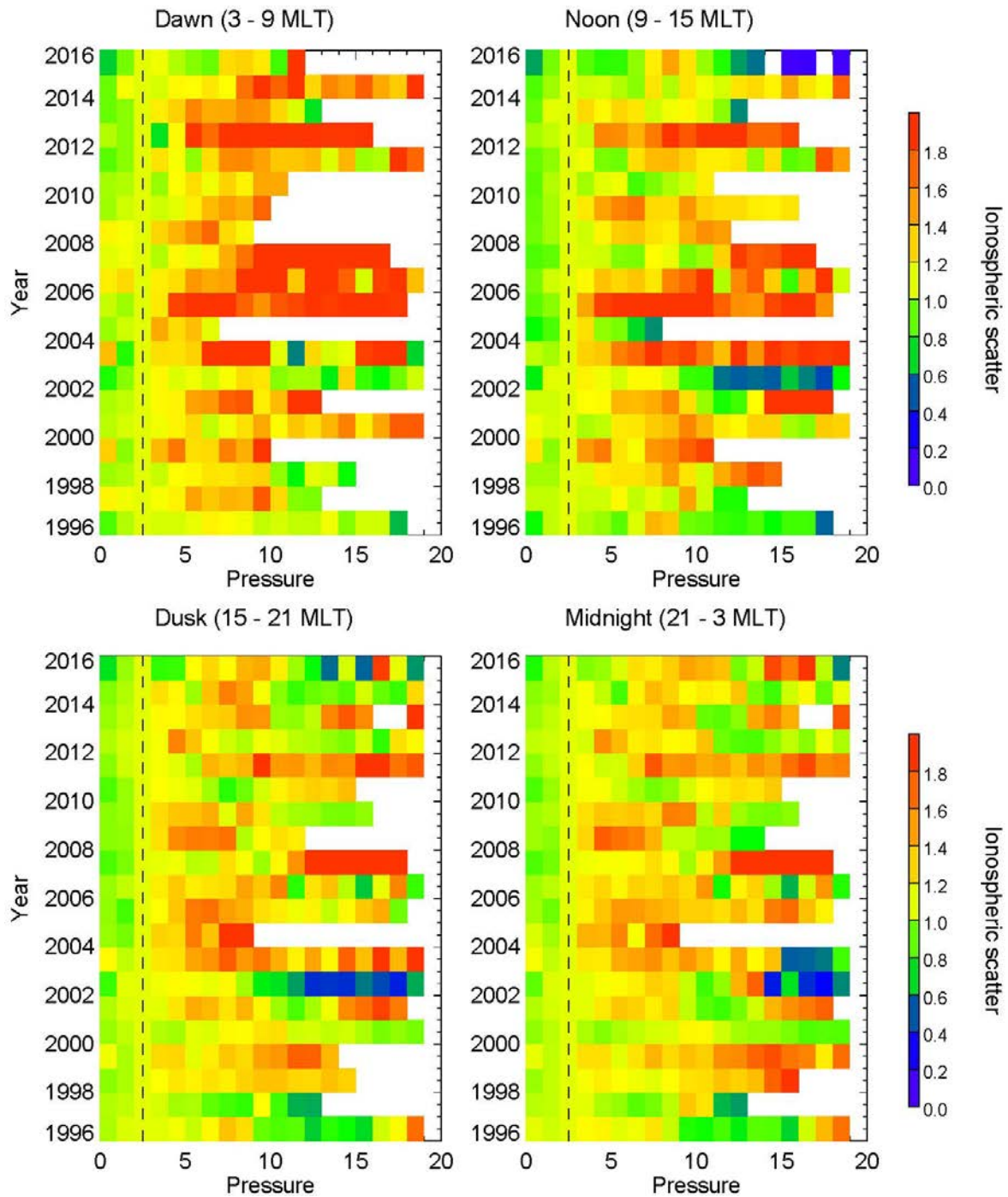


Figure A3.4a. Normalised percentage occurrence of ionospheric scatter as a function of Pressure (nT) from 1996 to 2015 sorted by MLT sectors for summer season. The dashed black line indicates the point of normalisation. The top left panel shows the dawn (03-09 MLT) sector, the right upper panel shows the noon (09-15 MLT) sector, the left lower panel shows the dusk (15-21 MLT) and the right lower panel shows the midnight (21-03 MLT) sector.

Pykkvibaer Ionospheric scatter against Pressure (Autumn)

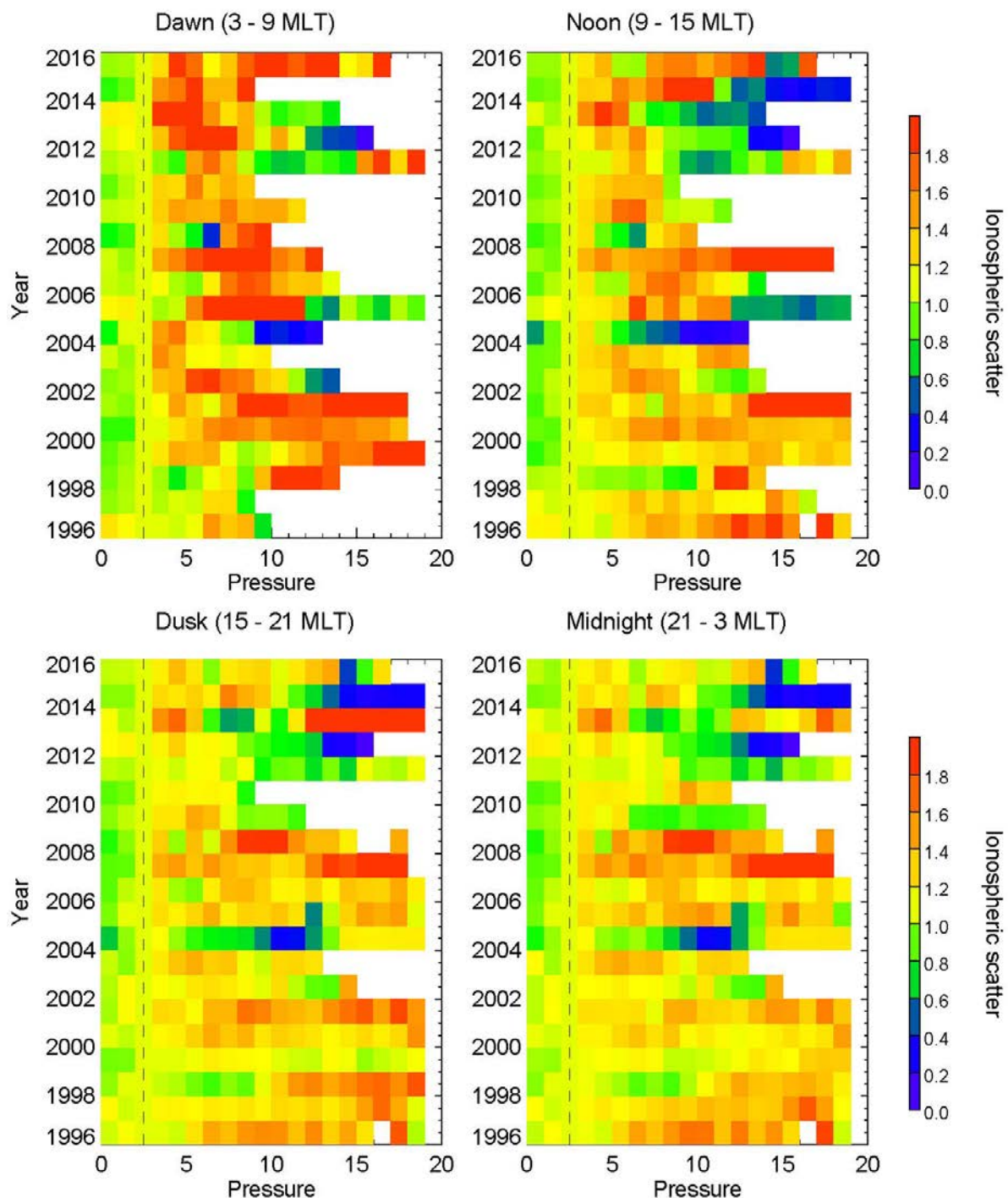


Figure A3.4b. Normalised percentage occurrence of ionospheric scatter as a function of Pressure (nT) from 1996 to 2015 sorted by MLT sectors for autumn season. The dashed black line indicates the point of normalisation. The top left panel shows the dawn (03-09 MLT) sector, the right upper panel shows the noon (09-15 MLT) sector, the left lower panel shows the dusk (15-21 MLT) and the right lower panel shows the midnight (21-03 MLT) sector.

Pykkvibaer Ionospheric scatter against Pressure (Winter Solstice)

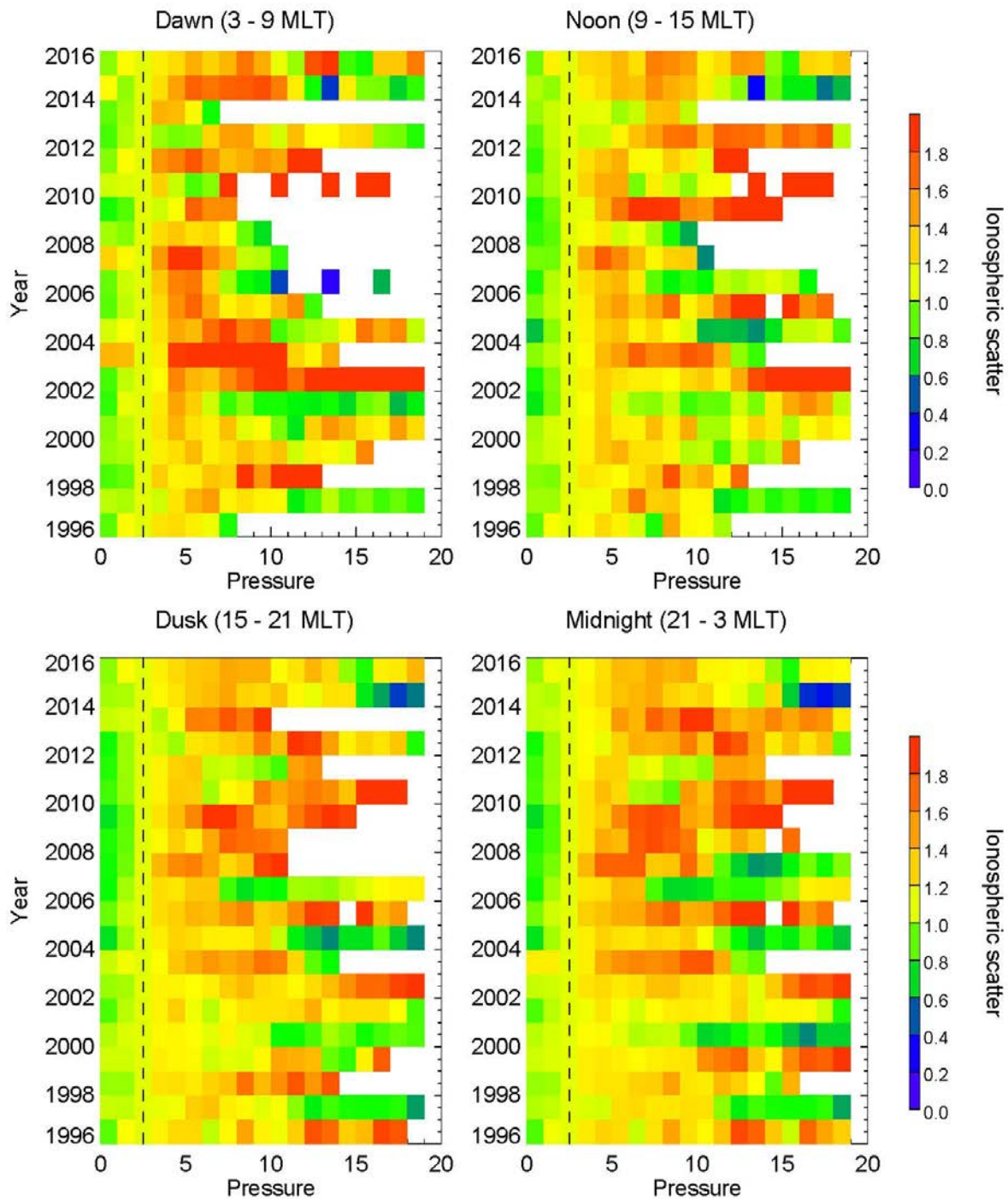


Figure A3.4c. Normalised percentage occurrence of ionospheric scatter as a function of Pressure (nT) from 1996 to 2015 sorted by MLT sectors for winter season. The dashed black line indicates the point of normalisation. The top left panel shows the dawn (03-09 MLT) sector, the right upper panel shows the noon (09-15 MLT) sector, the left lower panel shows the dusk (15-21 MLT) and the right lower panel shows the midnight (21-03 MLT) sector.

Pykkvibaer Ionospheric scatter against Bz(GSM) (Summer Solstice)

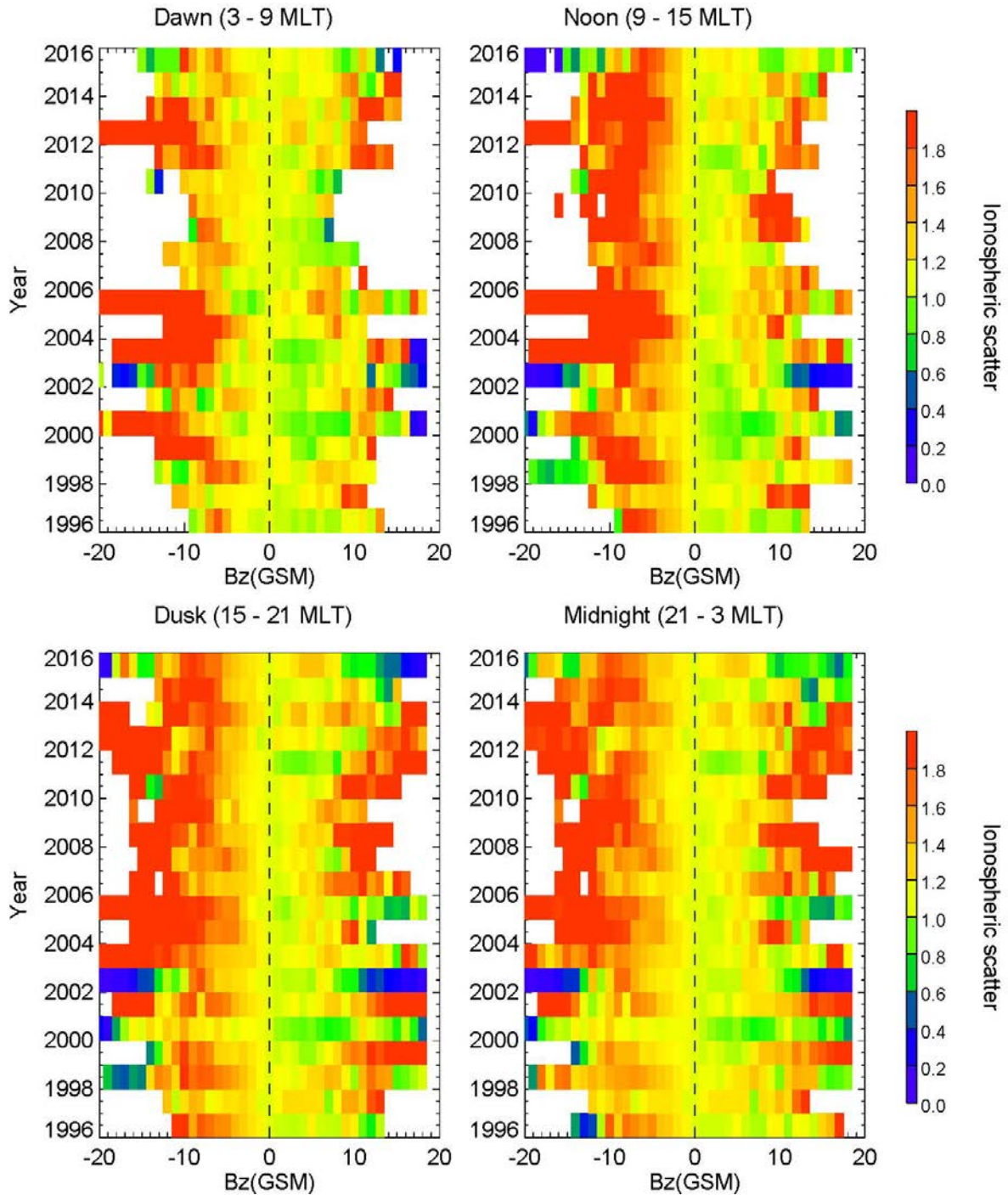


Figure A3.5a. Normalised percentage occurrence of ionospheric scatter as a function of Bz from 1996 to 2015 sorted by MLT sectors for Summer season. The dashed black line indicates the point of normalisation. The top left panel shows the dawn (03-09 MLT) sector, the right upper panel shows the noon (09-15 MLT) sector, the left lower panel shows the dusk (15-21 MLT) and the right lower panel shows the midnight (21-03 MLT) sector.

Pykkvibaer Ionospheric scatter against Bz(GSM) (Autumn)

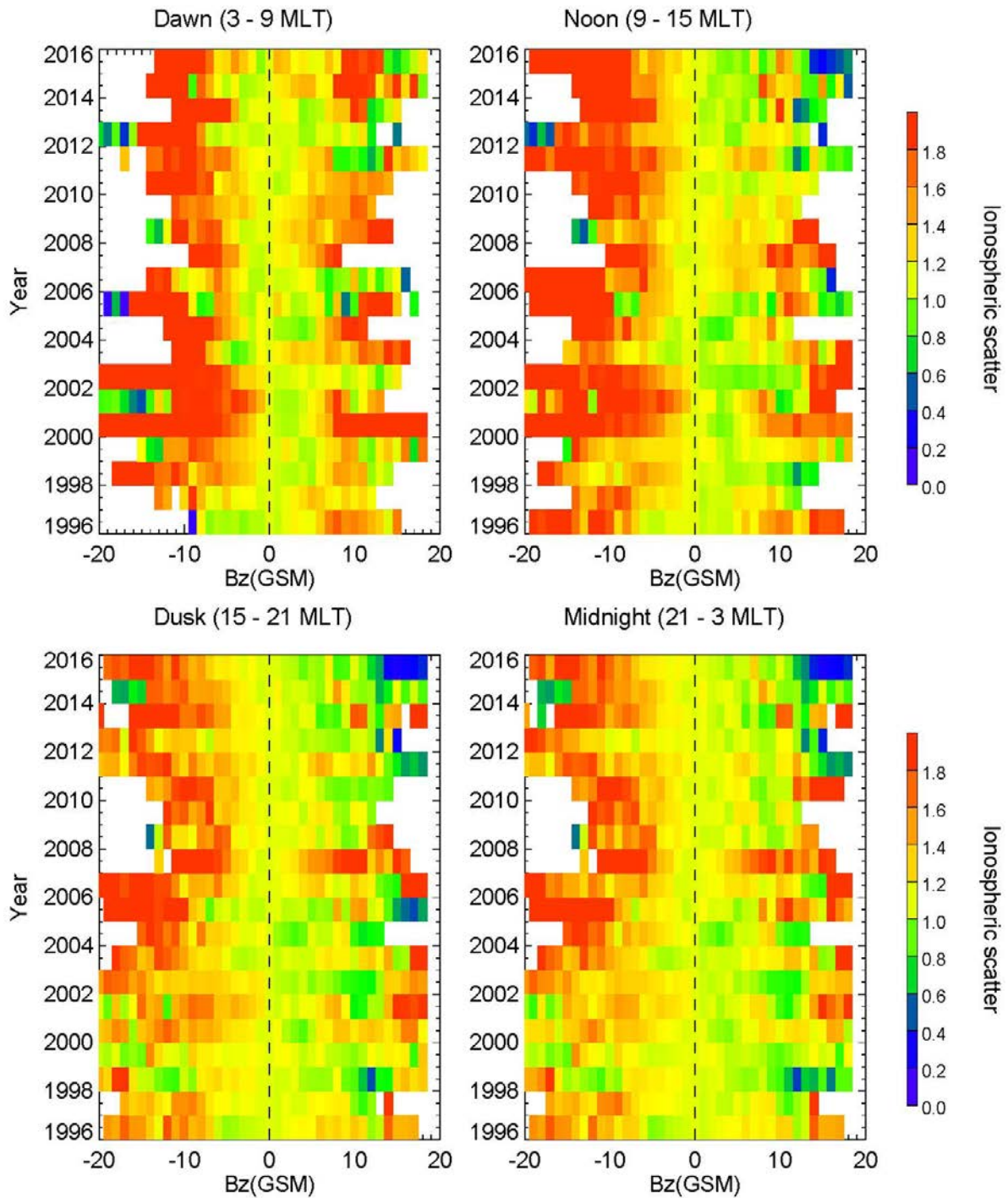


Figure A3.5b. Normalised percentage occurrence of ionospheric scatter as a function of Bz from 1996 to 2015 sorted by MLT sectors for Autumn season. The dashed black line indicates the point of normalisation. The top left panel shows the dawn (03-09 MLT) sector, the right upper panel shows the noon (09-15 MLT) sector, the left lower panel shows the dusk (15-21 MLT) and the right lower panel shows the midnight (21-03 MLT) sector.

Pykkvibaer Ionospheric scatter against Bz(GSM) (Winter Solstice)

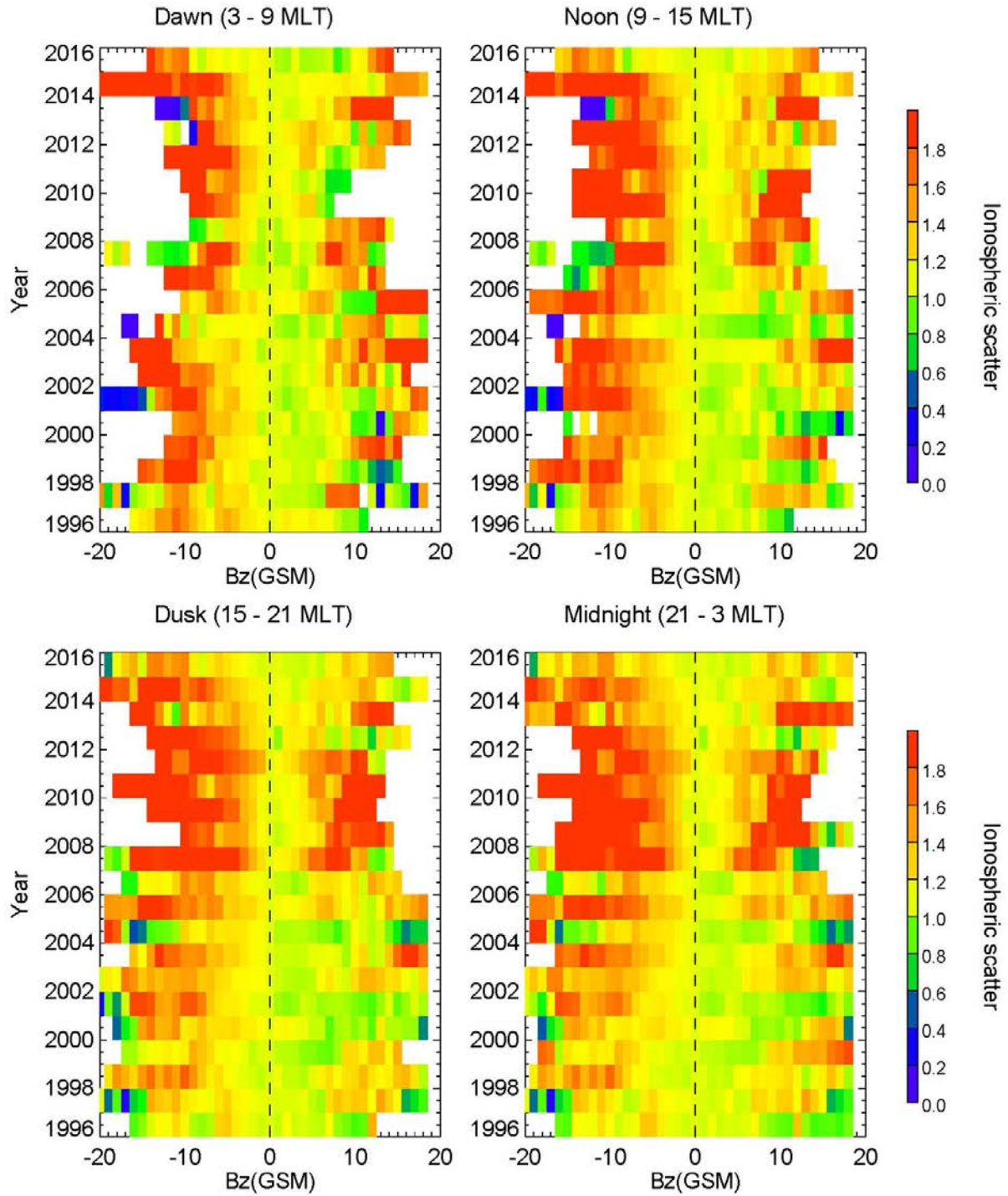


Figure A3.5c. Normalised percentage occurrence of ionospheric scatter as a function of Bz from 1996 to 2015 sorted by MLT sectors for Winter season. The dashed black line indicates the point of normalisation. The top left panel shows the dawn (03-09 MLT) sector, the right upper panel shows the noon (09-15 MLT) sector, the left lower panel shows the dusk (15-21 MLT) and the right lower panel shows the midnight (21-03 MLT) sector.

Pykkvibaer Ionospheric scatter against By(GSM) (Summer Solstice)

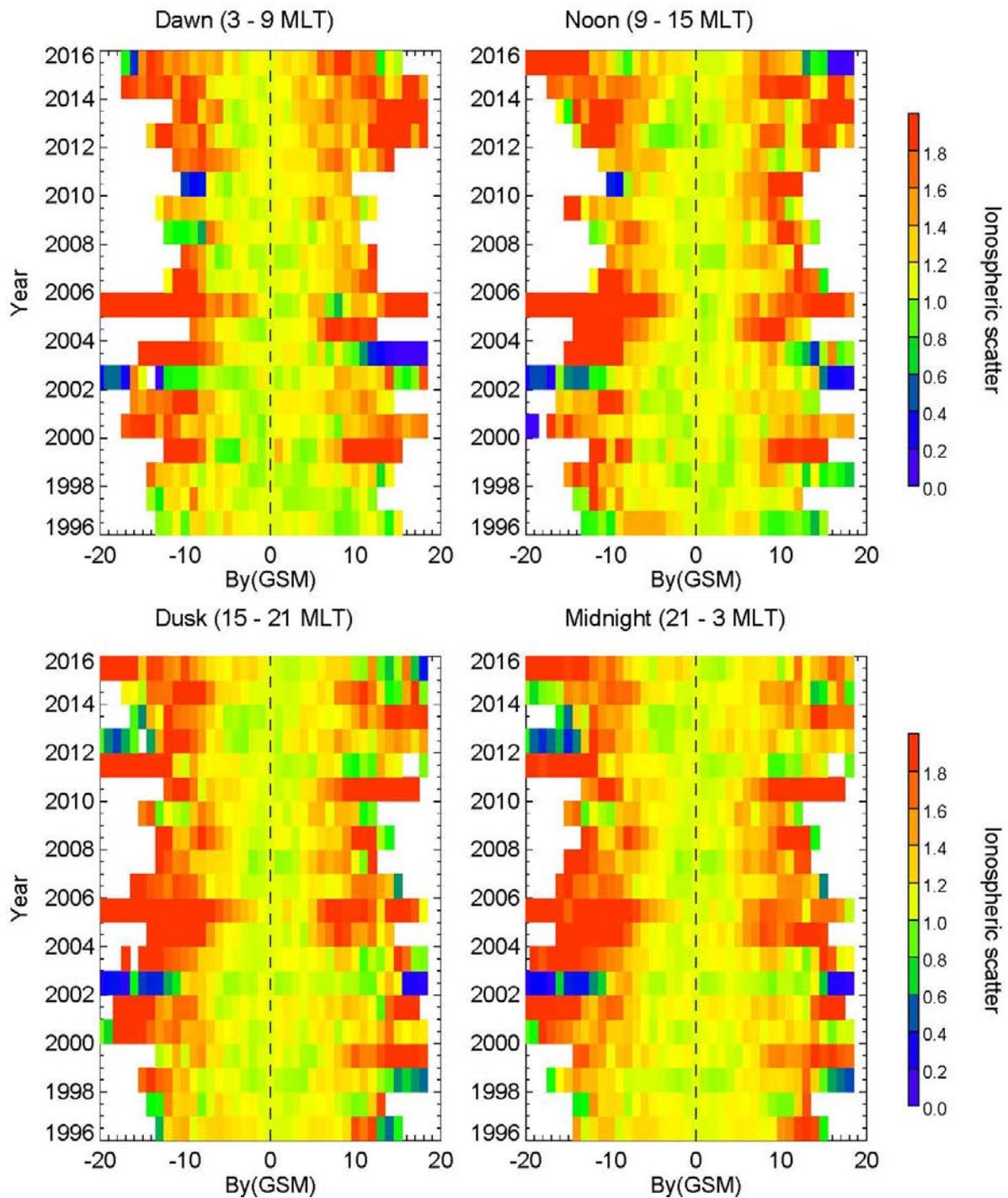


Figure A3.6a. Normalised percentage occurrence of ionospheric scatter as a function of By from 1996 to 2015 sorted by MLT sectors for Summer season. The dashed black line indicates the point of normalisation. The top left panel shows the dawn (03-09 MLT) sector, the right upper panel shows the noon (09-15 MLT) sector, the left lower panel shows the dusk (15-21 MLT) and the right lower panel shows the midnight (21-03 MLT) sector.

Pykkvibaer Ionospheric scatter against By(GSM) (Autumn)

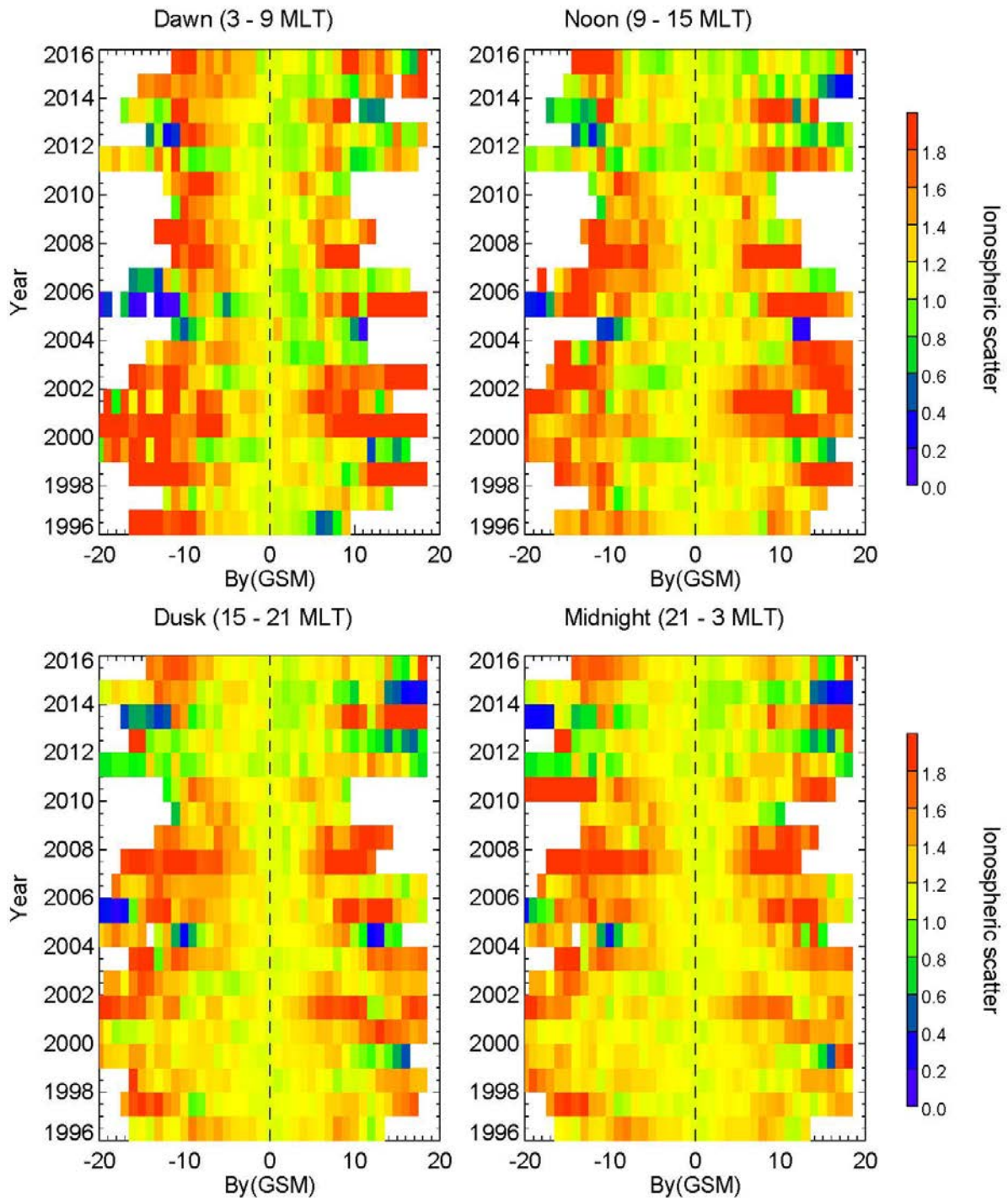


Figure A3.6b. Normalised percentage occurrence of ionospheric scatter as a function of By from 1996 to 2015 sorted by MLT sectors for Autumn season. The dashed black line indicates the point of normalisation. The top left panel shows the dawn (03-09 MLT) sector, the right upper panel shows the noon (09-15 MLT) sector, the left lower panel shows the dusk (15-21 MLT) and the right lower panel shows the midnight (21-03 MLT) sector.

Pykkvibaer Ionospheric scatter against By(GSM) (Winter Solstice)

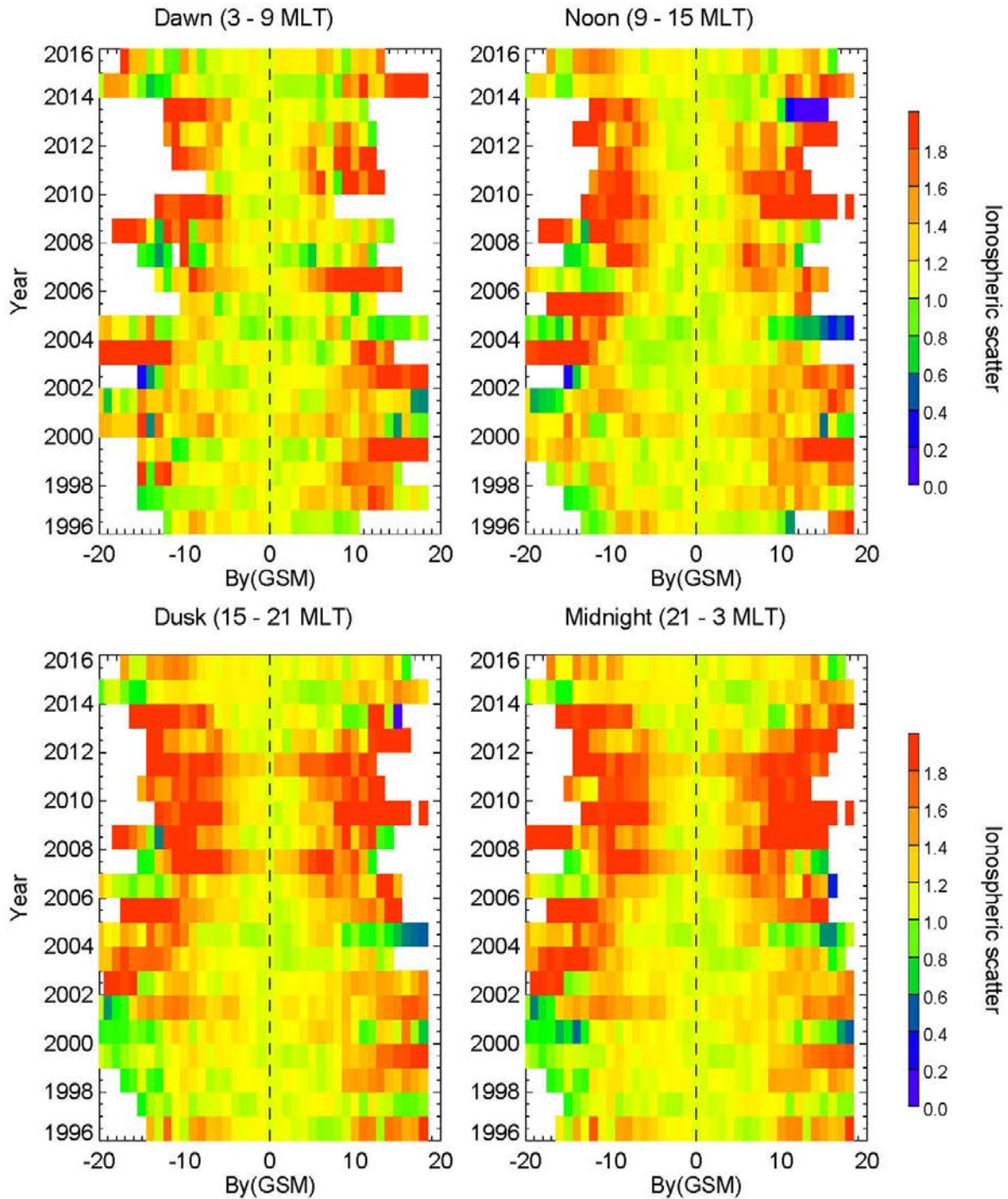


Figure A3.6c. Normalised percentage occurrence of ionospheric scatter as a function of By from 1996 to 2015 sorted by MLT sectors for Winter season. The dashed black line indicates the point of normalisation. The top left panel shows the dawn (03-09 MLT) sector, the right upper panel shows the noon (09-15 MLT) sector, the left lower panel shows the dusk (15-21 MLT) and the right lower panel shows the midnight (21-03 MLT) sector.

Hankasalmi Ionospheric scatter against AU (Summer Solstice)

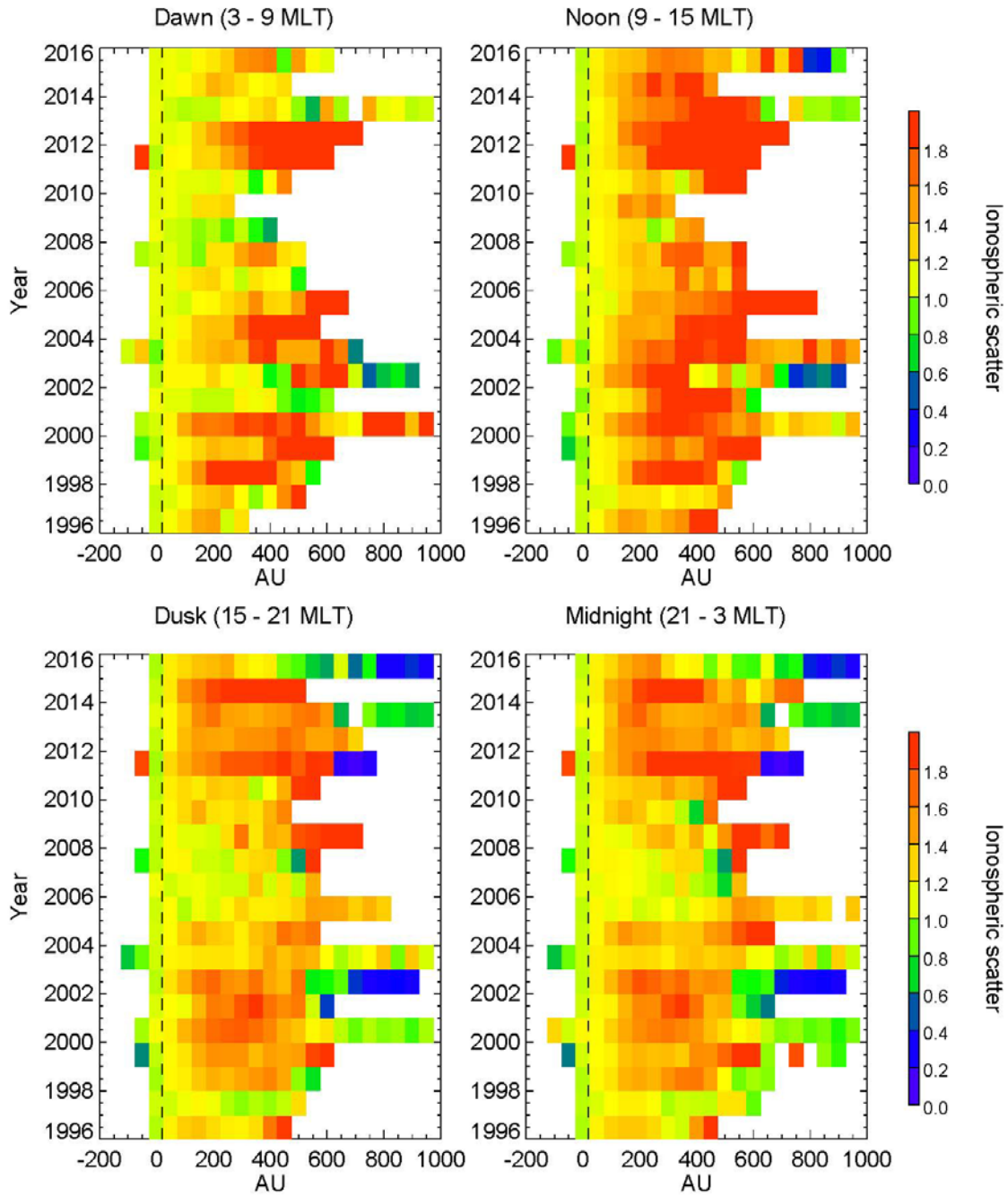


Figure A3.7a. Normalised percentage occurrence of ionospheric scatter as a function of AU from 1996 to 2015 sorted by MLT sectors for Summer season. The dashed black line indicates the point of normalisation. The top left panel shows the dawn (03-09 MLT) sector, the right upper panel shows the noon (09-15 MLT) sector, the left lower panel shows the dusk (15-21 MLT) and the right lower panel shows the midnight (21-03 MLT) sector.

Hankasalmi Ionospheric scatter against AU (Autumn)

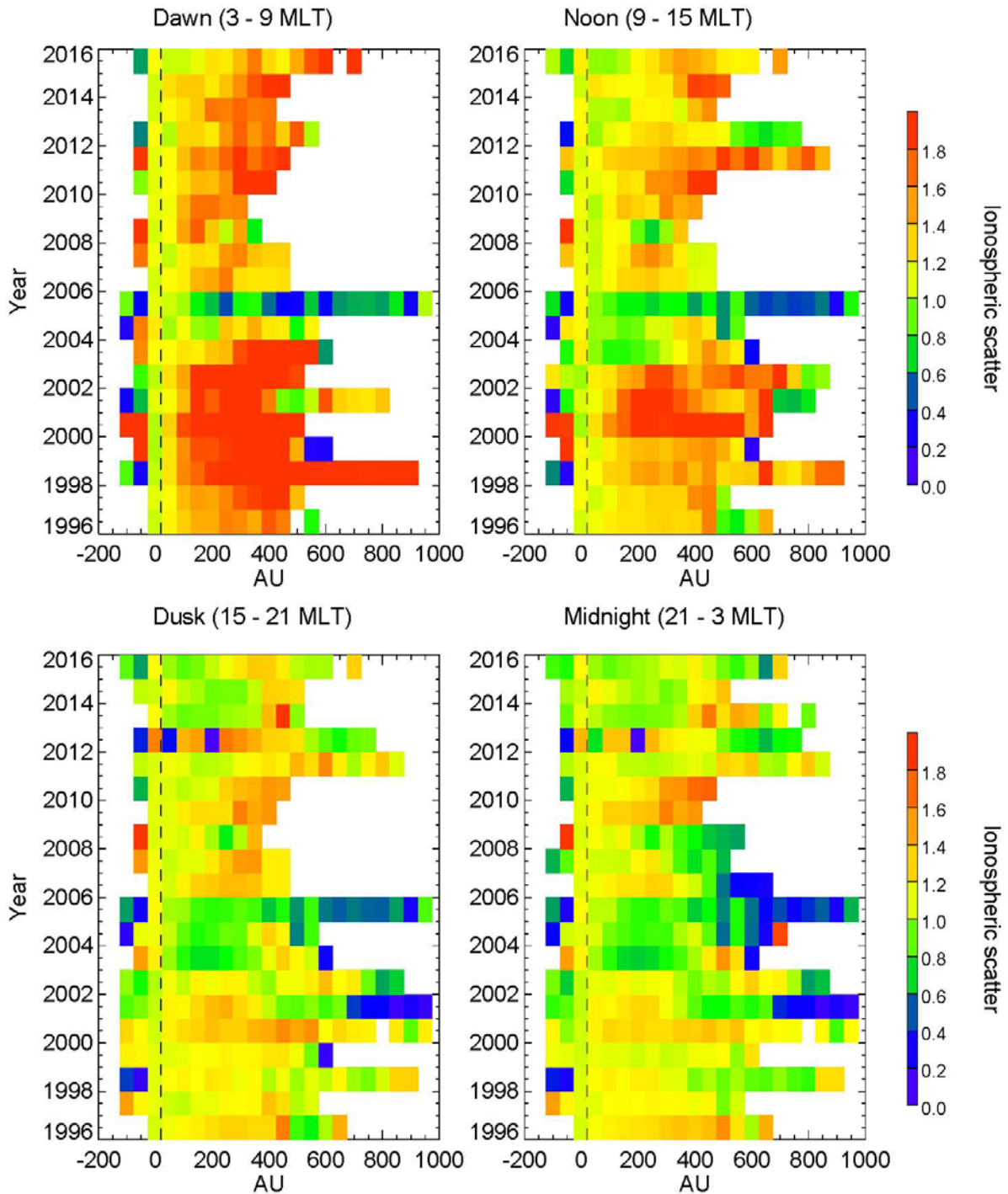


Figure A3.7b. Normalised percentage occurrence of ionospheric scatter as a function of AU from 1996 to 2015 sorted by MLT sectors for Autumn season. The dashed black line indicates the point of normalisation. The top left panel shows the dawn (03-09 MLT) sector, the right upper panel shows the noon (09-15 MLT) sector, the left lower panel shows the dusk (15-21 MLT) and the right lower panel shows the midnight (21-03 MLT) sector.

Hankasalmi Ionospheric scatter against AU (Winter Solstice)

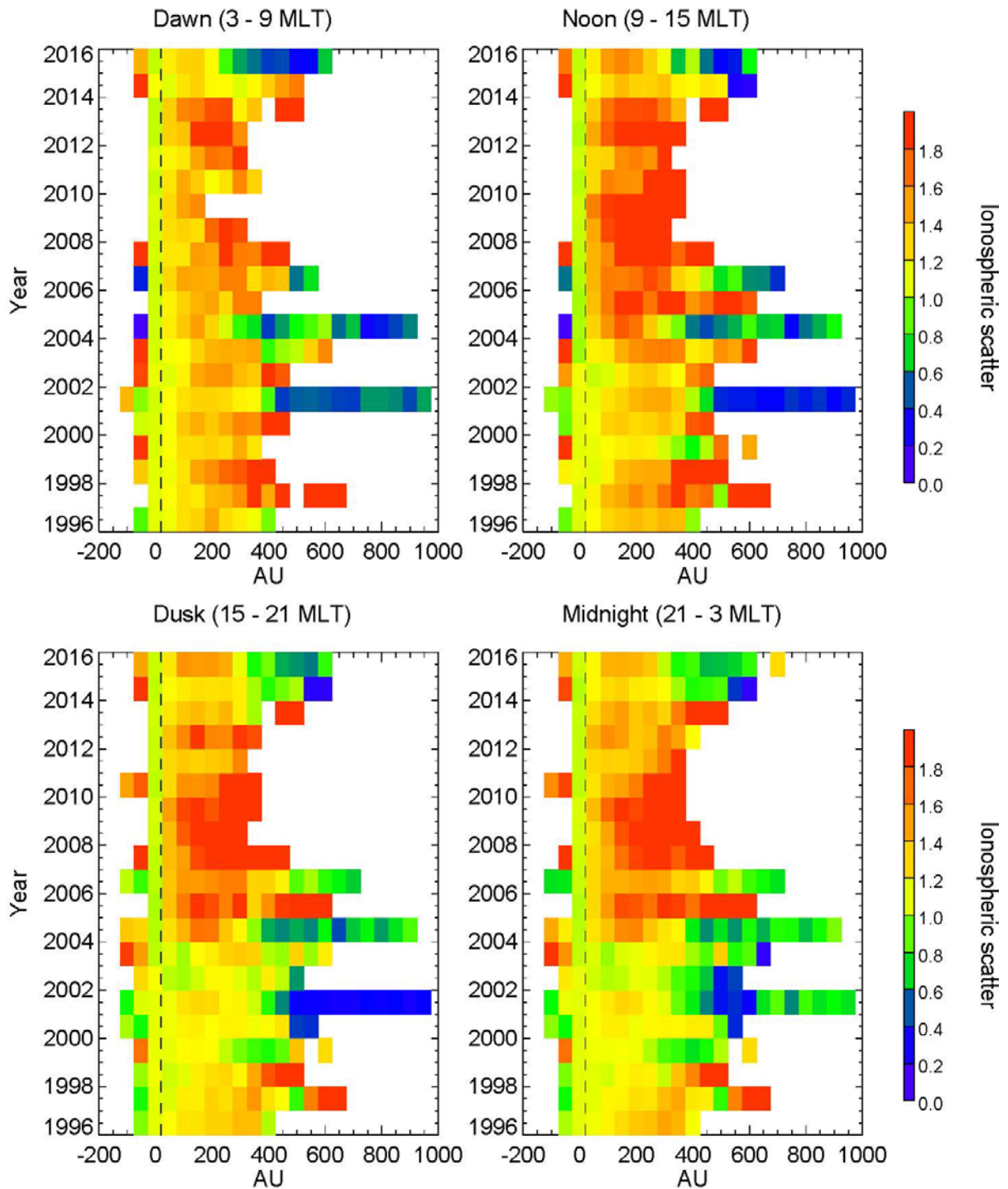


Figure A3.7c. Normalised percentage occurrence of ionospheric scatter as a function of AU from 1996 to 2015 sorted by MLT sectors for winter season. The dashed black line indicates the point of normalisation. The top left panel shows the dawn (03-09 MLT) sector, the right upper panel shows the noon (09-15 MLT) sector, the left lower panel shows the dusk (15-21 MLT) and the right lower panel shows the midnight (21-03 MLT) sector.

Hankasalmi Ionospheric scatter against AE (Summer Solstice)

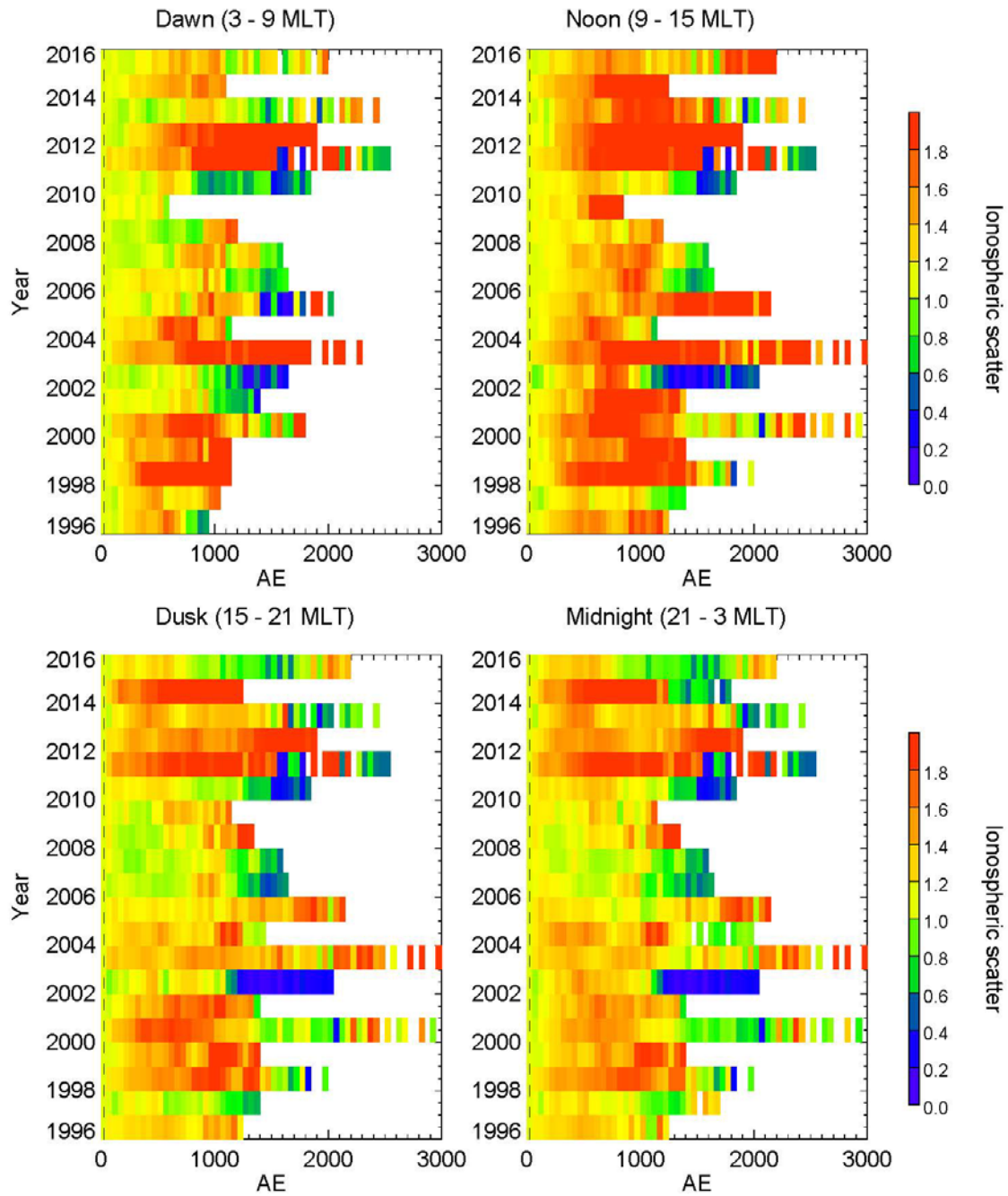


Figure A3.8a. Normalised percentage occurrence of ionospheric scatter as a function of AE from 1996 to 2015 sorted by MLT sectors for Summer season. The dashed black line indicates the point of normalisation. The top left panel shows the dawn (03-09 MLT) sector, the right upper panel shows the noon (09-15 MLT) sector, the left lower panel shows the dusk (15-21 MLT) and the right lower panel shows the midnight (21-03 MLT) sector.

Hankasalmi Ionospheric scatter against AE (Autumn)

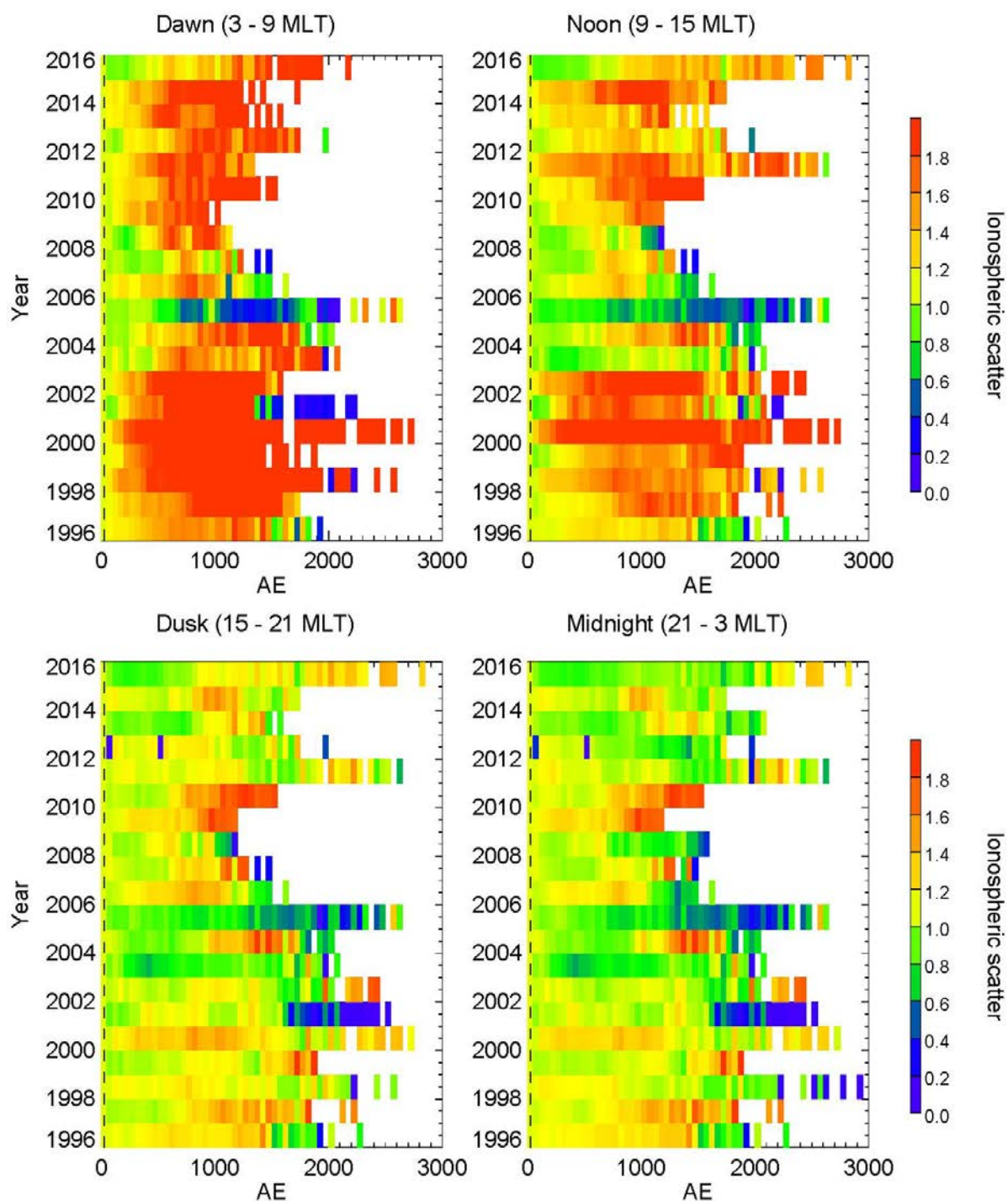


Figure A3.8b. Normalised percentage occurrence of ionospheric scatter as a function of AE from 1996 to 2015 sorted by MLT sectors for Autumn season. The dashed black line indicates the point of normalisation. The top left panel shows the dawn (03-09 MLT) sector, the right upper panel shows the noon (09-15 MLT) sector, the left lower panel shows the dusk (15-21 MLT) and the right lower panel shows the midnight (21-03 MLT) sector.

Hankasalmi Ionospheric scatter against AE (Winter Solstice)

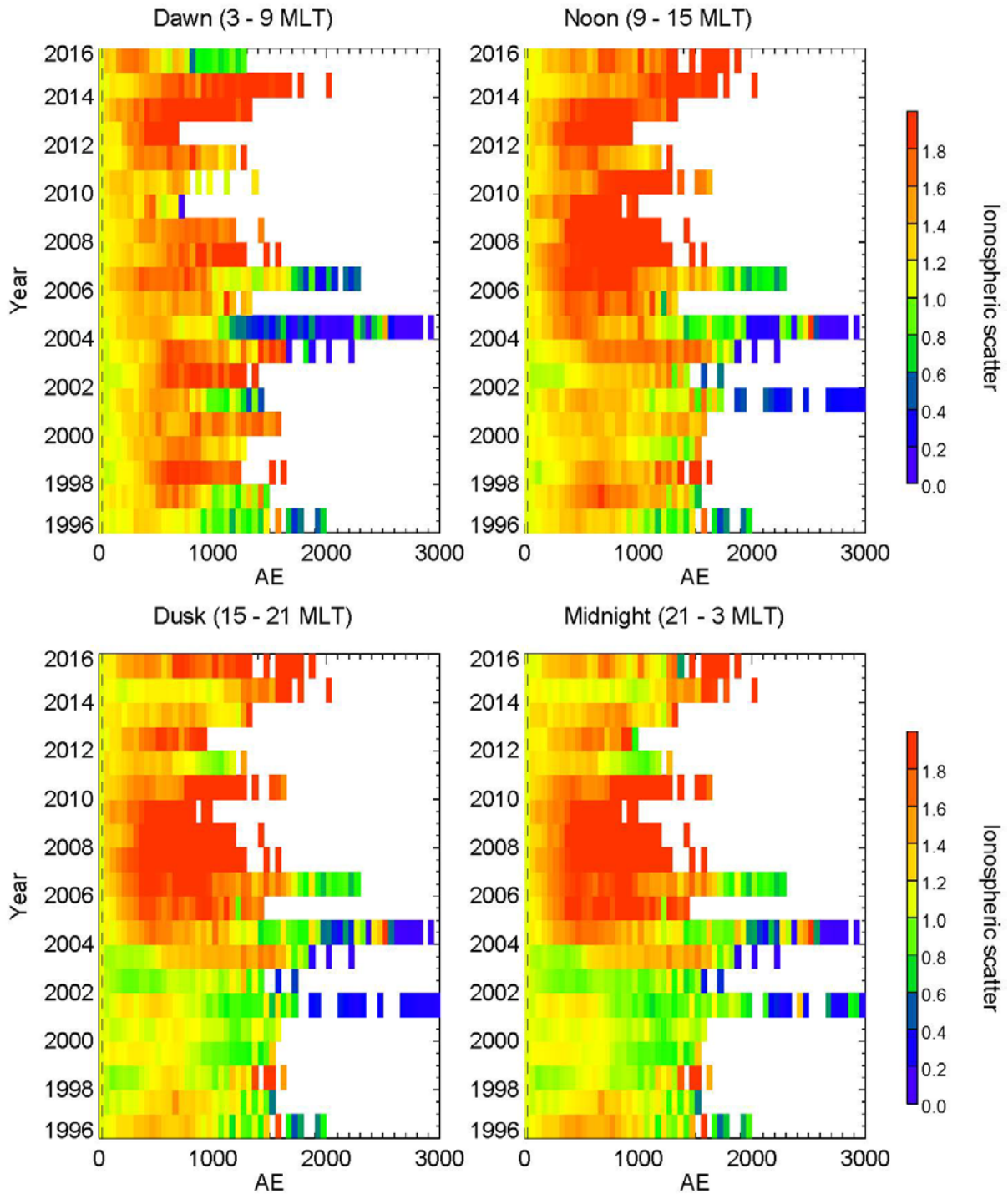


Figure A3.8c. Normalised percentage occurrence of ionospheric scatter as a function of AE from 1996 to 2015 sorted by MLT sectors for Winter season. The dashed black line indicates the point of normalisation. The top left panel shows the dawn (03-09 MLT) sector, the right upper panel shows the noon (09-15 MLT) sector, the left lower panel shows the dusk (15-21 MLT) and the right lower panel shows the midnight (21-03 MLT) sector.

Pykkvibaer Ionospheric scatter against AU (Summer Solstice)

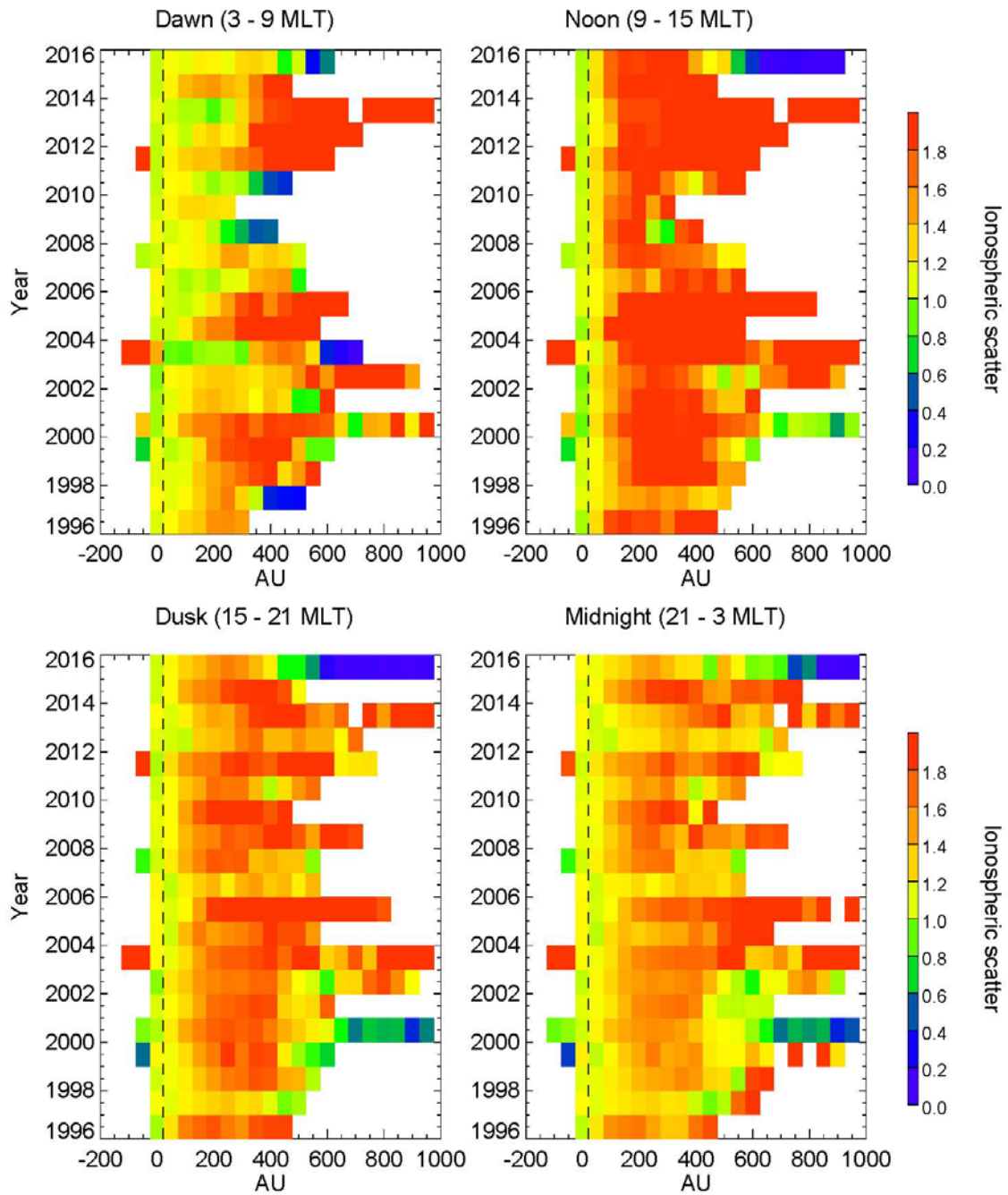


Figure A3.9a. Normalised percentage occurrence of ionospheric scatter as a function of AU from 1996 to 2015 sorted by MLT sectors for Summer season. The dashed black line indicates the point of normalisation. The top left panel shows the dawn (03-09 MLT) sector, the right upper panel shows the noon (09-15 MLT) sector, the left lower panel shows the dusk (15-21 MLT) and the right lower panel shows the midnight (21-03 MLT) sector.

Pykkvibaer Ionospheric scatter against AU (Autumn)

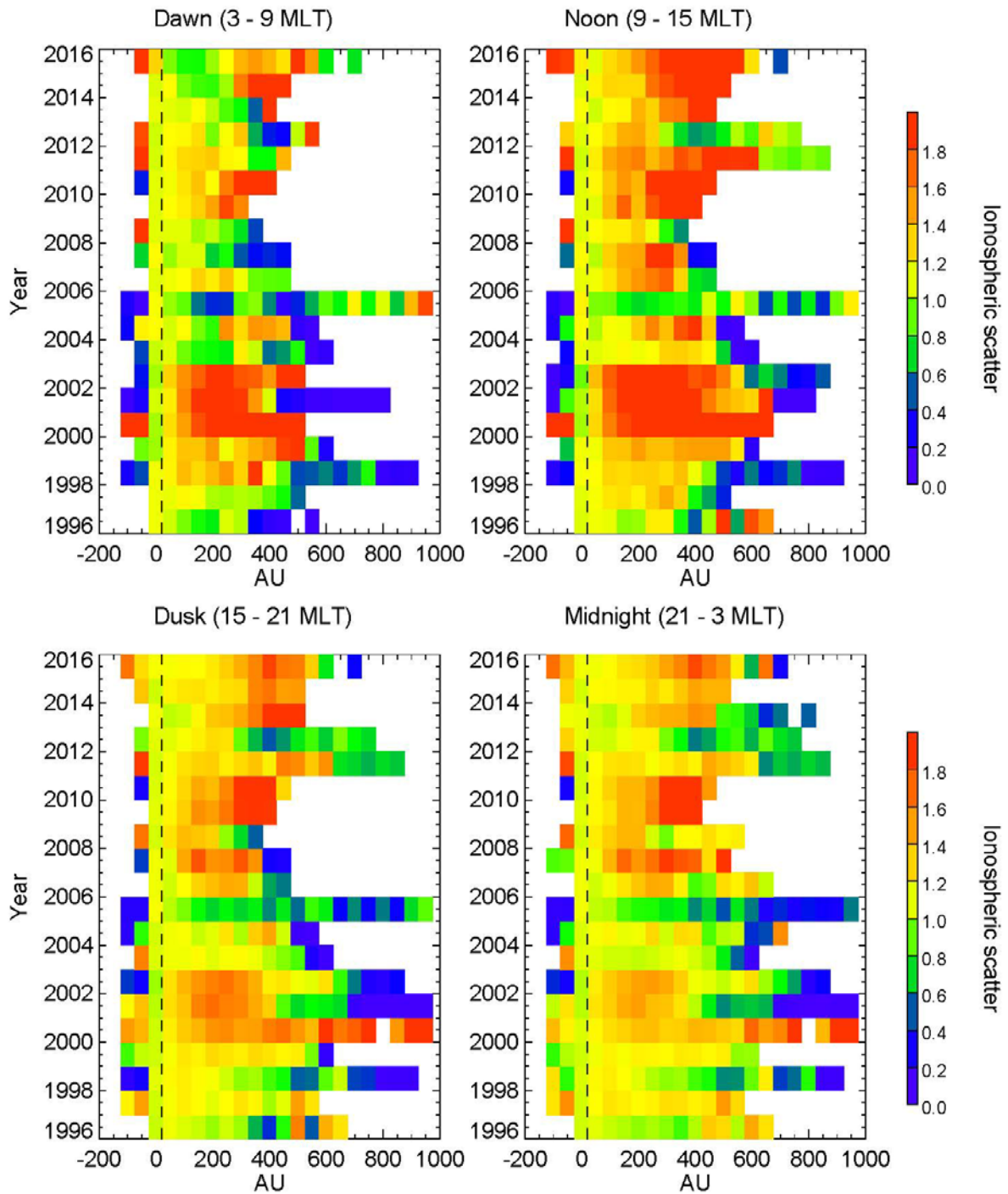


Figure A3.9b. Normalised percentage occurrence of ionospheric scatter as a function of AU from 1996 to 2015 sorted by MLT sectors for Autumn season. The dashed black line indicates the point of normalisation. The top left panel shows the dawn (03-09 MLT) sector, the right upper panel shows the noon (09-15 MLT) sector, the left lower panel shows the dusk (15-21 MLT) and the right lower panel shows the midnight (21-03 MLT) sector.

Pykkvibaer Ionospheric scatter against AU (Winter Solstice)

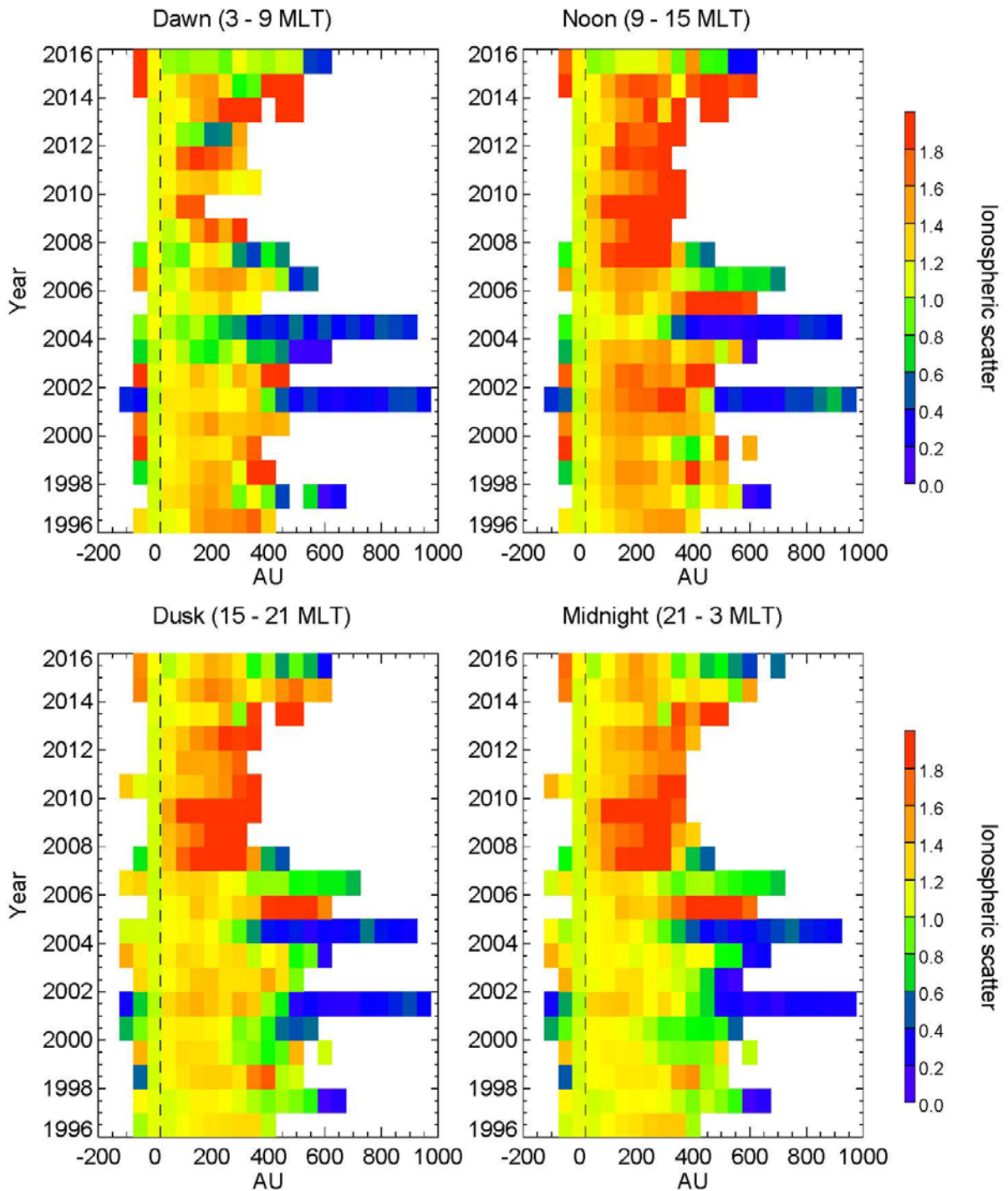


Figure A3.9c. Normalised percentage occurrence of ionospheric scatter as a function of AU from 1996 to 2015 sorted by MLT sectors for Winter season. The dashed black line indicates the point of normalisation. The top left panel shows the dawn (03-09 MLT) sector, the right upper panel shows the noon (09-15 MLT) sector, the left lower panel shows the dusk (15-21 MLT) and the right lower panel shows the midnight (21-03 MLT) sector.

Pykkvibaer Ionospheric scatter against AE (Summer Solstice)

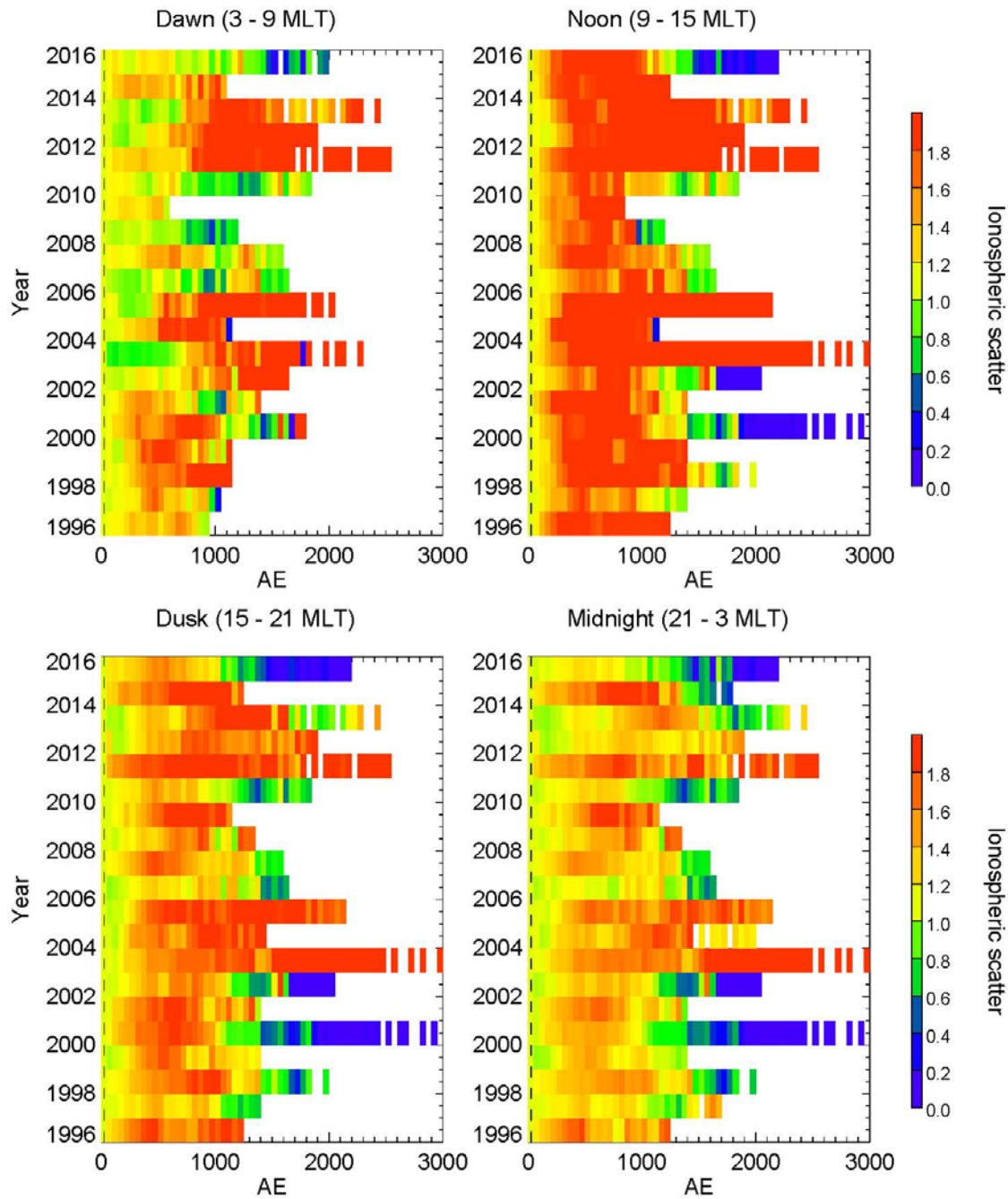


Figure A3.10a. Normalised percentage occurrence of ionospheric scatter as a function of AE from 1996 to 2015 sorted by MLT sectors for Summer season. The dashed black line indicates the point of normalisation. The top left panel shows the dawn (03-09 MLT) sector, the right upper panel shows the noon (09-15 MLT) sector, the left lower panel shows the dusk (15-21 MLT) and the right lower panel shows the midnight (21-03 MLT) sector.

Pykkvibaer Ionospheric scatter against AE (Autumn)

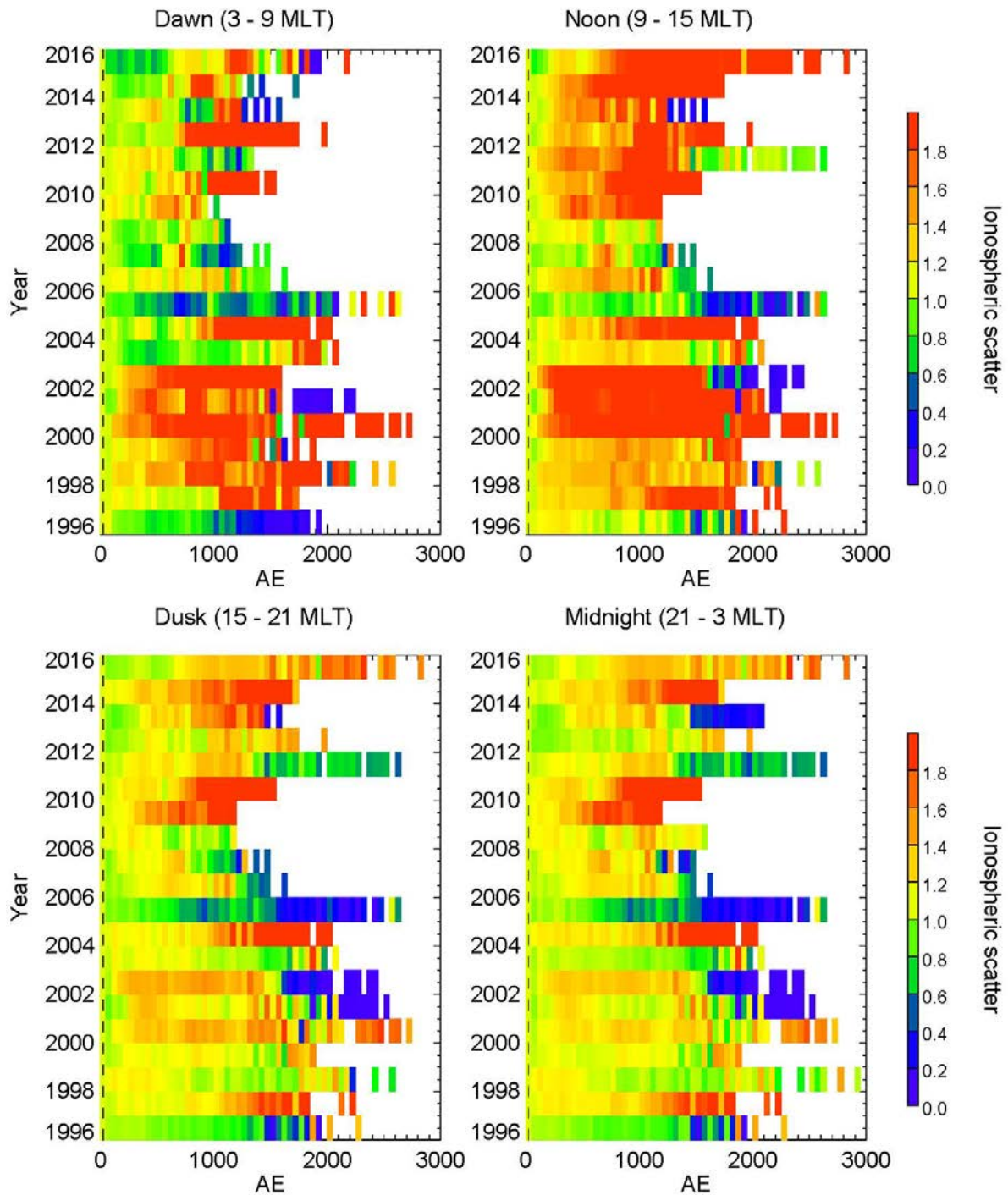


Figure A3.10b. Normalised percentage occurrence of ionospheric scatter as a function of AE from 1996 to 2015 sorted by MLT sectors for Autumn season. The dashed black line indicates the point of normalisation. The top left panel shows the dawn (03-09 MLT) sector, the right upper panel shows the noon (09-15 MLT) sector, the left lower panel shows the dusk (15-21 MLT) and the right lower panel shows the midnight (21-03 MLT) sector.

Pykkvibaer Ionospheric scatter against AE (Winter Solstice)

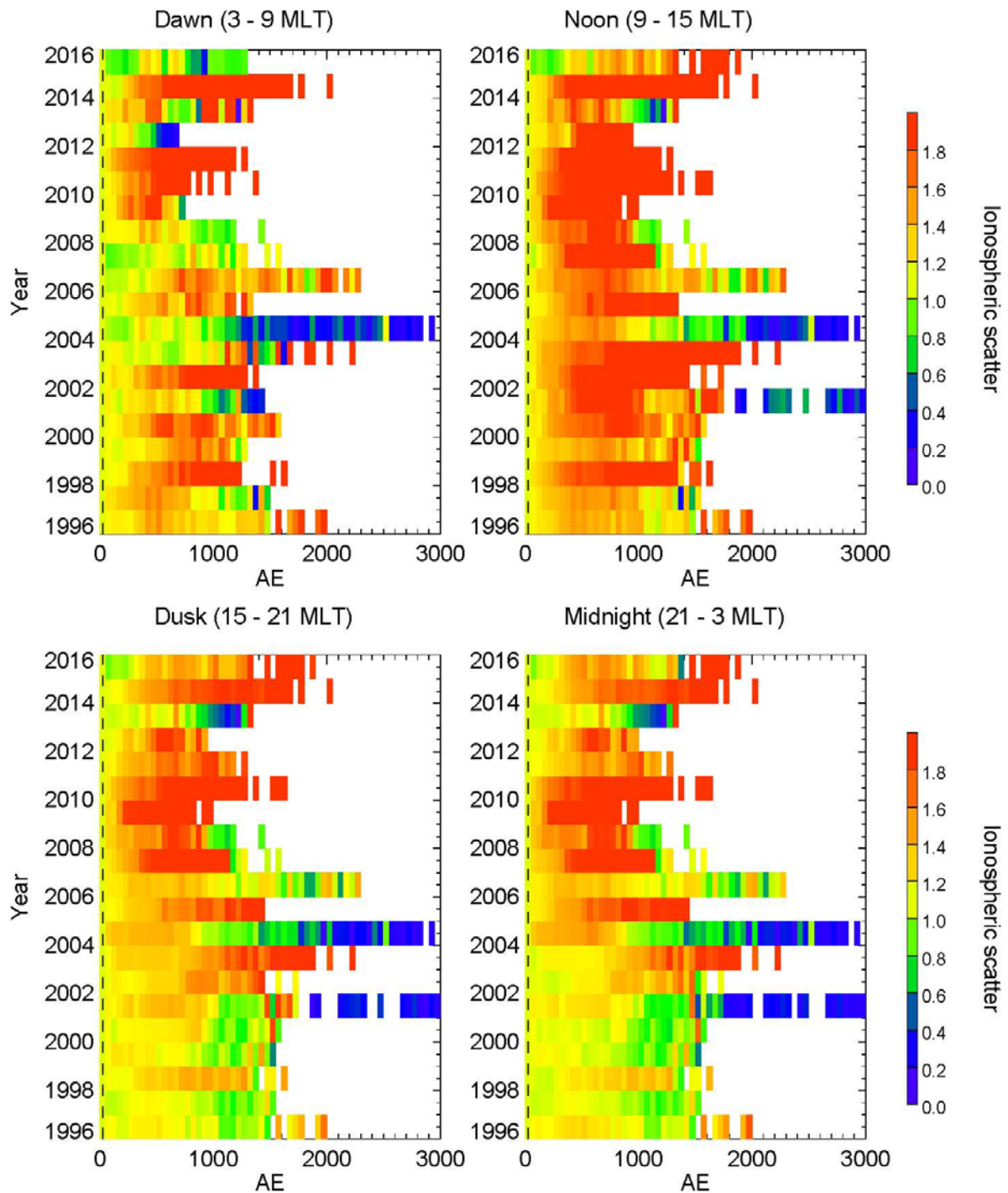


Figure A3.10c. Normalised percentage occurrence of ionospheric scatter as a function of AE from 1996 to 2015 sorted by MLT sectors for winter season. The dashed black line indicates the point of normalisation. The top left panel shows the dawn (03-09 MLT) sector, the right upper panel shows the noon (09-15 MLT) sector, the left lower panel shows the dusk (15-21 MLT) and the right lower panel shows the midnight (21-03 MLT) sector.

References

- Acuna, M., Ogilvie, K., Baker, D., Curtis, S., Fairfield, D., and Mish, W.: The Global Geospace Science Program and its investigations, *Space Science Reviews*, 71, 5–21, doi: 10.1007/BF00751323, 1995.
- Akasofu, S.-I.: The development of the auroral substorm, *Planetary and Space Science*, 12, 273 – 282, doi: [http://dx.doi.org/10.1016/0032-0633\(64\)90151-5](http://dx.doi.org/10.1016/0032-0633(64)90151-5), 1964
- Akasofu, S.-I.: The roles of the north-south component of the interplanetary magnetic field on large-scale auroral dynamics observed by the DMSP satellite, *Planetary and Space Science*, 23, 1349 – 1354, doi: [http://dx.doi.org/10.1016/0032-0633\(75\)90030-6](http://dx.doi.org/10.1016/0032-0633(75)90030-6), 1975.
- Baker K. SuperDARN. <http://bobweigel.net/spaceweather/images/SuperDARN-GMU.pdf>. Accessed December 12, 2015.
- Ballatore, P., Villain, J.P., Vilmer, N. & Pick, M. 2000, "The influence of the interplanetary medium on SuperDARN radar scattering occurrence", *Annales Geophysicae*, vol. 18, no. 12, pp. 1576-1583.
- Baumjohann, W. and Treumann, R. A., eds.: Basic Space Plasma Physics, Imperial College Press, London, UK, 1997.
- Burch, J.L. (1987) 'Plasma Populations in the Magnetosphere, in Akasofu, S.-I. and Kamide, Y. (eds.) The Solar Wind and the Earth 1987. Tokyo: Terra Scientific Publishing Company, pp. 103-122
- Carter, B.A. & Makarevich, R.A. 2010, "On the diurnal variation of the E-region coherent HF echo occurrence", *Journal of Atmospheric and Solar-Terrestrial Physics*, vol. 72, no. 7–8, pp. 570-582.
- Cowley, S. W. H.: Solar wind control of magnetospheric convection, in *Achievements of the International Magnetospheric Study (IMS)*, edited by B. Battrock and E. Rolfe, vol. 217 of ESA Special Publication, pp. 483–494, 1984.
- Chen Y.I., Liu J.Y., Chen S.C., Statistical investigation of the saturation effect on sunspot on the ionospheric foF2, *Phys. Chem. Earth(C)*, 25, 359-362, 2000.
- Chisham, G., Lester, M., Milan, S.E., Freeman, M.P., Bristow, W.A., Grocott, A., McWilliams, K.A., Ruohoniemi, J.M., Yeoman, T.K., Dyson, P.L., Greenwald, R.A., Kikuchi, T., Pinnock, M., Rash, J.P.S., Sato, N., Sofko, G.J., Villain, J.-. & Walker, A.D.M. 2007, "A decade of the Super Dual Auroral Radar Network (SuperDARN): scientific achievements, new techniques and future directions", *Surveys in Geophysics*, vol. 28, no. 1, pp. 33-109.
- Cowley, S. W. H.: Magnetosphere-ionosphere interactions: A tutorial review, in

Magnetospheric Current Systems, vol. 118 of Geophysical Monograph Series, pp. 91–106, American Geophysical Union, Washington, DC, USA, URL <http://www.agu.org/books/gm/v118/GM118p0091/GM118p0091.shtml>, 2000.

Davis, T. N., and M. Sugiura (1966), Auroral electrojet activity index a_e and its universal time variations, *J. Geophys. Res.*, 71, 785 – 801, doi:10.1029/JZ071i003p00785. 18, 171

Dryer, M. (1987) 'Solar Wind and Heliosphere', in Akasofu, S-I. and Kamide, Y. (eds.) *The Solar Wind and the Earth 1987*. Tokyo: Terra Scientific Publishing Company, pp. 21-35

Dungey, J. W.: Interplanetary magnetic field and the auroral zones, *Physics Review Letters*, 6, 47–48, 1961.

Farley, D. T. 1963, "A plasma instability resulting in field aligned irregularities", *J. Geophys. Res.*, 63, 6083-6097.

Fejer, B. G., and M. C. Kelley, Ionospheric irregularities, *Rev. Geophys. Space Phys.*, 18, 401, 1980.

Fejer, B. G. and J. F. Providakes. 1987, "High-latitude E-region irregularities: new results", *Phys. Scripta*, T18, 167 -178

Forbes J.M., Scott E.P., Xiaoli Z., Variability of the ionosphere, *J. Atmos. Solar- Terr. Phys.* 62, 685-693, 2000.

Grant, I. S. and Phillips, W. R.: *Electromagnetism*, John Wiley & Sons, Chicester, UK, 2 edn., 1990

Greenwald, R.A., Baker, K.B., Dudeney, J.R., Pinnock, M., Jones, T.B., Thomas, E.C., Villain, J.-., Cerisier, J.-., Senior, C., Hanuise, C., Hunsucker, R.D., Sofko, G., Koehler, J., Nielsen, E., Pellinen, R., Walker, A.D.M., Sato, N. & Yamagishi, H. 1995, "DARN/SuperDARN - A global view of the dynamics of high-latitude convection", *Space Science Reviews*, vol. 71, no. 1-4, pp. 761-796.

Greenwald, R.A., Baker, K.B., Hutchins, R.A. & Hanuise, C. 1985, "HF phased-array radar for studying small-scale structure in the high-latitude ionosphere.", *Radio Science*, vol. 20, no. 1, pp. 63-79.

Hapgood, M. (2002). *The Science of Space Weather*. *Annals Geophysicae* 20, 875-877.

Hargreaves J.K., *The upper Atmospheric and Solar-Terrestrial Relations, an introduction to the aerospace environment*, Van Nostrand Reinhold Company, New York, 1979.

Hargreaves, J. K. (1992) *The Solar-Terrestrial Environment*. Cambridge University

- Press. Hoh, F.C. (1963). Instability of penning-type discharge. *Physics of Fluids*, 6:1184.
- Imber, S. M., Milan, S. E., and Lester, M.: The Heppner-Maynard boundary measured by SuperDARN as a proxy for the latitude of the auroral oval, *Journal of Geophysical Research: Space Physics*, 118, 685–697, doi: 10.1029/2012JA018222, 2013a.
- Iyemori, T. (1990), Storm-time magnetospheric currents inferred from midlatitude geomagnetic field variations, *J. Geomagn. Geoelectr.*, 42, 1249.
- Jones, T.B., Lester, M., Milan, S.E., Robinson, T.R., Wright, D.M. & Dillon, R.S. 2001, "Radio wave propagation aspects of the CUTLASS radar", *Journal of Atmospheric and Solar-Terrestrial Physics*, vol. 63, no. 2–3, pp. 99-105.
- Kane R.P., Solar cycle variation of foF2, *J. Atmos. Terr. Phys.* 54, 1201-1205, 1992.
- Kane, T.A., Makarevich, R.A. & Devlin, J.C. 2012, "HF radar observations of ionospheric backscatter during geomagnetically quiet periods", *Annales Geophysicae*, vol. 30, no. 1, pp. 221-233.
- Kelley, M., (1989). *The Earth's Ionosphere, Plasma Physics and Electrodynamics*. San Diego, California, Academic Press, Inc.
- Kivelson, M. G., and C. T. Russell (1995), *Introduction to Space Physics*, Cambridge University Press. 3, 6, 7, 8, 10, 12, 14, 24, 33, 37, 41, 42, 44, 48
- Kivelson, M. G. and Russell, C. T., eds.: *Introduction to Space Physics*, Cambridge University Press, Cambridge, UK, 1995.
- Klenzing, J., Simoes, F., Ivanov, S., Heelis, R.A., Bilitza, D., Pfaff, R., Rowland, D., ~ 2011. Topside equatorial ionospheric density and composition during and after extreme solar minimum. *Journal of Geophysical Research* 116, A12330, <http://dx.doi.org/10.1029/2011JA017213>
- Klenzing, J., Burrell, A. G., Heelis, R. A., Huba, J. D., Pfaff, R., and Simões, F.: Exploring the role of ionospheric drivers during the extreme solar minimum of 2008, *Ann. Geophys.*, 31, 2147–2156, doi:10.5194/angeo-31-2147-2013, 2013.
- Kokubun, S., Yamamoto, T., Acuña, M. H., Hayashi, K., Shiokawa, K., and Kawano, H., The GEOTAIL magnetic field experiment, *J. Geomagn. Geoelectr.*, **46**, 7-21, 1994
- Koustov, A.V., Sofko, G.J., André, D., Danskin, D.W. & Benkevitch, L.V. 2004a, "Seasonal variation of HF radar F region echo occurrence in the midnight sector", *Journal of Geophysical Research: Space Physics*, vol. 109, no. A6.
- Lester, M. 2013, "The Super Dual Auroral Radar Network (SuperDARN): An overview of its development and science ", *Journal of Advances in Polar Science*, vol. 24(1), pp. 1.
- Lester, M., Chapman, P.J., Cowley, S.W.H., Crooks, S.J., Davies, J.A., Hamadyk, P., McWilliams, K.A., Milan, S.E., Parsons, M.J., Payne, D.B., Thomas, E.C., Thornhill, J.D., Wade, N.M., Yeoman, T.K. & Barnes, R.J. 2004, "Stereo

- CUTLASS - A new capability for the SuperDARN HF radars", *Annales Geophysicae*, vol. 22, no. 2, pp. 459-473.
- Liu J.Y., Chen Y.I., Lin J.S., Statistical investigation of the saturation effect in the ionospheric foF2 versus sunspot, solar radio noise, and solar EUV radiation. *J. Geophys. Res.*, 108(A2), 1067, doi: 10.1029/2001JA007543, 2003.
- Makarevich, R. A., A. V. Koustov, and B. A. Carter (2012), Interplanetary magnetic field control and magnetic conjugacy of auroral E region backscatter, *Geophys. Res. Lett.*, 117, A01309, doi:10.1029/2011JA016943.
- Mayaud, P. N. (1980), Derivation, Meaning, and Use of Geomagnetic Indices, *Geophys. Monogr. Ser.*, vol. 22, 154 pp., AGU, Washington, D. C., doi:10.1029/GM022
- McNamara L.F., Radio amateurs guide to the ionosphere, Krieger Publishing Company, 1994.
- McWilliams KA., Ionospheric signatures of dayside reconnection processes. [Doctor of Philosophy]. University of Leicester, 2001
- McPherron, R.L., 1995. Standard indices of geomagnetic activity. In Kivelson, M.G., and Russell, C.T. (eds.), *Introduction to Space Physics*. Cambridge, UK: Cambridge University Press, pp. 451–458.
- Milan, S. E., T.B. Jones, T.R.Robinson, E.C.Thomas, and T. K. Yeoman, Interferometric evidence for the observation of ground backscatter originating behind the CUTLASS coherent HF radars, *Ann. Geophysicae*, **15** , 29 - 39, 1997a.
- Milan, S.E., Yeoman, T.K., Lester, M., Thomas, E.C. & Jones, T.B. 1997, "Initial backscatter occurrence statistics from the CUTLASS HF radars", *Annales Geophysicae*, vol. 15, no. 6, pp. 703-718.
- Millward G.H., Rishbeth H., Fuller-Rowell T.J., Aylward A.D., Quegan S., Moffett R.J., Ionospheric F2- layer seasonal and semiannual variations, *J. Geophys. Res.* 101, 5149-5156, 1996.
- Mitchell, E.J, (2007). Magnetosphere-Ionosphere Coupling. GEM tutorial.
- Nielsen E. and Schlegel K., (1983). *J. Geophys. Res.*, 84,4189
- Ossakow, S.L. and Chaturvedi, P.K., (1979) Current convective instability in the diffuse aurora. *Geophysical Research Letters*, 6:332-334
- Perkins, F.W. 1975, "Ionospheric Irregularities", *Reviews of Geophysics and Space Physics*, vol. 13(3), pp. 884.
- Rishbeth H., Setty C.S.G.K., The F-layer at sunrise, *J. Atmos. Terr. Phys.* 20, 263-276, 1961.

- Rishbeth H., Garriott O.K., Introduction to ionospheric physics, Academic press, New York and London, 1969
- Rishbeth H. (1989). Basic Physics of the ionosphere: A tutorial review of International Centre on Theoretical Physics, Trieste, Italy.
- Rishbeth H., Mendillo M., Patterns of F2-layer variability, J. Atmos. Solar-Terr. Phys. 63, 1661-1680, 2001.
- Rottger J. Ionosphere and upper atmosphere research with radars. UNESCO Encyclopedia of Life Support Systems (EOLSS), Geophysics and Geochemistry, 6.16.5.3, Paris, 2004
- Ruohoniemi, J. M., and K. B. Baker (1998), Large-scale imaging of high-latitude convection with Super Dual Auroral Radar Network HF radar observations, J. Geophys. Res., 103(A9), 20797–20811, doi:[10.1029/98JA01288](https://doi.org/10.1029/98JA01288).
- Ruohoniemi, J.M. & Greenwald, R.A. 1997, Rates of scattering occurrence in routine HF radar observations during solar cycle maximum.
- Russell, C.T. (1987). 'The Magnetosphere', in Akasofu, S-I. and Kamide, Y. (eds.) The Solar Wind and the Earth 1987. Tokyo: Terra Scientific Publishing Company, pp. 73-100
- Russell, C.T. (2000). The Solar Wind Interactions with the Earth's Magnetosphere: A tutorial. IEEE Transactions on Plasma Science 28(6), 1818-1830.
- Schrijver, C. J., & Siscoe, G. L. (2009). Heliophysics: Plasma Physics of the Local Cosmos. Cambridge, Cambridge University Press.
- Schwenn, R. (2001). Solar Wind: Global Properties. Encyclopedia of Astronomy and Astrophysics 1-9.
- Schunk, R. W. and Nagy, A. F. (2009) Ionospheres, Physics, Plasma Physics and Chemistry. Cambridge: Cambridge University Press
- Simon A., (1963). Instability of partially ionized plasma in crossed electric and magnetic fields. Physics of Fluids, 6:382
- Solomon, S.C., Qian, L., Didkovsky, L.V., Viereck, R.A. & Woods, T.N. 2011, "Causes of low thermospheric density during the 2007-2009 solar minimum", Journal of Geophysical Research: Space Physics, vol. 116, no. 7
- Suzuki, T.K. (2012). Solar Wind and its Evolution. Earth Planets Space 64,201-206
- Torr M.R., Torr D.G., The seasonal behaviour of the F2-layer of the ionosphere, J. Atmos. Terr. Phys. 35, 2237-2251, 1973.

Tsunoda, R. T. (1988), High-latitude F region irregularities: A review and synthesis, Rev. Geophys., 26(4), 719–760, doi:[10.1029/RG026i004p00719](https://doi.org/10.1029/RG026i004p00719).

Vickrey J.F and Kelley M.C. 1983 Irregularities and instabilities in the auroral F-region. High-Latitude Space Plasma Physics (Edited by B. Hultqvist and T. Hagfors), pp. 95-113. Plenum, New York

Wright J.W., The F-region seasonal anomaly, J. Geophys. Res. 68, 4379-4381, 1963.

Zakharov, I.G. and Tyrnov, O.F., Short-term critical frequency variations and their predictions in the Multitude ionospheric F2 region, Phys. Chem. Earth, 24, 371-374, 1999.

Zolesi, B. and Cander, L.R. (2014). *Ionospheric prediction and forecasting*. Springer Geophysics ISBN 978-3-642-38430-1

Ionosphere Layers profile. Retrieved October 14, 2013 from <http://www.ion.le.ac.uk/ionosphere/profile.html>